

Platinum Catchment by Noble Metal Alloys

and structural studies of Pt- and Rh-containing perovskites

Asbjørn Slagtern Fjellvåg



Dissertation for the degree of Philosophiae Doctor

Nanostructures and Functional Materials

Department of Chemistry and

Centre for Materials Science and Nanotechnology

Faculty of Mathematics and Natural Sciences

University of Oslo

© **Asbjørn Slagtern Fjellvåg, 2022**

*Series of dissertations submitted to the
Faculty of Mathematics and Natural Sciences, University of Oslo
No. 2546*

ISSN 1501-7710

All rights reserved. No part of this publication may be
reproduced or transmitted, in any form or by any means, without permission.

Cover: Hanne Baadsgaard Utigard.
Print production: Graphics Center, University of Oslo.

Preface

This thesis is submitted in partial fulfilment of the requirements for the degree of *Philosophiae Doctor* at the Department of Chemistry, Faculty of Mathematics and Natural Sciences, University of Oslo (UiO). The experimental work has been carried out at the research group for Nanostructures and Functional Materials (NAFUMA) at UiO, Herøya research park and the industrial facility of Yara International, the Swiss-Norwegian beamlines (SNBL) and ID15A at the European Synchrotron Radiation Facility (ESRF), and the CRISMAT laboratory in Caen. The work was performed between August 2016 and June 2022 as a part of the strategic research initiative industrial Catalysis Science and Innovation (iCSI). Professor Dr. Anja Olafsen Sjøstad and Dr. David Waller have supervised the work. I want to express my sincere gratitude to Anja for helping me keep momentum on the PhD-work while supporting my dream of a cycling career. Thank you for guiding me through a long education and teaching me most of the practical laboratory skills I know today. And to David, thank you for many high-quality and in-depth scientific discussions, driving the project towards a common goal for fundamental research and the industry.

Thanks to my many co-authors: Johan Skjelstad, Thomas By, Peter Stanley Jørgensen, Marco Di Michiel, David Stephen Wragg, Susmit Kumar, Amund Ruud, Øystein Slagtern Fjellvåg, Yohann Breard, David Waller and Anja Olafsen Sjøstad. Thanks to Marco Di Michiel for having our tomography beamtime at ESRF as internal work at ID15A, and to Bruno, Øystein and David for joining the experiment. Thanks to Peter for showing great hospitality and patience during my two visits to DTU, before which I knew nothing about tomography analysis. Thanks to Øystein, Amund, Åse, Marit and Anja for providing valuable feedback on the writing and content of this thesis. Thanks to Julie for joining “Team Catchment” in the fall of 2019 and for continuing our dedication to noble metal catchment. To Oleksii, good shape! Thanks for the excellent discussions with everyone involved in the catchment project and the iCSI centre. To the entire NAFUMA group, I owe you all many thanks for all my enjoyable years here. Thanks to everyone in MenaMasters and friends from the beginning of our UiO careers. Special thanks to co-founder of hedgehog bar, Chris, long-term office mate Ingrid Marie, synthesis master Salah and of course the boss Nicolai.

I had several very nice visits in Caen, and for that I thank Yohann and Bruno. The cycling race of 2018 must be a highlight (ten seconde!). I also enjoyed the scientific stay in the spring of 2020 interrupted by the corona pandemic, and in the spring of 2022. Thanks to Bruno for travelling with me to and from Caen on several occasions, and saving me from the corona pandemic in March 2020. Thanks to Michael for very educational tours at the Normandy beaches, providing the perspective needed to stand up straight in tough times.

Thanks to Rasmus for being steadfast in our corona extension cause, moving the milestone for the PhD candidates forward. It is not about the salary; it is about being respected and listened to when there are important problems to address. I hope we achieved that. Thanks to all my

colleagues, friends and family who have had to hear me complain regularly over the last six years – I am truly grateful for your patience and support.

I have, and always will, value long “gæmping” rides with my cycling friends Vebjørn, Amund, Marius, Sindre, Øyvind, The Champ, Baoughen, teammates in Asker and OSI, and friends in the cycling community. I truly appreciate traditions such as Tour de Ferie, Balestrand opp, Gran Canaria cycling camp in December and January, many cycling races in Norway and abroad, and the end of season banquet. Holidays in Kil, Svalerødkilen and at Gålå, Vasaloppet with Helmer and friends, golf at Dynekilen, the annual decathlon, the fellowship of Braourskapet and pub-season in October-November are all highlights for me. I also enjoy our many training- and physiology discussions, Jon Åsbjørn and Amund, and our travels towards becoming better athletes. And of course, intervals in Grefsenkollen are always rewarding. These are activities that always provide me with energy and joy, my sincere thanks to you all.

To my close family and friends, thank you so much for helping me relax and de-stress. I have struggled to truly enjoy my holidays and time off, but you make it possible. Special thanks for the endless support from my parents, Åse and Helmer. To my brother Øystein, thanks for all our fun times at home, on the bike, on holiday in both summer and winter, and at UiO. I have enjoyed our combined cycling and scientific discussions, from zone 1 to zone 5, and our combined beamtime-training camps in Grenoble, and recently in Switzerland. I deeply appreciate your help with the two papers on oxides in this thesis. I am certain they would not have been finished without your help. Now you need to book time in your calendar for GC training camp in the winter! Finally, special thanks to Marit for helping me bounce back after a tough 2020 and 2021. Time to enjoy!

Summary

This thesis focuses on the industrially important research topic of platinum catchment. Since the invention of the Ostwald process and the use of a Pt-catalyst for high temperature ammonia oxidation, platinum loss has been an issue of the industrial catalyst. Though several different Pt-catchment solutions have been tested since the origin, the major turning point came in 1968. Pd/Au (88/12 at. %) wires were woven into a gauze and installed downstream of the Pt/Rh catalyst to capture the evaporated Pt. Today, a Pd/Ni (91/9 at. %) alloy is the industrially used Pt-catchment system.

Several studies have investigated the industrial Pd/Au and Pd/Ni gauzes and documented severe swelling and restructuring during operation. However, the exact origin of the phenomena was unknown at the start of this project in 2016. Our first experiments were carried out in a laboratory furnace using synthetic air, giving two major findings: 1) Pt-catchment alone (exposure in air + PtO₂) causes wire restructuring, and 2) Ni-loss is caused by water vapour and air, and the presence of Ni does not affect Pt-catchment on Pd/Ni significantly. These findings show that wire restructuring is in fact an intrinsic property of the system.

After establishing that Pt-catchment causes the Pd and Pd/Ni wire to restructure, pilot plant testing of a Pd gauze was performed to compare two scenarios: 1) the effect of the industrial gas mixture and the use of a Pt catalyst for NH₃-oxidation, a process that includes Pt-catchment, and 2) the effect of the industrial gas mixture with a LaCoO₃-based catalyst for NH₃-oxidation, a process that does not include Pt-catchment. The result was that both Pd gauzes reconstructed completely, but their morphology was different; Pt-catchment caused *edged* crystallites on the Pd-wire, while the Pd-wire below the oxide catalyst formed *rounded* crystallites.

There were in fact two different origins for wire restructuring, and the investigation continued with focus on the restructuring. To understand the *edged* restructuring caused by Pt-catchment, *in situ* X-ray absorption computed tomography (absorption-CT) was performed at ID15A at the ESRF, studying Pd- and Pd/Ni wires during Pt-catchment in dry air at 1000 °C. Absorption-CT allowed us to observe 3D objects of the restructured wires and extract quantitative information of the wire restructuring and Pt-catchment as a function of time. Pt-catchment is linear until ~1 at. % Pt is captured (~4 hours) before the rate is reduced, at which point internal porosity increases. Notably, a lower $p(\text{PtO}_2)$ result in reduced Pt-catchment.

SEM/EDX analysis of the same Pd- and Pd/Ni wires as studied in the absorption-CT experiments revealed a crucial detail. After 1 day of Pt-catchment, the grain boundaries (GBs) were full of Pt, while the bulk grains were still empty of Pt. The effect was stronger for Pd than for Pd/Ni and was visible also after 4 days. This implied that the GBs play a key role as a transport path for Pt into the Pd- and Pd/Ni wires. Quasi-monocrystalline Pd- and Pd/Ni wires (grain size 20-200 μm), obtained by annealing in vacuum at 1100 °C for 7 days, restructured significantly less than the polycrystalline wires. The quasi-monocrystalline wires seemed limited by bulk diffusion, causing Pt to cover only the surface of the samples. They

also showed little restructuring. Diffusion simulations using reported diffusion coefficients supported a bulk diffusion limitation; solid-state diffusion of Pt into Pd is too slow to account for the Pt-content observed in Pt-catchment experiments. We therefore explain the observed grain reconstruction of the polycrystalline Pd- and Pd/Ni wires as restructuring due to rapid GB diffusion. Additionally, the fact that Pd-diffusion is reported to be more rapid than Pt-diffusion suggests that Kirkendall voids may participate in the formation of porosity.

To explore alloys with enhanced the bulk diffusion, several Pd/Au samples were tested as potential Pt-catchment materials. Laboratory experiments of polycrystalline wires showed two main findings: 1) The wire restructuring was reduced with increasing Au-content up to Pd/Au (50/50 at. %), and 2) Pt-catchment was similar for Pd/Au and Au, but their Pt-catchment was lower than for Pd. Alloying Pd with Au clearly improved bulk diffusion, and Pt-catchment was enhanced for the quasi-monocrystalline samples.

To test the samples at industrial conditions, a 5 months' industrial experiment was performed, including both poly- and quasi-monocrystalline versions of all samples. The wire restructuring was lowest for the Pd/Au (50/50 at. %) sample, and it showed little porosity caused by the aggressive gas/temperature conditions. However, the measured Pt-concentration was higher for the Pd-rich samples (Pd, Pd/Ni and Pd/Au (91/9 at. %)). Additionally, also the quasi-monocrystalline wires restructured in a similar way as their polycrystalline counterparts. The restructuring of the monocrystalline wires is likely caused by the Kirkendall effect and formation of internal porosity that becomes open porosity allowing continued restructuring.

The current industrial Pt-catchment material (Pd/Ni) is a metallic alloy, but other material types may also be suited for catchment. Within the iCSI Centre, perovskite-based oxides are currently under evaluation as future candidate materials for Pt-catchment, and several Pt- and Rh-containing perovskites are studied to establish a knowledge-base for these investigations. RE_2MPtO_6 ($RE = La, Nd$; $M = Ni, Co$) are *B*-site ordered double perovskites with Pt(IV) and Ni(II)/Co(II). Attempted syntheses with $M = Fe$ were unsuccessful as Fe is not easily reduced to Fe(II) at the high pO_2 conditions required for the synthesis of oxides with Pt(IV). Attempted syntheses with $RE = Y$ resulted in multiphase samples with a Pt-rich pyrochlore ($Y_2Pt_{2-x}M_xO_3$) and *M*-rich perovskite ($YM_{1-x}Pt_xO_3$). Non-equimolar compositions in the system $LaNi_{1-x}Pt_xO_3$ with $x \geq 0.20$ are monoclinic ($P2_1/n$) and have *B*-site ordering to a degree correlating with the Pt-content. The samples ($x \geq 0.20$) also show a domain structure with La_2NiPtO_6 -like (Pt-rich) domains and $LaNiO_3$ -like (Pt-depleted) domains due to Pt requiring oxidation state +IV.

For the Rh-containing perovskites, also Y can be used as the *A*-site cation ($YM_{0.50}Rh_{0.50}O_3$, $M = Co, Fe$), but for $M = Ni$, the sample contained several impurities. *B*-site ordering is absent for all Rh-containing perovskites regardless of the *A*-site cation. The absence of *B*-site ordering imply that the oxidation states are likely *M*(III) and Rh(III). However, both the unit cell volume, XAS-, and magnetic measurement indicate that Ni(II) and Rh(IV) is present to a significant degree in $LaNi_{1-x}Rh_xO_3$, especially for the Rh-rich samples ($x \geq 0.60$). The unit cell volume of $YM_{0.50}Rh_{0.50}O_3$ ($M = Co, Fe$) also indicate some degree of mixed valence (60-70 % +III/+III).

Table of content

Preface	iii
Summary	v
Table of content	vii
List of papers.....	ix
List of abbreviations	xi
1. Introduction.....	1
1.1. Historical background.....	1
1.2. Motivation behind the catchment project.....	4
1.3. Scope of work	7
2. Scientific background	9
2.1. The Ostwald process	9
2.1.1. Details on ammonia oxidation	9
2.2. Platinum catchment.....	11
2.3. Pt-catchment on LaNiO ₃ – experiments prior to the catchment project.....	14
2.4. Noble metals and their oxidation	15
2.4.1. Structure, bonding and mechanical aspects	15
2.4.2. Diffusion	17
2.4.3. Oxidation of Pd, Pt, Rh, Au and Ni	19
2.5. Perovskite oxides	22
2.5.1. An extra note on relevant perovskite oxides	23
3. Experimental setup and characterization methods.....	27
3.1. Pt-catchment experiments	27
3.1.1. Sample information.....	27
3.1.2. Laboratory Pt-catchment experiment.....	27
3.1.3. Pt-catchment during <i>in situ</i> tomography	29
3.2. Scanning electron microscopy and energy dispersive X-ray spectroscopy	31
3.2.1. Sample preparation for cross section imaging	32
3.3. Synthesis of perovskite oxides	33
3.4. Powder diffraction	33
3.4.1. Rietveld refinements	35
4. Results and discussion	37

4.1.	Pt-catchment by noble metal alloys.....	37
4.1.1.	Role of Ni in the Pd/Ni-alloy (Paper I)	38
4.1.2.	Role of PtO ₂ – the first sign of swelling and porosity (Paper I).....	41
4.1.3.	Pilot plant experiments – identifying two causes for porosity (Paper I)	42
4.1.4.	Understanding Pt-catchment on Pd – <i>in situ</i> tomography (Paper II).....	43
4.1.5.	Role of grain size on Pt-catchment on Pd- and Pd/Ni wires (Paper II)	45
4.1.6.	Pt-catchment on Pd/Au alloys (Paper III)	47
4.1.7.	Pt-catchment at industrial conditions (Paper III).....	50
4.1.8.	Short analysis of 28 days long pilot plant experiment.....	54
4.1.9.	Limiting factors for Pt-catchment (Paper II and III)	55
4.1.10.	Mechanism of grain reconstruction (Paper II and III).....	61
4.1.11.	Restructuring of the quasi-monocrystalline samples.....	62
4.2.	Structural aspects of Pt- and Rh-containing perovskites	63
4.2.1.	Synthesis and structural aspects of Pt-containing double perovskites.....	63
4.2.2.	Synthesis and structural aspects of Rh-containing double perovskites	68
4.2.3.	Combined Pt- and Rh-perovskites.....	72
5.	Summarizing discussion and outlook.....	75
	Appendix	79
	References	85

List of papers

Paper I:

Grain Reconstruction of Palladium and Palladium-Nickel Alloys for Platinum Catchment

A. S. Fjellvåg, D. Waller, J. Skjelstad and A. O. Sjøstad

Johnson Matthey Technology Review, **2019**, 63, (4), 236

Paper II:

Mechanism of grain reconstruction of Pd and Pd/Ni wires during Pt-catchment

A. S. Fjellvåg, P. S. Jørgensen, D. Waller, D. S. Wragg, M. D. Michiel and A. O. Sjøstad

Materialia, **2022**, 21, 101359

Paper III:

Platinum catchment using Pd/Au alloys: Effect of enhanced diffusion

A. S. Fjellvåg, D. Waller, T. By and A. O. Sjøstad

Submitted to *Industrial & Engineering Chemistry Research*

Paper IV:

Structural disorder and antiferromagnetism in $\text{LaNi}_{1-x}\text{Pt}_x\text{O}_3$

A. S. Fjellvåg, Ø. S. Fjellvåg, Y. Breard and A. O. Sjøstad

Journal of Solid State Chemistry, **2021**, 299, 122181

Paper V:

Interplay of valence states and magnetic interactions in the perovskite system $\text{LaNi}_{1-x}\text{Rh}_x\text{O}_3$

A. S. Fjellvåg, Ø. S. Fjellvåg, S. Kumar, A. Ruud and A. O. Sjøstad

Journal of Solid State Chemistry, **2021**, 298, 122124

List of abbreviations

CRISMAT	-	Laboratoire de Cristallographie et Science des Matériaux
CT	-	Computed tomography
DTU	-	Technical University of Denmark
EDX	-	Energy-dispersive X-ray spectroscopy
ESRF	-	European synchrotron radiation facility
<i>et al.</i>	-	And more
<i>e.g.</i>	-	For Example
GB	-	Grain boundary
ICP-OES	-	Inductively coupled plasma – optical emission spectrometry
iCSI	-	Industrial Catalysis, Science and Innovation
ID	-	Inner diameter
<i>i.e.</i>	-	That is
MS	-	Mass spectrometry
NAFUMA	-	Research group for nanostructures and functional materials
OD	-	Outer diameter
PDF	-	Pair distribution function
SEM	-	Scanning electron microscopy
SNBL	-	Swiss-Norwegian beam lines
SR	-	Synchrotron radiation
TG	-	Thermogravimetry
XAS	-	X-ray absorption spectroscopy
XPS	-	X-ray photoelectron spectroscopy
XRD	-	X-ray diffraction
XRF	-	X-ray fluorescence
3D	-	3 dimensional

1. Introduction

1.1. Historical background

At the dawn of the 20th century, the human population was facing a great challenge known as *The Nitrogen Problem*. Sir William Crookes presented in 1898 a concern for the world's supplies of wheat and that the increasing human population would soon overwhelm the production rates of wheat [1]. Guano (ammonia-rich bird excrement; NH_3) and Chile saltpetre (NaNO_3) were at this time the primary sources of nitrogen-based fertilisers used for agriculture and wheat production. There was a clear need to either increase recycling of nitrogen-rich waste or fixate nitrogen from the air, to be used as fertilisers. Otherwise, it was estimated that the world could not sustain a population larger than approximately 2 billion people [2].

Guano was mined along the west coast of Chile and Peru (Figure 1), and Chile saltpetre from the Atacama Desert. The fight over these valuable resources was decided in The War of the Pacific in 1884 (Saltpeter War; *Salpeterkrigen* in Norwegian), when Chile gained control over most of the export of fixated nitrogen to the rest of the world [3], at the cost of Peru and Bolivia. The supplies from Chile were gradually depleted, especially Guano, and consequently, the need to fixate nitrogen from the air was increasing. This fact boosted the research on ammonia (NH_3) and nitric acid (HNO_3) production in the early 1900s. Ammonia and nitric acid are the two main chemical components in nitrogen-based fertilisers.

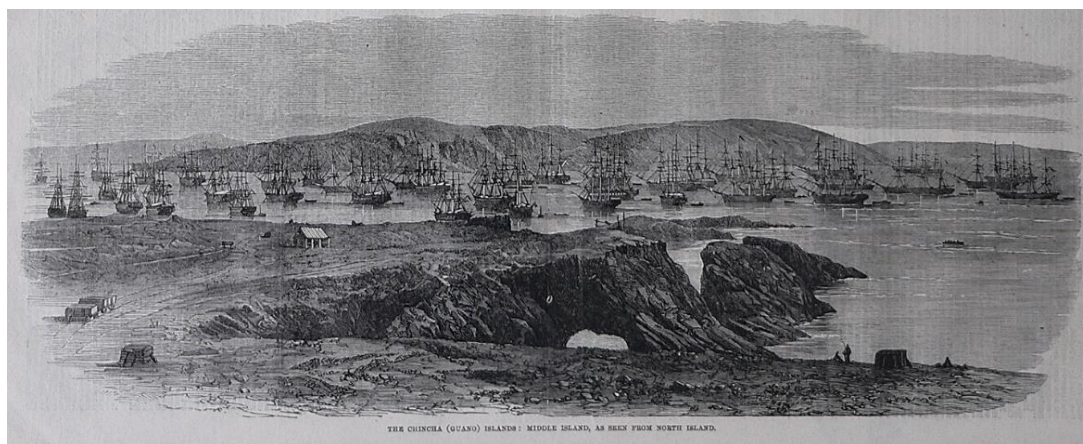


Figure 1. The Chincha Islands outside the west coast of Peru and the Peruvian fleet, in 1863. Guano mining was significant at this time for Peru, but the deposits at the Chincha Islands were gradually depleted during the 1870s. Credits: Manuel González Olaechea y Franco [4].

When *The Nitrogen Problem* was presented to the German Professor Wilhelm Ostwald, he addressed the task of nitric acid production, considering it his duty to contribute in making his country independent of Chile saltpetre. Two possible routes were considered for the manufacture of nitric acid; a direct reaction between nitrogen (N_2) and oxygen (O_2) from the air or oxidation of ammonia. He assumed it would be simpler to react nitrogen from ammonia rather than fixating nitrogen from the stable nitrogen molecule (N_2), hence he chose oxidation of ammonia. Notably, oxidation of ammonia was first performed by Isaac Milner in 1789, and

1. Introduction

later by Frédéric Kuhlmann in 1838 [1]. When Ostwald started his laboratory work in 1901 (Figure 2a) he was unaware of Kuhlman's previous experiments on ammonia oxidation with a platinum (Pt) catalyst at 300 °C. However, Ostwald was the first to study ammonia oxidation in a systematic manner. He understood that the key to the process was a high flow rate over the Pt-catalyst, which stabilises the product (nitric oxide; NO) due to the short contact time between the gas and the catalyst [1]. Further oxidation to nitrogen dioxide (NO₂) and reaction with water forms the final product, nitric acid. Ostwald and Brauer built a pilot plant (Figure 2b) for testing in 1904. The first large scale plants were built in 1906 and 1908, the latter producing 3 tons of 53 % nitric acid (in water) per day [1]. A picture of large-scale ammonia burners from the 1960s is provided in Figure 2c. The reaction of ammonia to nitric acid has certainly been optimised since Ostwald's invention, but the key steps of *The Ostwald Process* are still the same.

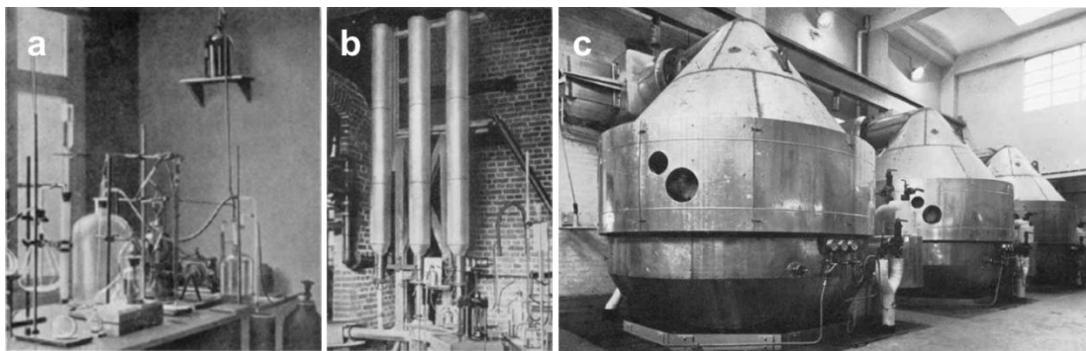


Figure 2. a) Ostwald's laboratory setup for ammonia oxidation, b) the pilot plant for ammonia oxidation by Ostwald and Brauer from 1904 [1], and c) three parallel ammonia burners from the 1960s [5]. The pictures are reused with permission from Johnson Matthey Plc.

The second part of *The Nitrogen Problem* was the production of ammonia. The Haber-Bosch process presented a solution for the synthesis of ammonia at the early 1900s. A high-pressure reaction between the two pure gases of hydrogen (H₂) and nitrogen (N₂) over an iron oxide-based catalyst was industrialised in Germany [6], and the first plant in Oppau was finished in 1913 (Figure 3). The fact that supplies of Guano- and Chile saltpetre were considered unreliable in the case of war was a second motivation for inventing a large-scale production process for ammonia synthesis in the early 1900s; a hard-learned lesson for both Britain and USA, considering that World War I started in 1914. At first, ammonia production was used to supply Germany with raw material for explosives during World War I. Without the Haber-Bosch process at hand, it is said that Germany would have run out of explosives, and the war would have ended one, perhaps two, years earlier [7]. After World War I, ammonia production expanded world-wide for the production of fertilisers and the first plant in Great Britain was finished in 1924 at Billingham (Figure 3) [2]. Since then, the Haber-Bosch process has dominated the global production of ammonia, where approximately 80 % of all produced ammonia is used for nitrogen-based fertilisers [6].



Figure 3. Left: The first Haber-Bosch ammonia production facility located in Oppau, Germany. The picture is a reproduction of a painting by Otto Bollhagen from 1914, reused with permission from BASF [8]. Right: A high pressure reactor for ammonia synthesis from the plant at Billingham, reused with permission from Johnson Matthey Plc [2].

Another industrial fertiliser production path was developed in Norway in the early 1900s. Unlike the Ostwald process, the Birkeland-Eyde process was based on the direct fixation of nitrogen from the air using large high temperature furnaces and the electric arc technology (Figure 4) [9]. This was the first industrial production of synthetic fertiliser worldwide, marking the beginning of the industrial adventure of the Norwegian company Norsk Hydro (later Yara International), established in 1905. The process was based on passing air through an electric arc, causing nitric oxide (NO) to form due to the extreme amount of energy present, similar to a lightning bolt during a thunderstorm. The three plants at Notodden (smaller test facility) and Rjukan (Rjukan I (Figure 4) and Rjukan II) were built from 1905-1920. The maximum capacity was 140 tonnes of fertiliser per year at the end of the 1920s. At peak production, the two plants at Rjukan had 139 electric arc furnaces with a total power consumption of 245 MW, equivalent to the power consumption of approximately 130 000 households in Norway in 2016 [10]. Such extreme power consumption was mainly possible to sustain in Norway due to access to cheap hydropower. The Birkeland-Eyde process was mainly industrialised in Norway and a few other countries. However, also for Norsk Hydro, the Haber-Bosch (NH_3 -production) and Ostwald processes (reaction of NH_3 to HNO_3) outcompeted the Birkeland-Eyde process, requiring only one quarter of the energy. This caused Norsk Hydro to gradually transform the facility through the 1930s, even though industrial facilities for the Haber-Bosch and Ostwald process were highly complex in comparison. The combination of the Haber-Bosch and Ostwald processes has dominated the production of nitric acid since then [9]. Today, Yara International is one of the world leading companies in the production of nitrogen-based fertilisers, and the facility at Herøya (Porsgrunn, Norway) is one of the largest nitric acid production plants in the world. The plant is capable of producing up to 3500 tonnes of nitric acid per day [11]. Similar to ammonia, approximately 80 % of the global production of nitric acid is used to produce fertilisers.

1. Introduction

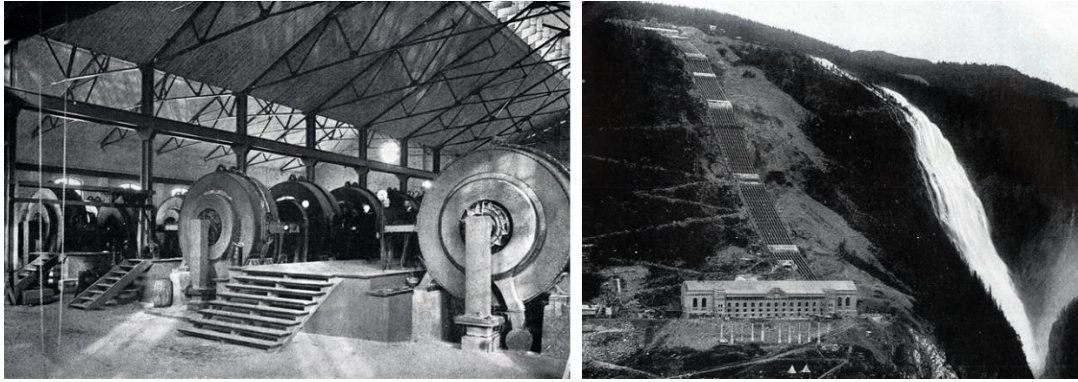


Figure 4. Left: The Birkeland-Eyde furnaces used for nitric oxide production, from the factory at Notodden in 1907. Right: The new factory at Rjukan in 1911 when the factory was operational for the first time. Reused with permission from Hydro [9].

The most common nitrogen compounds in fertilisers are currently ammonium nitrate (NH_4NO_3) and urea ($\text{CO}(\text{NH}_2)_2$). Potassium nitrate (KNO_3) and different ammonium phosphate compounds ($(\text{NH}_4)_2\text{HPO}_4$, $(\text{NH}_4)_2\text{HPO}_4$) make up the rest. In terms of nutrients, approximately 55 % of the global fertiliser consumption is nitrogen, 25 % is phosphorus and 20 % is potassium [12]. It is today estimated that ~ 40 % of the current population worldwide would not be alive without the use of synthetic fertiliser. This is why fertiliser production has increased enormously the last century, correlating with the increase in the human population. Large-scale production of synthetic nitrogen-based fertiliser could very well be the most important invention of the 20th century [6].

1.2. Motivation behind the catchment project

Nitric acid is today produced via the Ostwald process, where the first of three steps is the selective oxidation of ammonia (NH_3) to nitric oxide (NO). The reaction is performed at high temperature (800 – 950 °C) and moderate pressure (1 – 14 bar) over a Pt/Rh (91/9 – 83/17 at. %) catalytic gauze (Figure 6) [13]. Further details are provided in section 2.1. During industrial operation, the input gas (NH_3 and air) only holds a temperature of ~ 300 °C before the combustion reaction (Eq. 2-1; -227 kJ/(mol NH_3)), and it is purely the heat of the reaction that causes the gas to obtain a temperature of 800 – 950 °C.

The extreme heat of the reaction has some side effects. Pt, and some Rh, evaporate in the form of the volatile molecule PtO_2 (and RhO_2) [14]. Parts of the evaporated PtO_2 (and RhO_2) condense on the catalyst surface, but significant quantities are permanently lost to the gas stream. Interestingly, the condensation of the Pt and Rh causes the growth of a very strange cauliflower-like feature on the surface of the catalyst (Figure 7), which are actually quite rich in Rh [14].

The noble metal loss of Pt (and Rh) has been an issue with the Pt/Rh catalyst since the invention of the ammonia oxidation process, originally based on a pure Pt catalyst. A noble metal loss of 0.05-0.2 g/tonne HNO_3 is expected even for modern plants, depending on operating conditions [13] (up to 0.40 g/tonne HNO_3 in old high-pressure plants [15]). With

reference to the Herøya site, which produces 3500 tonnes of HNO_3 per day [11], this corresponds to a Pt loss of 175-700 grams per day, translating to 64-256 kg per year and an annual cost of approximately 19-76 MNOK (1.8-7.2 MEUR)(Appendix: Figure A1). Low-pressure (atmospheric) plants have a lower noble metal loss, but many more ammonia oxidation reactors (as the one in Figure 5) are needed to produce the same quantity of acid. This translates to high investment- and low operating costs; historically chosen in Europe due to high energy costs [13]. However, high-pressure reactors are smaller, fewer in number, and have low investment- and high operational costs; historically chosen in America. The high pressure plants (10-14 bar) usually need to change the Pt/Rh gauzes every 4-6 weeks, while atmospheric/low pressure plants may run for a whole year before changing the Pt/Rh gauzes [13]. Today, medium- and high pressure plants are favoured over atmospheric plants.

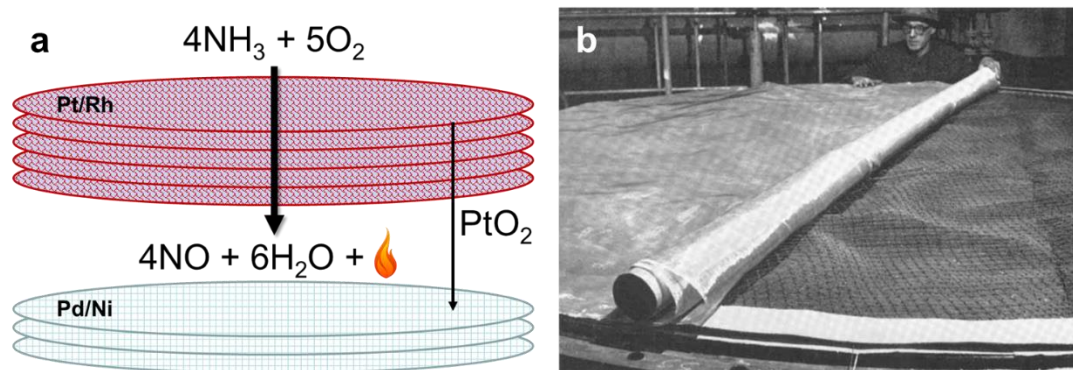


Figure 5. a) Illustration showing the concept of ammonia oxidation over several Pt/Rh catalytic gauzes and Pt-catchment on two Pd/Ni catchment gauzes. b) Picture showing the installation of a catalytic gauze in an ammonia oxidation reactor, reused with permission from Johnson Matthey Plc [16]. When the reactor is closed, the gas flows down through the reactor as illustrated in a).

Mitigation of noble metal loss has been a topic of investigation since the development of the Oswald process, and various Pt-catchment systems have been explored. In the early phase, physical gas filtering solutions such as glass wool filters, Rachig rings and marble chips were explored, but the recovery of noble metals was very low. In 1968, Holzmann [17] invented a Pd/Au (88/12 at. %) gauze to be used for Pt-catchment, consisting of a woven net of 70-120 μm wires (Figure 6a). The net was located below the Pt/Rh catalyst in the ammonia oxidation reactor, also at approximately 900 $^{\circ}\text{C}$, and separated from the catalyst using a Megapyr alloy (Fe-Cr-Al alloy). This was the birth of the original Pd-based Pt-catchment system.

In the early phase of the development of the Pt catchment technology, the plant operators observed an increase in mass and volume of the nets during operation, and microscopy documented changes in the surface morphology, indicating that the system successfully captures Pt. A single Pd/Au (88/12 at. %) net captured between 65 and 10 % of the lost Pt, depending on the operational pressure in the reactor. Notably, a high operational pressure result in higher Pt-loss and lower relative Pt-catchment [15, 16]. A stack of several nets can thus capture a large fraction of the evaporated Pt even in high pressure reactors.

The Pd/Au (88/12 at. %) alloy is today replaced by a Pd/Ni (91/9 at. %) alloy, which was introduced during the 1990s, reducing both cost and improving the Pt-catchment efficiency

1. Introduction

[18]. However, a large change in morphology occurs for both the old Pd/Au and the new Pd/Ni gauzes, causing the nets to lose mechanical strength and grow into something more similar to a porous plate (Figure 6b). This restricts gas flow through the gauze pack and causes a large pressure drop through the reactor (Figure 6c), limiting the number of catchment nets that can be installed simultaneously.

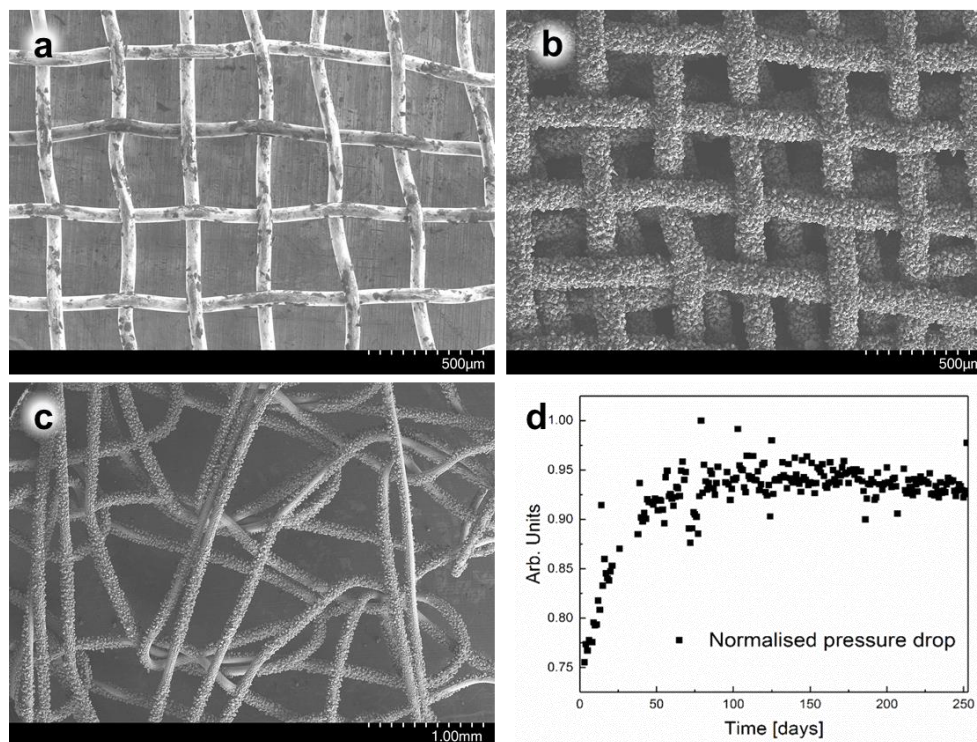


Figure 6. a) Pd/Ni (91/9 at. %) net before installation, b) Pd/Ni (91/9 at. %) net after 45 days of operation, c) knitted Pt/Rh (91/9 at. %) gauze after 46 days of operation, d) Normalised pressure drop observed during the ammonia oxidation reaction at the facility of Yara International (Herøya, Norway).

Unfortunately, the Pd-based catchment system suffers from a significant loss of Pd during operation. This was not a big issue when the system was invented in 1968, as the price of Pd was much lower than that of Pt. In fact, at the start of the current investigation in 2016, the price of the two elements were approximately equal, while Pd is today more than twice as expensive as Pt (Appendix: Figure A1). This makes Pd-loss a detrimental issue of the Pd-based Pt-catchment system. The most expensive noble metal is currently rhodium (Rh), priced at 4309 NOK/g in June 2022 (Appendix: Figure A1). Even though the loss of Rh is lower than that of Pt, it may cause industry to gradually increase focus on reducing the use and increasing the recovery of Rh as well.

Despite their high price and low abundance, the noble metals are used in several different applications, such as in chemical- and petrochemical processes and equipment, fuel cells and in electronics. It is therefore a continuous task for the industry to reduce the need for noble metals, and to develop new technology with the aim of minimizing the permanent loss of noble metals. Within this responsibility comes the task of ensuring recycling of the noble metals. In terms of innovation, it is highly favourable with technological improvements that can be implemented within the framework of an existing technology; improvements that do not

require drastic changes to the production facilities. Such an example is the Pd-based Pt-catchment system. After its invention in 1968, it could simply be added to the bottom of the gauze pack in most nitric acid plants without large modifications of the reactor, and it could immediately be implemented in nitric acid plants world-wide.

In many ways, minimizing costs and following regulations are frequently the main driving forces behind technological improvements and environmental efforts in the industrial sector. An example is the significant tax to be paid for N₂O emissions, which resulted in a large industrial focus on N₂O abatement in the nitric acid production in the 1990s; another example of technological improvements that are compatible with the existing technology. At the time, ~50 % of the greenhouse gas emissions (in CO₂-equivalents) from nitric acid production came from N₂O, which is today decomposed catalytically [19].

Over the last decades, several research projects at the NAFUMA group (UiO) have focused on industrially relevant topics in collaboration with Yara International and K. A. Rasmussen. An example is the PhD-work by Lenka Hannevold from 2005 focusing on the Pt/Rh catalyst for ammonia oxidation [14], establishing that the loss of Pt and Rh was due to evaporation of the oxide molecules PtO₂ and RhO₂. It was also established that the Pt- and Rh-loss from the Pt/Rh catalyst was, to a large extent, unavoidable. Around 2008, a project led by K. A. Rasmussen focused on reducing N₂O emissions, a bi-product from the ammonia oxidation reaction and a strong green-house gas. Different oxide based catalysts were tested, and the candidate material LaNiO₃, deposited on a metallic net, was tested in Yara's pilot plant for that purpose. A few years after the project had finished, in 2013, the LaNiO₃ nets arrived in the NAFUMA group for chemical analysis. Both Pt and Rh were identified using SEM-EDX, and powder X-ray diffraction indicated formation of the double perovskite La₂NiPtO₆ and some LaNi_{1-x}Rh_xO₃, in addition to Pt metal (see section 2.3). These findings set the scene for my own master project from 2014-2016, exploring fundamental properties of the perovskite systems LaNi_{1-x}M_xO₃, M = Rh, Pt and their catalytic activity towards decomposition of N₂O [20]. Simultaneously, the idea of possible Pt-catchment using LaNiO₃ was born. Along with the issues of the industrial Pd/Ni (91/9 at. %) Pt-catchment system, the topic of Pt-catchment came on the agenda, as a part of the iCSI centre hosted by NTNU (2016-2023). One of the original topics was indeed Pt-catchment on LaNiO₃, and it is now handled by the second PhD work in the catchment project, Julie Hessevik (from 2019). In this work, structure-property relations of Pt- and Rh-perovskites were investigated, with the application of Pt-catchment (and Rh-catchment) in mind. My main focus in the iCSI centre has been to understand the mechanism of Pt-catchment using Pd-based catchment materials, and look for possibilities for improving metal based systems for Pt-catchment, relevant for the industrial ammonia oxidation process.

1.3. Scope of work

When this study started in the autumn of 2016, the origin behind the swelling and the restructuring of the industrial Pd/Ni (91/9 at. %) alloy was not understood. Only a handful of

1. Introduction

papers [15-17, 21-34] and patents [18, 35-41] were published on the topic, and our first task was to find the parameter(s) that cause the wire restructuring (section 4.1.1 – 4.1.3, Paper I):

- Construct a reactor system for performing gas transport experiments (including Pt-catchment) with various gas mixtures.
- Understand the role of Ni in the Pd/Ni catchment system, and identify if Pd and Pd/Ni catchment systems behave differently during Pt-catchment
- Simulate the industrial scale Pt-catchment process (without NH_3/NO_x in the gas mix) and identify the parameters that cause swelling, porosity and the restructuring (grain reconstruction) of the Pd and Pd/Ni wires.
- Identify the origin of Pd-loss from the industrial Pd/Ni (91/9 at. %) Pt-catchment alloy.

This investigation (Paper I) led us to understand that catchment of Pt from PtO_2 causes grain reconstruction, an intrinsic property of the Pd and Pd/Ni system during Pt-catchment. A major part of the project was spent on understanding the mechanism behind the restructuring process (section 4.1.4 – 4.1.11, Paper II and Paper III):

- Perform *in situ* tomography (absorption-CT) to view the structural development of the wires during Pt-catchment
- Understand the mechanism for the grain reconstruction process, and derive parameters which can be adapted to produce an improved Pt-catchment system.
- Explore the role of diffusion during Pt-catchment, and investigate the effect of enhanced bulk diffusion of the catchment material by use of Pd/Au alloys.
- Test the improved Pd/Au catchment system in an industrial experiment to test the real potential of this catchment system.

As a pre-project to Pt-/Rh-catchment on perovskites, structural aspects of Pt- and Rh-containing perovskites were of high interest from the start of the project. The main objectives can be summarized as the following (section 4.2, Paper IV and Paper V):

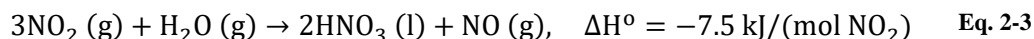
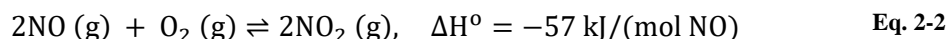
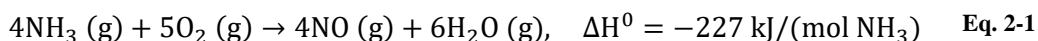
- Perform synthesis and compare structural aspects of several Pt- and Rh-containing double perovskites $RE_2MM'O_6$ ($RE = \text{La, Nd, Y}$; $M = \text{Ni, Co, Fe}$; $M' = \text{Pt, Rh}$).
- Investigate the perovskite systems $\text{LaNi}_{1-x}M'_x\text{O}_3$ ($M' = \text{Pt, Rh}$), with focus on structural aspects, B-site ordering and oxidation states.

2. Scientific background

This chapter covers background information on the scientific topics relevant for this thesis. This includes the Ostwald process for production of nitric acid, previous work on Pt-catchment, and general scientific background on the relevant metal used for Pt-catchment and the perovskite oxides that are studied.

2.1. The Ostwald process

Large-scale production of synthetic nitrogen-based fertilizers is primarily performed through two processes: 1) the Haber-Bosch process to produce NH_3 [6], and 2) the Ostwald process to produce HNO_3 from NH_3 . The Ostwald process consist of three main steps, where the first step is the selective oxidation of NH_3 to NO at high temperature (800-950 °C) and medium pressure (1-14 bara) over a Pt/Rh (91/9 – 83/17 at. %) catalytic gauze (Eq. 2-1) [13]. The second step is the oxidation of NO to NO_2 performed at 1-10 bar and 150 – 450 °C (Eq. 2-2), and the third is absorption of NO_2 in water to form HNO_3 (Eq. 2-3) [13, 42].

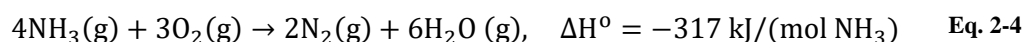


Oxidation of NO to NO_2 is performed as a homogeneous reaction proceeding without a catalyst. The operational efficiency may be improved by the use of a solid-state catalyst. However, the reaction is favoured by low temperatures and high pressure, and it is difficult to obtain a sufficient conversion rate to make the catalytic process with a solid-state catalyst beneficial [43]. Despite these challenges, ongoing research at the iCSI centre work towards the development of a catalyst for NO oxidation [43].

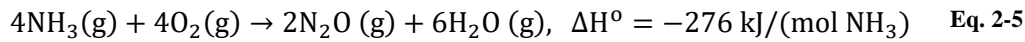
In the third step (Eq. 2-3), NO_2 is absorbed in water in a precipitation column, where it disproportionates into HNO_3 (N(V)) and NO (N(II)). The liquid HNO_3 is extracted from the bottom of the column in a concentration between 50 and 70 wt. % [13], while $\text{NO}(\text{g})$ is recycled back to be oxidized to NO_2 (Eq. 2-2). HNO_3 is the final product of the Ostwald process and is reacted with calcium, ammonia or phosphates to form the final fertilizer product.

2.1.1. Details on ammonia oxidation

It is extremely important that the ammonia oxidation (Eq. 2-1) reaction have a high yield and high selectivity towards NO . Two other undesired side reactions may occur (Eq. 2-4 and Eq. 2-5):



2. Scientific background



Both side reactions have a more negative enthalpy (ΔH°) than the desired reaction (Eq. 2-1), making them likely to occur if the catalyst (Pt/Rh) and conditions (temperature, pressure, O_2/NH_3 -ratio, gas velocity) are not optimized towards NO formation. For this purpose, the gas velocity is kept high in order to keep the residence time at the catalyst surface suitably low, in the range of 1 – 10 ms [13]. The reaction time itself is actually in the range of 10^{-11} s, and it is likely the diffusion of ammonia and oxygen to the catalyst surface that are the rate controlling factors. If the residence time (1 – 10 ms) is too high, there is a risk of NO decomposing, while too short residence times may cause unreacted ammonia to slip through the catalyst. This affects the number of Pt/Rh gauzes that is installed. A sufficient number of gauzes is needed to oxidize almost all ammonia, while too many gauzes result in the decomposition of NO. The gauze packs are designed to optimize selectivity, and the Pt/Rh gauzes are today usually knitted (Figure 6c).

A selectivity of 94 – 98 % towards NO is today's industry standard achieved with the Pt/Rh catalyst, with a lower selectivity at higher pressure. 0.013-0.26 % N_2O is formed, a small concentration of unreacted ammonia remains (~ 0.02 %) and the rest is N_2 [19]. Low selectivity towards NO is costly in the sense that NH_3 is wasted, but N_2O is in addition a greenhouse gas that is 265-310 times more powerful than CO_2 [19]. A specific catalyst ($\text{Co}_2\text{AlO}_4 - \text{CeO}_2$) is therefore installed below the gauze pack to decompose the formed N_2O , in the form of oxide pellets [19]. Other NH_3 -oxidation catalysts (Eq. 2-1) can produce lower N_2O -emissions than Pt/Rh, such as the perovskite oxide LaCoO_3 , however, the obtained NO-selectivity is lower than with the Pt/Rh catalyst.

As mentioned in the introduction, the gas mixture is only pre-heated to a temperature of ~ 300 °C before it arrives at the Pt/Rh-catalyst. It is the extreme heat released by the ammonia oxidation reaction (Eq. 2-1) that causes the process temperature to maintain around 800 – 950 °C. It is reported that local hotspots with temperatures up to 1100 °C and possibly more are present on the catalyst surface [14]. The hotspots are active centres for ammonia oxidation and are located close to defects. One consequence of the extreme heat and hotspots is evaporation of Pt and Rh (mainly Pt) in the form of oxide molecules, PtO_2 and RhO_2 [14]. Gaseous PtO_2 and RhO_2 is transported to colder zones on the Pt/Rh catalyst surface, and due to a vapour-condensation mechanism, beautiful cauliflower-like shapes grow on the catalyst surface during operation (Figure 7). The cauliflowers are quite rich in Rh, with up to 45 at. % Rh near the surface, compared to the nominal composition (9-19 at. % Rh) [14]. Not all PtO_2 and RhO_2 condense on the wire surface, and a significant and permanent loss occurs, mainly of Pt. The noble metal loss from the catalyst is intrinsic of the system, but is lower for a Pt/Rh alloy compared to pure Pt [13]. A further change in alloy composition can reduce the noble metal loss, such as the use of Pt/Rh/Pd alloys. This is believed to be related to the low volatility of Pd and PdO [44]. However, this affects also the selectivity of the catalyst towards NO formation [25]. Ammonia oxidation performed with Pt/Rh/Pd alloys or the pure metals of each element all lead to some sort of surface restructuring.

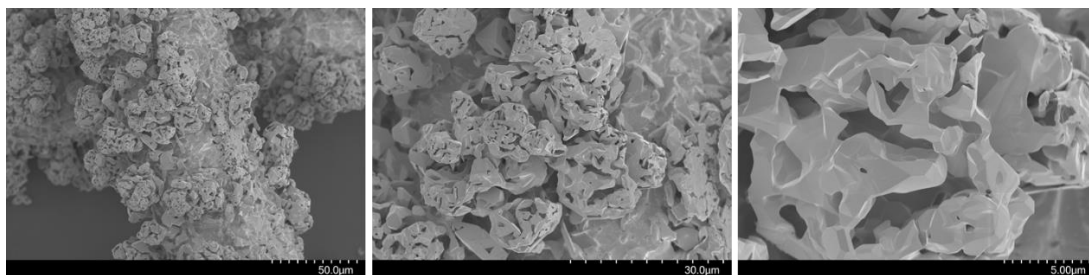


Figure 7. SEM images of the surface of a Pt/Rh (91/9 at. %) combustion gauze operated for 46 days, showing the cauliflowers that grow on the surface during the ammonia oxidation reaction.

The ammonia oxidation catalyst is replaced when the conversion and selectivity to NO is no longer satisfactory, or when the mechanical strength of the catalyst becomes too low. It is believed that the enrichment in Rh in % contributes in the deactivation of the catalyst by formation of Rh_2O_3 . The deactivation is accelerated if the catalyst is contaminated by Fe, or if the temperature in the reactor becomes too low. A high purity NH_3 -feed and good control of the operating conditions is the key to a long catalyst lifetime [45].

At other process conditions and with a different catalyst, the favoured product can be changed (NO , N_2 , N_2O). An example is the ammonia slip reaction (Eq. 2-4), where the favoured product is N_2 . Industrial use of the ammonia slip reaction comprises the addition of NH_3 to the diesel engine exhaust for the reduction of NO_x to N_2 , and the remaining NH_3 is thereafter decomposed to N_2 in the ammonia slip reaction. Pt/Rh catalysts are also under investigation for this purpose, where different compositions and conditions are needed to obtain the desired product (N_2) [46]. The conditions are quite different from ammonia oxidation in the Ostwald process, typically moderate temperature (200-500 °C), ambient pressure and excess oxygen are used (500 ppm NH_3 and 5 % O_2) [47].

2.2. Platinum catchment

The Pt- (and Rh-) loss from the Pt/Rh catalyst is largely unavoidable, and modifications of the Pt/Rh catalyst has not been successful in avoiding a noble metal loss. Recovery of Pt (and Rh) was for long attempted using physical gas filtering systems down-stream of the catalyst, but the efficiency was generally low. A Pd/Au (88/12 at. %) alloy was in 1968 presented as a high quality Pt-catchment system by Holzmann and the Degussa company [16, 17]; a vast improvement in Pt-catchment technology. Several patents have been filed since this invention, with different variations in composition. To reduce costs and improve efficiency, Au has been substituted with simple metals such as Ni, Co and Cu [23, 36]. The Pd/Ni (91/9 at. %) alloys is today the most common Pt-catchment system. A different solution was at first used in Russia, where a calcium oxide (CaO) based sorbent [48] was used to capture both volatilized metal-oxide molecules and physical particles, with a Pt-recovery of ~50 %. Hybrid solutions with both Pd-gauges and the calcium oxide sorbent has also been used in Russia [49].

Holzmanns' two papers from 1968 and 1969 [16, 17] investigate the selected composition throughout the entire Pd/Au-system, showing that Pt-catchment is highest for the Pd sample. For the Pd/Au alloys, the Pt-catchment is reduced with increasing Au-content. However, Au

2. Scientific background

capture almost as much Pt as Pd/Au (78/22 at. %) (Figure 8). Pd and Pd/Au alloys furthermore suffer from significant Pd-loss, and for every gram of Pt captured, 0.22-0.39 g of Pd is lost. This includes the Pd/Au alloys, and the Pd-loss is higher for the Pd-rich samples. Because the observed Pt-catchment is lower for the Pd/Au alloys, the Pd-loss in mass is half for Pd/Au (50/50 at. %) compared to Pd. Holzmann also reports that structural changes occur to the wires, but does not pursue it in his studies.

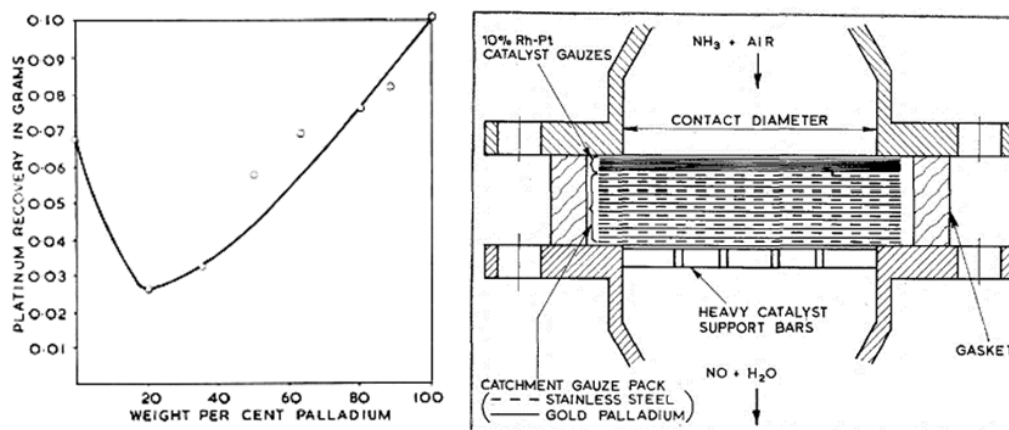


Figure 8. Left: Mass (gram) Pt recovered by using different Pd/Au alloys as Pt-catchment material, reused with permission from Johnson Matthey Plc [16]. b) Schematic of how the Pt/Rh and Pd/Au gauzes were mounted together in the same gauze pack, reused with permission from Johnson Matthey Plc [15].

In the 1970s and 1980s, focus was on the implementation and procedures for using the Pd/Au catchment system, reported by Heywood [15, 21]. The gauze pack design depended on plant conditions in terms of pressure and Pt-loss, and economic perspectives were important. Between 10 and 65 % of the evaporated Pt could be captured with a single Pd/Au (88/12 at. %) gauze, with lower recovery for higher pressure (gauze loading). Using several gauzes, more than 60 % of the lost Pt were regularly being recovered. A schematic of how the Pd/Au gauzes were installed below the Pt/Rh gauzes is shown in Figure 8.

Simultaneously, there was a transition from the original Pd/Au (88/12 at. %) alloy to Pd/Ni, Pd/Co and Pd/Cu alloys (typically 95/5 wt. %), reported in several patent applications [35, 38-41]. Heywood also described the sensitivity of the ammonia oxidation reactor to pressure drop and how this is related to the low success of the glass wool filters and marble chips. The glass wool filters became too tight when catching physical particles, limiting gas flow through the filter. The marble chips worked better in the first place, but became fine powder if the reactor was cooled and heated during a campaign. This would happen for an unplanned shutdown of the plant. Due to the presence of water vapour in the reactor, $\text{Ca}(\text{OH})_2$ formed from the marble chips during the cooling and decomposed during the heating, causing the marble chips to become fine powder and limit gas flow significantly.

For atmospheric plants, the sensitivity to pressure drop is so high that Pt-catchment could in practice not be performed with such setups; pressure drop should preferably be absent. The Pd-based Pt-catchment system performed much better while keeping the pressure drop within acceptable limits. An interesting note is that the metallic gauze pack (Pt/Rh + Pd/Ni nets)

causes the main pressure drop through the ammonia oxidation reactor, while the oxide pellets used for N_2O decomposition today (section 2.1.1) do not contribute that much. This implies that the large swelling of the Pd/Ni nets during operation is highly unfavourable.

Fierro *et al.* [22-24] was the first to investigate and publish scientific analysis of the spent Pt-catchment materials (Pd/Ni and Pd/Cu), suggesting in 1989 [23] that trace amounts of unreacted ammonia act as the reducing agent for capturing Pt from PtO_2 . However, this conclusion is considered unlikely due to results from this project, showing Pt-catchment in the absence of NH_3 . The investigated Pd/Ni and Pd/Cu samples also showed significant swelling, recrystallization and faceting (Figure 9), and the Pt-content in the gauzes varied with up/down side and location in the gauze pack. The most Pt were captured on the up side of the top gauze. Rh_2O_3 particles were also found randomly distributed on the Pd-alloy surface, and a Rh-recovery of 15-19 % is reported.

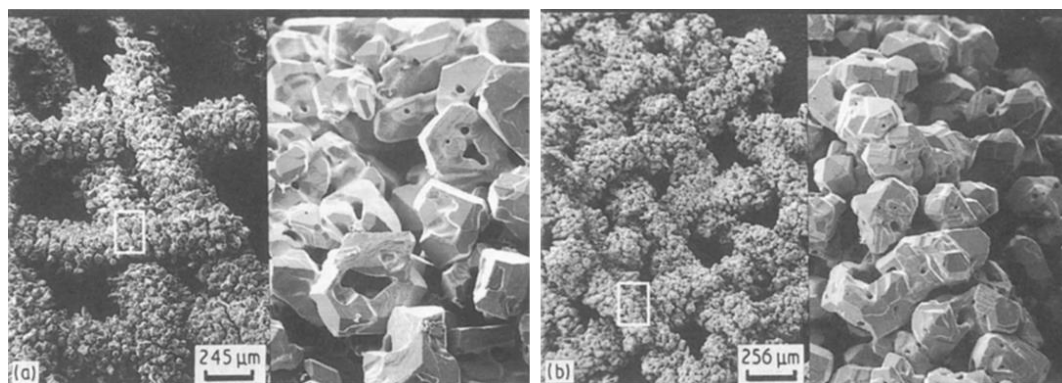


Figure 9. SEM images of the top side of Pd/Ni (91/9 at. %) gauzes used in a) a high-pressure plant (8 bar) and b) a medium-pressure plant (4 bar). Reused with permission from Springer Nature [22].

From 1995-1999, Ning and Yang *et al.* [25-28] addressed Pt-catchment and the restructuring of the Pd/Ni catchment gauze. They observed faceted crystals with a 14-faced body. The top side of the upper gauzes generally show the most faceted crystals (Figure 10a), while the bottom side of the lower gauzes show more rounded crystals (Figure 10b). They suggested a mechanism where a re-alloying and recrystallization process occurs during Pt-catchment, and that ladder-like growth and screw-growth causes this crystal to grow (Figure 10c).

They also suggested a mechanism for Pt-catchment in 1995 [28], based on a redox reaction; Pd is oxidized to PdO, allowing PtO_2 to be reduced to Pt and deposit on the Pd surface (Figure 11a). This would occur because Pd have a higher affinity to oxygen than Pt [28]. This sounds reasonable from a chemical perspective considering the higher stability of solid PdO versus PtO_2 . However, considering the fact that the original work by Holzmann [17] also showed significant Pt-catchment on Au and several Pd/Au-alloys, the mechanism seems less probable.

2. Scientific background

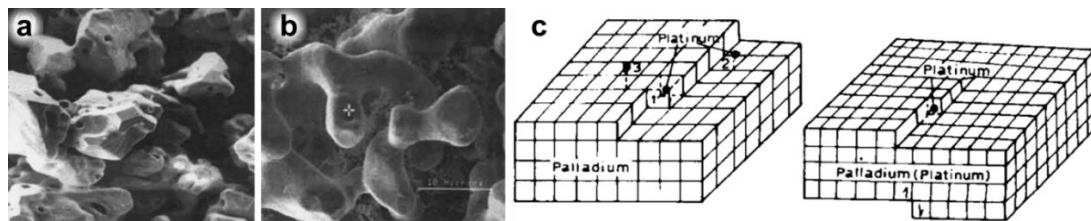


Figure 10. a) SEM image of the front side of the top gauze, b) SEM image of the back side of the second gauze, and c) suggested mechanism by Ning *et al.* for the structural reconstruction of the Pd-alloys during Pt-catchment. Reused with permission from Johnson Matthey Plc [27].

Rapid oxidation of Ni to NiO during operation was also observed, and that Ni/NiO do not interact much with Pt during the recrystallization process [25-28]. NiO is also completely lost from the Pd/Ni alloy during operation. Pura *et al.* [29-31] supported this in 2013 and 2016, when performing the most recent investigations of Pd/Ni and Pd/Au used for Pt-catchment. Ni was found to diffuse rapidly into the grain boundaries (GBs) and to the surface, and was subsequently oxidized to NiO (Figure 11b). Thereafter, the GBs with a large grain angle was more strongly etched than other GBs, causing the formation of porosity. The NiO located in the grain boundaries was also significantly etched, causing a rapid Ni-loss. The Pd/Ni wire was also observed to swell significantly in size and be unrecognizable in terms of shape after 6 months industrial operation (Figure 11b). Several gauzes was also reported to grow together at certain locations [29-31].

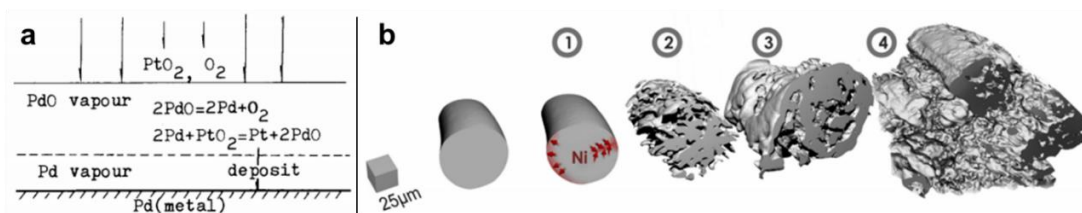


Figure 11. a) Suggested mechanism for Pt-catchment by Yang *et al.* [28]. b) reconstruction of the Pd/Ni wire during industrial operation, as suggested by Pura *et al.* [31]. Both figures are reused with permission from Elsevier.

With the latest publication by Pura *et al.* [31], it was known that the Pd/Ni catchment system is victim to severe reconstruction during industrial operation as a Pt-catchment material, but the cause and restructuring mechanism behind was still not described. The role of Ni was in question, the cause of Ni-loss was unknown, and there was a Pd-loss of unknown origin.

2.3. Pt-catchment on LaNiO₃ – experiments prior to the catchment project

As mentioned in the introduction (section 1.2), it was discovered that LaNiO₃, explored as a N₂O decomposition catalyst, captured both Pt and Rh during a 20 days' test in the pilot plant. The LaNiO₃ material was deposited on a megapyr net prior to the experiment. After the experiment, powder was scraped off from the net and XRD was performed, see Figure 12a. The XRD pattern showed a critical change of the starting material LaNiO₃. Through careful analysis, it was discovered that the platinum-containing double perovskite La₂NiPtO₆ had formed.

Almost the entire XRD pattern could be accounted for by Rietveld refinements using the structure of LaNiO_3 , $\text{La}_2\text{NiPtO}_6$ and NiO , see Figure 12b. The structure of LaNiO_3 included 10 at. % Rh-substitution at the B-site of LaNiO_3 ($\text{LaNi}_{0.9}\text{Rh}_{0.1}\text{O}_3$) and refinements showed increased unit cell parameters compared to regular LaNiO_3 . The observed unit cell parameters for $\text{La}_2\text{NiPtO}_6$ were slightly smaller than the reported values [50]. This demonstrated the capability of LaNiO_3 to capture Pt and Rh during the industrial ammonia oxidation reaction. For the current PhD-work, this finding set the scene for exploring structural aspects RENiO_3 (RE = rare earth element) with B-substitution of Pt and Rh (section 4.2, Paper IV and Paper V).

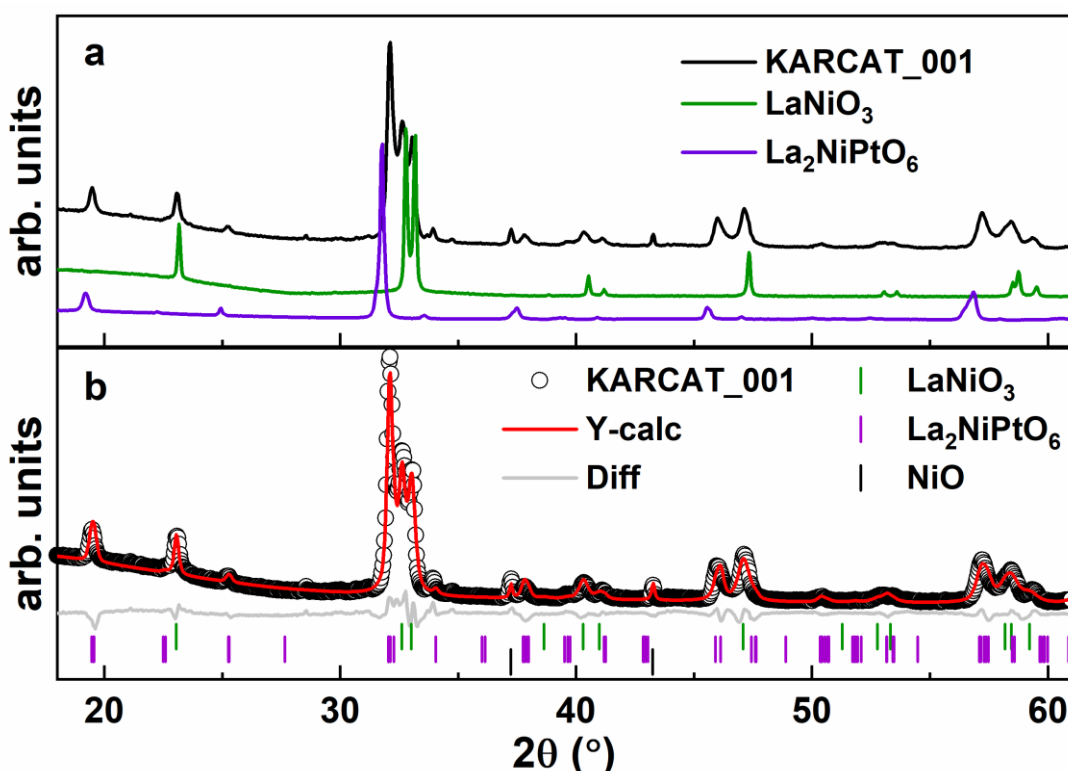


Figure 12. a) X-ray diffraction pattern of the LaNiO_3 sample tested as a N_2O decomposition catalyst (KARCAT_001), compared to the diffraction pattern of the starting compound LaNiO_3 , in addition to $\text{La}_2\text{NiPtO}_6$. b) Rietveld refinements of the KARCAT_001 sample using the structure data of LaNiO_3 with 10 % Rh-substitution at the B-site [51], $\text{La}_2\text{NiPtO}_6$ [50] and NiO [52]. The data is collected using $\text{Cu K}\alpha_1$ radiation ($\lambda = 1.5406 \text{ \AA}$).

2.4. Noble metals and their oxidation

2.4.1. Structure, bonding and mechanical aspects

We all know metals; they can be used as construction materials, both heavy (steel alloys) and light (Mg, Al) in weight; they can be ductile or brittle; many are excellent electronic conductors (Cu, Au); many are good thermal conductors; some are resistant to harsh chemical environments; all depending on the metal/alloy composition. The noble metals are also good electronic and thermal conductors, some are highly ductile, and they resist oxidation at high temperature.

2. Scientific background

In terms of atomic arrangement, metals can be considered as a pack of spheres stacked together (Figure 13). The atoms pack themselves as densely as possible to minimize the energy (maximize density), and the two main forms of sphere packing are the dense-packed ABC- and ABA-types (Figure 13). The dense packed ABC- and ABA-type structures have a density of ~74 %. ABC-type packing is the most common among the noble metals (Appendix: Figure A2), known as cubic close packing (ccp) and corresponds to the face centred cubic (fcc) unit cell (Figure 14a). ABA-type packing corresponds to the hexagonal close packing (hcp) (Figure 14c). Other sphere-packed structures also occur for the elements (Appendix: Figure A2), and one common structure is the body centred cubic packing (bcc, ~68 % dense) (Figure 14b), which is common for the group 1, 5 and 6 elements. For detailed information, the reader referred to dedicated literature [53, 54].

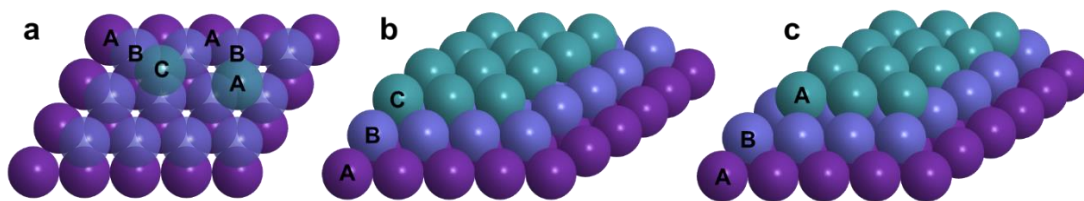


Figure 13. Illustration of the dense-packing of spheres, as in the structure of metals. a-b) ABC-packing, corresponding to ccp packing and a fcc unit cell (Figure 13a), c) ABA-packing, corresponding to hcp-packing with a hexagonal unit cell (Figure 13c).

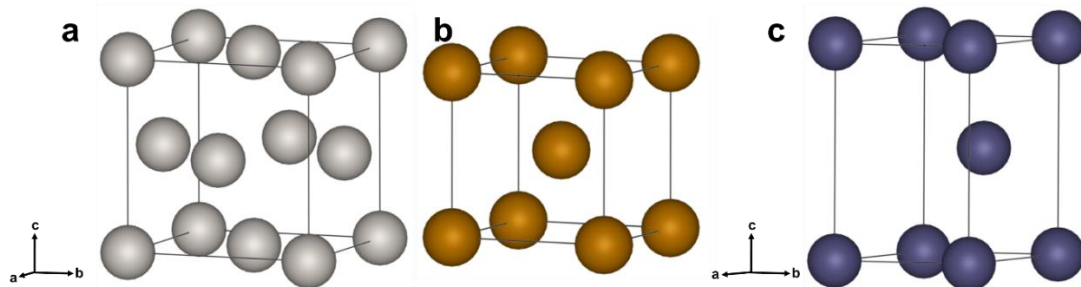


Figure 14. Illustration of the unit cell of the noble metals a) Pt (ccp/fcc, $a = 3.93 \text{ \AA}$) [55], b) Fe (bcc, $a = 2.86 \text{ \AA}$) [56] and c) Ru (hcp, $a = 2.686 \text{ \AA}$, $c = 4.289 \text{ \AA}$) [55].

The chemical bond in metals (metallic bond) consists of sharing of the valence electrons between all the elements, causing the electrons to be delocalized over the entire structure. This is the cause for the good (and “metallic”) electronic conduction in metals compared to ionic and covalent solids. Defects are always present in the metal structure, such as interstitial atoms, vacancies, line defects and dislocations. The metallic bond is itself quite strong, but the dislocations make it possible to physically deform a metal (reshape) without breaking too many metallic bonds simultaneously [53]. This is the cause for the ductile behaviour of the metals that allow them to be reshaped easily without braking, *e.g.* into wires and woven/knitted into nets.

When a metal (solute) is mixed in a host metal (solvent), the alloy can only maintain the structure of the host metal until a certain concentration of the solute. To obtain a homogeneous alloy with a high solid solubility, the Hume-Rothery criteria for the solute and solvent must be

met: 1) the atomic radius must differ by no more than 15 %, 2) the crystal structures must be similar, 3) the valency must be similar, and 4) the electronegativity must be similar [57]. The Pd-Pt and Pd-Ni systems (Figure 15a-b) are two examples of systems with a high solid solubility. Less similar elements show a low solubility with each other and segregate into ordered phases, such as the Au-Pd system (Figure 15c) or separate phases such as the Au-Pt system (Figure 15d) upon mixing. It is worth noting that the Au-Pd and Au-Pt system have high solid solubility in each other compared to other systems [58]. A general overview of some physical properties for the noble metals relevant for this thesis are shown in Table 1.

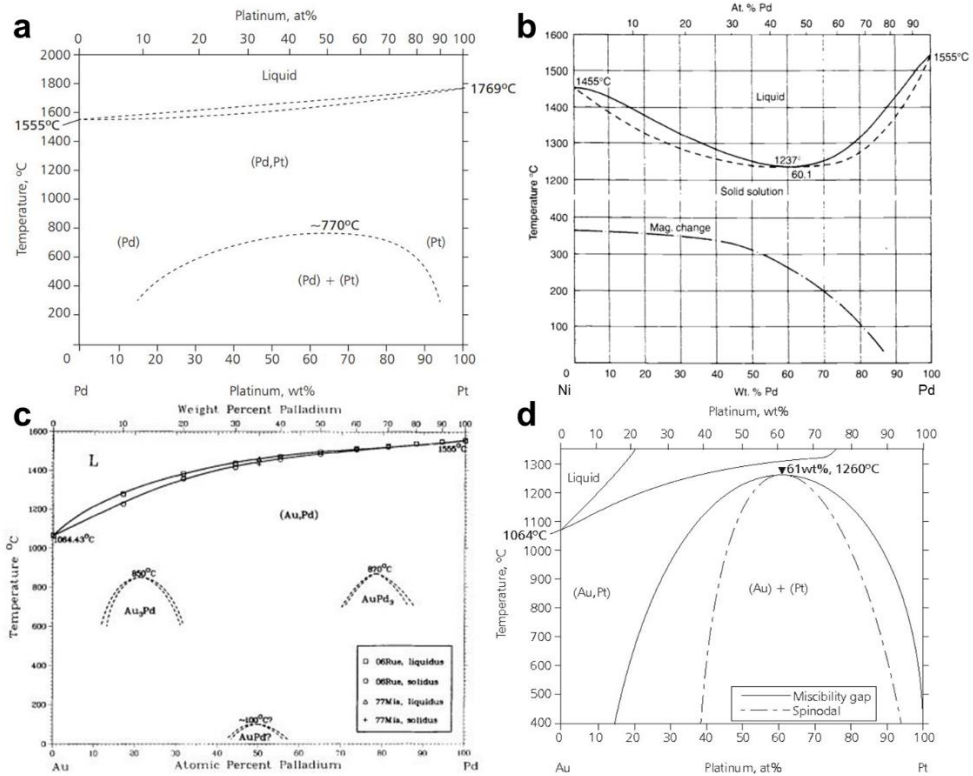


Figure 15. Phase diagrams for the binary systems a) Pd-Pt [59], b) Pd-Ni [58], c) Au-Pd [60] and d) Au-Pt [59]. The figures are reused with permission from Johnson Matthey Plc (a and d), Butterworth-Heinemann (b) and Springer Nature (c).

Table 1. Overview of different properties for selected noble metals. The data is collected from Smithells metals reference book [58].

	Pt	Pd	Rh	Au	Ni
Atomic number	78	46	45	79	28
Atomic weight [g/mol]	195.08	106.42	102.91	196.97	58.69
Melting point [°C]	1769	1552	1964	1064	1450
Self-diffusion, 900 °C [cm ² /s]	1.7×10 ⁻¹³	3.5×10 ⁻¹³	-	1.2×10 ⁻⁹	4.4×10 ⁻¹³
Density at 20 °C [g/cm ³]	21.45	12.02	12.41	19.30	8.91
Packing type	ccp	ccp	ccp	ccp	ccp

2.4.2. Diffusion

Diffusion is a process resulting from the random motion of atoms and molecules that causes a net movement of something (*e.g.* molecules, atoms or heat) in a potential gradient. Diffusion

2. Scientific background

in solids refer to transport of atoms, ions or molecules from a region of high concentration to a region of low concentration. The rate of diffusion in a solid is tabulated as the diffusion coefficient D (Table 1; Appendix: Table A1) and is dependent on several factors, such as the diffusing species, the structure and bonding of the host material, the temperature, pressure and gas atmosphere. Diffusion can take place via the bulk lattice, but also through other pathways such as surfaces, grain boundaries and dislocations, where the diffusion is generally more rapid than through the lattice [53].

In metals, the main mechanism for bulk diffusion is vacancy diffusion, *i.e.* atoms hopping to a vacant atomic site nearby [53]. Most metals contain a fair concentration of vacancies at high temperature that facilitates diffusion. For this reason, metals generally show rapid diffusion compared to *e.g.* ionic and covalent solids. Additionally, metals have a non-directional chemical bond without an electric field (in contrast to ionic and covalent solids), which allow the diffusing species to easily exchange site with a vacancy without a too high activation energy.

When two different elements with different diffusion coefficient diffuses into each other, one element may diffuse faster than the other. Because of the vacancy diffusion mechanism, there is a net flux of vacancies in the opposite direction of the fastest diffusing species. This is known as the Kirkendall effect. The large concentration of vacancies may agglomerate and form voids known as Kirkendall voids, which acts as a sink for vacancies [61]. The Kirkendall effect is common in interdiffusion systems, even with a difference in diffusion coefficient of only 1-2 orders of magnitude, as in the Pd-Pt system [62]. The oxidation of Ni to NiO is also influenced by the Kirkendall effect. Here, Ni-diffusion is slower than O-diffusion through the formed NiO layer during oxidation, causing internal porosity [63, 64].

As a rule of thumb, the rate of diffusion at a given temperature usually increase for metals with a low melting point, because of the proximity to its melting point. An example is that Au ($T_M = 1063$ °C [58]) show a more rapid diffusion than Pd ($T_M = 1552$ °C [58]) at the same temperature conditions (*e.g.* 900 °C). On average, diffusion becomes appreciable at the temperature that is approximately half of the melting point [65], and sintering become active at 2/3 – 3/4 of the melting point [66]. For the elements relevant for this thesis, self-diffusion and tracer-diffusion is clearly most rapid in Au (Appendix: Table A1). For Pd/Au alloys, the diffusion rate increases with increasing Au-content [67], which is expected due to the increase in melting point (Figure 15). Several studies are reported for the Pd-Au and Pd-Au-Pt systems [60, 67-71], but diffusion coefficients for Pt in mixed Pd-Au alloys are not reported. The self-diffusion coefficient for Au is ~ 4 orders of magnitude higher than for Pd. In the Pd-Pt alloy system, the Pd diffusion coefficient is 1-2 orders of magnitude higher than the Pt diffusion coefficient [62]. In the Pd/Ni system, Pd is the faster diffusing species by a small margin [72]. Analysis of diffusion experiments is well covered in the literature [73]. Details on diffusion analysis relevant for this work is provided in the supplementary section in Paper II and Paper III.

2.4.3. Oxidation of Pd, Pt, Rh, Au and Ni

In the ammonia oxidation reactor, ~6 % O₂ is present, and the effect of oxygen on the elements present may be significant. The oxidation behaviour of the elements is therefore relevant background knowledge before investigating Pt-catchment (section 4.1) and before studying of mixed oxides (section 4.2).

The general characteristic of the noble metals is that they are resistant to oxidation in air at high temperature. Still, most noble metals have a versatile and reactive chemistry, with oxidation states ranging from 0 to +VI. For the metals of main investigation in this thesis, Pd, Pt, Ni and Au, oxidation states 0, +II, +III and +IV are most common [74]. In fact, Ni, Pd and Pt are all located in group 10 in the periodic table of the elements. In general, we expect the similar chemistry for elements within the same group.

2.4.3.1. Structural chemistry of bulk oxides

Ni is not a noble metal, and is oxidized to NiO upon heating. NiO contains Ni(II) in octahedral coordination and obtains the rock salt (NaCl, Fm-3m) structure. Ni(III) does not exist in a binary oxide, although nanoparticles of hydrated Ni₂O₃ have been synthesized [75]. Furthermore, NiO₂ is only made as the Li-intercalated LiNiO₂, where delithiation could in principle provide Ni(IV) in NiO₂ [76]. Ni is reported in oxidation +I (and mixed +I/+II) in exotic compounds such as LaNiO₂, LaSrNiRuO₄ and La₄Ni₃O₈ [77-81], but the synthesis is difficult. Ni(III) can easily be prepared in *e.g.* LaNiO₃, Ni(II) in La₂NiO₄, and in mixed valence in *e.g.* La₄Ni₃O₁₀ (Ni(II) and Ni(III)).

Pd is located below Ni in the periodic table and prefers similar oxidation states, 0 and +II. Unlike Ni, bulk PdO decomposes to Pd-metal above ~800 °C in 10 % O₂ in N₂ and 877 °C in 1 bar O₂ [82]. Re-oxidation of Pd to PdO occurs below ~750 °C in 10 % O₂ [83], and formation of the bulk oxide is kinetically hindered [84]. The PdO structure (Figure 16a) contains corner- and edge-sharing PdO₄ square planes facing towards each other, thus having a direct Pd-Pd interaction, quite different from NiO. Because of the long reach of the *d*-orbitals causing a strong crystal field splitting, the *d*⁸-electron configuration causes Pd(II) to prefer square planar coordination in oxides, while weak ligands such as halides can stabilize Pd(II) in octahedral coordination [74]. The binary oxides of Pd(III) and Pd(IV) are not reported as stable, however, high pressure synthesis can produce Pd-oxides such as LaPdO₃ [85], Zn₂PdO₄ [86] and RE₂Pd₂O₇ (RE = rare earth) [87]. Pd(III) in LaPdO₃ has a Jahn-Teller active *d*⁷ low spin electron configuration, which is less stable because of the large crystal field splitting of the *d*-electrons in the octahedral field. Ni(III) has the same *d*⁷-configuration, but is still stable in octahedral coordination, although Ni(III) also shows Jahn-Teller related structural effects in several nickelates [88]. Mixed oxides with Pd(IV) is thus considered more stable because of the *d*⁶ low spin electron configuration.

Pt differs from Pd and Ni in that it prefers oxidation state +IV as a binary oxide. PtO₂ exists in two polymorphs, *α*- and *β*-PtO₂ (Figure 16b-c), where both structures have Pt in octahedral coordination with the stable *d*⁶ low spin electron configuration. *β*-PtO₂ forms at high

2. Scientific background

temperature and high pO_2 (Figure 17a), crystallising in the $CaCl_2$ structure ($Pnmm$), and decomposes above ~ 595 °C in air [89]. The β - PtO_2 structure is similar to the rutile structure ($P4_2/mnm$), consisting of chains of edge-sharing PtO_6 -octahedra along the c -axis (Figure 16c). The chains are linked together by corner-sharing octahedral across the chains. The fact that β - PtO_2 crystallises in the $CaCl_2$ -structure and not the rutile structure has been considered as evidence for a slightly covalent (low ionic) character of the Pt-O bonds [90]. α - PtO_2 crystallises in the CdI_2 structure and consists of layers of edge-sharing PtO_6 -octahedra (pseudo two-dimensional), and forms at intermediate temperatures and high pO_2 (Figure 17a)[91]. Pt_3O_4 is another common Pt-oxide, which is stable at high temperatures and intermediate pO_2 . The structure is similar to that of PdO , with face sharing square planes of PtO_4 . Besides that, a difference is that Pt_3O_4 have only corner sharing PtO_4 square planes (Figure 16d), while PdO have both corner and edge sharing PdO_4 square planes (Figure 16a). The phase diagram for the binary Pt-oxides and their stability regimes are shown in Figure 17a. Several mixed Pt-oxides are also reported, often in combination with basic elements from group 1 and 2 (e.g. $NaPt_3O_4$ and $CaPt_2O_4$ [91]). In these materials, stacks of square planar Pt(II) are often present to form a metallic Pt-Pt interaction [91]. PtO is not reported as a stable bulk oxide, and Pt-O (as in Pt(II)) is mainly found as a surface state in Pt-containing alloys [92].

Rh is most stable in oxidation state 0 and +III. Rh_2O_3 is the most common Rh-oxide, crystallising in the corundum structure. Rh_2O_3 is also the most stable of the binary oxides of Pd, Pt and Rh [44]. RhO_2 is stable at moderate temperatures and pO_2 (Figure 17), and crystallises in the rutile type structure. RhO_2 and PtO_2 with the high pressure PdF_2 -structure type have recently been synthesized using a 11-17 GPa pressure [93]. Both Rh(III) and Rh(IV) can be readily prepared in mixed oxides.

Au is generally difficult to oxidize, but both Au(I) and Au(III) have been reported. Several Au-molecules can furthermore be synthesized and are actively used in homogeneous catalysis [94]. For reactions with oxygen, Au prefers oxidation state +I and +III, but only Au_2O_3 has been reported as a stable bulk oxides, which decomposes at approximately 160-180 °C [74, 95].

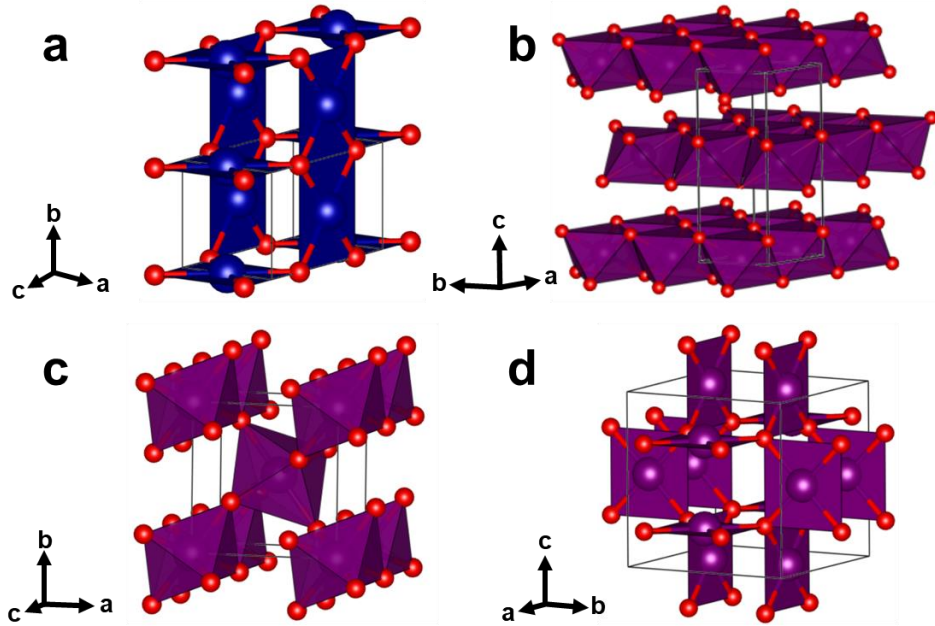


Figure 16. Structure drawing of a) PdO ($P4_2/mmc$) [96], b) α -PtO₂ ($P6_3mc$) [97], c) β -PtO₂ ($Pnmm$) [98] and d) Pt₃O₄ ($Pm-3n$) [99]. The blue elements are Pd, the purple are Pt and the red are O. The figures are drawn using Vesta [100].

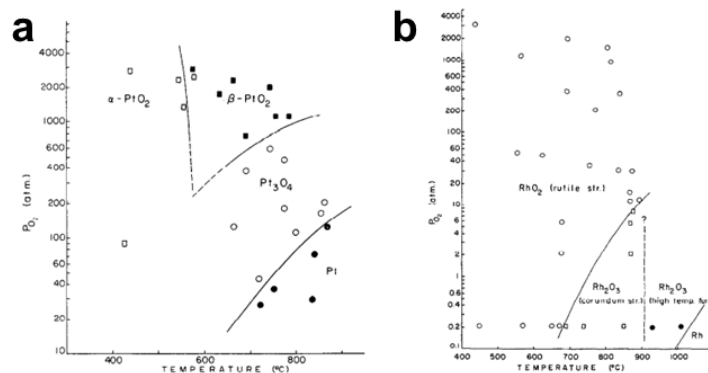


Figure 17. Phase diagram of the systems a) Pt-O and b) Rh-O. Reused with permission from Elsevier [99].

2.4.3.2. Surface oxidation, volatility, oxygen diffusion and oxygen solubility

Oxidation of ternary Pt/Rh/Pd alloys at 800 °C show formation of Rh₂O₃ on the surface and a metallic Pd/Pt layer below, depleted in Rh [44]. Rh₂O₃ is also formed on the surface in binary Pt/Rh alloys at 800 °C [101]. PdO is generally formed on the surface of Pd-rich alloys below 800 °C due to the stability of PdO at such temperatures [102]. For Pd/Rh (93.6/6.4 at. %). PdO forms faster than Rh₂O₃ at 600 °C, while at 900 °C and above, Rh₂O₃ dominates the surface [102]. In Pt/Pd (69/31 at. %), PdO forms a thin oxide layer at 500 °C and a thicker PdO bulk oxide on the surface at 600 °C. At 700 °C and above, Pt dominates the surface [103]. For a Pd/Pt (50/50 at. %) alloy, all surface Pd is completely oxidized at 400-600 °C, while only 50-70 % of the Pt is oxidized [104]. Nanoparticles of PdO decompose to Pd metal in the range of 680 to 810 °C [105], depending on size and the support material. Smaller Pd-particles oxidize more easily to PdO [106].

2. Scientific background

Pd/Pt nanoparticles also form PdO on the surface, although the reported temperatures varies between studies [82, 92]. Interestingly, a study showed that PdO nanoparticles reacted with metallic Pt nanoparticles at 650 °C in air to form bimetallic Pd/Pt nanoparticles [82]. It is believed that Pt aided the reduction of PdO to Pd, and that the oxygen is simply desorbed from the material. Finally, in a Pd/Au alloy in NO gas, Pd is also attracted to the surface. However, the study was performed at only 300 °C [44].

At high temperatures, *e.g.* above 800 °C, a metal loss (volatilization) occurs, see Appendix: Table A1. In vacuum, Pd and Au have by far the highest vapour pressure of the noble metals. In oxidizing conditions, Osmium (Os) has the largest vapour pressure of the noble metals. Of the elements relevant for this thesis, Pt has the highest vapour pressure in oxidizing conditions. Experiments show that Pd has 1 order of magnitude lower mass loss than Pt in oxidizing conditions [107]. However, several studies mention that PdO has a very low vapour pressure [82, 108]. It is difficult to unify the literature on this point. It has been shown that water vapour do not promote Pd-loss compared to oxygen gas [109]. Rh forms a protective surface oxide below 1000 °C, and a mass loss above. The Rh-loss is 1-2 order of magnitude lower than that of Pt at temperatures above 1000 °C. Unfortunately, the discrepancies between different studies are large [107] (Appendix: Table A1). The mass losses of Pt and Rh in oxygen and in the industrial ammonia oxidation reaction (section 2.1) are believed to be caused by the PtO₂ and RhO₂ molecules [14]. In the Pt-catchment project, it is Pt-catchment from the gas phase molecule PtO₂ that is performed.

For alloys consisting of one noble metal and a non-noble metal, such as Pd/Ni, Pd/Fe and Au/Fe, selective oxidation of the non-noble metal may occur. Experiments with internal oxidation of such alloys, *e.g.* Pd/Fe (98/2 at. %), can be used to calculate the oxygen diffusion and –solubility in a metal [110]. At 900 °C, the solubility of oxygen in Pd is 2.4 at. %, and in the range of 1-2 at. % in Pt (Appendix: Table A1). The diffusion coefficient of oxygen in Pd and Pt is ~4 orders of magnitude higher than the bulk metal diffusion (Appendix: Table A1). Oxygen diffusion and solubility is extremely low in Au [111].

2.5. Perovskite oxides

In order to understand the potential use of perovskites as Pt-catchment materials, it is beneficial to know about the crystal structure and chemistry of perovskites. This chapter covers the basics of perovskites, and the interested readers are referred dedicated literature [112, 113]. Perovskites are a class of materials with very similar structure and the general formula ABX_3 (Figure 18). The structure is commonly formed for ternary oxides because it is one of the most energetically favourable ways of packing one large cation (*A*), one small cation (*B*) and an anion (*X*) together. Typically, the anion is oxygen (*X*), but can also be *e.g.* a halide. The large cation (*A*) is typically a group 1-2 and 4f-block element and the small cation (*B*) a *d*-block element.

A large number of elements can be involved in the formation of the ABX_3 . This is due to the possibility of combining elements with variations in both size and charge. It is required that

the elements obtain charge neutrality, *i.e.* that their total oxidation state adds up to 6 in the case of O as the anion, as in $A^I B^V O_3^{-II}$, $A^{II} B^{IV} O_3^{-II}$ and $A^{III} B^{III} O_3^{-II}$. In addition, further flexibility in oxidation state is obtained in double perovskite ($AA'BB'O_6$) and non-stoichiometric perovskites ($A_{1-x}A'_x B_{1-y}B'_y O_3$). When the sizes of the A-, B- and X-elements match perfectly, the structure is cubic, as in the classical example of $SrTiO_3$ (Figure 18). However, when the size of the elements deviates from the ideal scenario, the structure distorts by tilting of the octahedra while maintaining the perovskite structure. The degree of octahedral tilting is described by the Goldschmidt t -factor given by (Eq. 2-6)

$$t = \frac{r_A + r_X}{\sqrt{2}(r_B + r_X)} \quad \text{Eq. 2-6}$$

The cubic perovskite is obtained for $t = 1.00$, described in space group $Pm-3m$. The perovskite structure is considered unstable for $t < 0.71$ and $t > 1.00$, at which point other structures than the perovskite are formed [113]. When the t -factor is reduced, octahedral tilting occur, associated with a reduction in symmetry. For example, $LaNiO_3$ has $t = 0.97$, giving rise to a rhombohedral symmetry ($R-3c$) (Figure 19a), while $LaRhO_3$ ($t = 0.92$) is described in the orthorhombic space group $Pnma$ (Figure 19b). A small A-site and/or a large B-site cation reduces the t -factor and distorts the perovskite structure. However, the t -factor less accurate for highly distorted perovskites, and is more of a theoretical value than practically useful. This is related to variations in the A-O bond distances and coordination number for highly distorted perovskites.

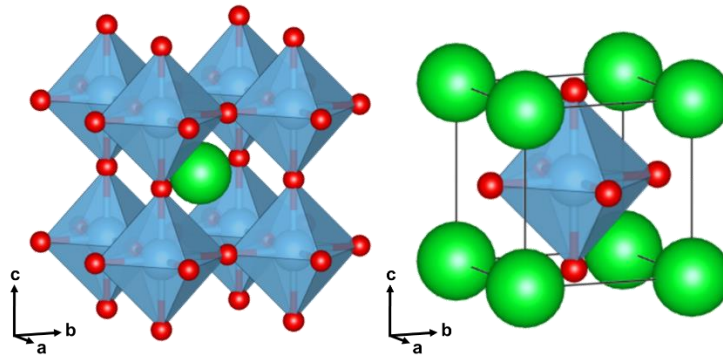


Figure 18. Structure of $SrTiO_3$ ($Pm-3m$) [114], a cubic perovskite. Green atoms correspond to Sr, blue to Ti and red to O. The figures are drawn using Vesta [100].

2.5.1. An extra note on relevant perovskite oxides

2.5.1.1. $LaNiO_3$

$LaNiO_3$ is a widely studied rhombohedral perovskite, which is best described in the space group $R-3c$ (Figure 19a) [115-119]. In $LaNiO_3$, Ni has a $t_{2g}^6 e_g^1$ (d^7) electron configuration, which should be a Jahn-Teller active state. However, the single e_g -electron of Ni is itinerant, *i.e.* $LaNiO_3$ display metallic conductivity [116]. This hinders the Jahn-Teller distortion to occur because this type of distortion require a localized e_g -electron. For $RENiO_3$ (RE = rare earth element), the structural distortion induced by a rare earth element smaller than La causes

2. Scientific background

the e_g -electron of Ni to be localized and $RENiO_3$ to become insulating at low temperatures [120]. In the insulating state, the Jahn-Teller effect distort the Ni(III) octahedra. For $YNiO_3$, the structure is shown to become monoclinic ($P2_1/n$) and have B -site (Ni-site) ordering, containing one large and one small Ni-site [88]. This is by many considered as a charge disproportionation of Ni(III) into Ni(III + δ) and Ni(III - δ). The instability of Ni(III) also imply that it is far more difficult to synthesize $RENiO_3$ with a small rare earth element, requiring a pO_2 in the range of 100-200 bar for $YNiO_3$ [121]. $LaNiO_3$ is thermally stable up to ~ 900 °C in air, and above this temperature it decomposes to NiO and $La_4Ni_3O_{10}$, which in turn decomposes to NiO and La_2NiO_4 above 1200 °C [122]. The decomposition path of $LaNiO_3$ demonstrates how Ni prefers oxidation state +II.

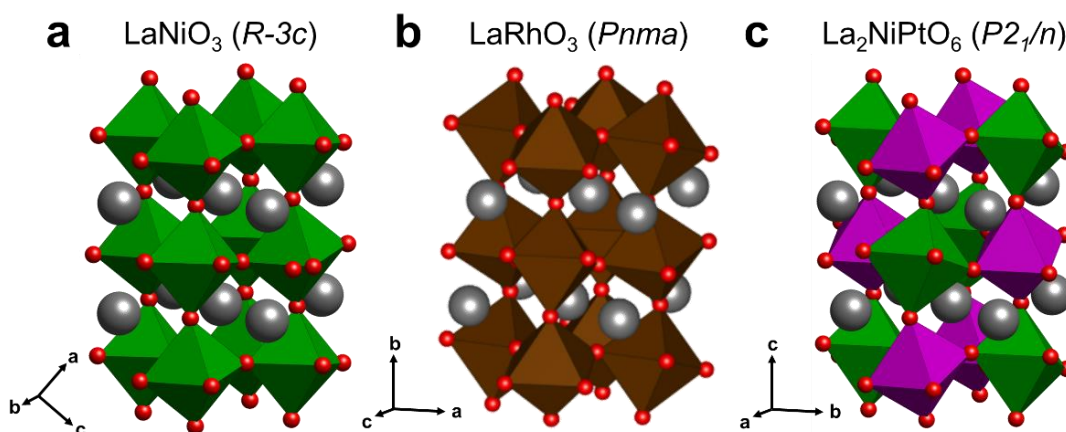


Figure 19. Crystal structure of a) $LaNiO_3$ ($R-3c$) [51], b) $LaRhO_3$ ($Pnma$) [123] and c) La_2NiPtO_6 ($P2_1/n$) [50]. La is coloured grey, O red, Ni green, Rh dark brown and Pt magenta. The figures are drawn using Vesta [100].

2.5.1.2. $LaRhO_3$ and $LaNi_{0.50}Rh_{0.50}O_3$

$LaRhO_3$ is significantly less investigated than $LaNiO_3$. $LaRhO_3$ is a diamagnetic insulator because of the $t_{2g}^6 e_g^0$ -electron configuration of Rh(III). Due to the larger size of Rh compared to Ni, $LaRhO_3$ is more distorted (Figure 19), orthorhombic and is described in space group $Pnma$; a very common space group for perovskites. The same applies to $LaNi_{0.50}Rh_{0.50}O_3$ ($Pnma$), which is a B -site disordered double perovskite, *i.e.* there is no ordering between Ni and Rh [124-126]. The thermal stability of $LaRhO_3$ and $LaNi_{0.50}Rh_{0.50}O_3$ is much higher than for $LaNiO_3$, and the final annealing temperature during solid state synthesis of $LaNi_{0.50}Rh_{0.50}O_3$ has been performed at 1275 °C [126], and similar for $LaRhO_3$.

The scientific reports are slightly ambiguous in the description of the oxidation state for Ni and Rh [124, 125, 127]. Structurally, B -site disorder indicates that both elements are +III [128], which were supported by the original publications on this compound [124, 125]. However, magnetic measurements have indicated that Ni(II) and Rh(IV) may be the correct oxidation states, or that a mixture in oxidation state can occur [126]. This is supported by thermoelectric measurements on the non-equimolar compositions $LaNi_{1-x}Rh_xO_3$ ($0.70 \leq x \leq 1.00$) [127]. The isoelectronic system $LaNi_{1-x}Co_xO_3$ show a very similar trend, where the sample with $x = 0.50$

have III/III as the *B*-site oxidation states, while Co-rich samples ($x > 0.50$ in $\text{LaNi}_{1-x}\text{Co}_x\text{O}_3$) show a partly change in oxidation states to Ni(II) and Co(IV) [129-131]. For double perovskites with Co/Rh, a similar mix in oxidation states are reported (Table 2), while Fe/Rh double perovskites have III/III in oxidation states (Table 2).

Table 2. Overview of relevant double perovskites and their oxidations states and *B*-site ordering.

$\text{LaB}_{0.50}\text{B}'_{0.50}\text{O}_3/\text{La}_2\text{BB}'\text{O}_6$	Space group	<i>B</i> -site ordering	Oxidation state <i>B</i>	Oxidation state <i>B'</i>	<i>t</i> -factor*	Reference
$\text{LaNi}_{0.50}\text{Rh}_{0.50}\text{O}_3$	<i>Pnma</i>	No	Mix of	Mix of	0.93	[124-126]
$\text{LaCo}_{0.50}\text{Rh}_{0.50}\text{O}_3$	<i>Pnma</i>	No	Mix of	Mix of	0.91	[132]
$\text{LaFe}_{0.50}\text{Rh}_{0.50}\text{O}_3$	<i>Pnma</i>	No	III	III	0.91	[128]
$\text{LaNi}_{0.50}\text{Co}_{0.50}\text{O}_3$	<i>R-3c</i>	No	III	III	0.94	[131]
$\text{La}_2\text{NiPtO}_6$	<i>P2_1/n</i>	Yes	II	IV	0.92	[50]
$\text{La}_2\text{CoPtO}_6$	<i>P2_1/n</i>	Yes	II	IV	0.91	[50]

**t*-factor is calculated based on tabulated ionic radii from Shannon [133].

2.5.1.3. $\text{La}_2\text{NiPtO}_6$

Very few detailed studies are reported on Pt-containing perovskites. Ouchetto *et al.* [50] published in 1997 a nice overview of several Pt-containing double perovskites and their structure. $\text{La}_2\text{NiPtO}_6$ show a very large degree of *B*-site ordering, with a charge division into Ni(II) and Pt(IV), contributing to the *B*-site ordering. The *B*-site ordering can be considered a rock salt type ordering between the Ni- and Pt-octahedra (Figure 19c), *i.e.* where every other octahedra is either NiO_6 or PtO_6 . The structure is best described in space group *P2₁/n*, where the β -angle is close to 90° , implying that $\text{La}_2\text{NiPtO}_6$ can be considered as pseudo orthorhombic. The main difference between the structure of $\text{La}_2\text{NiPtO}_6$ (*P2₁/n*) and LaRhO_3 (*Pnma*) is therefore only the *B*-site ordering. The thermal stability of $\text{La}_2\text{NiPtO}_6$ is higher than LaNiO_3 , and $\text{La}_2\text{NiPtO}_6$ is reported to decompose around 1200°C . In terms of electronic properties, no detailed studies are performed on $\text{La}_2\text{NiPtO}_6$. However, $\text{La}_2\text{CoPtO}_6$ is reported to be antiferromagnetic below 28 K [134].

3. Experimental setup and characterization methods

This chapter provides an overview of the instrumentation used for Pt-catchment experiments and general information on the preparations needed before doing *in situ* tomography experiments. The main characterization methods used (SEM/EDX and XRD) are also covered, along with the method used for synthesis of perovskite oxides.

3.1. Pt-catchment experiments

3.1.1. Sample information

Noble metal wires and nets with compositions Pd, Pd/Au (85/15 wt. %, 91/9 at. %), Pd/Au (35/65 wt. %, 50/50 at. %), Au and Pd/Ni (95/5 wt. %, 91/9 at. %) were obtained with a purity > 99.9 % (K. A. Rasmussen, Hamar, Norway). The wire diameters were 76 μm for all Pd-containing samples and 100 μm for Au. During production, the metals are mixed, melted and solidified into bolts. The bolts are drawn gradually into thinner wires to obtain the desired wire diameter. The grain size is generally small ($\sim 5 \mu\text{m}$) after production. To obtain quasi-monocrystalline wires (grain size in the range of 20-200 μm), the wires were annealed for 7 days at 1100 °C (900 °C for Au) in a double evacuated quartz ampoule, prior to further experiment work.

3.1.2. Laboratory Pt-catchment experiment

Pt-catchment experiments were performed using a six-zone furnace (Figure 20a), and a few experiments in a five-zone furnace, allowing temperature control in the different steps of the reaction. A typical experiment used a temperature of 1000 °C for the Pt-source (rolled up Pt-net of 300-350 mg) located in the second zone, allowing the gas to heat up to 1000 °C before reacting with the Pt-source. The Pt-catchment material, *e.g.* Pd, was typically located in the fifth zone with a temperature of 900 °C. Further experimental details for the Pt-catchment experiments are presented in Paper I-III.

To make sample mounting as simple as possible, a double tube (tube in a tube) solution was used for the zone-furnaces (Figure 20b-c). The furnace has a large outer tube along the entire reactor length (10 mm ID), with a smaller inner tube (6 mm ID, 8 mm OD) inserted from each side of the furnace (Figure 20b). The Pt-source is on the inlet side and the Pt-catchment material is on the outlet side. The tubes are easily connected together using standard Swagelok reducers and Teflon ferrules. An air flow of 1 L/min was used in most experiments because it provides a comparable gas velocity (0.59 m/s) as in the industrial reactor. The laboratory experiments were run at ambient pressure compared to 5 bar in the pilot- and medium pressure plant where the industrial experiments were performed.

To obtain reproducible and comparable results, it is important to mount the samples in a similar way in each experiment and to ensure that sample analysis is as easy as possible. Further important aspects are:

3. Experimental setup and characterization methods

- Mass changes: The sample must be large enough for mass changes during the experiment to be measurable, if present. If the sample is too large, the Pt-concentration may be inhomogeneous in the sample and the calculated at. % Pt is not representative of the real Pt-catchment.
- Sample shape: wire or net: A net (gauze) sample is easiest to place in a vertical tube furnace, while this work has used a horizontal tube furnace. If placed properly in the tube furnace, the sample should obtain a homogeneous Pt-catchment. For a horizontal furnace, the net must be stabilized between *e.g.* two pieces of alumina. The sample size is in this case small (6 mm diameter net) and handling is tricky. The sample must be cut before SEM/EDX and ICP-OES analysis, but the sample can be mechanically weak and easily deformed during handling.

The advantage of a wire is that it is easier to cut a piece for SEM/EDX and for ICP-OES, and handling is easier without changing the overall appearance of the wire. The disadvantage is that the Pt-distribution may be inhomogeneous along the wire length in the case of a too long spiral. However, sample mounting is easy in a horizontal tube furnace, where the sample is placed as a spiral. Two pieces of alumina is used to keep the spiral from flowing downstream with the gas flow during operation.
- ICP-OES: The sample must be large enough to spare a piece for ICP-OES, which is a destructive technique. The sample quantity needed is only a few mg, but 10 mg or more is optimal.
- Pt-source: It is important that it is easy to measure mass changes of the Pt-source before and after the experiment in order to estimate the $pPtO_2$ during the experiment. It is also important that the mass loss is reproducible, *i.e.* similar between parallel and consecutive experiments. In our furnace, three parallel experiments were run simultaneously (Figure 20). A rolled up net is very easy to weigh, but there can be some variation in mass loss between experiments, even though the nets have approximately the same mass and shape. A stack of many nets after each other may give a more reproducible Pt-loss, but mass determination and re-stacking of the nets between experiments can be difficult. If just one 6 mm diameter Pt-net is used, the Pt-loss is very low.

Most of the issues summarised above are easily solved by using a pilot plant reactor. Here, the temperature and gas mixture are the same as in the industrial reactor and the sample mounting (nets/gauzes) allow the gas to react homogeneously with the entire area of the sample. The pilot plant is ~25 cm in diameter, and several smaller samples can be placed simultaneously. However, the pilot plant experiments are expensive and the laboratory experiments allow the use of individual gas constituents at a more reasonable price.

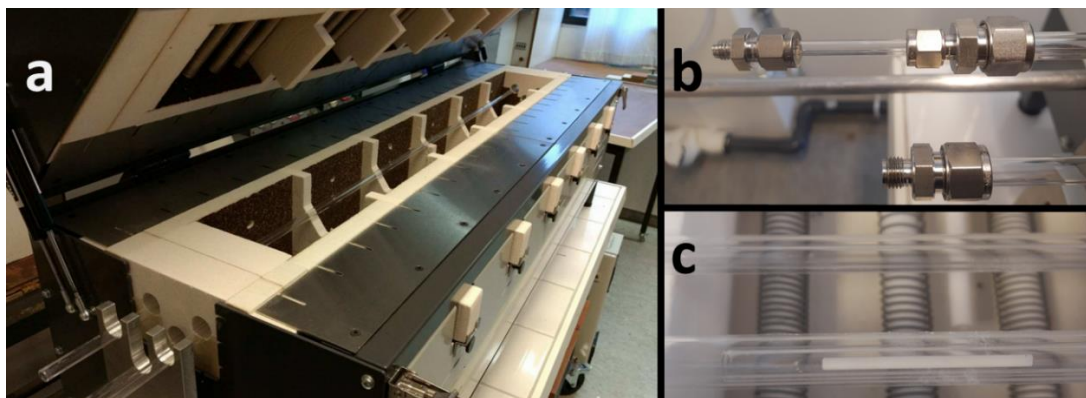


Figure 20. Picture of a) the six-zone furnace with three parallel quartz tubes used for laboratory Pt-catchment experiments, b) the double tube solution and c) an alumina piece inside an inner tube inside the reactor system.

3.1.3. Pt-catchment during *in situ* tomography

3.1.3.1. About the X-ray computed tomography technique

In the current work, *in situ* absorption-CT was used to study the microstructural development of the Pd and Pd/Ni wires during Pt-catchment. Several techniques can be used to obtain tomography images, each with its own advantages and drawbacks. The classical tomographic approach is based on X-ray absorption and do not provide quantitative information. In recent years, several catalyst- [135-137], battery- [138] and fuel cell- [139, 140] investigations have used more advanced tomographic probes to understand the active state of the material, the chemical distribution of the elements and oxidation state during the chemical reaction. By using a micro meter sized beam and scanning across the sample, both XRD, XAS, PDF and XRF can be used as contrast to investigate the chemical state of the sample, providing quantitative information in each voxel of the tomogram. However, data collection depends strongly on the chosen resolution (beam size) and sample volume to be probed, and can thus be time consuming. Data collection of 1-5 seconds per data collection can be expected, and sample need both to be rotated and translated, causing long data collection time for large samples [135]. Additionally, thick (*e.g.* 76 μm) noble metal samples may have a problem with high X-ray absorption making data collection difficult. The data analysis is also demanding as each voxel contains an individual data set that needs to be analysed.

The sample morphology should not change during the data collection time. However, if morphological changes occur continuously during the experiment, the data collection (tomography probe) must be faster than the morphological changes. The latter is the case for our reaction, and the data collection time would be limited to ~ 1 -10 minutes. Additionally, if the sample moves 1 μm in this time window, a similar resolution is lost. Furthermore, the crystallites observed on the Pd and Pd/Ni wires during Pt-catchment are 5-20 μm in diameter, hence a large sample size is desired for the measurement, and the total data collection time becomes high.

3. Experimental setup and characterization methods

3.1.3.2. About the *in situ* tomography experiment

For our experiments, we decided to perform X-ray absorption computed tomography (absorption-CT), which is perhaps the least advanced technique of those mentioned in terms of data collection. During absorption-CT, a monochromatic X-ray beam passes through the sample and the intensity of the X-ray beam attenuates (reduces) correlating with the sample absorption. A camera captures a radiograph (image) of the sample, as illustrated in Figure 21a. The sample is rotated 180°, capturing radiographs from different angles (900 frames in 10 seconds in our work). A tomogram (3D-image) is reconstructed from the radiographs using the filtered back projection algorithm. The pixel size of the camera (0.7 μm) sets the lower resolution limit of the tomogram. The main disadvantage of the technique is the non-quantitative information. The average absorption measured for a material is generally consistent, but there are large variations between each voxel due to statistical photon noise in addition to surface effects giving varying intensity. It is crucial that the chosen energy of the X-ray beam provides an as high absorption contrast between the elements as possible. In certain cases, it is difficult to distinguish between several constituents, *e.g.* in the current work we have good contrast between Pd and voids/air, but the contrast between voids/air and Ni has been low. Pt metal has been observed to mix with Pd metal and provide an increase in absorption, but quantification was not possible. If allowed by the instrumentation, absorption-CT using several energies could provide optimal contrast between the different elements.

Pt-catchment performed during *in situ* absorption-CT was similar to a regular laboratory experiment. The main differences were that a small custom-built furnace was used for the experiment (Figure 21a) with the sample was mounted in a sapphire tube (Figure 21b). The furnace used was 10x10x12 cm, with one hole through for the sample and one for the X-ray beam. The furnace was built in order to maintain an isothermal zone of several centimetres along the sapphire tube length so that both the sample (Pd and Pd/Ni) and Pt-source held high temperature.

The mounting of the sample should keep the sample in a stable position simultaneously as Pt is captured over a large area of the sample. A sapphire tube (2 mm OD, 1 mm ID) was used as the reactor tube, fixated to the 1/16" Swagelok coupling on the goniometer head (Figure 21b). A short piece of the Pd or Pd/Ni wire (~3 mm long) was mounted between two pieces of quartz wool in the end of the sapphire tube, with the length of the Pd or Pd/Ni wire positioned along the length of the sapphire tube. This would allow us to study the reaction along the wire length. The end-pieces of quartz wool were squeezed tightly together (before mounting) to make sure the sample position is stable. The sample was heated from room temperature to 1000 °C under a 1 ml/min air flow before the air flow was set to 28 ml/min during the dwell at 1000 °C, to make sure the quartz wool sticks properly to the sapphire tube. This was necessary as the overpressure inside the sapphire tube was ~0.4 bar when operated at 1000 °C. Below the sample (upstream with respect to gas flow), ~130 mg of Pt-wire was packed between two more pieces of quartz wool as the PtO₂ (g) source. We estimate that the $p(\text{PtO}_2)$ was approximately the same as in the home lab experiments, based on a similar gas flow, temperature and amount of Pt stacked in the tube relative to the tube size ($p(\text{PtO}_2)$ of $\sim 5 \times 10^{-8}$ atm).

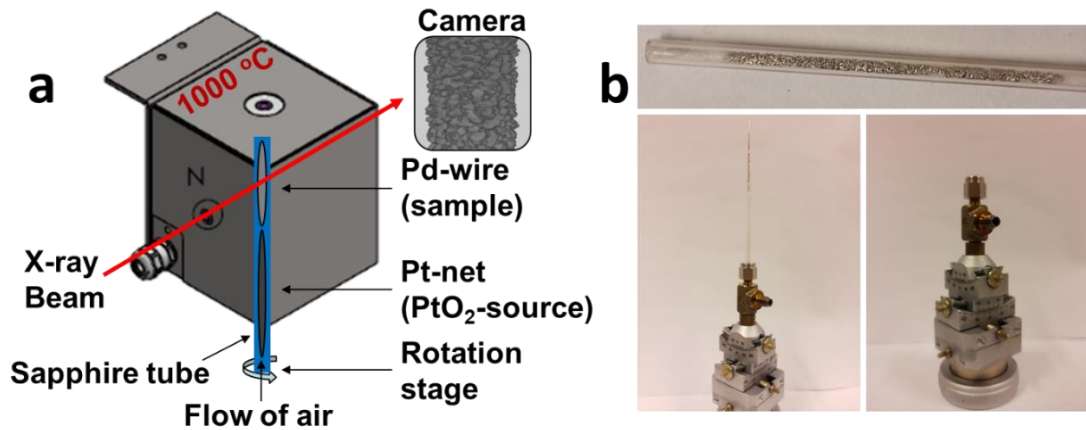


Figure 21. a) Illustration of the furnace used for *in situ* absorption-CT experiments, b) picture of the sapphire tube used to mount the sample and Pt metal during the experiment. The sample is located at the left end of the sapphire tube (top picture) between two pieces of quartz wool. Pt metal fills the rest of the tube (right part of the top picture). Reused with permission from Elsevier [141].

3.2. Scanning electron microscopy and energy dispersive X-ray spectroscopy

Scanning electron microscopy (SEM) is an imaging technique based on similar principles as light microscopy, although with higher resolution. Because of the low wavelength of highly accelerated electrons, the resolution of the instrument is in the range of nanometres. The electrons are scattered out of the specimen and collected to an image. The SEM uses a high-energy and focused electron beam (0.1 – 30 kV) and scans over the surface of an object to obtain an image. The instrument used in this work was a high-resolution Hitachi Regulus 8230 field-emission scanning electron microscope (Figure 22a).

Depending on the electron beam interaction with the material, different types of information can be obtained. The beam interaction volume increases with increasing energy of the beam, (Figure 22b). For the collection of secondary electrons (Figure 22b), topological information is obtained. A low energy beam, with a smaller interaction volume, is therefore used when acquiring high resolution images of the specimen surface. The secondary electrons are ejected from the specimen after energy transfer from the beam and have low kinetic energy (<50 eV). For the collection of backscattered electrons, the contrast is largely based on difference in the atomic number. Heavy elements have a higher signal in images based on back scattered electrons and will appear brighter in the image. A higher beam energy is preferred to obtain good contrast between elements. The backscattered electrons are electrons from the original beam elastically backscattered from the sample after interactions with the electric fields of the specimen with a kinetic energy is close to the original beam energy [142].

Energy dispersive X-ray spectroscopy (EDX) also originates from electrons deep in the interaction volume of the sample (Figure 22b). EDX is based on the collection of characteristic X-rays after the relaxation of electrons between different energy levels in the specimen. The electrons from the beam will excite an electron from a core level (*e.g.* 1s orbital, K-level) to a higher energy level, or remove it complete from the material. An electron from a higher energy

3. Experimental setup and characterization methods

state (*e.g.* 2p orbital, L-level) is subsequently relaxed to this vacant lower energy state and a characteristic electron is emitted from this relaxation (*e.g.* 2p → 1s emits $K\alpha$). The energy of the incident beam must thus be sufficiently high to excite the core electron out of its original state. Each element in the periodic table has several characteristic energies for the relaxation of electrons from a high-energy states to a lower energy states. An EDX spectrum is analysed by comparing the observed energies to literature values, and the signal is integrated for quantification. EDX is a quantitative technique, but the uncertainty is sometimes high because of the advanced data analysis and many factors that influences the observed signal. EDX is thus often considered semi-quantitative. For more details on SEM/EDX and other forms of electron microscopy, the reader is referred to dedicated literature [142, 143].

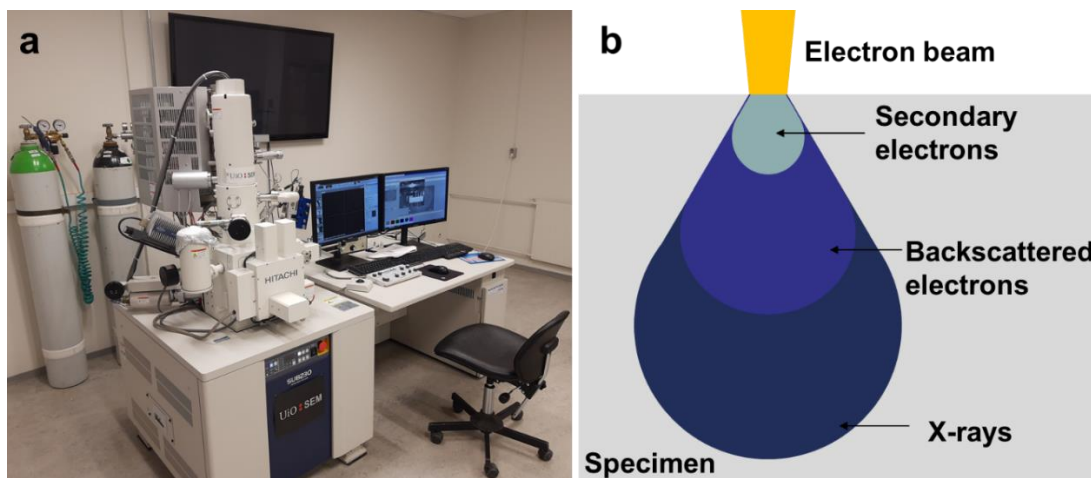


Figure 22. a) Picture of the Hitachi Regulus SU8230 SEM and b) illustration of the interaction volume of the electrons with the specimen.

3.2.1. Sample preparation for cross section imaging

To obtain high quality SEM/EDX images the sample should be conducting, alternatively a conducting coating (typically gold or carbon) can be applied before imaging. For cross-section imaging, the sample is first cast in a resin. A conducting resin is preferably used, like Polyfast (Struers), but it requires hot pressing at elevated temperature (180 °C) and pressure (40 MPa). Some samples will not have the mechanical strength to withstand hot pressing. Cold mounting using epoxy requires the application of conducting coating before SEM/EDX analysis.

After mounting, the sample is grinded and polished to obtain a flat and scratch free surface before imaging. The noble metals are soft (especially Au) and are after mounting located in a harder medium. Grinding and polishing the noble metals generally requires low force (~5 N) and long grinding/polishing times. Too high force will easily form scratches in the metal from the diamonds/SiC and from the polishing cloth. Too high force may also cause the noble metal wire to be grinded faster than the harder epoxy around, resulting in a non-flat surface. Details on metallographic and materialographic preparation is thoroughly described for all kinds of materials by Geels [144].

3.3. Synthesis of perovskite oxides

When synthesizing perovskite oxides, the goal is to achieve a homogeneous and phase pure product. The traditional method for oxide synthesis is the solid-state reaction method, where reactants, typically binary oxides, are mixed together, grinded and pelletized, before heat treatments at high temperature. This generally works well if the desired product is thermodynamically more stable than the reactants. However, the approach requires high temperature heat treatment to become phase pure, which may not be possible depending on the desired product.

In this work, the citric acid synthesis route has been applied to the synthesis of all Pt- and Rh-containing perovskites oxides, which is similar to the Pechini method [145]. The synthesis starts by the cations in solution, *e.g.* by dissolving nitrate salts or similar in water or nitric acid. Thereafter, 50-100 g of citric acid, per gram of expected product, is added to the solution. The citric acid dissolves in the water, and the solution is boiled until all water and nitrates have evaporated, leaving the molten citric acid with the cations dissolved. The sample is then heated over night at 180 °C before calcination at 400 °C for 12 hours. The latter step decomposes all the organic material in the sample and an amorphous mix of the elements is obtained. High temperature annealing is the final step to obtain the desired material. Lower annealing temperatures are often needed to obtain the desired material compared to the solid-state synthesis route, and it may be easier to synthesize certain compounds.

3.4. Powder diffraction

Powder diffraction is a widespread technique used for the identification, determination and refinements of the atomic structures of microcrystalline solids using X-rays, neutrons, or electrons. The probes offer different contrasts based on the scattering mechanism and is considered complimentary. For detailed information in the techniques, the reader is referred to dedicated literature [146, 147].

In this thesis, X-ray powder diffraction (XRD) is used to study the crystal- and micro-structure of microcrystalline powder samples. The possibility to have home-lab instrumentation, high intensity sources (synchrotrons) and efficient large area 2D detectors, makes XRD a versatile technique used for *e.g.* simple checks of sample quality, accurate structural descriptions, monitoring fast chemical reactions, and *in situ* experiments.

XRD is based on the coherent scattering of an X-ray beam and the constructive interference of the scattered beam, which in simplified terms are described by Bragg's law (Eq. 3-1; Figure 23a).

$$n\lambda = 2d_{hkl} \sin \theta \quad \text{Eq. 3-1}$$

Where n is an integer, λ is the wavelength, d_{hkl} is the distance between the lattice plane with Miller indices hkl and θ is the scattering angle. Bragg's law predicts that Bragg reflections (constructive interference) occur at specific scattering angles based on the wavelength and

3. Experimental setup and characterization methods

interlayer spacing. The dimensions and symmetry of the lattice thus determine the positions of the Bragg reflections. A momentum transfer (Q) occurs during the scattering at an angle θ , which is commonly used to compare diffraction data obtained using different wavelengths and is provided by the following relation (Eq. 3-2):

$$Q = \frac{4\pi \sin \theta}{\lambda} = \frac{2\pi}{d_{hkl}} \quad \text{Eq. 3-2}$$

X-rays are scattered by the electronic cloud of an atom. The strength of the interaction between the X-rays and electron cloud scales with the atomic number (Z), and is provided by the X-ray form factor (f_j). The intensity of a Bragg reflection is given by the structure factor (F_{hkl}) (Eq. 3-3)

$$F_{hkl} = \sum_j f_j o_j e^{2\pi i(hx_j + ky_j + lz_j)} e^{-\frac{B_j^2 \sin^2 \theta}{\lambda^2}} \quad \text{Eq. 3-3}$$

The structure factor of a Bragg reflection thus depends on the form factor (f_j) of the elements in the different sites (in position x, y, z), their occupancy o_j and a last term describing the thermal displacement parameter, B_j , and its dependence with θ (related to momentum transfer during scattering). The fact that the form factor scales with the atomic number imply that having two atoms with large difference in atomic number (*e.g.* Ni and Pt) can yield good elemental contrast in diffraction experiments compared to elements of similar atomic number. Some Bragg reflections may thus have strong intensity in some materials and vanishing in others, despite structural similarities (see example in section 4.2). Neutron diffraction can be advantageous to distinguish neighbouring elements, as the neutron scattering length do not depend on the number of electrons.

In this work, synchrotron XRD experiments have been performed using Debye-Scherrer geometry (Figure 23b), while experiments in the home lab have mainly used transmission geometry, which is similar to Debye-Scherrer geometry. Bragg-Brentano geometry is also common for home laboratory XRD experiments, and is based on reflection rather than transmission.

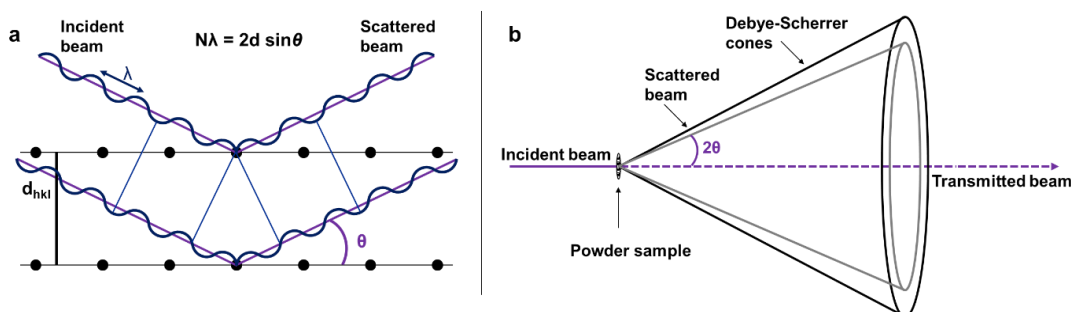


Figure 23. a) Illustration of constructive interference the meet the requirements of Bragg's law, b) illustration of the Debye-Scherrer geometry used for synchrotron radiation X-ray diffraction experiments. The equation that describes Bragg's law is provided in a.

3.4.1. Rietveld refinements

The most common technique for structural analysis of powder samples today is the Rietveld method. The method evaluates a simulated pattern (Y_{ic}) calculated from an input set of structural data against the experimental diffraction pattern (Y_{io}), weighted by w_i . By a least squares method, the refinements minimize the function M (Eq. 3-4) by refining the input structural data until it converges.

$$M = \sum_i w_i (Y_{io} - Y_{ic})^2 \quad \text{Eq. 3-4}$$

One of the strong advantages of the Rietveld method is the capability to analyse overlapping reflections, which may come from different Bragg reflections or different phases. Rietveld refinements can be used to assess the purity of a sample, to extract detailed structural parameters (requires high quality data sets) and to describe composition and microstructure. The quality of the refinements can be assessed by different R-factors and the expression for the commonly used R_{wp} is given below (Eq. 3-5).

$$R_{wp} = \sqrt{\frac{\sum_i w_i |Y_{io} - Y_{ic}|^2}{\sum_i w_i Y_{io}^2}} \quad \text{Eq. 3-5}$$

Although not a quantitative, it can help to trace how much the refinement improves by applying different features to the structural model. However, there is no threshold that indicates a good fit. In general, visual inspection is the most powerful tool to investigate the quality of a refinement.

4. Results and discussion

This chapter presents the main findings obtained in this work and is divided into two sections. The first part (section 4.1) is the primary investigation of the thesis, focusing on Pt-catchment using Pd, Pd/Ni and Pd/Au metal wires and nets, which are reported in Paper I-III. The section first describes the effect of heating Pd/Ni (and Pd) in dry and wet air at high temperatures. Thereafter, our first observations of Pt-catchment, swelling and restructuring are presented. Both these topics are published in Paper I. In-depth studies of Pt-catchment using *in situ* absorption-CT combined with SEM/EDX analysis address the mechanism for restructuring and are published in Paper II. An important outcome of Paper II is the effect of solid-state diffusion, leading us to investigate Pd/Au and Au as potential Pt-catchment materials due to the enhanced bulk diffusion achieved by Au-substitution. In addition to laboratory experiments, a 5 month experiment in an industrial reactor was performed. Pt-catchment with Pd/Au and Au is reported in Paper III. At the end of this section (0), the restructuring mechanism is discussed for both Pd, Pd/Ni and Pd/Au samples based on Paper II and Paper III.

The second part of this chapter (section 4.2) investigates structural aspects of Pt- and Rh-containing perovskite oxides. The topic originates from the idea of using oxide materials as Pt- (and potentially Rh-) catchment materials as a competitive alternative to noble metal alloys. Previous work (section 2.3) indicates that LaNiO₃ can capture Pt and Rh through *B*-site substitution in the system LaNi_{1-x}M'_xO₃, *M'* = Pt, Rh. The current work is a study to establish a knowledge-base on the synthesis and structural aspects of Pt- and Rh-containing perovskites, while Pt-catchment using oxides is addressed in a different PhD work [148]. The focus of the section is the stoichiometric double perovskites RE₂MM'O₆ (*RE* = La, Nd, Y; *M* = Ni, Co, Fe; *M'* = Pt, Rh) with particular attention to *B*-site ordering and oxidation states. The two perovskite systems LaNi_{1-x}M'_xO₃, *M'* = Pt, Rh, are published in Paper IV and Paper V, respectively.

4.1. Pt-catchment by noble metal alloys

The origin of the swelling and structural reconstruction of the Pd/Ni gauzes used for Pt-catchment during the industrial ammonia oxidation reaction, as shown in Figure 6 and Figure 11, was not understood prior to the start-up of this project. In this section, the results obtained for the state-of-the-art Pt-catchment system, Pd/Ni (91/9 at. %), are described, together with Pd and the Pd/Au system. This part of the work aimed to identify the origin of the swelling and structural reconstruction that occurs during Pt-catchment. One of the critical parameters of the metallic Pt-catchment systems is the mobility of Pt and the constituents of the catchment alloy. The primary motivation behind investigating the Pd/Au system is that Pt-mobility in the Pd/Au alloys is several orders of magnitudes higher than in Pd. In addition, our studies have benefitted from studying both polycrystalline and quasi-monocrystalline samples to manipulate and tune the number of grain boundaries (GB). By tuning bulk mobility and the number of grain boundaries, the experiments allow us to unravel the role of bulk diffusion relative to GB diffusion.

4.1.1. Role of Ni in the Pd/Ni-alloy (Paper I)

In the industrial reactor for ammonia oxidation, many chemical constituents are present that can react with the Pd/Ni wire; O₂ (~6 %), H₂O (~15 %), NO (~10 %), NH₃ (~100 ppm), N₂O (0.1-1 %), PtO₂ (~5 × 10⁻⁸ bar) evaporated from the Pt/Rh catalyst, and the balance gas N₂ (~68 %). In our first experiments, we first use dry air to see the effect of oxygen on the Pd and Pd/Ni wires (section 4.1.1.1 – 4.1.1.2), and then wet air to see the effect of water and oxygen combined (33 % H₂O and 67 % air) (section 4.1.1.3).

4.1.1.1. Effect of oxygen on the Pd/Ni alloys

When the Pd/Ni wire is exposed to a flow of dry air at 900 °C, a total weight increase of ~1.47 % is observed over the course of 24 hours, indicating complete oxidation of all Ni to NiO in the Pd/Ni (91/9 at. %) alloy. Pd does not oxidize in these experiments as 900 °C is above the stability temperature of PdO (Appendix: Figure A3). SEM/EDX images show oxygen propagating inwards and formation of NiO particles inside the sample, where the largest particles form in the grain boundaries and quite near the surface (Figure 24b and d). Before oxidation, the Ni-distribution in the Pd/Ni alloy is homogeneous and the grain size is ~5 μm (Figure 24a). However, after oxidation, NiO has precipitated mainly in the GBs, and the Pd grain size is much larger; in the range of 10-25 μm (Figure 24f). Ni located in the wire core is attracted to the formed NiO particles (Figure 24d), as seen from the EDX-map showing areas within the NiO layer (20 μm into the cross section) with a darker colour and less Ni. The fact that NiO precipitates mainly in the GBs in the polycrystalline Pd/Ni wire indicates a high GBs mobility of Ni in Pd.

A strong contrast is seen to the oxidation of a monocrystalline Pd/Ni wire, where the oxidation is homogeneous in the sample, and all the NiO particles are small (Figure 24c and e). The inwards oxygen diffusion is almost equally fast in the quasi monocrystalline sample as in the polycrystalline sample (Figure 24b-c). This is supported by the fact that the diffusion rate of oxygen is faster than that of metal in the bulk of the Pd-alloys (Appendix: Table A1). However, literature values (Appendix: Table A1) imply that the expected diffusion depth of the internal oxidation is ~112 μm per hour [110], significantly more than our observations (15-20 μm). No mass gain is observed for Pd (Appendix: Figure A5).

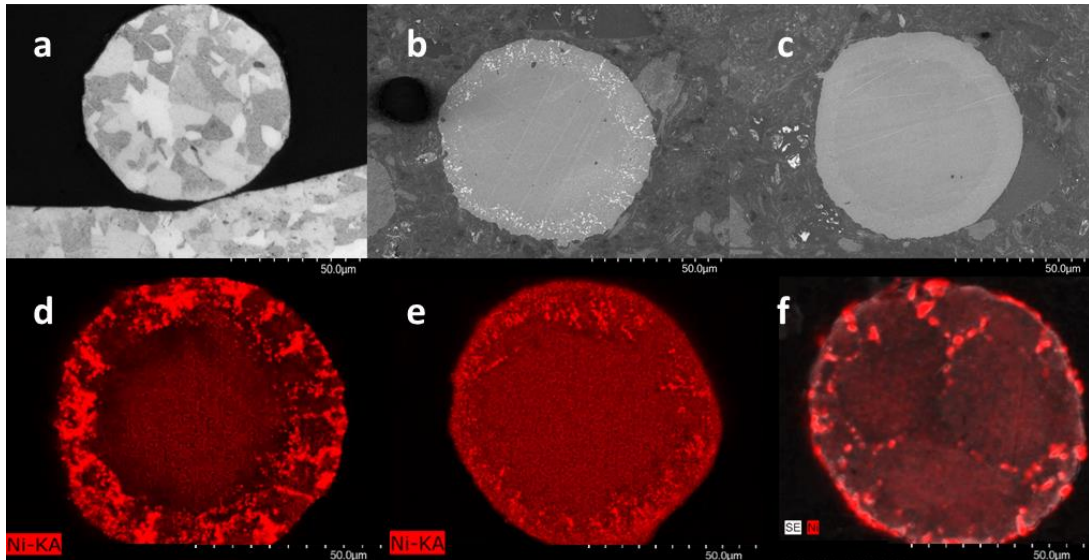


Figure 24. SEM images and EDX maps of the cross section of a) a fresh Pd/Ni wire etched in aqua regia for 30 sections to see the grain structure, b) a polycrystalline Pd/Ni wire heated for 1 hours in air at 900 °C, c) a quasi-monocrystalline Pd/Ni wire heated for 1 hours in air at 900 °C, d) a polycrystalline Pd/Ni wire heated for 2 hours in air at 900 °C, e) a quasi-monocrystalline Pd/Ni wire heated for 2 hours in air at 900 °C, f) EDX-mapping of a polycrystalline 76 μm Pd/Ni wire heated at 900 °C for 30 days in a muffle furnace (air) and etched for 30 seconds in HNO₃ before imaging to reveal grain boundaries. Edited and reused with permission from Johnson Matthey Plc [149].

4.1.1.2. Effect of diffusion rates and oxygen solubility during internal oxidation

The diffusion rates and solubility of oxygen in an alloy are two key factors that affects internal oxidation of an alloy composed of two elements with different nobility. It is reported that Au has a 2-7 orders of magnitude lower oxygen permeability than other fcc metals [150] and a more rapid bulk diffusion than Pd (Appendix: Table A1). During oxidation of Au/Fe (98.5/1.5 at. %) in air at 800 °C, a thick Fe₂O₃ layer is formed on the surface of the wire (Figure 25a-c), in addition to Pt-crystals on the wire surface because a Pt net was placed upstream of the sample during the experiment. For Pd/Ni (91/9 at. %) at 900 °C, internal oxidation is observed in air ($pO_2 = 0.20$ bar), while a surface layer of NiO is formed in a flow of inert gas (N₂ ≥ 99.999%) (Figure 25d-f). There was likely a small O₂-concentration present in the inert gas stream for the Pd/Ni experiment. Au/Fe (98.5/1.5 at. %) in air and Pd/Ni (91/9 at. %) in a low pO_2 behave similarly, where the least noble element diffuse to the surface to oxidize. This shows how the solubility and diffusion (permeability) of oxygen and the diffusion rate of the metal species is critical for how the oxidation occurs; as internal oxidation (Figure 24) or surface oxide formation (Figure 25).

4. Results and discussion

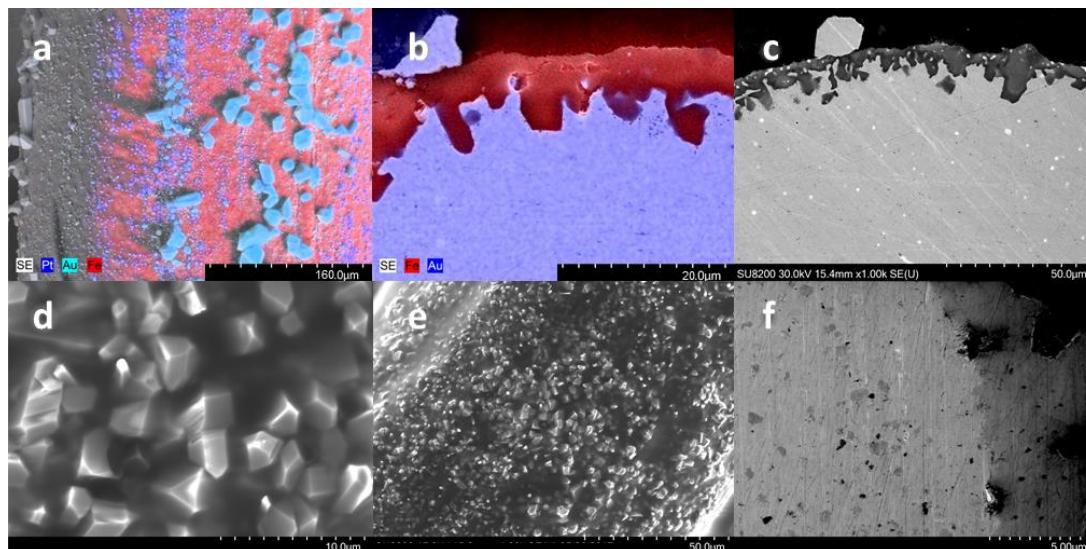


Figure 25. SEM/EDX of a) surface and b-c) cross section of the Au/Fe (95/5 at. %) wire after 10 days' heat treatment in a flow of air at 800 °C with a Pt-net upstream to simultaneously test the Pt-catchment abilities of this sample, resulting a few Pt-crystals to also be present on the wire surface. D-e) SEM of surface and f) cross section of Pd/Ni (91/9 at. %) treated in a flow of N₂ (≥ 99.999 %) for 6 days at 1000 °C.

4.1.1.3. Effect of water vapour on Pd/Ni

In the industrial gas mix for ammonia oxidation, water vapour is present in a concentration around 15 vol. % as a result of the ammonia oxidation process (section 2.1). When water vapour is included in the air flow and reacts with the Pd/Ni sample, the internal oxidation of Ni to NiO still occurs in a similar manner as in dry air, forming internal precipitates of NiO (Figure 26a). However, another effect appears. After two weeks' heat treatment in a flow of wet air (33 % H₂O) at 1050 °C, a significant Ni-loss is observed. Both mass changes and ICP-OES/MS show that the Ni-content is reduced from 8.7 to ~4.9 at. % (from 5 to ~2.7 wt. %). This is easily seen in the wire cross section, as the outer 5-15 μm of the wire is depleted in NiO, and the NiO particles remain only in the wire centre (Figure 26a-b). Additionally, some surface roughness appears (Figure 26c), but no porosity is observed.

The Pd/Ni catchment system is known to be completely depleted in Ni after industrial operation (section 2.2). From these results, we believe that water vapour is the key constituent causing Ni-loss, and that the Ni-loss occurs as formation and evaporation of the volatile Ni(OH)₂. This is also in accordance with literature reports on volatilization of Ni in wet conditions [151]. An interesting question regarding the NiO-loss is how the transport of NiO occurs from deep inside the wire and out the surface. From Figure 26b, there is seemingly depletion of NiO in the GBs, which may aid the transport of NiO to the surface. However, which species (Ni, NiO particles, molecular NiO, Ni(II), Ni(OH)₂) that diffuses towards the surface is unknown.

Finally, the experiment did not show a Pd-loss close to the industrially observed Pd-loss from the Pd/Ni catchment unit, which is ~1/3 of the Pt-loss in mass. A very small Pd-loss in dry and wet air is supported by a report by Opila *et al.* [109] and our own TG-experiments (Appendix: Figure A5).

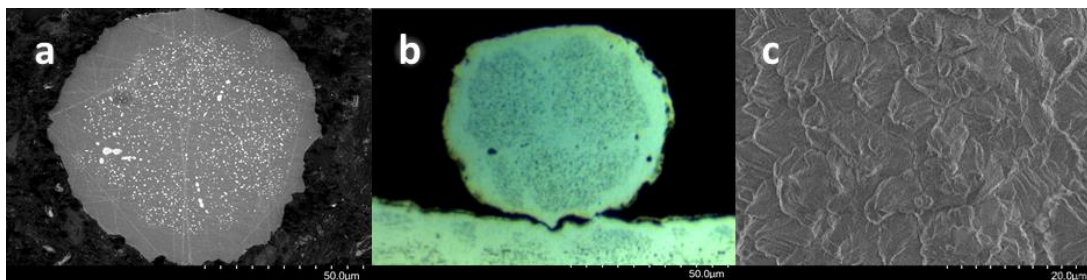


Figure 26. Images of the 76 μm Pd/Ni wire treated in wet air at 1050 $^{\circ}\text{C}$ for 2 weeks. a) SEM image of the cross section, b) light microscope image of the cross section and c) SEM image of the surface. Edited and reused with permission from Johnson Matthey Plc [149].

4.1.2. Role of PtO_2 – the first sign of swelling and porosity (Paper I)

From section 4.1.1 we have a good overview of the effect of oxygen and water vapour on the Pd/Ni and pure Pd wires. Though both internal oxidation and Ni-loss occurs for the Pd/Ni wire, no porosity was observed, only surface roughness. By placing a rolled up Pt-net upstream of the sample, PtO_2 is added to the dry/wet air. Pt-catchment is then simulated in a similar way as in the industrial reactor for ammonia oxidation, except that the gas mixture does not contain NH_3 and NO. The experiments are performed at 1050 $^{\circ}\text{C}$ to provoke the reconstruction reaction to be as rapid as possible; a decision based on that we upfront had no information on how rapid it was before starting the experimental study.

During Pt-catchment experiments in dry air at 1050 $^{\circ}\text{C}$, rapid morphological changes are observed for both the Pd- and Pd/Ni wires (Figure 27). After 10 hours, several surface crystallites have appeared, and the only visible difference between Pd and Pd/Ni is several NiO particles located on the surface of the Pd/Ni wire (Figure 27a and d). After 10 days, a significant restructuring has occurred, causing the surface to be covered by beautiful Pd-Pt crystallites (Figure 27b and e). EDX mapping of the Pd/Ni wire cross section after 20 days show that NiO is present mainly between the Pd-Pt crystallites (Figure 27f), *i.e.* it has been pushed out of the formed Pd/Pt crystals. After 30 days treatment in wet air, a similar quantity of Ni is lost as in the experiment without PtO_2 (section 4.1.1.3), simultaneously as the reconstruction into Pd-Pt crystallites occur in a similar manner as in dry air (Figure 27c). We therefore believe that grain reconstruction is caused by Pt-catchment, while Ni-loss is caused the presence of water vapour in the gas stream, and that these are separate phenomena.

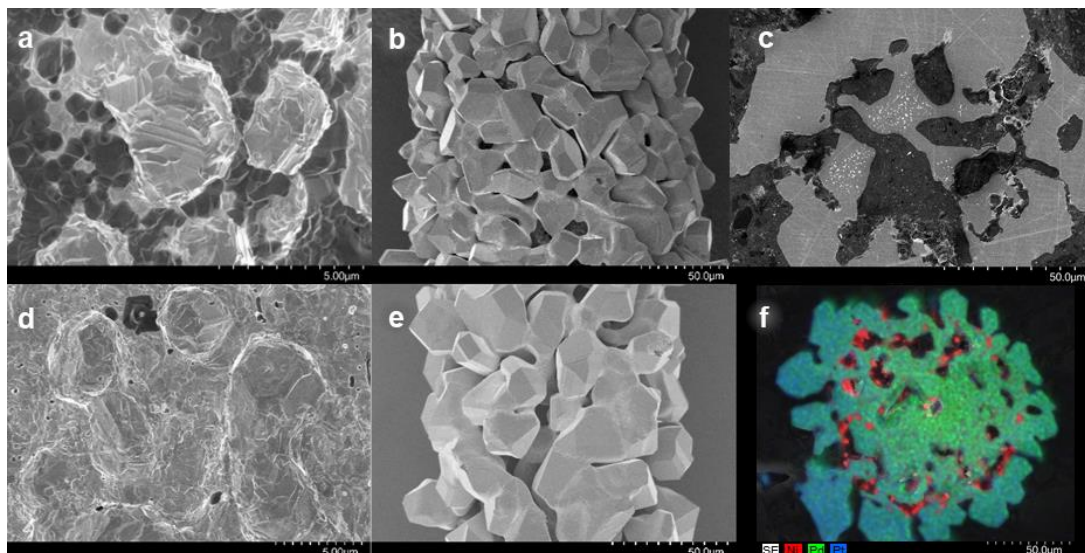


Figure 27. SEM images of Pd (76 μm) and Pd/Ni (120 μm) wires after Pt-catchment experiments at 1050 $^{\circ}\text{C}$. a) Pd/Ni after 10 hours in dry air, b) Pd/Ni after 20 days in dry air, c) Pd/Ni after 30 days in wet air (cross section), d) Pd after 10 hours in dry air, e) Pd after 20 days in dry air and f) Pd/Ni after 20 days in dry air (EDX map of cross section). Edited and reused with permission from Johnson Matthey Plc [149].

4.1.3. Pilot plant experiments – identifying two causes for porosity (Paper I)

The laboratory experiments described above (section 4.1.2) confirms the cause-effect relation between Pt-catchment and grain reconstruction. However, the experiments are a simplification in terms of the gas atmosphere, as only dry- and wet air was used. In order to investigate the effect of the real (industrial) gas mixture and temperature (~ 900 $^{\circ}\text{C}$), two pilot plant experiments were performed. For both experiments, a pure Pd catchment net was used, but the experiments differ in terms of the ammonia oxidation catalyst. One experiment used a Pt catalyst for ammonia oxidation (not Pt/Rh), while the other experiment used a LaCoO_3 -based catalyst (Pt-free catalyst). This allow us to see the difference between having and not having volatile PtO_2 in the gas stream. SEM images of the surfaces of the Pd catchment material reveal that both samples have swelled and obtained significant porosity during the experiment (Figure 28a and c). However, the appearance of the Pd sample surfaces are different; the sample with a Pt-catalyst has an *edged* shape of the surface crystallites (Figure 28b), while the sample with the LaCoO_3 -catalyst has a *rounded* shape of the surface crystallites (Figure 28d). While significant amounts of Pt is captured by the sample with a Pt-catalyst upstream (~ 14 at. % Pt), no Pt is captured by the sample with the LaCoO_3 -catalyst upstream. This allow us to conclude that there are two causes for porosity in the Pd-based Pt-catchment system: 1) grain reconstruction caused by Pt-catchment giving *edged* crystallites and 2) pore-formation due the extreme gas/temperature conditions ($\text{O}_2/\text{H}_2\text{O}/\text{NH}_3/\text{NO}$ at 900 $^{\circ}\text{C}$) giving *rounded* crystallites.

Furthermore, ICP-OES/MS reveal a very similar Pd-loss for both samples, with a loss of 7-8 at. % (7-8 wt. %) of the installed Pd over a 19 days long experiment (~ 0.033 g/ton HNO_3 produced). We therefore conclude that the Pd-loss is not caused by the Pt-catchment process, dry air or wet air, but by the aggressive gas/temperature conditions of the industrial ammonia oxidation reactor.

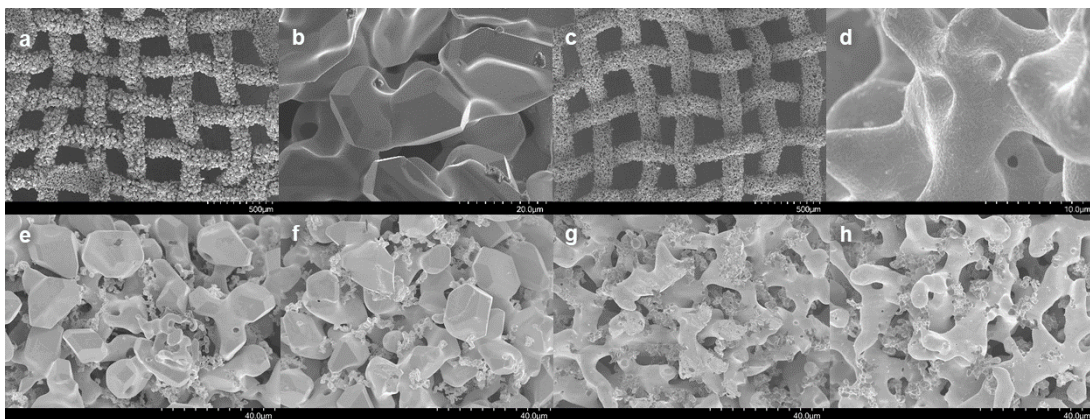


Figure 28. SEM images of the surface of the Pd nets tested in the pilot plant with a-b) a Pt catalyst and c-d) a LaCoO_3 -based catalyst. SEM images of the surface of several used Pd/Ni catchment nets after 46 days of operation at industrial conditions ($900\text{ }^\circ\text{C}$, 10 % NH_3 , 5 bar, Pt/Rh catalyst), where e) is the top side of the first Pd/Ni catchment gauze in the pack, f) is the top side of the second Pd/Ni catchment gauze in the pack, g) is the bottom side of the second Pd/Ni catchment gauze in the pack, and h) is the bottom side of the third Pd/Ni catchment gauze in the pack. Edited and reused with permission from Johnson Matthey Plc [149].

In fact, both *edged* and *rounded* crystallites are formed for Pd/Ni nets used for Pt-catchment at industrial conditions. This is nicely seen by investigating a gauze pack operated at industrial conditions (46 days, $900\text{ }^\circ\text{C}$, 10 % NH_3 , 5 bar, Pt/Rh catalyst) with three Pd/Ni-catchment nets (Figure 28e-h). On the top side of the first gauze (Figure 28e), the surface looks like the surface reconstructed by Pt-catchment, with *edged* crystallites (Figure 28a-b). However, the bottom side of the third (final) gauze in the pack (Figure 28h) looks like the surface reconstructed by the extreme gas/temperature conditions, with *rounded* crystallites (Figure 28c-d). The top and bottom side of the second gauze looks like something in between (Figure 28f-g).

4.1.4. Understanding Pt-catchment on Pd – *in situ* tomography (Paper II)

Knowing that the grain reconstruction is an intrinsic property of the Pd- and Pd/Ni wires during Pt-catchment, mechanistic insight into this process is highly desired to understand how the Pd/Ni catchment system can be improved. For this reason, we also lower the temperature of the laboratory experiments from $1050\text{ }^\circ\text{C}$ to $900\text{ }^\circ\text{C}$ in order to replicate the industrial Pt-catchment conditions. As will be shown, the Pt-catchment and resulting wire restructuring is fast also at $900\text{ }^\circ\text{C}$ in dry air.

To investigate the real time development of grain reconstruction, *in situ* synchrotron X-ray absorption tomography (absorption-CT) experiments were performed using both Pd- and Pd/Ni wires. The absorption-CT experiments were performed at $1000\text{ }^\circ\text{C}$ to make sure sufficient Pt-catchment was possible during the experiment (experimental details in Paper II and section 3.1.3). For practical reasons, the absorption-CT experiments were split into sessions of 12 hours, allowing us to follow the development of grain reconstruction over a larger time scale. Several samples were pre-treated in the home laboratory to allow us to study selected samples from *e.g.* 0 to 12 and 24 to 36 hours, without having to do the experiment in-between.

4. Results and discussion

A visual overview of the first 34 hours of Pt-catchment is summarized in Figure 29. At first, surface roughness appears on both wires, and Ni is gradually oxidized to NiO. After 4h, a volume increase of 4.6 % has occurred for Pd/Ni; the same volume increase as expected for complete internal oxidation of all internal Ni to NiO, but in a shorter time than expected (Paper I). Pd show a volume increase of ~1 %, and it is likely that both samples have captured a similar amount of Pt after 4h (~1 at. % Pt). After 12h, several surface crystals have formed on the surface of both wires, and large NiO particles are formed, mainly located on the outer half of the wire. As this continues, the wires obtain a completely restructured surface after 34h, with surface crystals of 5-10 μm , and both wires have open porosity near the wire surface.

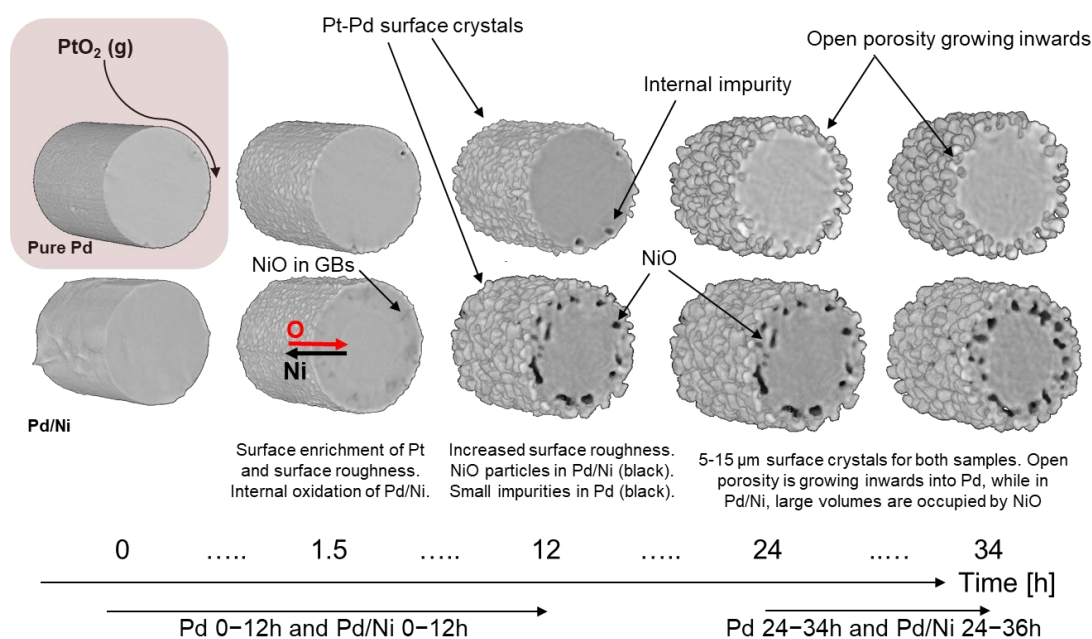


Figure 29. Schematic illustration of the morphological changes and chemical dynamics of Pd and Pd/Ni (91/9 at. %) wires after 0, 1.5, 12, 24 and 34 hours of Pt catchment at 1000 °C during *in situ* absorption-CT experiments in synthetic air with $p(\text{PtO}_2) \approx 5 \times 10^{-8}$ bar. The large NiO particles and the impurities inside the Pd/Ni and Pd wires, respectively, are manually coloured black. Reused with permission from Elsevier [141].

Quantitative data analysis was only possible to perform for the Pd wire, and not the Pd/Ni wire, due to difficulties in separating NiO and voids in the analysis (see Paper II). For the Pd wire, a rapid increase in Pt-concentration (calculated from volume increase) occurs over the first 4 hours (Figure 30a), before a slower increase is maintained for the rest of the experiment. Simultaneously, an increase in both surface area and porosity is observed (Figure 30b-c). While the Pt-concentration has a rapid increase the first 4 hours of the experiments, this is not the case for the surface area and porosity. The porosity within the original radius of the wire represents porosity that has developed into the wire; not a restructuring of the outer surface. During the first 4 hours (when there is rapid Pt-catchment; Figure 30a), the surface area increases steadily, supporting a restructuring of the outer surface (Figure 29). The porosity increases mainly later in the experiment, after ~5h, indicating that the initial Pt-catchment on the outer surface occurs prior to the start-up of the inwards porosity.

Looking even more detailed into the Pt-catchment rate, we can view the volume increase and porosity along the length of the Pd-wire in the experiment (Figure 30d-e), from the gas inlet side to the gas outlet side. This tells us that both Pt-catchment and porosity is higher near the gas inlet side, and that there is a correlation between high Pt-catchment and more rapid restructuring of the Pd-wire. Additionally, by calculating the Pt-catchment efficiency along the wire length, we can see how much Pt that is captured onto the Pd-wire from the gas phase (Figure 30f). After 3 hours, $\sim 40\%$ of the Pt is captured (Figure 30f), and the non-linear line shape indicates that the Pt-catchment is higher on the inlet side of the wire (indicated by striped line in Figure 30f). After 6 hours, the trend is similar, while after 33 hours, the Pt-catchment rate is similar along the wire length, and the total Pt-catchment over the entire wire accumulates to only $\sim 20\%$ of the PtO_2 in the gas stream. An overview of the complete grain reconstruction process for both Pd and Pd/Ni from 0 to 10 days is summarized in Paper II (Paper II, Figure 6).

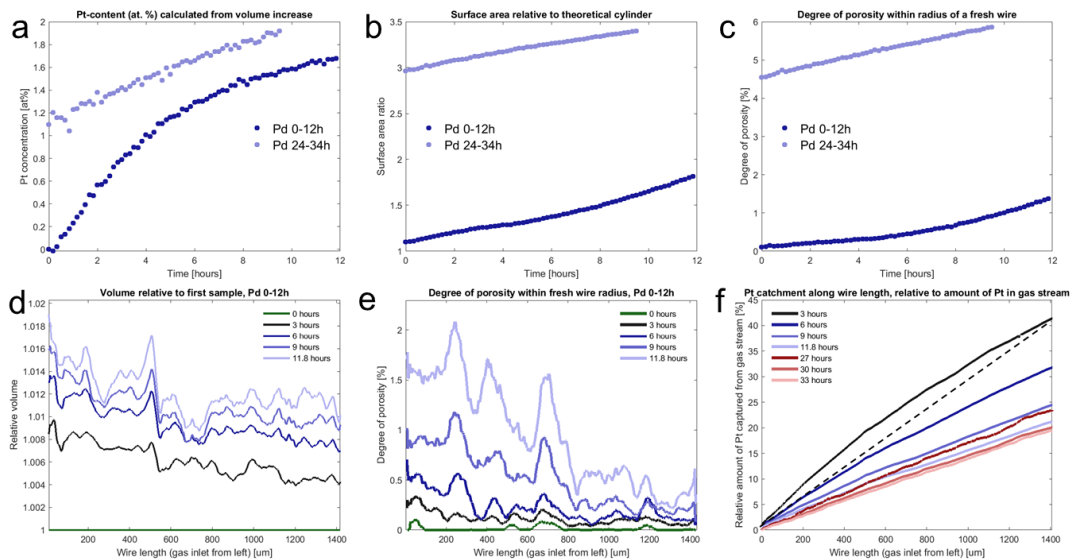


Figure 30. Results from the quantitative analysis of the Pd wires during absorption-CT experiments. a) Pt-concentration versus time, b) surface area relative to a theoretical cylinder versus time, c) degree of porosity within the original radius of the wire versus time, d) volume relative to the first sample in the series versus wire length, e) degree of porosity within the original radius ($76\ \mu\text{m}$) of the wire versus wire length, and f) Pt-catchment along the wire length at selected time intervals in the experiment (0-3h, 3-6h, 6-9h, 9-12h, 24-27h, 27-30h, 30-33h). Reused with permission from Elsevier [141].

4.1.5. Role of grain size on Pt-catchment on Pd- and Pd/Ni wires (Paper II)

After the 10 days long Pt-catchment experiment described above, the Pd- and Pd/Ni wires consists solely of an assembly of $10\text{-}20\ \mu\text{m}$ crystallites (Paper II, Figure 6). The size of the formed crystallites are similar to the grain sizes present in the Pd- and Pd/Ni wires after a short heat treatment (Figure 24), which imply that it is natural to consider how the original grain structure influences the wire restructuring. To investigate this fact, both Pd- and Pd/Ni nets were pre-annealed for 7 days at $1100\ \text{°C}$ in vacuum to facilitate grain growth. The resulting wires were in practice quasi-monocrystalline, with a grain size ranging from 20 to $200\ \mu\text{m}$. The grain size can easily be seen visually after Pt-catchment experiments (Figure 31e and g), where the grain boundaries cross the wire cross section at certain locations.

4. Results and discussion

We can now compare the polycrystalline samples used in the absorption-CT experiment with the quasi-monocrystalline samples, to study the effect of the grain structure. There is quite significant difference in Pt-catchment rate for the two sets of samples. For both Pd and Pd/Ni, the amount of Pt captured after 1 day using a polycrystalline wire (3.3 and 4.6 at. %) is higher than what a monocrystalline wire can capture over 10 days (2.3 and 2.6 at. %) (Table 3). Furthermore, the surface of the quasi-monocrystalline samples are significantly less restructured than the polycrystalline samples (Figure 31e and g).

Table 3. Results from ICP-OES analysis of the four polycrystalline samples shown in Figure 31. The estimated Pt-concentration in the monocrystalline samples are based on mass changes.

Polycrystalline	Time [d]	Pd [at. %]	Pt[at. %]	Ni [at. %]	Pt/(Pd+Pt+Ni)	Ni/(Ni+Pd)
Pd/Ni	1	85.6	4.6	9.8	4.6	10.3
Pd/Ni	4	87.6	3.7	8.7	3.7	9.0
Pure Pd	1	96.7	3.3	-	3.3	-
Pure Pd	4	93.6	6.4	-	6.4	-
Monocrystalline	Time [d]	Pt-concentration calculated from weight change [at. %]				
Pd/Ni	10				2.6	
Pure Pd	10				2.3	

The EDX-maps of the wire cross sections reveal a large difference between the poly- and quasi-monocrystalline samples. After 1 day of Pt-catchment on the polycrystalline wire, a pattern of Pt crossing the wire cross section is seen from EDX, most strongly seen in Pd (Figure 31a). The lines of Pt crossing the wire is believed to be elevated concentrations of Pt in the grain boundaries; an effect that is absent in the monocrystalline wire. The grain boundary pattern is still visible in the polycrystalline Pd-sample after 4 days (Figure 31b). The same effect is present also for the polycrystalline Pd/Ni wires, but to a lower extent (Figure 31c-d). After 4 days, the Pt-content in the core of the Pd-wire is 1.4-3.2 at. %, and only 0.1 % for Pd/Ni. However, for the monocrystalline samples after 10 days, the Pt-concentration is zero deeper than $\sim 10 \mu\text{m}$ into the wire, and definitely 0 at. % in the wire core.

For both the quasi-monocrystalline Pd and Pd/Ni samples, a low surface restructuring of the wires is observed after 10 days (Figure 31e-h). However, for the Pd/Ni wire, there is more surface roughness than for Pd, especially at certain (seemingly random) locations, and the grain boundaries show some porosity inside the wire. Additional Pt-catchment experiments performed on Pd and Pd/Ni show in addition that the Pd- and Pd/Ni quasi-monocrystalline wires can restructure at the most exposed regions of the sample (*e.g.* at the end of a wire) in a high gas flow of PtO_2 . We also observe that Pd/Ni is more prone to restructure than Pd in the quasi-monocrystalline state. Additional SEM/EDX data is presented in the supplementary section of Paper II.

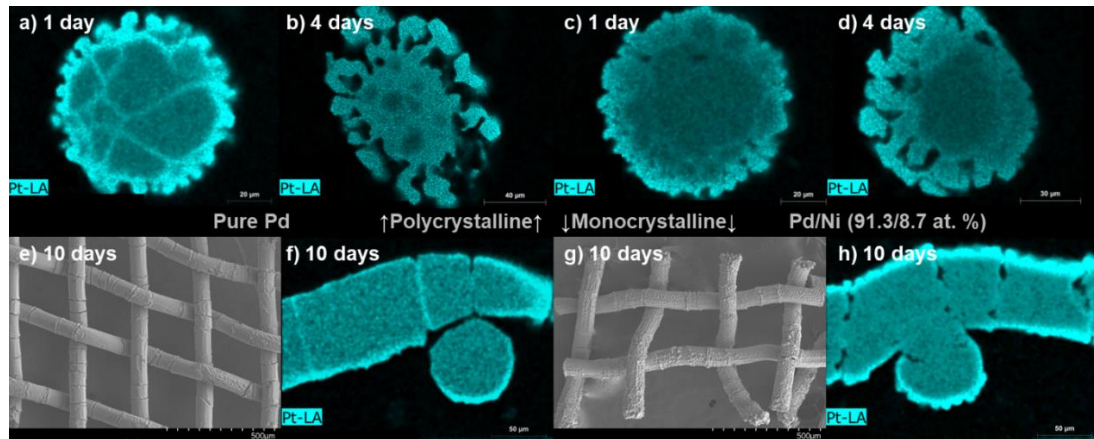


Figure 31. SEM and EDX analysis of the surface and cross section of the polycrystalline Pd- (a-b) and Pd/Ni (c-d) wires tested for Pt-catchment at 1000 °C for 1 and 4 days, and the quasi-monocrystalline Pd- (e-f) and Pd/Ni (g-h) wires after Pt-catchment at 900 °C for 10 days. Additional EDX maps for the polycrystalline samples are provided in Figure S11 in Paper II, and additional SEM/EDX data for the quasi-monocrystalline samples are provided in Figure S12 – S18 in Paper II. Edited and reused with permission from Elsevier [141].

4.1.6. Pt-catchment on Pd/Au alloys (Paper III)

From the EDX map of the monocrystalline wires (Figure 31f and h) it is pressing to consider if slow bulk diffusion is the cause for why Pt is only present near the surface of the wires. It is commonly considered that metallic elements with a high melting point have a lower diffusion coefficient when compared at the same temperature, and that diffusion is low at temperatures far below the melting point (section 2.4.2). Pd has a melting point of 1555 °C and Pt of 1768 °C [58], and the mobility of Pt in Pd is quite low at 900 °C (diffusion length of Pt is $\sim 3.6 \mu\text{m}$ per day [62]).

In order to have more rapid diffusion in the alloy during Pt-catchment, one option is to increase the temperature. However, there are limitations to how relevant this is for industrial applications that are limited by the optimal reaction temperature of the chemical reaction in question. Additionally, previous experiments (section 4.1.2) have shown significant restructuring also at 1050 °C. However, a change in the alloy composition could help in improving the atomic mobility. This brings to mind the original Pt-catchment alloys introduced by Holzmann [17]; the Pd/Au alloys. Au has a melting point of 1064 °C [58]. Au-substitution in Pd significantly improves bulk diffusion at 900 °C compared to Pd (Appendix: Table A1). For this reason, two Pd/Au alloys (wire diameter of 76 μm) and Au (wire diameter of 100 μm) were tested for Pt-catchment. Both poly- and quasi-monocrystalline alloys were tested, and the quasi-monocrystalline alloys were obtained by pre-annealing at 1100 °C (900 °C for Au) for 7 days in vacuum.

4.1.6.1. Quasi-monocrystalline Pd/Au samples

After Pt-catchment on the quasi-monocrystalline Pd/Au samples we expected to see a significant improvement of the Pt-diffusion compared to the Pd and Pd/Ni wires. In the Pt-catchment experiment (20 days of Pt-catchment at 900 °C), the two Pd/Au alloys behave as expected and no significant structural reconstruction occurs (Figure 32a-b, d-e). However, the Au wire restructure completely (Figure 32c). Although the restructuring is similar to Pd, it is

4. Results and discussion

different in the sense that the crystallites are larger ($\sim 40 \mu\text{m}$) than for Pd ($\sim 20 \mu\text{m}$), and the wire core remains intact after the Pt-catchment experiment was completed after 20 days (Figure 32f). EDX mapping further show that the Pt-distribution is indeed different for the different samples (Figure 32d-f). The samples with a higher Au content show a more homogeneous distribution of Pt through the wire cross section, and a higher Pt-concentration in the centre of the wire core (Table 4). For Au, the Pt-concentration is completely homogeneous throughout the entire sample, from the tip of the surface crystals to centre of the wire core.

Finally, ICP-OES show that there is a very small difference Pt-content in the three samples; 7 at. % Pt in Pd/Au (91/9 at. %) and almost 10 at. % Pt in the Pd/Au (50/50 at. %) and Au samples. However, EDX quantification show that Pd/Au (91/9 at. %) has zero Pt in the wire core, while Au has 10 at. % Pt uniformly distributed in the entire wire cross section. This demonstrates the effect of improved diffusional properties, and how the Pt-catchment changes with composition.

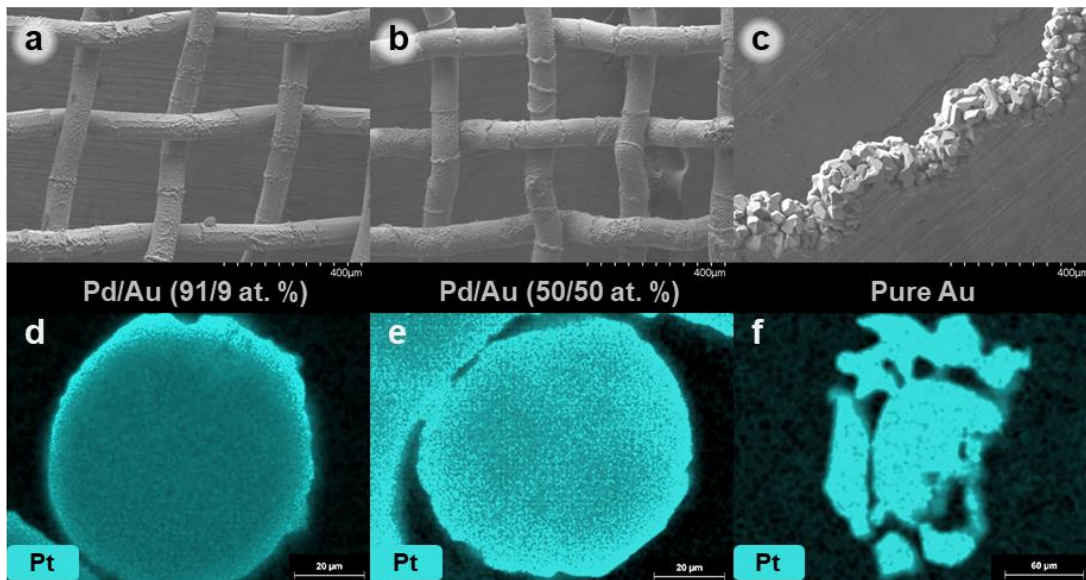


Figure 32. a-c) SEM images of the surface and d-f) EDX maps of the cross section of the quasi-monocrystalline Pd/Au samples tested as Pt-catchment materials at $900 \text{ }^\circ\text{C}$ for 20 days. a) and d) Pd/Au (91/9 at. %), b) and e) Pd/Au (50/50 at. %), c) and f) Au.

Table 4. Results summarizing the Pt-concentration [at. %] in the different Pd/Au samples by EDX analysis of the surfaces and cross section of the wires, and ICP-OES analysis summarizing the total quantity of elements present in the samples. Both poly- and quasi-monocrystalline wires are included in the table. CS notes analysis performed on the wire cross section.

	Pd/Au (91/9 at. %)		Pd/Au (50/50 at. %)		Pure Au
	Pt [at. %]	Pd/(Pd+Au) [at. %]	Pt [at. %]	Pd/(Pd+Au) [at. %]	Pt [at. %]
Monocrystalline, 20 days					
Surface	12	95	15	57	10
CS, 2 μm into core	16	95	11	55	10
CS, 12 μm into core	2	91	3	48	10
CS, centre of wire core	0	92	3	50	10
ICP-OES analysis	7.1	90.9	9.7	49.0	9.6
Polycrystalline, 20 days	Pt	Pd/(Pd+Au)	Pt	Pd/(Pd+Au)	Pt
Surface	29	96	34	61	12
CS, surface crystal	22	94	30	58	10
CS, 2 μm into core	15	91	16	49	10
CS, centre of wire core	8/10*	88	3	43	10
ICP-OES analysis	9.9	90.3	10.1	50.4	10.1

*dark/bright regions in the EDX-map in Figure 33d.

4.1.6.2. Polycrystalline Pd/Au samples

For the polycrystalline Pd/Au samples, Pt-catchment experiments were performed using the same conditions as the quasi-monocrystalline samples (20 days, 900 °C). The grain structure of these samples are similar to those of the Pd- and Pd/Ni samples after production ($\sim 5 \mu\text{m}$; Paper III). After 20 days of Pt-catchment, the Pt-concentration (at. %) is similar for all samples and around 10 at. % Pt is obtained (Table 4). A significant surface restructuring has occurred for both the Pd/Au (91/9 at. %) and pure Au wires (Figure 33), while the Pd/Au (50/50 at. %) sample has only gone through a mild restructuring of the surface (Figure 33b).

From EDX mapping of the wire cross sections, we can see that the Pt-distribution is again different depending on composition. Pd/Au (91/9 at. %) has Pt-rich surface crystals containing up to 30 at. % Pt, and a grain boundary pattern in the cross section that is similar to that of Pd (Figure 31a-b). The Pt-concentration is in the range of 8-10 at. % in the wire core, far above that of the quasi-monocrystalline version of the Pd/Au (91/9 at. %) sample, which had zero Pt in the wire core. This sample behaves in many ways similarly to the Pd and Pd/Ni samples.

For Pd/Au (50/50 at. %), the surface crystals are equally rich in Pt as the Pd/Au (91/9 at. %) sample, with up to 30 at. % Pt on the surface. However, the grain boundary pattern in the wire cross section is less visible and is seen only as a single line. The Pt-concentration in the wire core is 3 at. % Pt; the same as for the quasi-monocrystalline Pd/Au (50/50 at. %) sample. Altogether, this indicates that grain boundaries play a much less important role in the Pt-distribution in Pd/Au (50/50 at. %). For Au, the Pt-distribution is completely homogeneous, with 10 at. % Pt throughout the wire cross section, similar as for the quasi-monocrystalline Au samples. The only exception is a measured surface concentration of 12 at. % Pt by EDX.

4. Results and discussion

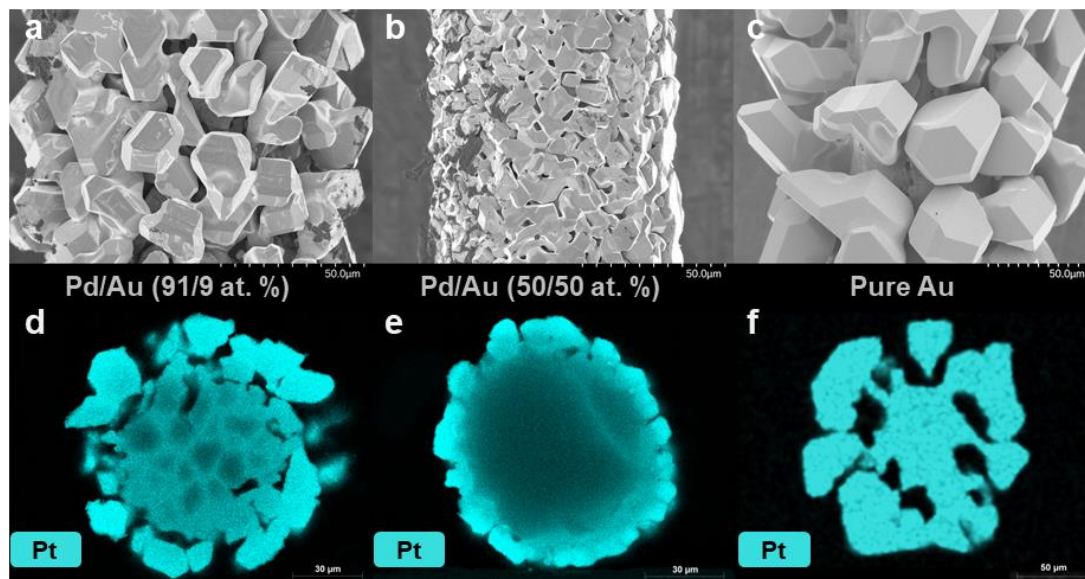


Figure 33. a-c) SEM images of the surface and d-f) EDX maps of the cross section of the polycrystalline Pd/Au samples tested as Pt-catchment materials at 900 °C for 20 days. a) and d) Pd/Au (91/9 at. %), b) and e) Pd/Au (50/50 at. %), c) and f) Au.

One additional factor is that for all Pd/Au samples, a small increase in Pd/(Pd+Au) ratio is observed near the surface, and a correspondingly lower Pd/(Pd+Au) ratio (higher Au/(Pd+Au) ratio) is observed in the wire centre. This shows that Pd clearly has a stronger desire to be located near the surface than Au during the Pt-catchment experiments. SEM analysis of Pd/Au samples heated for 1 week in air (without Pt-catchment) demonstrate that the Pd/Au samples maintain a uniform composition both near the surface and inwards into the wire core. We therefore believe that Pd has a higher preference for Pt on the surface at the used Pt-catchment conditions. It is possible that this is related to the mechanism for Pt-catchment on Pd and Au, and that Pd prefers Pt-catchment to a higher extent than Au. This would correlate with the fact that Pd captures more Pt than Au does during the Pt-catchment experiments, however, the Pd-rich Pd/Au samples do not show a higher Pt-catchment than the other Pd/Au samples or Au. A complete presentation of Pt-catchment on the Pd/Au alloys is given in Paper III.

4.1.7. Pt-catchment at industrial conditions (Paper III)

In order to collect information on how the different samples perform in the industrial gas/temperature conditions, a full set of samples were tested for 5 months in an industrial reactor for ammonia oxidation. The samples were the same as those tested in the laboratory experiments, with both poly- and quasi-monocrystalline versions of Pd, Pd/Ni (91/9 at. %), Pd/Au (91/9 at. %), Pd/Au (50/50 at. %) and Au.

The samples were carefully weighed before and after the experiment, and the mass changes (normalised to the same volume of metal installed) were observed to be in the following order (Table 5, Δm)

$$\text{Pd/Au (50/50 at. \%)} \gg \text{Pd/Au (91/9 at. \%)} > \text{Pd} > \text{Pd/Ni (91/9 at. \%)} \gg \text{Au}$$

In general, all the samples capture less Pt than in the laboratory experiments, which may be because the samples were placed below the industrial Pd/Ni nets in the gauze pack. From ICP-OES analysis, the maximum Pt-catchment was 15 at. % Pt in the quasi-monocrystalline Pd/Ni (91/9 at. %) sample (Table 5). The worst sample was clearly Au, as it had reacted strongly with the environment during the experiment (Figure 34) as well as it had suffered from a large mass loss during the experiment (Table 5).

The quantity of Pt collected (at. % Pt), measured by ICP-OES, was observed to decrease in the following order (Table 5, m(Pt)):

Pd/Ni (91/9 at. %, pre annealed) > Pd \approx Pd/Au (91/9 at. %) > Pd/Au (50/50 at. %) > Au.

However, for both the poly- and quasi-monocrystalline Pd/Au (50/50 at. %) samples, the ICP-OES data show a much lower Pt-concentration than expected from the mass changes. Notably, no other elements are detected from neither the ICP-OES analyses nor SEM-analyses (see below) that can explain the deviation. ICP-OES detect that a small amount of Rh (up to 0.2 at. %) along with minor quantities of Al and Cr in the range of 0.01-0.02 at. %.

Recalculating the quantity of Pd, Au and Pt from wt. % to a mass of sample, show that all of the Pd-rich samples have a significant Pd-loss (Table 5, Pd-loss). However, for the Pd/Au (50/50 at. %) samples, the mass of Pd and Au has increased by 8-11 %. This is highly unlikely to occur. Though Pd may be captured because of a Pd-loss from the industrial Pd/Ni net installed in the reactor, it is unlikely that any Au is present in the gas stream and can be captured. The same kind of increase in Au-content occurs for the Pd/Au (91/9 at. %) samples, even though this and the other Pd-rich samples report a reasonable Pd-loss in the range of 11-16 %. Thorough EDX analysis on both the top and bottom side of the nets at different locations, and of the wire cross sections, give a homogeneous Pt-concentration all over the sample in the range of 4-6 at. % Pt, as observed with ICP-OES. The positive side is that this must imply that the Pd- and Au-loss from this composition is negligible during Pt-catchment at industrial conditions. The cause for the surprisingly high mass increase of the Pd/Au (50/50 at. %) remains unexplained in this experiment. However, an additional pilot plant study is performed to follow up on the result (section 4.1.8).

4. Results and discussion

Table 5. Results from mass change analysis (left) and ICP-OES analysis (right) of the samples tested in the industrial plant. For direct comparison, regardless the sample size, the mass changes are normalized to the sample volumes. The two columns named Pd-loss and Au-loss is the difference in metal (in mass) from before the experiment to after the experiment, divided to the mass of metal before the experiment. *I.e.* the percentage of lost/gained metal, where positive values means a nett loss from the sample.

Polycrystalline	Mass change Δm [mg]	ICP-OES				
		m(Pt) [mg]	Pt [at. %]	Rh [at. %]	Pd-loss	Au-loss
Pure Pd	8	19	10	0.2	13 %	-
Pd/Au (91/9 at. %)	12	20	10	0.2	12 %	-21 %
Pd/Au (50/50 at. %)	26	11	5	0.0	-10 %	-11 %
Pure Au	-34	4	3	0.0	-	55 %
Pd/Ni (91/9 at. %)*	0.2	0.0	5	-	16 %	-
Monocrystalline	Δm [mg]	m(Pt) [mg]	Pt	Rh	Pd-loss	Au-loss
Pure Pd	10	23	12	0.2	12 %	-
Pd/Au (91/9 at. %)	12	20	10	0.2	11 %	-18 %
Pd/Au (50/50 at. %)	25	8	4	0.0	-8 %	-11 %
Pure Au	-91	2	2	0.1	-	23 %
Pd/Ni (91/9 at. %)	8	27	15	0.2	4 %	-

*This sample was installed in a different package than the other samples and may have experienced a different gas/Pt exposure as a result of that.

SEM/EDX analysis shows how the samples have transformed structurally during the campaign, and the Pt-distribution in the samples (Figure 34). For the Pd-rich samples (Pd, Pd/Ni (91/9 at. %) and Pd/Au (91/9 at. %)), the expected grain reconstruction process occurs. Surprisingly, it occurs for both the poly- and quasi-monocrystalline samples, and the surface of the samples are similar. A small deviation is the quasi-monocrystalline Pd/Ni sample, where the surface crystallites have a slightly different shape than the polycrystalline sample. A more distinct deviation is observed for the Au sample, which was completely destroyed during the experiment and has clearly reacted strongly with the environment during the experiment. ICP-OES show that ~3 at. % Pt is present in the remaining Au. Some Au has also diffused into the megapyr net around the Au sample during the experiment, which may be a participating cause for why Au has reacted. Surprisingly, ICP-OES show that 2 at. % Pd is present in the Au samples, supported by EDX analysis that show up to 20 at. % Pd at certain locations.

For the Pd/Au (50/50 at. %) samples, a similar surface reconstruction occurs as in the home laboratory, causing only a minor increase in wire radius during the experiment. Some small Rh-oxide particles are identified on the surface of several of the samples. Rh do not mix with Pd in the metallic state, correlating well with the oxidation properties of Rh (section 2.4).

All samples further show an uneven Pt-distribution in the cross sections, where one side during Pt-catchment has the highest Pt-concentration (most likely the up-side). In the Pd/Au (50/50 at. %) sample, a weak grain boundary pattern can also be seen. Also for these samples, a slightly higher Pd/(Pd+Au) ratio is observed near the sample surfaces, and a correspondingly lower Pd/(Pd+Au) ratio near the wire centres, similar as for the laboratory samples (section 4.1.6). A summary of the main observations are given in Figure 35 as function of composition,

and the region believed to contain the optimal Pd/Au composition for Pt-catchment is coloured red. A complete presentation of the 5 months industrial experiment is given in Paper III.

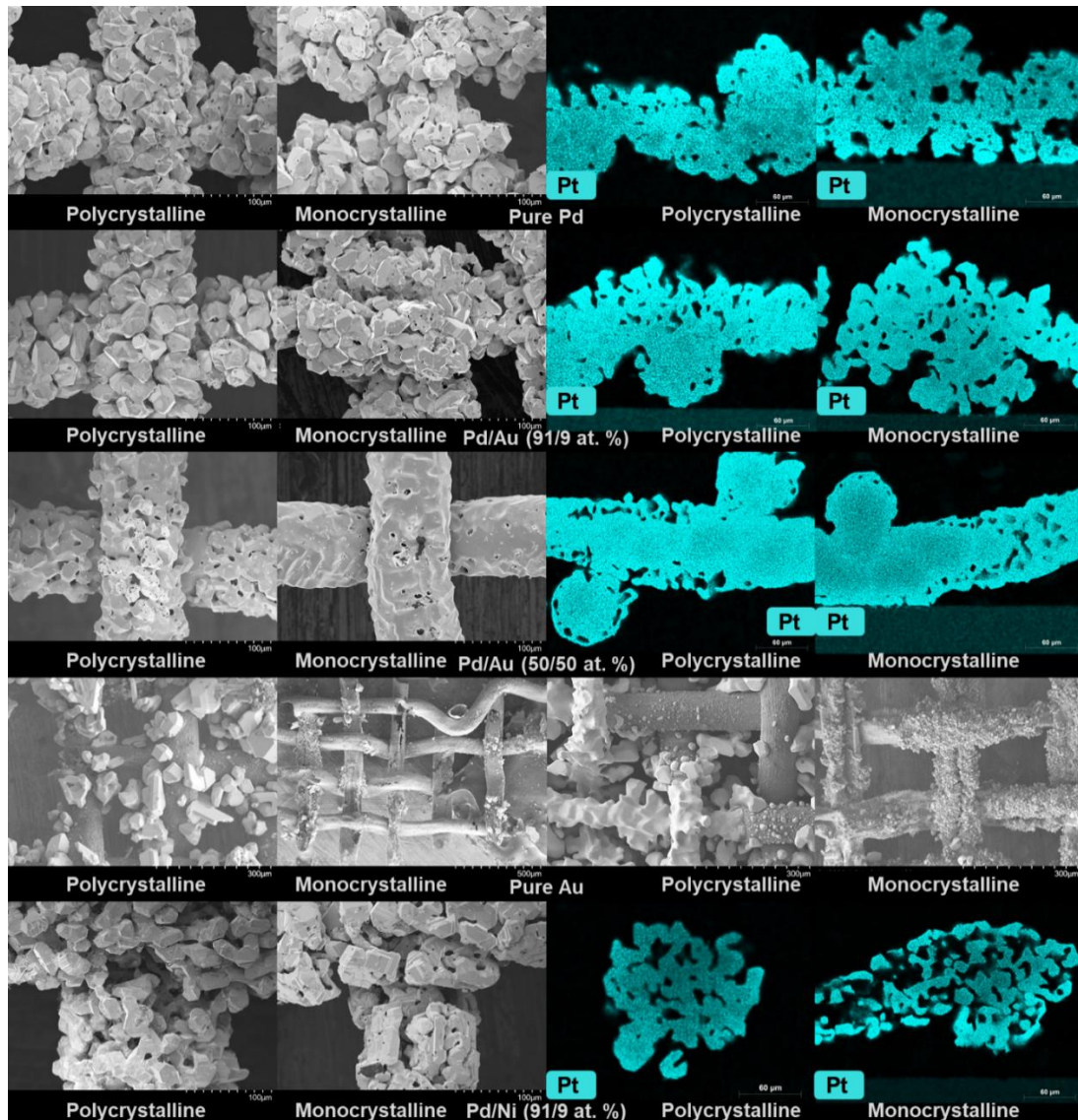


Figure 34. SEM images of the top side of the surface of the samples (left) and EDX maps of the cross sections of the samples (right). The sample compositions and grain structure are indicated in the figure. For Au, the right side show SEM surface images of the down side of the samples.

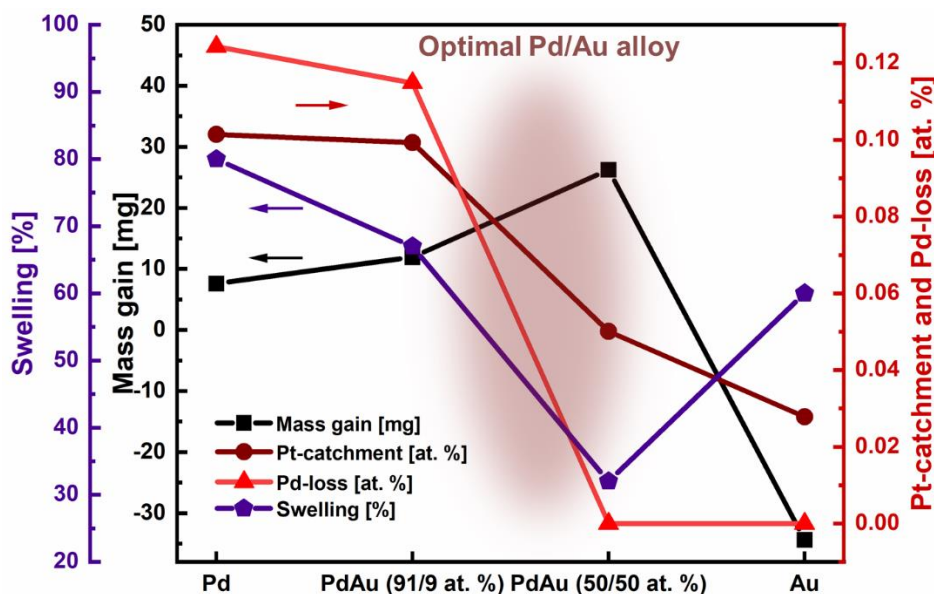


Figure 35. Summary of the mass gain [mg], Pt-catchment [at. %], Pd-loss [at. %] and swelling [%] for the Pd/Au samples treated in the industrial plant for 5 months. The swelling of the Au samples is taken from the laboratory experiments. The predicted optimal Pd/Au alloy for Pt-catchment is shaded dark red in the figure.

4.1.8. Short analysis of 28 days long pilot plant experiment

The industrial experiment (section 4.1.7) largely agreed with the laboratory Pt-catchment experiments in terms of restructuring and Pt-catchment. However, there was a discrepancy in the observed mass gain and Pt-concentration determined from ICP-OES for the Pd/Au (50/50 at. %) sample. To investigate this discrepancy, a 28 days long pilot plant experiment was performed. All the same ten samples as in the industrial experiment were tested, including both poly- and quasi-monocrystalline versions of Pd, Pd/Au (91/9 at. %), Pd/Au (50/50 at. %), Au and Pd/Ni (91/9 at. %). The operating conditions were 900 °C, 5 bara and 10 vol. % NH₃ in air, and Pt/Rh (91/9 at. %) catalyst was used. The samples have a similar development in overall morphology as in the industrial experiment (Figure 36), without going into restructuring details. The obtained mass changes of all the samples and results from ICP-OES of Pd/Au (50/50 at. %) are summarised in Table 6.

All the samples show a similar mass gain in the current experiment, except Au, which was also completely destroyed in this experiment. The mass gain for the Pd-containing samples was in the range of 6.6-10.3 mg for a sample size normalised to that of polycrystalline Pd. The wire diameter (76 µm) and weave was the same for all the Pd-containing samples. All the Pd-containing samples, except Pd/Au (50/50 at. %), show a larger mass gain for the quasi-monocrystalline version compared to the polycrystalline version.

ICP-OES experiments show an almost identical Pt-concentration for the two Pd/Au (50/50 at. %) samples (7.8-7.9 at. %), a concentration higher than in the industrial experiment (Table 5). A Pd-loss of 8-9 at. % (of the original Pd in the alloy) is observed, and an Au-loss of 1-2 at. % (of the original Au in the alloy) is observed. In weight, the Pd-loss is 0.28-0.30 g of Pd lost per gram of Pt captured. This Pd-loss is the same as Holzmann observed for the same

Pd/Au (50/50 at. %) alloy [17] and higher than we have observed in the industrial experiment (section 4.1.7).

The industrial experiment (section 4.1.7) was surprising as it indicated an increase in Pd- and Au content (*i.e.* Pd- and Au-catchment) during operation, a result we struggled to explain. It is now clear from the 28 days long pilot experiment that a Pd-loss is expected also for Pd/Au alloys installed in the ammonia oxidation reactor. The observed Pd-catchment in the industrial experiment (section 4.1.7) can thus originate from catchment of Pd evaporated from the Pd/Ni catchment gauze installed along with the Pt/Rh catalyst. Such a Pd/Ni catchment gauze was not installed in the 28 days pilot plant experiment, which is why this experiment showed a Pd-loss. The increase in Au-content in the industrial experiment remains unexplained. An important conclusion is that the main advantage of the Pd/Au (50/50 at. %) and similar alloys is the reduced wire restructuring and swelling.

Table 6. Results from mass analysis (top) and ICP-OES analysis (bottom) of the samples treated in the pilot plant for 28 days.

Mass analysis	Pd	Pd/Au (91/9 at. %)	Pd/Au (50/50 at. %)	Pd/Ni (91/9 at. %)
Poly: Δm norm [mg]	7.2	8.6	8.6	6.6
Mono: Δm norm [mg]	9.4	10.3	7.2	7.3
ICP-OES analysis	Pt [at. %]		Pd-loss [at. %]	Au-loss [at. %]
Poly: Pd/Au (50/50 at. %)	7.8		8.9	1.3
Mono: Pd/Au (50/50 at. %)	7.9		8.3	2.0

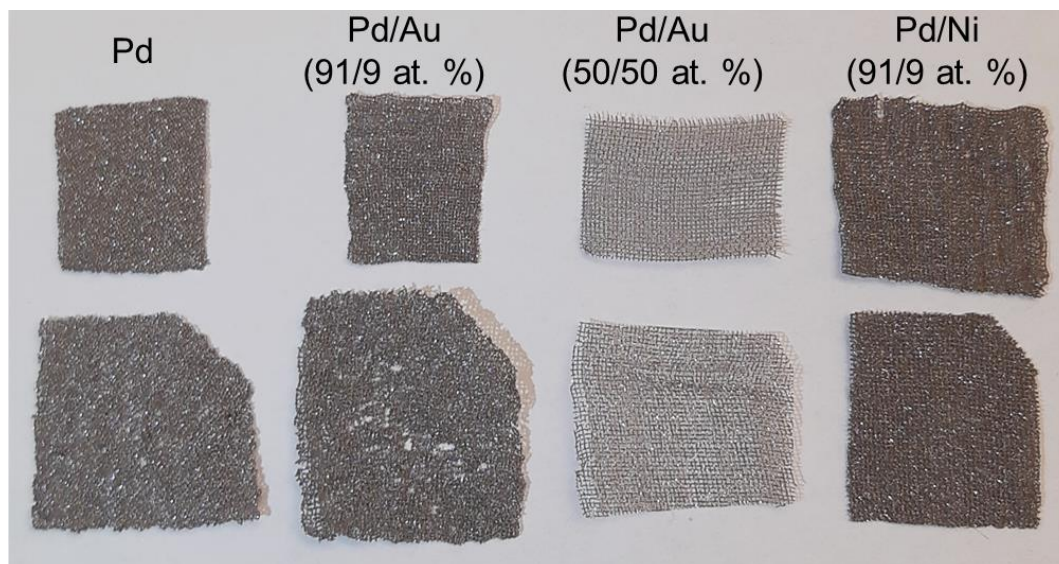


Figure 36. Picture of the Pd-containing samples after the 28 days pilot plant experiment. The sample compositions are indicated in the figure. The top samples are the polycrystalline and the bottom samples are the quasi monocrystalline.

4.1.9. Limiting factors for Pt-catchment (Paper II and III)

We have now been through most of the results that make up the basis for our understanding of Pt-catchment on Pd-based alloys, and it is time to discuss Pt-catchment from a more

4. Results and discussion

mechanistic perspective. The reader is referred to the discussion sections of Paper II and Paper III for a more complete discussion, and for complementary information not presented here.

In short, the restructuring that occurs during Pt-catchment can be considered as corrosion by platination (Pt-catchment). The Pt-catchment process consists of two main steps: 1) catchment of Pt from PtO₂ and onto a surface, and 2) solid state diffusion of Pt into the catchment material, as illustrated in Figure 37a. There is a need to identify the limitations of Pt-catchment and the rate-determining step.

4.1.9.1. Pt-deposition onto a surface

When Pt is captured on the surface of either of the metallic samples investigated (Pd, Pd/Au, Au, Pd/Ni), SEM/EDX observations point toward that a metallic Pd/Au/Pt alloy is obtained and the oxygen concentration in the alloy is very low. TG experiments also show that the decompositions temperatures of the bulk oxides PdO and PtO₂ are below the operating temperatures and pO_2 (Appendix: Figure A3 and Figure A4). We therefore assume that when Pt is captured from PtO₂ (g), oxygen is released as Pt enters the Pd (Pd/Au) wire (Figure 37a).

In terms of the Pt-catchment rate, we have seen from the *in situ* absorption-CT studies using Pd-wires (section 4.1.4) that the Pt-catchment rate is reduced when $p(PtO_2)$ is lowered (Figure 37b). Additionally, the catchment rate become lower when the Pt-concentration in the catchment alloy is increased (Figure 37c). This converges to a limiting Pt-concentration in the Pd-based catchment material, which will depend strongly on $p(PtO_2)$ [152].

The Pt-catchment experiments demonstrate that Pt-catchment is fast when the catchment alloy is pristine and free of Pt. It is therefore likely that the kinetics for Pt-catchment onto the Pd-surface is fast and that the reaction $PtO_2(g) \rightarrow Pt(\text{on surface}) + O_2(g)$ is not the rate limiting step in the system.

Interestingly, TG experiments of the decomposition of solid PtO₂ (Appendix: Figure A4) show that oxygen remains related to Pt even at 1050 °C in O₂, and to a lesser extent in N₂. PdO is, on the other hand, fully decomposed to Pd metal (Appendix: Figure A3). Pt seems to have a stronger interaction with oxygen at temperatures above 900 °C compared to Pd, which is supported by the literature [101-103]. This imply that the decomposition of PtO₂ molecules on a Pd/Au surface may be an equilibrium where the pO_2 and Pt-concentration in the alloy play key roles. The role of O₂ in the system is not addressed in this work as Pt is found to be captured as metallic Pt in the bulk of the catchment material.

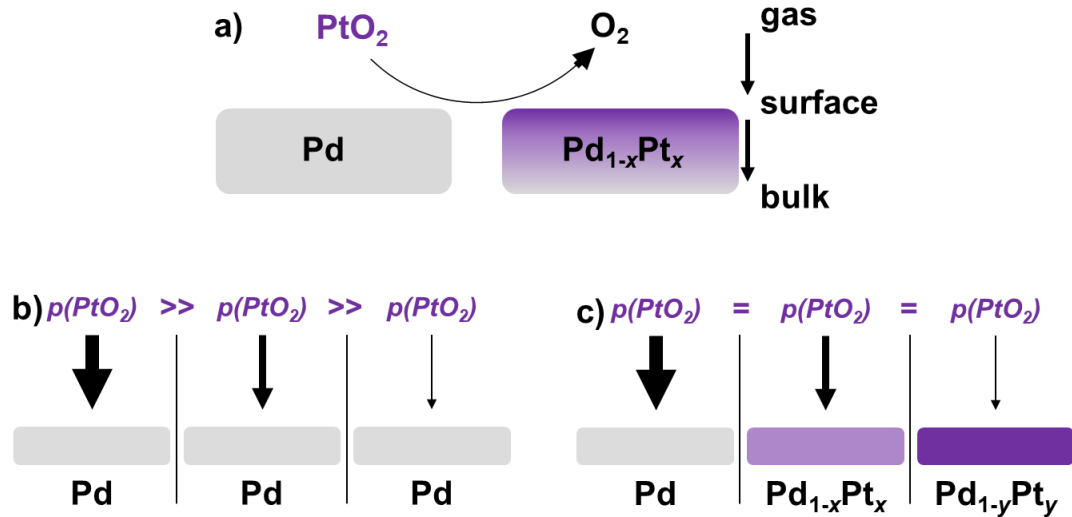


Figure 37. Schematic illustration of key features of the Pt-catchment process. a) catchment of metallic Pt in an alloy with Pd through decomposition of the PtO_2 molecule. b) For three equal Pd-samples exposed to different $p(\text{PtO}_2)$, the sample that experiences the highest $p(\text{PtO}_2)$ will capture the most Pt. c) For three Pt-catchment experiments with the same $p(\text{PtO}_2)$, but the Pd-samples contains various amount of Pt, the sample with the least Pt will capture Pt most rapidly. Edited and reused with permission from Elsevier [141].

4.1.9.2. Diffusional aspects

From the section above (4.1.9.1), we learned that Pt arrives on the Pd (Pd/Au) surface and is ready for mixing with Pd (Pd/Au) in the solid state. This leads us to analyse the solid-state diffusion of Pt in Pd and Pd/Au based on the information below.

- EDX-analysis (Figure 31) and diffusion experiments (Paper II, section 4.4) show that Pt-diffusion is significantly faster in the GBs compared to the bulk (Appendix: Table A1).
- Au-rich alloys have a much faster bulk diffusion than Pd-rich alloys (Figure 32).
- Pd is the main outwards diffusing species of Pd and Au during Pt-catchment (Table 4).

The different diffusion paths in these systems are illustrated in Figure 38. Pt and Pd/Au are expected to diffuse towards each other and mixing when Pt is present on the wire surface, both via the bulk and the GBs. The GBs and the surface serve as rapid diffusion path for both Pd, Pt and possibly Au. The difference in diffusion rates between the GBs and the bulk become smaller with increasing Au-content (Figure 38c), but not equal.

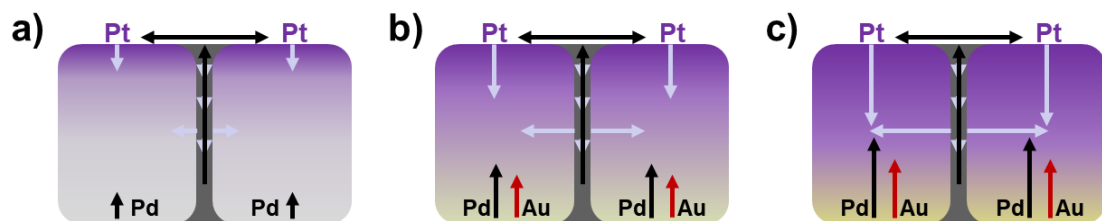


Figure 38. Illustration of the expected diffusion paths for Pd, Au and Pt during Pt-catchment, where both bulk and grain boundary diffusion play a key role. a) is pure Pd, b) is a Pd-rich Pd/Au alloy and c) is an Au-rich Pd/Au alloy. The arrows illustrate the diffusion rates, where longer arrows indicate more rapid diffusion. This is the case when more Au is present in the Pd/Au alloy. Observations indicate that Pd is the main diffusing species of Pd (black arrow) and Au (red arrow) towards Pt (bright arrow), hence a longer arrow for Pd compared to Au. Edited and reused with permission from Elsevier [141].

4. Results and discussion

4.1.9.3. Simulated diffusion model

We now implement the different diffusion paths and the diffusion rates of Pt in the Pd/Au alloys (Appendix: Table A1) in a simplified 2D diffusion model developed in Matlab [153]. In the model, a circular sample is used to simulate the Pt-diffusion into the Pd- and Pd/Au wires, and it allows us to follow the development of Pt-distribution in the samples. The input parameters were the diffusion coefficients for Pt in Pd, Pt in Au, Pt in the Pd/Au alloys (estimated) and the GB diffusion coefficient for Pt in Pd, along with other parameters relevant for Pt-catchment ($T = 900 - 1000$ °C, $p(\text{PtO}_2) = 5 \times 10^{-8}$ bar, $c_{max} = 0.20$ and 0.35) (more information in Paper II, Supplementary section S.3.).

Several factors influence how rapid a Pd- or Pd/Au wire can absorb Pt by solid-state diffusion. These factors are:

- 1) The diffusion coefficients (bulk and GB), which are dependent on alloy composition and temperature (Appendix: Table A1).
- 2) The maximal surface concentration of Pt (between 0 and 1).
- 3) The rate of Pt-catchment onto the surface (Pt-catchment per time).

Three different scenarios were explored using the diffusion model:

1. *Monocrystalline Pd- and Pd/Au wires (Figure 39a-e)*: This model is the simplest one, featuring Pt around a sample with a bulk diffusion coefficient depending on composition (Pd/Au content). A radial diffusion profile is obtained for simulations using this model, and the diffusion profiles reach significantly deeper for the Au-rich alloys.
2. *Filling of the GBs in polycrystalline Pd and Pd/Au wires (Figure S25, Supplementary section of Paper II)*: This model takes into account both bulk and GB diffusion. Because the GB diffusion is significantly more rapid than bulk diffusion in Pd, the GBs are filled with Pt already after 200-500 seconds. However, as the Au-content is increased in the alloys, the GBs need much more time to be filled since the faster bulk diffusion allows a more significant absorption of Pt in the bulk grains. Due to the high GB diffusion coefficient in this simulation, the time step (dt) must be very small, causing the simulation to be very slow, and only short simulations are performed ($t \leq 500$ s).
3. *Polycrystalline Pd- and Pd/Au after the GBs are full of Pt (Figure 39f-j)*: This model simulates diffusion including both bulk and the GBs, but uses only the bulk diffusion coefficient to do this. The model assumes the GBs to be filled with Pt and that they act as a surface the same way as the outer surface, *i.e.* we have several small monocrystalline samples capturing Pt that are clamped together. This is a simplification and overestimates the total diffusion. The computational time of the simulation is much shorter, and we can easily simulate a 10 days Pt-catchment experiment.

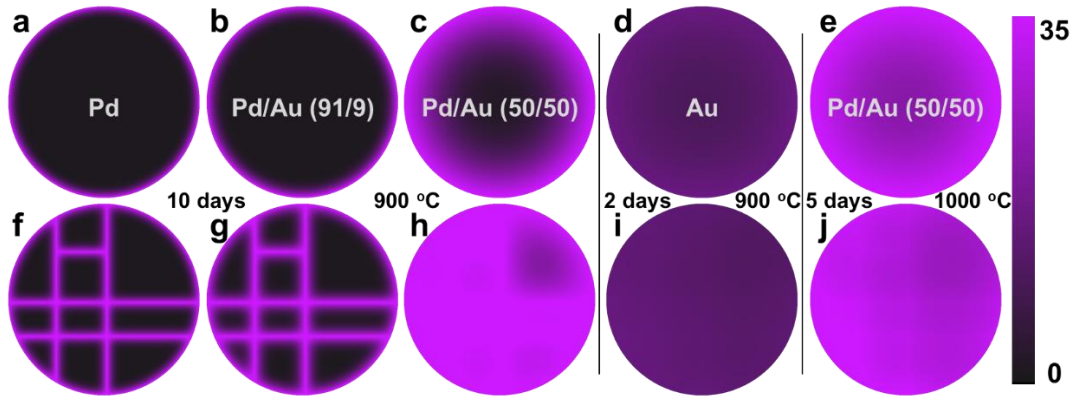


Figure 39. Results from the diffusion simulation using circular samples that represent the cross section of a 76 μm wire. a-e) are monocrystalline samples and f-j) are polycrystalline samples. a) and f) Pd at 900 $^{\circ}\text{C}$ after 10 days, b) and g) Pd/Au (91/9 at. %) at 900 $^{\circ}\text{C}$ after 10 days, c) and h) Pd/Au (50/50 at. %) at 900 $^{\circ}\text{C}$ after 10 days, d) and i) Au at 900 $^{\circ}\text{C}$ after 2 days, e) and j) Pd/Au (50/50 at. %) at 1000 $^{\circ}\text{C}$ after 5 days.

The diffusion simulation shows a large difference in Pt-distribution depending on Pd/Au composition and grain structure at 900 $^{\circ}\text{C}$ (Figure 39, Figure 40). The two Pd-rich alloys can absorb much more Pt in the polycrystalline scenario at 900 $^{\circ}\text{C}$ (Figure 39a-c), while for Pd/Au (50/50 at. %) at 1000 $^{\circ}\text{C}$ and Au at 900 $^{\circ}\text{C}$ (Figure 39c-d), the effect of the GBs is almost minimal because bulk diffusion is sufficiently rapid.

For Pd/Au (50/50 at. %) in Pt-catchment experiments, both the poly- and monocrystalline samples captures equally much Pt and has the same Pt-concentration in the wire core after a 10 days long experiment (Table 4; Figure 33). This indicates that the GBs are not contributing much to the Pt-diffusion in the Pd/Au (50/50 at. %) sample. The low influence of the GBs in Pd/Au (50/50 at. %) correlates well with the EDX map showing few Pt-rich GBs in the cross section of this sample (Figure 33e).

Another feature implemented in the diffusion model is a maximal rate of Pt-catchment, limiting the maximal increase in Pt-concentration on the surface of the sample during the simulation. The *in situ* absorption-CT experiment showed that 1 at. % Pt is obtained after 4 hours of Pt-catchment on Pd, before the Pt-catchment rate is reduced (Figure 30). In the diffusion model, this manifests itself as a linear increase in Pt-concentration (versus time) in the beginning of the simulation (striped line in Figure 40a). Thereafter, the surface is saturated with Pt (20 or 35 at. % Pt). Without this limitation, the increase in Pt-concentration is strongly overestimated in the beginning of the experiment (Figure 40b, “mono, constant”).

4. Results and discussion

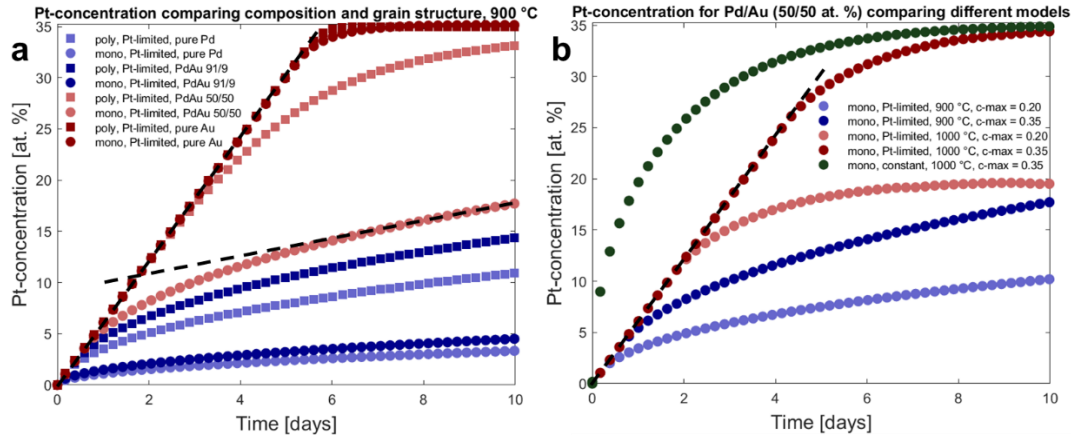


Figure 40. Pt-concentration versus time for the samples displayed visually in Figure 39. The results are obtained from the simulated diffusion model developed in matlab. a) Pt-concentration for the mono- and polycrystalline model for different compositions at 900 °C, including the limiting Pt-catchment rate. The grain structure and compositions are indicated in the figure. b) Pt-concentration for only the monocrystalline model for the Pd/Au (50/50 at. %) sample, showing the dependencies of temperature (900 or 1000 °C) and maximal surface concentration of Pt (20 or 35 at. % Pt), both of which are indicated in the figure. The sample indicated “mono, constant” has not used a limiting Pt-catchment rate.

4.1.9.4. Correlated diffusion limitation – deposition limitation

Based on the diffusion model described above (section 4.1.9.3), we find that there are two limitations for the Pt-catchment process: 1) a Pt-catchment limitation in the beginning of the experiment (Pt-deposition) and 2) a diffusion limitation later in the experiment, as indicated by the two striped lines in Figure 40a. However, one can argue and say that there is only one limitation in the system. That limitation is the Pt-catchment rate, *i.e.* the Pt-deposition on the surface, but it is influenced by the diffusion. Slow bulk diffusion causes the surface to be saturated with Pt. If the surface saturation did not cause a reduction in Pt-catchment, a thick layer of pure Pt should form on the Pd wire surface during Pt-catchment, which is not observed [17]. We thus have a correlated Pt-diffusion – Pt-deposition limitation. This correlates well with the report from Holzmann that a pure Pt net does not capture any Pt [17].

4.1.9.5. Role of the grain boundaries

The driving force for Pd/Pt diffusion is to reduce the surface concentration of Pt by interdiffusion, it is the chemical potential of the system. This is beneficial due to the energetic gain of mixing Pd and Pt in the solid state ($E_{mix,Pt-Pd} = -2.9$ kJ/mol [154]), supported by the fact that Pd and Pt form a complete solid solution at 900 °C [58]. However, inwards Pt-diffusion is highly limited through the bulk grains.

The GBs are the most rapid diffusion path in the system. The GBs are narrow and are filled with Pt within 1 day of Pt-catchment (Figure 31). Pt-diffusion is thereafter from the GBs into the bulk. The GBs may, however, serve as a diffusion path for transporting Pd outwards to react with the Pt on the surface. Pd diffusion from the bulk into the GBs will also be limited by bulk diffusion, although the bulk diffusion for Pd is more rapid than for Pt (Appendix: Table A1). It is therefore likely that the net outwards Pd-diffusion is higher than the net inwards Pt-diffusion, and that a net inwards diffusion of vacancies will occur. If a large

concentration of vacancies are present inside the Pd-wire, these may agglomerate to form internal voids (Kirkendall voids) in the bulk or in the GBs.

Potential Kirkendall voids have been predominantly observed as open porosity in the GBs of the monocrystalline wires (Paper II and Paper III). Only for the quasi monocrystalline Pd/Au (50/50 at. %) sample have we observed internal voids which we believe to be Kirkendall voids (Paper III, Figure 6). Unfortunately, for the other samples, our observations cannot distinguish if the pores/voids form sub surface before they become open porosity. Either way, the rapid GB diffusion and possible formation of Kirkendall voids may cause the GBs to open and expose areas of fresh Pd. Regions of fresh Pd would serve as rapid Pt-catchment locations due to the low Pt-concentration. Formation of porosity will in this way enhance Pt-catchment.

4.1.10. Mechanism of grain reconstruction (Paper II and III)

We now aim to describe the grain reconstruction of the polycrystalline Pd-, Pd/Ni- and Pd/Au wires. The GBs play an active role in the restructuring of the polycrystalline wires, which proceeds as follows.

Pd, Pd/Ni (91/9 at. %) and a Pd-rich alloy such as Pd/Au (50/50 at. %)

- 1) The wires are rapidly covered with Pt (first ~1 hour, Figure 41a and e).
- 2) Pt diffuses into the wire, and toward the wire core via the GBs. Pt and Pd (Pd/Au) mix and small surface crystals are formed (Figure 41b). After ~1 day, the surface is covered with Pd/Pt (Pd/Au/Pt) crystallites of 5-10 μm in size.
- 3) The surface is covered in Pd/Pt (Pd/Au/Pt) crystallites, but the core is still intact (Figure 41c). The grain boundaries in the remaining core transport Pd (Pd/Au) atoms to the surface, which causes more Pt-catchment and a continuation of the grain reconstruction process (1 – 4 days). See comparison with SEM/EDX in Figure 41d.
- 4) With more time, the process continues until the entire wire is completely reconstructed and consists only of 10 – 20 μm crystals (7 – 10 days for 76 μm wire). The grain reconstruction is like a self-repeating process for the polycrystalline Pd-based wire, which begins near the surface and continuous until the entire wire is completely reconstructed.

Pd/Au (50/50 at. %) and similar alloys

- 1) The Pd/Au wire is rapidly covered with Pt (first ~1 hour, Figure 41a and e).
- 2) Bulk diffusion contributes significantly to the transport of Pt into the wire, reducing the contribution from the GBs. This limits the wire restructuring (Figure 41f).
- 3) Bulk diffusion has caused an almost homogeneous Pt-distribution in the sample (Figure 41g), and the reconstruction has only penetrated the outer ~10 μm of the wire (Figure 41h), and the swelling is insignificant.

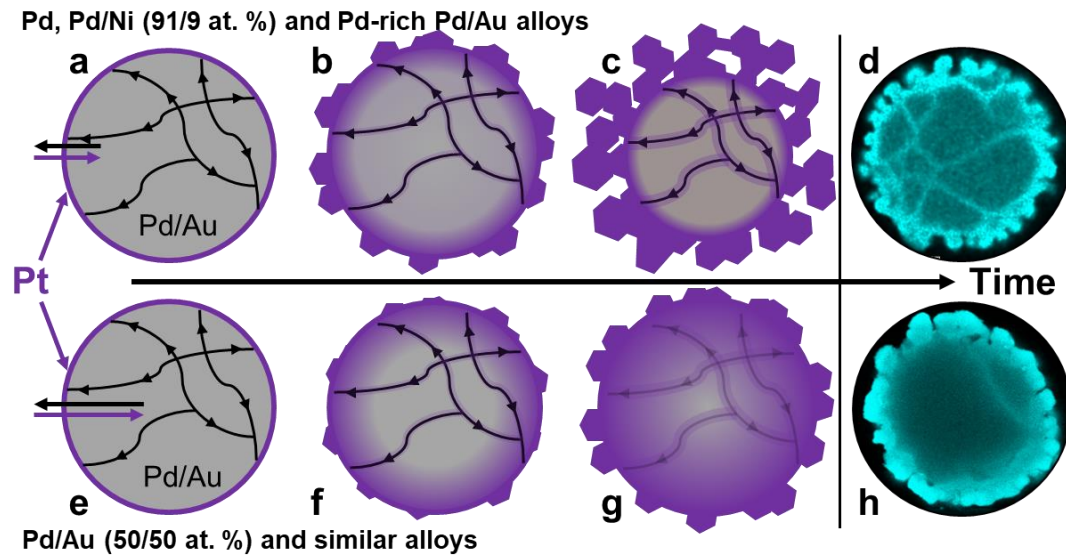


Figure 41. Suggested mechanism for grain reconstruction of polycrystalline Pd, Pd/Ni and Pd-rich wires (a-c) and for Pd/Au (50/50 at. %) and similar alloys (e-g). The EDX maps show d) pure Pd after 1 day Pt-catchment at 1000 °C and h) Pd/Au (50/50 at. %) after 20 days Pt-catchment at 900 °C. Edited and reused with permission from Elsevier [141].

4.1.11. Restructuring of the quasi-monocrystalline samples

Only certain parts of the quasi-monocrystalline samples have shown restructuring during laboratory experiments (section 4.1.5, Paper II-III), while all the quasi-monocrystalline samples restructured in the industrial experiment (section 4.1.7). The cause for the grain reconstruction of the polycrystalline wires is possibly due to the formation of Kirkendall voids inside the GBs (section 4.1.9.5). For the restructuring of the quasi-monocrystalline wires, the theory of Kirkendall voids is the one we find the most likely. Other alternatives would be the formation of sub-surface gas molecules, *e.g.* O₂, which causes porosity upon evaporation [155], which we find less likely.

The GBs are absent in the quasi-monocrystalline samples, which implies that bulk is the main diffusion path. With the Pd-diffusion being faster than Pt-diffusion in Pd/Pt alloys (Appendix: Table A1), a net inwards flux of vacancies are expected. If we assume that Pd-diffusion is more rapid than Pt-diffusion also in the Pd/Au samples investigated, an inwards flux of vacancies would occur also for Pd/Au alloys. For the quasi-monocrystalline Pd/Au (50/50 at. %) sample, a narrow void is formed 10-15 μm below the surface of the sample, and we believe this to be an internal Kirkendall void (Paper III, Figure 6). We therefore find that formation of Kirkendall voids is a likely mechanism for the restructuring of the quasi-monocrystalline Pd-based alloys (Figure 42; Paper III).

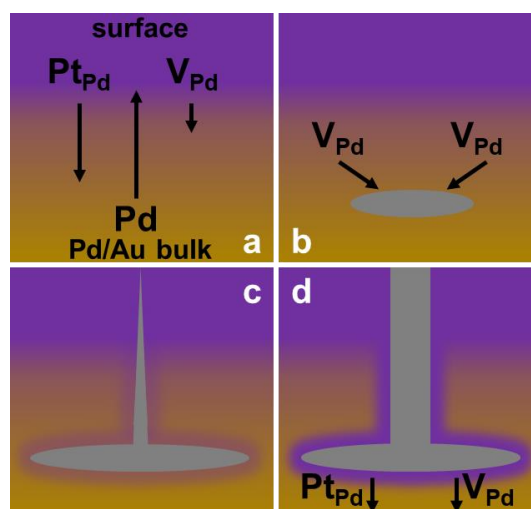


Figure 42. Illustration of the formation of a Kirkendall void in a monocrystalline Pd-based sample during Pt-catchment. a) diffusion of the different species (arrow indicates diffusion flux), b) formation of an internal Kirkendall void, c) a Kirkendall void growing towards the wire surface, and d) a Kirkendall void with open porosity that starts to facilitate Pt-diffusion even deeper into the sample.

4.2. Structural aspects of Pt- and Rh-containing perovskites

This section focuses on syntheses and structural aspects of Pt- and Rh-containing perovskite oxides, primarily the stoichiometric double perovskites, $RE_2MM'O_6$ ($RE = \text{La, Nd, Y}$; $M = \text{Ni, Co, Fe}$; $M' = \text{Pt, Rh}$). The governing aspects for the stability of the double perovskites are addressed, primarily structural distortions and oxidation states. The presence of *B*-ordering is also discussed in light of the oxidation states of the elements. Among the observed phenomena in $\text{LaNi}_{1-x}M'_x\text{O}_3$ ($M' = \text{Pt, Rh}$) is the formation of a domain structure with Pt-rich and Pt-depleted regions in $\text{LaNi}_{1-x}\text{Pt}_x\text{O}_3$, and an interplay of oxidation states in $\text{LaNi}_{1-x}\text{Rh}_x\text{O}_3$.

4.2.1. Synthesis and structural aspects of Pt-containing double perovskites

Synthesis of Pt-containing perovskite oxides with the aim of obtaining Pt in the +IV oxidation state requires elevated $p\text{O}_2$ during annealing, and Pt-metal impurities are easily formed. Some studies use Pt metal directly in the synthesis [50], and some use PtO_2 [156]. In this work, the citric acid complexation method (section 3.3) was used for the synthesis of the perovskites, allowing minimal Pt-impurities in several of the products after annealing at high temperature (1000 °C) in 8 bar O_2 in quartz ampoules (Table 7) (chemicals are listed in Appendix: Table A4). Annealing in air or a flow of O_2 (ambient pressure) produced significant Pt-metal impurities. Once the Pt-impurities had formed, long annealing periods of 2 weeks in 1 atm. O_2 improved the sample purity, but some Pt-metal remained. For samples with a low Pt-content ($x \leq 0.25$ in $\text{LaNi}_{1-x}\text{Pt}_x\text{O}_3$), an O_2 -flow was sufficient to produce phase pure samples without Pt-metal.

4.2.1.1. Effect of ionic radii on structural distortions

XRD data for selected samples are presented in Figure 43. The structure of the double perovskites $\text{La}_2\text{NiPtO}_6$, $\text{La}_2\text{CoPtO}_6$, $\text{Nd}_2\text{NiPtO}_6$ and $\text{Nd}_2\text{CoPtO}_6$ are well described in space group $P2_1/n$ with a beta angle close to 90 °C, although the equivalent setting $P2_1/c$ and a large beta angle ($\sim 125^\circ$) is also commonly used for several heavily distorted double perovskites

4. Results and discussion

(Y_2NiRuO_6 [157]). The XRD patterns for the samples are similar (Figure 43). Still, three distinct features are clear: 1) the diffraction peaks shift to higher Q for a smaller A -cation, *e.g.* Nd compared to La, 2) they shift to lower Q for a larger B -cation, *e.g.* Co compared to Ni (Table 8), and 3) several reflections split when Nd (A -site) and Co (B -site) are introduced. The peaks split because of structural distortions induced by the larger size of the B -cation and/or smaller size of the A -cation, *i.e.* increased octahedral tilting and reduced t -factor (Table 7; section 2.5). The distortions result in more anisotropy, and the reflections split into different Q -values. The distortions also result in the Ni-O-Pt bond angle being reduced (on average) from 154.5° to 150.8° from $\text{La}_2\text{NiPtO}_6$ to $\text{Nd}_2\text{NiPtO}_6$. The M -O-Pt bond angle depends strongly on the oxygen positions. Unfortunately, the quality of the XRD data collected in the home-laboratory for the synthesized double perovskites is insufficient to extract reliable bond angles for the other compositions.

4.2.1.2. B -site substitution and ordering

Upon Pt-substitution into LaNiO_3 ($\text{LaNi}_{1-x}\text{Pt}_x\text{O}_3$), the rhombohedral symmetry ($R\bar{3}c$) is preserved up to $x = 0.05$. A structural phase transition occurs between $0.05 < x < 0.20$, after which the monoclinic structure of $\text{La}_2\text{NiPtO}_6$ with B -site ordering is formed ($P2_1/n$). Samples with $x > 0.50$ contain $\text{La}_2\text{NiPtO}_6$ with additional impurities and higher Pt-concentrations than $x = 0.50$ cannot be obtained in the $\text{LaNi}_{1-x}\text{Pt}_x\text{O}_3$ system. All the $\text{LaNi}_{1-x}\text{Pt}_x\text{O}_3$ samples with $x \geq 0.20$ show B -site ordering to a degree correlating with the substitution of Pt (x). B -site ordering generally only occur if the B -cations have different charge [128], which in this case is likely because Pt prefers oxidation state +IV and the A -site cation prefers oxidation state +III, forcing Ni to take oxidation state +II. The degree of B -site ordering is easily seen from the intensity of specific diffraction peaks (Figure 43: $Q = 1.37$ and 2.63 \AA^{-1} for $\text{La}_2\text{NiPtO}_6$) originating from the structural B -site ordering, as illustrated for $\text{Nd}_2\text{CoPtO}_6$ in Figure 44a. The peaks are frequently used as a descriptor for long range B -site ordering in perovskites [158]. B -site ordering is present for the other Pt-containing perovskites with Ni and Co, with nearly perfect ordering from Rietveld refinements (Table 7).

4.2.1.3. When the redox state is the limitation, Fe(II)

For the attempted synthesis of $\text{La}_2\text{FePtO}_6$ and $\text{Nd}_2\text{FePtO}_6$, significant Pt-impurities are formed (Table 7), causing the perovskite to be Fe-rich and the degree of ordering to be low, even though 8 bar O_2 was used in the annealing. $\text{La}_2\text{FePtO}_6$ has not been successfully synthesized in this work or by others, likely because of the necessity of having Fe(II) and Pt(IV) to obtain the perovskite. A high $p\text{O}_2$ during synthesis will stabilize Pt(IV), but at the same time destabilize Fe(II). The higher stability of Co and Ni in oxidation state +II compared to Fe is likely why perovskites with Co/Ni are easier to synthesize. In contrast, synthesis of LaSrFePtO_6 proved more fruitful, where only 20 % of the Pt used in the synthesis became Pt metal impurities, showing that Fe(III) is more stable in the perovskite structure. However, the diffraction peaks were very broad (Figure 43). The higher amount of Pt-impurities in $\text{Nd}_2\text{FePtO}_6$ compared to $\text{La}_2\text{FePtO}_6$ may be related to the larger degree of structural distortion expected for the Nd-based perovskite.

4.2.1.4. Y as A-site cation – pyrochlore structure

Synthesis with the even smaller A-site cation Y did not yield perovskites as intended (Y_2MPtO_6 , $M = Fe, Co, Ni$). However, only small quantities of Pt-metal impurities were present after the synthesis (Figure 43), and only a small quantity of perovskite had formed. The rest of the diffraction pattern could be indexed with a large cubic unit cell fitting well with a Pt-rich pyrochlore ($Fd-3m$), that had formed in addition to some M-rich (Fe, Co) perovskite. Synthesis with $M = Ni$ formed a mix of Y_2O_3 , NiO and Pt metal.

There is a close structural similarity between the pyrochlore ($Nd_2Pt_2O_7$: $Fd-3m$, $a = 10.404 \text{ \AA}$ [159]) and Y_2O_3 ($Ia-3$, $a = 10.604 \text{ \AA}$ [160]), both having a large cubic unit cell with a similar cell parameter. However, the low angle reflection (111) at $Q = 1.07 \text{ \AA}^{-1}$ ($Fd-3m$) confirm the pyrochlore structure, and refinements indicate that there is some site exchange, with Y at the Pt-site (~30 %) and some Fe at the Y-site (~20 %). The structural similarity between Y_2O_3 and the pyrochlore may be why such large quantities of Y can be located at the B-site in the pyrochlore. We can also expect that the oxygen-content will deviate from seven if the oxidation state of M is below +IV ($Y_2Pt_{2-y}M_yO_{7-y}$). Pyrochlores have a large structural flexibility in terms of site exchange and oxygen content, e.g. the Bi_2MnTiO_7 pyrochlore show a significant flexibility in Mn-content, positioned both at the A- and B-site, and with oxygen content well below 7 [161]. Better data quality is needed to determine the exact structural details of this material, and phase pure samples would also be beneficial.

In terms of the structure of the Pt-containing oxides, we consider the turning point from the stability of the perovskite structure (Nd (9-coordinated): $r = 1.163 \text{ \AA}$ [133]) to the pyrochlore structure (Y (9-coordinated): $r = 1.075 \text{ \AA}$ [133]) to be around $r(A) \approx 1.1 \text{ \AA}$, because of the structural distortions correlating with the t -factor. All attempted syntheses are listed in Table with comments on the outcome.

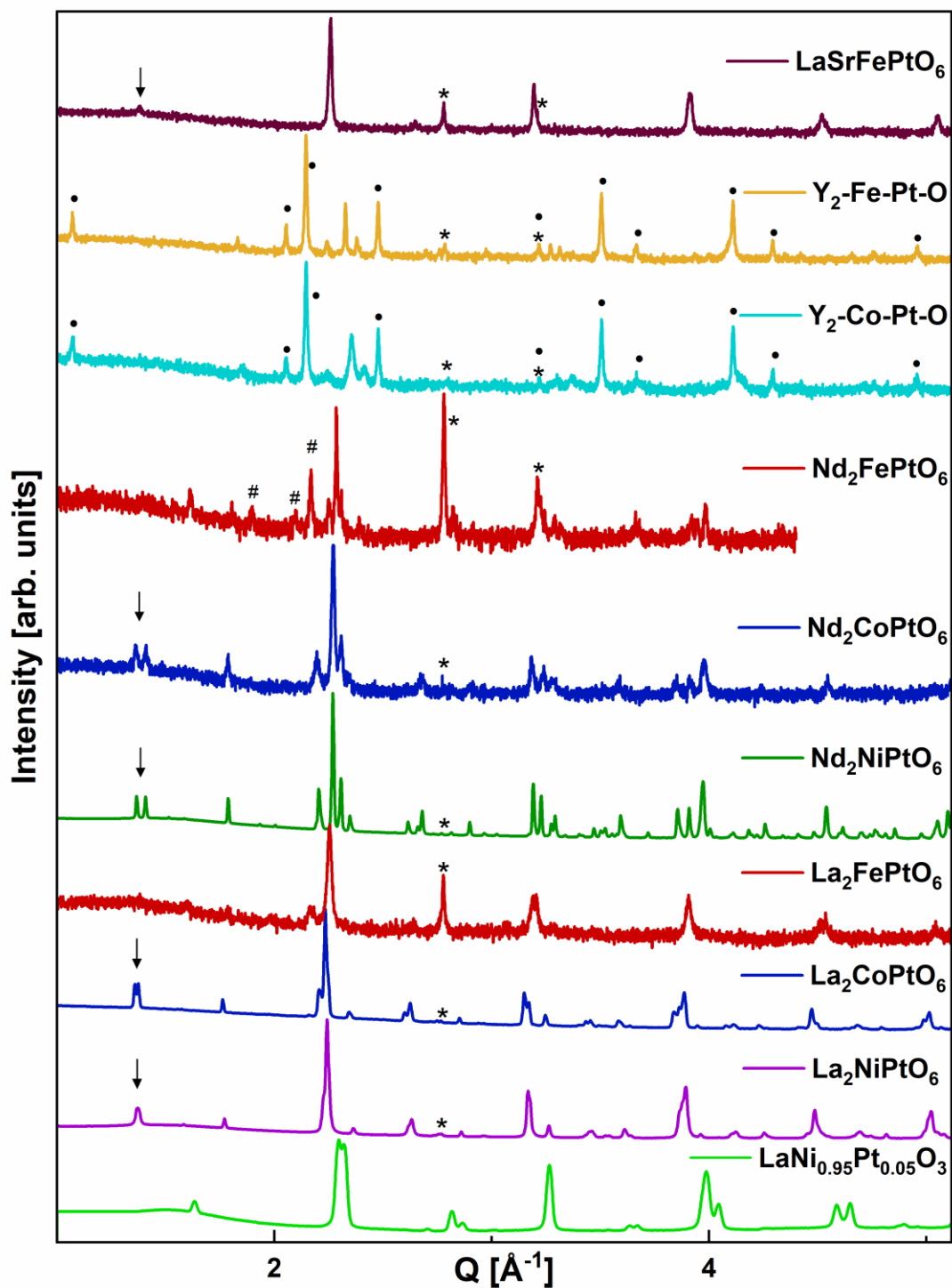


Figure 43. Comparison of the XRD patterns for $\text{LaNi}_{0.95}\text{Pt}_{0.05}\text{O}_3$ and the different RE_2MPtO_6 double perovskites, where $\text{RE} = \text{La}, \text{Nd}, \text{Y}$ and La/Sr , and $M = \text{Ni}, \text{Co}, \text{Fe}$. The sample compositions are written in the figure. * corresponds to the diffraction peaks of Pt metal, # to Nd_2O_3 , • to the pyrochlore structure, and the remaining peaks correspond to the perovskite structure. The arrow is pointing at the (011)(left) and (101)/(10-1)(right) peaks that indicate B -site ordering ($P2_1/n$). The data sets for $\text{La}_2\text{NiPtO}_6$, $\text{La}_2\text{CoPtO}_6$, $\text{Nd}_2\text{NiPtO}_6$ and $\text{LaNi}_{0.95}\text{Pt}_{0.05}\text{O}_3$ were measured with synchrotron radiation (SNBL, ESRF), while the rest of the samples were measured in the home laboratory.

Table 7. Selected structural information about LaNiO_3 and the Pt-containing perovskites, including Pt metal impurities, obtained from Rietveld refinements using Topas [162]. The t -factor is calculated from reported ionic radii [133]. The B -site ordering is provided by the long range order parameter S [163], calculated as $\text{Occ}(\text{Pt}_{\text{Pt}})/(1-x)$, with x in $\text{La}_2\text{M}_{1-x}\text{Pt}_x\text{O}_6$. The reported Pt metal impurities are the percent (%) of the Pt used in the synthesis which became Pt metal and not the perovskite, extracted from Rietveld refinements.

	Space group	a [Å]	b [Å]	c [Å]	β [°]	Volume [Å ³]	B -site ordering	t -factor	Pt metal
LaNiO_3	$R-3c$	5.455	5.455	13.134	-	338.5	-	0.97	-
						(*225.7)			
$\text{La}_2\text{NiPtO}_6$	$P2_1/n$	5.583	5.643	7.913	90.02	249.2	93 %	0.92	1.6 %
$\text{La}_2\text{CoPtO}_6$	$P2_1/n$	5.591	5.686	7.922	90.00	251.7	100 %	0.91	0.3 %
$\text{La}_2\text{FePtO}_6$	$P2_1/n$	5.570	5.576	7.863	90.07	244.2	-	0.90	51 %
$\text{Nd}_2\text{NiPtO}_6$	$P2_1/n$	5.448	5.698	7.787	90.03	241.7	100 %	0.88	1.0 %
$\text{Nd}_2\text{CoPtO}_6$	$P2_1/n$	5.444	5.718	7.758	90.00	241.5	99 %	0.87	0.6 %
$\text{Nd}_2\text{FePtO}_6$	$P2_1/n$	5.445	5.583	7.755	89.98	239.2	-	0.86	100 %
LaSrFePtO_6	$P2_1/n$	5.579	5.548	7.857	90.02	243.2	77 %	0.90	19 %

*Cell volume of LaNiO_3 recalculated to the same unit cell as the monoclinic cell.

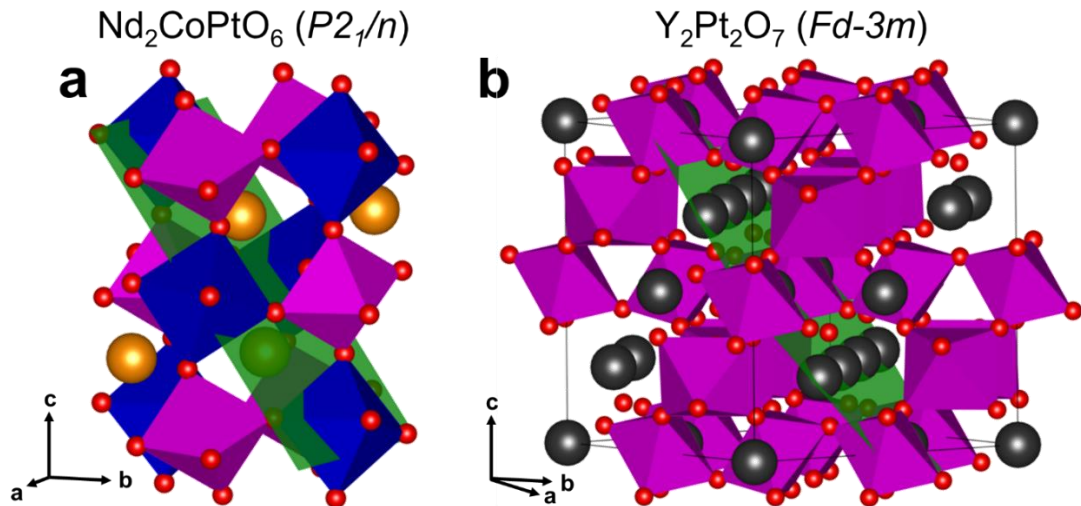


Figure 44. Structure illustration of a) the ordered double perovskite $\text{Nd}_2\text{CoPtO}_6$ ($P2_1/n$) with Co (blue) and Pt (pink) at different sites and with the (011) diffraction plane drawn in (green), and b) the pyrochlore $\text{Y}_2\text{Pt}_2\text{O}_7$ ($Fd-3m$) with Y (black) and Pt (pink) at different site (without site exchange), with the (111) diffraction plane drawn in (green). O is coloured red. The figures are drawn using Vesta [100].

4.2.1.5. Domain-structure in $\text{LaNi}_{1-x}\text{Pt}_x\text{O}_3$ (Paper IV)

In the discussion about the Pt-containing double perovskites RE_2MPtO_6 , we have assumed that Pt is in oxidation state +IV and we see that B -site ordering occurs to a very large extent. But how does the B -site ordering present itself in the non-equimolar compositions? Paper IV looks into structural aspects of the solid solution system $\text{LaNi}_{1-x}\text{Pt}_x\text{O}_3$ with a thorough analysis of SR-XRD data.

For samples with $x \geq 0.20$, the structure of the ordered double perovskite $\text{La}_2\text{NiPtO}_6$ ($P2_1/n$) is obtained, with B -site ordering. However, due to the non-equimolar ratio between Ni and Pt, complete ordering is not possible. The XRD data have broad and asymmetrical peaks. We hypothesize that Pt-rich and Pt-depleted domains are formed. Some domains with Pt content

4. Results and discussion

close to $\text{La}_2\text{NiPtO}_6$ with a large degree of B -site ordering, in addition to Pt-depleted domains, as in $\text{LaNi}_{1-x}\text{Pt}_x\text{O}_3$ where x is low and B -site ordering is nearly absent. The quantity and size of such domains depends on the composition (x -value).

The reason for this behaviour can be rationalized through the ionic approximation and the oxidation states of the Ni and Pt atoms. When an Ni(III)/Ni(III) or an Ni(II)/Pt(IV) pair of octahedra are located next to each other (Figure 45a), the oxygen in between them is satisfied in terms of charge (-II), as in LaNiO_3 and $\text{La}_2\text{NiPtO}_6$, respectively. However, for a non-equimolar $\text{LaNi}_{1-x}\text{Pt}_x\text{O}_3$ sample, a third situation occurs. If we assume that all Ni located next to Pt(IV) is Ni(II), then the oxygen located between Ni(II) and Ni(III) (red sphere in Figure 45a) is uncompensated in terms of charge. In a realistic scenario, the oxidation states will then have to deviate from nominal values to create the average +III oxidation state required. However, Pt is not known to take oxidation state +III in octahedral coordination in oxides, and the energy difference to reduce Pt from +IV ($t_{2g}^6 e_g^0$) to +III ($t_{2g}^6 e_g^1$) is the crystal field splitting, which is presumably quite high for a $5d$ element in an oxide. This implies that some oxygen will have to be undercompensated in terms of charge (between Ni(II+ δ)/Ni(III)) and overcompensated in terms of charge (between Ni(II+ δ)/Pt(IV)). This may be a driving force strong enough to cause the Pt-atoms to cluster together in $\text{La}_2\text{NiPtO}_6$ -like domains with a large degree of Ni-Pt ordering (Figure 45b), to minimize the amount of uncompensated oxygen atoms, which would be higher for a random Pt-distribution (Figure 45c). The variations in oxidation state leads us to describe the system $\text{LaNi}_{1-x}\text{Pt}_x\text{O}_3$ ($0 \leq x \leq 0.50$) with the formula $\text{La}_2\text{Ni}_y^{\text{II}}\text{Ni}_{2-2y}^{\text{III}}\text{Pt}_y^{\text{IV}}\text{O}_6$, $0 \leq y \leq 1$, which includes the oxidation states of the B -site elements. The presented results agree with magnetic measurements, for which the reader is referred to Paper IV.

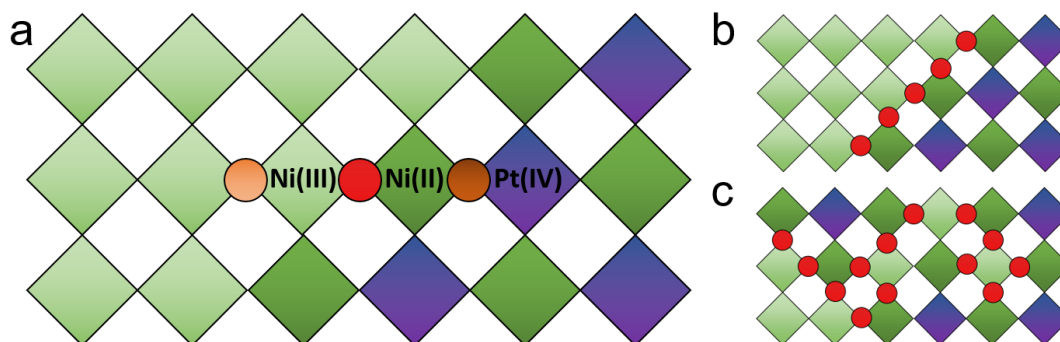


Figure 45. (a) Illustration of the different “type” of octahedral corner sharing oxygen ions (the circles) in $\text{LaNi}_{1-x}\text{Pt}_x\text{O}_3$. The bright orange oxygen ions are positioned between two Ni(III) ions, the red is positioned between one Ni(II) and one Ni(III) ion, and the brown in positioned between one Ni(II) and one Pt(IV) ion. (b) Illustration of the number of uncompensated O-ions in the case of clustering and (c) random Pt-distribution. Reused with permission from Elsevier [164].

4.2.2. Synthesis and structural aspects of Rh-containing double perovskites

Quite many Rh-containing double perovskites are reported [128]. However, few Rh-perovskites with Y as the A -site cation is reported, and few solid solutions systems ($\text{RE}M_{1-x}\text{Rh}_x\text{O}_3$) are investigated. In this work, the three stoichiometric Rh-containing perovskites have

been investigated ($YM_{0.50}Rh_{0.50}O_6$, $M = Ni, Co, Fe$), along with the solid solution system $LaNi_{1-x}Rh_xO_3$.

Unlike the Pt-containing perovskites, Rh-containing perovskites can be synthesized using the solid-state synthesis route with Rh_2O_3 as a precursor to obtain several compounds, such as $LaRhO_3$ [165] and $LaNi_{0.50}Rh_{0.50}O_3$ [124, 125]. However, in the present work, the solid-state synthesis route did not prove successful in producing phase pure non-equimolar samples in the system $LaNi_{1-x}Rh_xO_3$. The citric acid synthesis route (section 3.3) was used in the synthesis of the series $LaNi_{1-x}Rh_xO_3$ ($0 \leq x \leq 1$) (Paper V) in addition to the perovskites $YM_{0.50}Rh_{0.50}O_3$, $M = Ni, Co, Fe$ (3 + 30 days annealing at 1000 °C in O_2 /flow). The samples are phase pure except $LaRhO_3$ (< 1 mol. % Rh_2O_3) and $YCo_{0.50}Rh_{0.50}O_3$ (~ 1 mol. % Co_3O_4), while $YNi_{0.50}Rh_{0.50}O_3$ contains significant impurities. Structural studies of $YCo_{0.50}Rh_{0.50}O_3$ and $YFe_{0.50}Rh_{0.50}O_3$ are not previously reported.

Through the sample series, the XRD pattern develops in a similar way as for the Pt-perovskites; upon reducing the size of the A -cation the main perovskite peak splits (Figure 46), correlating with increased structural distortions in terms of a reduced t -factor and sharper $M-O-M'$ bond angles (Table 9). The peaks also shift to lower Q as the size of the B -site element increases.

The samples with $x \leq 0.10$ in $LaNi_{1-x}Rh_xO_3$ (Paper V) have the rhombohedral symmetry of $LaNiO_3$ ($R\bar{3}c$), while samples with $x \geq 0.30$ are orthorhombic like $LaRhO_3$ ($Pnma$). The $YM_{0.50}Rh_{0.50}O_3$ perovskites are also orthorhombic ($Pnma$, Table 9) and none of the Rh-based samples show long range B -site ordering. In the case of B -site ordering, the (011), (101) and (10-1) reflections in space group $P2_1/n$ are expected to show strong intensity (arrow in Figure 43). For $YM_{0.50}Rh_{0.50}O_3$ in $P2_1/n$, (011) and (101)/(10-1) are split in the same way as the main perovskite reflections ($Q = 2.2 - 2.5 \text{ \AA}^{-1}$, Figure 46), like for Nd_2NiPtO_6 (Figure 43). The intensity is zero where (011) in $P2_1/n$ is expected, which imply that long range B -site ordering is absent. (101)/(10-1) in $P2_1/n$ is located at the same Q as (011) in $Pnma$, where a low intensity is observed, fitting well with Rietveld refinements of a disordered perovskite $YM_{0.50}Rh_{0.50}O_3$. The samples in the $LaNi_{1-x}Rh_xO_3$ system show a similarly low intensity of the (011) reflection ($Pnma$), indicating B -site disorder, in line with previous reports [124-126]. For this reason, it is likely that the oxidation states are +III for M (Ni, Co, Fe) and Rh, while the $M(II)/Pt(IV)$ scenario led to ordered double perovskites (section 4.2.1.2).

Detailed investigations of the oxidation state of Ni/Rh show that the +III/+III scenario is not the completely correct way to describe the system $LaNi_{1-x}Rh_xO_3$ (Paper V). The volume increases with increasing Rh-content (x), but do not follow the linear trend of Vegard's law (Figure 48). Using reported ionic radii (Table 8), the volume increase is estimated for both the +III/+III and the +II/+IV scenario for the oxidation state of Ni/Rh, and the experimental volume is somewhere in between these two models (Figure 48). Furthermore, X-ray absorption spectroscopy (XAS) show that the $LaNi_{1-x}Rh_xO_3$ samples have a shift in the absorption edge from the reference sample $LaRhO_3$ (Rh(III)) to La_2MgRhO_6 (Rh(IV)), correlating with the Rh-content (x), although not completely over to Rh(IV). We therefore conclude that there is mixed

4. Results and discussion

valence with both Ni(II)/Rh(IV) and Ni(III)/Rh(III), which is also supported by analysis of the paramagnetic signal from a series of magnetic measurements (Figure 48; Paper V). Despite this fact, we do not find evidence for long range *B*-site ordering in any of the samples.

In YNiO_3 , Ni is known to disproportionate due to the unstable nature of the e_g^1 -electron configuration [166]. Based on the analysis of $\text{LaNi}_{1-x}\text{Rh}_x\text{O}_3$ above, and it is likely that $\text{YNi}_{0.50}\text{Rh}_{0.50}\text{O}_3$ would contain a fair amount of Ni(II) and Rh(IV). The Ni(II)/Rh(IV) pair has a larger average ionic radii than Ni(III)/Rh(III) (Table 8) and may contribute to destabilize the $\text{YNi}_{0.50}\text{Rh}_{0.50}\text{O}_3$ perovskite. The fact that Co and Fe are more stable in oxidation state +III may contribute to why they are almost phase pure. However, by comparing the unit cell volume of the experimental samples with reported unit cell volumes, a certain degree of mixed valence is likely present also in the $\text{YCo}_{0.50}\text{Rh}_{0.50}\text{O}_3$ and $\text{YFe}_{0.50}\text{Rh}_{0.50}\text{O}_3$ samples, estimated to $\sim 60\%$ and $\sim 69\%$ +III/+III, respectively (Table A2).

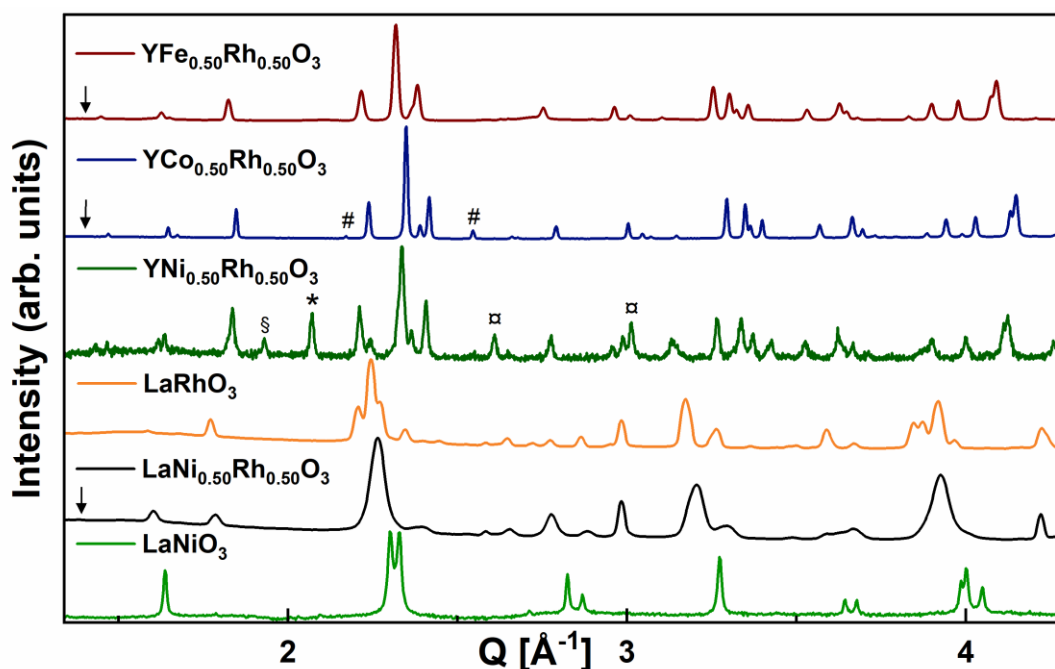


Figure 46. XRD pattern of LaNiO_3 , $\text{LaNi}_{0.50}\text{Rh}_{0.50}\text{O}_3$, LaRhO_3 and $\text{YM}_{0.50}\text{Rh}_{0.50}\text{O}_3$ ($M = \text{Ni}, \text{Co}, \text{Fe}$). *correspond to the diffraction peaks of Y_2O_3 , # to Co_3O_4 , x to NiO, § to an unknown impurity, and the remaining peaks correspond to the perovskite structure. The arrow is pointing at where the (011) and (101)/(10-1) peaks that indicate *B*-site ordering ($P2_1/n$) are expected. The data sets for $\text{YNi}_{0.50}\text{Rh}_{0.50}\text{O}_3$ and LaNiO_3 were measured in the home laboratory, while the rest of the samples were measured with synchrotron radiation (SNBL, ESRF).

Table 8. Preferred oxidation states for the different elements and reported ionic radii [133]. HS = high spin electron configuration, LS = low spin electron configuration. The coordination number is six for all the elements, except Pt(II) which is in square planar coordination (4-coordinated).

	Ni	Co	Fe	Rh	Pt
Preferred oxidation states	+II, +III	+II, +III, +IV	+II, +III, +IV	+III, +IV	(+II), +IV
Ionic size (+II) [Å]	0.69	0.65 (LS) 0.745 (HS)	0.61 (LS) 0.78 (HS)	-	0.80
Ionic size (+III) [Å]	0.56 (LS)	0.545 (LS) 0.61 (HS)	0.55 (LS) 0.645 (HS)	0.665 (LS)	-
Ionic size (+IV) [Å]	-	0.53 (HS)	0.585 (HS)	0.60 (LS)	0.625

Table 9. Selected structural information on the different Rh-perovskites. The t -factor is calculated from reported ionic radii [133]. Atomic positions for $\text{YCo}_{0.50}\text{Rh}_{0.50}\text{O}_3$ and $\text{YFe}_{0.50}\text{Rh}_{0.50}\text{O}_3$ are reported in Table A3 (Appendix). The B -site coordination number is six for all samples. The A -site coordination number is between 12 and 8 depending on degree of distortion, but depends strongly on oxygen positions and is not determined accurately.

	Space group	a [Å]	b [Å]	c [Å]	Volume [Å ³]	M -O- M' angle	t -factor
LaNiO_3	$R\bar{3}c$	5.455	5.455	13.134	338.5 (*225.7)	165.4	0.97
$\text{LaNi}_{0.50}\text{Rh}_{0.50}\text{O}_3$	$Pnma$	5.560	7.819	5.542	241.0	152.6, 158.3	0.94
LaRhO_3	$Pnma$	5.689	7.893	5.526	248.1	152.2, 144.4	0.92
$\dagger\text{YNi}_{0.50}\text{Rh}_{0.50}\text{O}_3$	$Pnma$	5.692	7.542	5.230	224.5	-	0.85
$\text{YCo}_{0.50}\text{Rh}_{0.50}\text{O}_3$	$Pnma$	5.611	7.501	5.197	218.8	140.6, 144.9	0.84
$\text{YFe}_{0.50}\text{Rh}_{0.50}\text{O}_3$	$Pnma$	5.666	7.607	5.272	227.2	141.0, 145.0	0.83

*Cell volume of LaNiO_3 recalculated to the same unit cell as the orthorhombic cell.

\dagger Contains significant impurities, see section above.

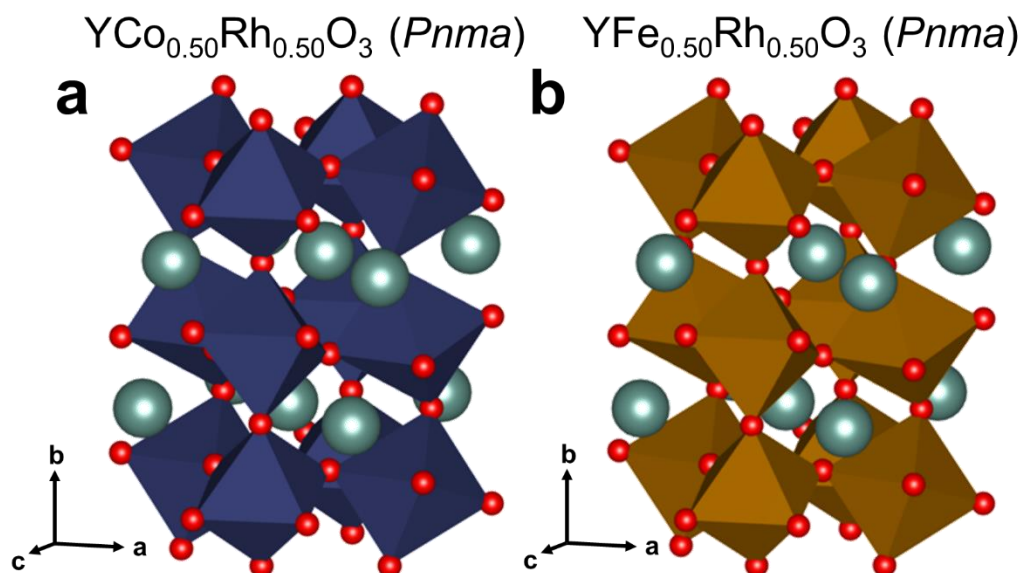


Figure 47. Structure illustration of the B -site disordered perovskites a) $\text{YCo}_{0.50}\text{Rh}_{0.50}\text{O}_3$ ($Pnma$) and b) $\text{YFe}_{0.50}\text{Rh}_{0.50}\text{O}_3$ ($Pnma$) where the B -site (octahedra) is half Co/Fe and half Rh. O is red, Co/Rh dark blue, Fe/Rh brown and Y dark cyan. The figures are drawn using Vesta [100].

4. Results and discussion

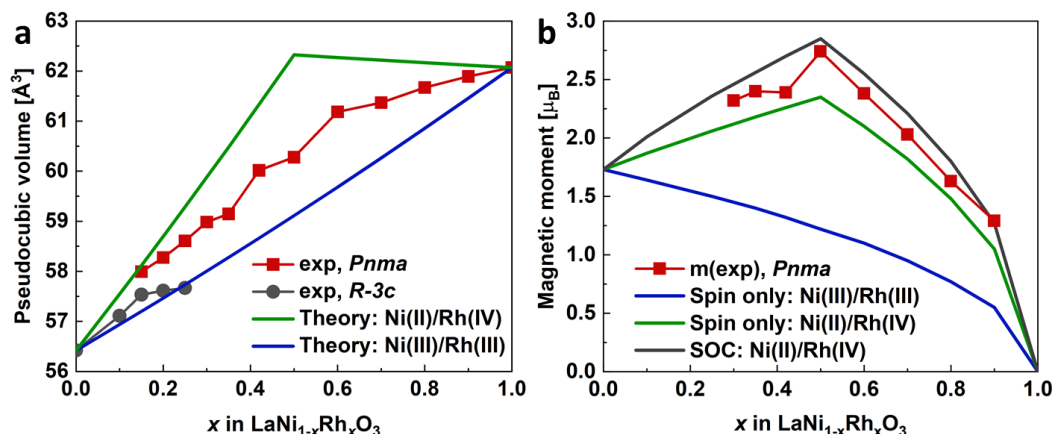


Figure 48. a) Pseudocubic volume through the perovskite system $\text{LaNi}_{1-x}\text{Rh}_x\text{O}_3$ comparing with theoretical volume for Ni(III)/Rh(III) and Ni(II)/Rh(IV) calculated based on ionic radii (Table 8). b) paramagnetic moment calculated from the Curie-Weiss region of magnetic measurements compared with theoretical values for Ni(III)/Rh(III) and Ni(II)/Rh(IV) in the spin only approximation and for Ni(II)/Rh(IV) including spin orbit coupling (SOC) for Rh(IV) ($t_{2g}^5 e_g^0$). Reused with permission from Elsevier [167].

4.2.3. Combined Pt- and Rh-perovskites

Pt is in the ammonia oxidation process transported as the volatile oxide molecule PtO_2 (section 2.1.1). It could therefore be beneficial to capture Pt in an oxide material, in addition to oxide materials being less costly than noble metals. In the case of Pt-catchment in a double perovskite, the low angle peak ($Q = 1.37 \text{ \AA}^{-1}$ for $\text{La}_2\text{NiPtO}_6$, Figure 43) can be used as a fingerprint for the double perovskite phase where Pt is captured, even if both Pt and Rh is captured. This is the case for the LaNiO_3 sample described briefly in section 2.3.

There is an interesting contrast between Pt- and Rh-containing perovskites in terms of the oxidation state; all Pt-perovskites have Pt(IV) and long range B -site ordering, while the Rh-perovskites mainly have Rh(III) and do not have long range B -site ordering. This limits the range of compositions possible to synthesize with Pt(IV), and the oxidation state must be kept in mind.

Even though Pt- and Rh-perovskites have different symmetry, mixed Pt-Rh-perovskites can also form. Because of the possible oxidation states for B -site substituted LaNiO_3 , Ni(II)/Pt(IV), Ni(III)/Rh(III) and Ni(II)/Rh(IV), a mixed Pt-Rh-perovskite cannot form where Pt (Rh) is required to take an oxidation state below +IV (+III). The two formulas that satisfy these requirements are:

- $\text{La}_2\text{NiPt}_{1-x}\text{Rh}_x\text{O}_6$, where Pt(IV) is replaced by Rh(IV), or an Rh(III) that oxidizes a Ni(II) to Ni(III).
- $\text{La}_2\text{Ni}_{1-y}\text{Pt}_{1-y}\text{Rh}_{2y}\text{O}_6$, where the Ni(II)/Pt(IV) pair is replaced by two Rh(III) atoms.

A mixed system between these two is also possible: $\text{La}_2\text{Ni}_{2-\alpha-\beta}\text{Pt}_\alpha\text{Rh}_\beta\text{O}_6$, $\alpha + \frac{1}{2}\beta \leq 1$

$\text{La}_2\text{NiPt}_{0.50}\text{Rh}_{0.50}\text{O}_6$ and $\text{La}_2\text{NiPt}_{0.80}\text{Rh}_{0.20}\text{O}_6$ synthesized with the citric acid synthesis route show XRD data which fit well with a perovskite with some site exchange between Ni, Pt and Rh (Figure 49). For $\text{La}_2\text{Ni}_{0.50}\text{PtRh}_{0.50}\text{O}_6$, Pt metal impurities are present in the sample (Figure

49). However, this sample do not fulfil the requirements for oxidation states mentioned above, and we can conclude that if a too high Pt and Rh content is used, Pt metal impurities will form.

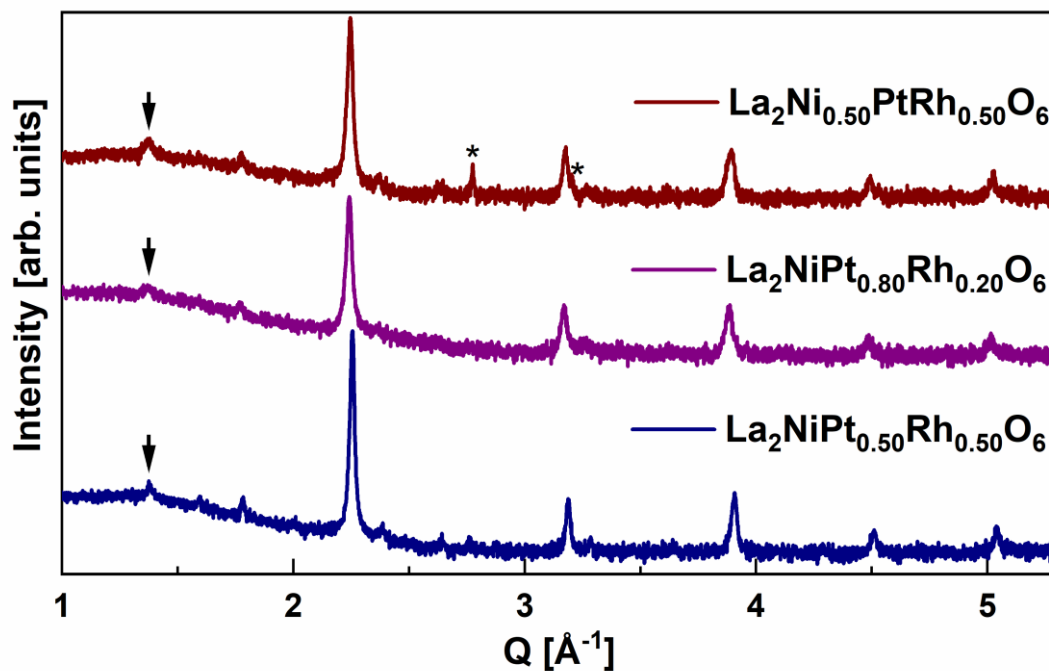


Figure 49. XRD of three samples with both Ni, Pt and Rh at the *B*-site. The chemical formula is written in the figure. The arrow is pointing at the (011), (101) and (10-1) peak that indicates *B*-site ordering in the ordered double perovskite ($P2_1/n$). * indicates the main reflections of Pt-metal, while the other peaks belong to the perovskite.

5. Summarizing discussion and outlook

The Ostwald process and industrial production of nitric acid have been a vital part of the chemical process industry for more than 100 years, and it is equally needed in the future to maintain agriculture [6]. Platinum loss has been an issue of the industrial Pt/Rh-catalyst since the development of the ammonia oxidation process, and despite intensive research, the Pt- (and Rh-) loss seems inevitable [25, 168]. Pt-catchment therefore plays a crucial role in the ammonia oxidation process today. Pt can be captured without influencing the catalytic oxidation of ammonia to nitric oxide. State of the art technology comprises the use of a Pd/Ni (91/9 at. %) gauze for Pt-catchment, which is victim to severe restructuring and swelling during industrial operation, in addition to both Pd- and Ni-loss. The swelling of the Pd/Ni gauzes causes a significant pressure drop through the gauze pack, limiting the installation of a sufficient number of gauzes to capture all of the evaporated Pt.

This thesis has addressed the Pd and Pd/Ni wire swelling and concludes that the issue is a result of two key factors: 1) Grain reconstruction due to Pt-catchment, causing an *edged* crystallite shape on the wire surface, and 2) pore formation due to the high temperature and aggressive gas mixture, causing a *rounded* crystallite shape on the wire surface. Previous reports consider the effect of Ni in the Pd/Ni alloy and if it contributes to Pt-catchment or pore formation [30, 31]. We conclude that Ni has no significant effect on Pt-catchment and does not cause porosity when evaporating from the wire in the form of Ni(OH)₂ in wet air. However, the industrial experiment (section 4.1.7) shows the highest Pt-concentration for the quasi-monocrystalline Pd/Ni gauze and indicate that Ni/NiO may aid the Pt-catchment process.

In situ absorption-CT was applied to study the mechanism of the Pt-catchment process, a powerful technique allowing 3D visualization of objects and extraction of quantitative information on morphological development. Absorption-CT shows that the Pt-catchment ability decreases with increasing Pt-concentration in the catchment alloy and reducing $p(\text{PtO}_2)$. SEM/EDX analysis indicates that GB diffusion is rapid and bulk diffusion is slow. Slow bulk diffusion results in an elevated Pt-concentration on the surface and causes reduced Pt-catchment, as observed from absorption-CT. We thus have a correlated diffusion limitation – Pt-catchment limitation. The limitation causes a complex interdiffusion phenomenon during Pt-catchment, with Pt diffusion inwards and Pd diffusion outwards. The possibility of rapid GB diffusion causes the polycrystalline Pd- and Pd/Ni wires to restructure completely, evident from the fact that the restructuring is significantly slower for the quasi-monocrystalline samples. Due to Pd-diffusion being more rapid than Pt-diffusion in Pd and Pd/Pt alloys [62], it is likely that a net inwards flux of vacancies can result in the formation of internal voids (Kirkendall voids) [63]. However, we have not observed internal voids in Pd or Pd/Ni, only open porosity in the GBs, and only what we believe to be Kirkendall voids in the quasi-monocrystalline Pd/Au (50/50 at. %) sample.

A suggestion for future work is to investigate the interdiffusion phenomena that occur during Pt-catchment; if there is an inwards flux of vacancies and if internal voids are formed.

5. Summarizing discussion and outlook

Tomography is a possible technique to investigate internal porosity, but absorption-CT is not suited as quantitative information is required. Although a destructive technique, FIB-SEM tomography is an option as the Pd-based wire samples are easily prepared by laboratory experiments. It would remove the problem of possible artefacts introduced during the preparation of a cross-section for SEM. It is difficult to determine if, and to what degree, internal voids are present from a single SEM cross-section. If internal voids are present, the formation of Kirkendall voids is a likely mechanism for the formation of porosity and wire restructuring.

Regarding wire restructuring, we have observed that all investigated noble metal wires restructure to some extent during Pt-catchment. The Pd/Au samples have an enhanced bulk diffusion and are less likely to be diffusion-limited in the same way as Pd. GB diffusion is barely visible for Pd/Au (50/50 at. %) and absent for Au. The higher bulk diffusion is one reason why Pd/Au (50/50 at. %) has significantly reduced wire restructuring. However, Au restructures as both a poly- and quasi-monocrystalline wire and in a different manner than Pd. A second reason for the low restructuring of Pd/Au (50/50 at. %) may thus be that both the restructuring mechanism of Pd and Au affects Pd/Au (50/50 at. %) during Pt-catchment and that they cancel each other out.

Au wires shows crystals growing on top of the surface rather than a restructuring of already existing grains. Why Au restructures in a special manner is a key question to answer; it may be related to rapid bulk (and surface) diffusion, the low melting point or to an energetic gain of recrystallizing and exposing clear faceted crystals. The latter energy gain is likely dependent on the Pt-concentration in the alloy. Further experiments are needed to understand this restructuring process. The Au wires saturate at ~10 at. % Pt, and the restructuring stops up or become slower at this point. Investigations of Pt-catchment using several Au/Pt alloys with 1 – 15 at. % Pt is recommended to study surface restructuring and the driving force behind it.

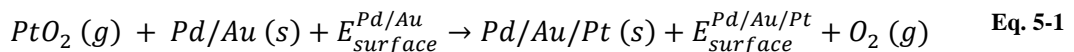
We have found that a significant Ni-loss occurs in wet air without the formation of porosity (section 4.1.1.3). Notably, Ni-loss from Pd/Ni and Pt-catchment with Pd (Pd/Ni) have an interesting similarity: in both situations there are species diffusing from the wire bulk and outwards to the surface. However, such outwards diffusion only results in porosity during Pt-catchment. The main difference between the two situations is the Pt-catchment process and subsequent surface diffusion of Pt, which is absent during Ni-loss from Pd/Ni. When Pt is captured on the Pd (Pd/Ni) wire surface, it has a driving force to find a place in the atomic structure. Ni evaporates as Ni(OH)₂ and does not affect the surface structure in a similar way. To understand such surface diffusion and the driving forces behind is likely key knowledge needed to understand the restructuring phenomena observed in this work.

The Pd/Au (50/50 at. %) alloy stands out as a potential candidate for Pt-catchment due to minimal wire swelling. However, a drawback of the Pd/Au (50/50 at. %) alloy is the lower Pt-catchment compared to the Pd-rich samples in the industrial experiment, as well as lower Pt-catchment compared to Pd in the laboratory experiments (dry air + PtO₂). The phase diagram

of the Pd-Au-Pt system shows a solid solution up to 25-30 at. % Pt at 900 °C for a 50/50 at. % Pd/Au alloy [70, 71]. Therefore, a limited solid solution is not the cause for the limited Pt-catchment by the Pd/Au alloys. Unfortunately, the Au-sample from the industrial experiment was destroyed, and we cannot determine the Pt-catchment of Au compared to Pd/Au (50/50 at. %) at industrial conditions. There is also a limit of ~35 at. % Pt for Pt-catchment by Pd, likely due to a gas-surface interaction limiting further catchment. We can speculate if oxygen play a role in this system and if surface segregation of Pt occurs, causing a reduced Pt-catchment. Studies of surface segregation at relevant temperatures and conditions are recommended.

While the laboratory experiments only use synthetic air, several more gas constituents are present in the industrial experiments. Insight into how these species interact and possibly form surface species on the catchment material would be very useful knowledge to understand the behaviour of the different catchment materials; both in terms of restructuring, Pt-catchment abilities depending on the alloy composition as well as loss of catchment material (Pd-loss). Different spectroscopy techniques (Raman, IR) could help in identification of the surface- and gas species of Pd, Pt and Au related to the gas mixture (O₂, H₂O, NO, NH₃, N₂). However, the concentration of such gas species is low and detection will be difficult. Surface species are more likely to exist in measureable quantities. It is in both situations likely necessary to use synchrotron radiation for the experiments, in combination with modelling of expected spectra. NAP-XPS may also be suited to study surface species, although the temperature may be a limitation and the pressure is in the range of mbar, which may be insufficient. Modelling of the stability of different gas species is highly recommended.

We find the suggested mechanism for Pt-catchment by Yang *et al.* (2Pd + PtO₂ → 2PdO + Pt) [28] unlikely because Au-containing alloys and Au are also capable to capture Pt. We find it more likely that PtO₂ simply decompose into Pt (s) and O₂ (g) when Pt is captured. However, it likely involves an equilibrium of Pt-concentration in the alloy and on the surface, $p(\text{PtO}_2)$ and $p\text{O}_2$. Furthermore, it is possible that Pt is transported as other species beside PtO₂ because we observe a different Pt-catchment for the Pd/Au alloys in the laboratory (air + PtO₂) relative to the industrial/pilot experiments. Molecules with Pt may have different reaction energies depending on the gas species and catchment alloy compositions (Pd, Au, Pt), which implies that the Pt-catchment mechanism is difficult to describe with one single reaction. We suggest that the total energy of PtO₂ reacting with an alloy to form a Pt-containing alloy is the best descriptor for high Pt-catchment (Eq. 5-1).



Other Pt-species can take the place of PtO₂ in the equation above (Eq. 5-1) if identified to contribute significantly to Pt-transport. Identification of gas/surface species would also be vital in identifying the origin of Pd-loss, which is a thermal loss related to the temperature and aggressive gas conditions. Our result from the 28 days pilot plant experiment show a similar Pd-loss for Pd/Au (50/50 at. %) as reported by Holzmann [17]. Notably, Au captured volatile Pd evaporated from the industrial Pd/Ni gauze during the industrial experiment (section 4.1.7).

5. Summarizing discussion and outlook

Although the Au sample was largely destroyed during the industrial experiment, it demonstrated that Pd can be captured if necessary. It is reported that PdO has a lower vapour pressure Pd metal [107], which implies that it could be beneficial to capture Pd in an oxide.

To conclude on the topic of Pt-catchment, a note on the factors that determine a good metal-based Pt-catchment system is provided. Firstly, the Pt-catchment capacity must be high. Literature reports indicate that too high quantities of non-noble metals lead to the formation of binary oxides on the wire surface that inhibit Pt-catchment, *i.e.* there must be a sufficient quantity of noble metals in the alloy. Furthermore, the noble metal loss from the catchment material should be low. The restructuring and swelling of the wire should be limited, but a small increase in surface area can be beneficial to increase Pt-catchment, *e.g.* achieved by Au-substitution in Pd. A wide weave can be used to avoid a large pressure drop, but the system must maintain sufficient mechanical strength to prevent a physical loss or that the gauze breaks during operation. This can be achieved by thicker Pd/Au wires, although thicker wires are associated with higher investment costs. To obtain rapid Pt-catchment, the material used should preferably avoid significant surface segregation of Pt, *i.e.* Pt should diffuse rapidly into the material and do not have a larger preference for the surface (surface activity) than the other elements in the alloy. Au can improve bulk diffusion in Pd, or GB diffusion can be utilized to transport Pt rapidly into the wire. In the latter case it is important to have little grain growth, which can be achieved by different additives (grain refiners). This work indicates that 9 at. % Ni are more than necessary and GB diffusion seems blocked by the large quantity of NiO in the GBs, in addition to that Ni-loss may facilitate grain growth (significant GB diffusion occurs). It may be beneficial to test with several additives simultaneously and in smaller concentration, preferably with a low vapour pressure, *e.g.* Mn, Zr and Y [169, 170]. The additives are expected to oxidize by internal oxidation, similar to Ni. It may be favourable that the precipitates do not mix structurally as oxides to maintain several small particles rather than large ones located in the GBs. Further research on this topic is recommended.

This work has also focused on establishing a baseline of knowledge on Pt- and Rh containing perovskite oxides. While Pt-containing double perovskites have *B*-site ordering ($P2_1/n$), the Rh-containing ($Pnma$) do not. The Rh-perovskites are also stable with a smaller rare earth element than Pt. This implies that in an industrial experiment, Pt- and Rh-catchment can be quantified by XRD and Rietveld analysis. Pt forms an ordered double perovskite with a signature peak near $Q = 1.4 \text{ \AA}^{-1}$ for a sufficiently large *A*-site cation (*e.g.* Nd), while Rh forms a disordered perovskite regardless of the *A*-site element. The capture of Pt/Rh in a perovskite will also increase the volume of the perovskite and will be visible in the lattice parameters.

We foresee that Pt- and Rh-catchment using oxide materials has the potential to improve current catchment technology. It can reduce costs, reduce the use of scarce noble metals and provide a system with a similar or lower pressure drop than the gauze-based system (the oxide pellets from the N_2O decomposition catalyst provide a low pressure drop; section 2.1). A PhD project is currently ongoing in the iCSI centre for the study of Pt-catchment using oxide materials [148].

Appendix

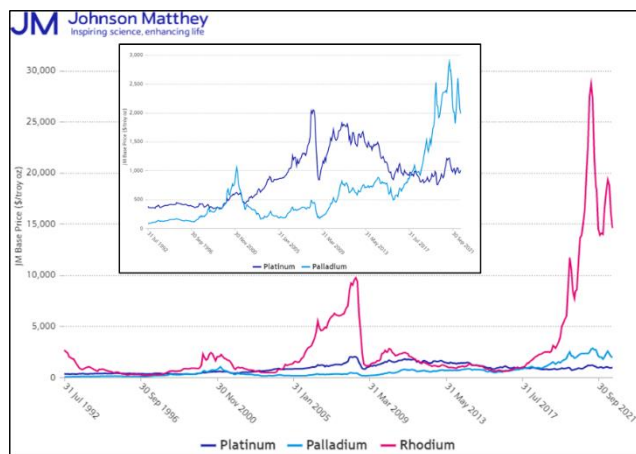


Figure A1. Price of Pt, Pd and Rh in US dollars per troy oz from June 12th 1992 to June 12th 2022, collected from Johnson Matthey [171]. 1 troy oz is the same as 31.1 g. The metal prices on June 12th 2022 was thus: Pt = 301 NOK/g, Pd = 597 NOK/g, Rh = 4309 NOK/g.

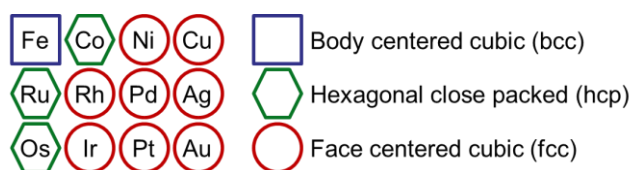


Figure A2. Overview of the different packing type for selected metallic elements in the periodic table. The figure is drawn by inspiration of Woodward *et al.* [172].

Appendix

Table A1. A) Self-diffusion and b-c) tracer- and impurity- diffusion coefficients, respectively, at 900 °C relevant for the present work, d) oxygen diffusion and solubility in the metals at 900 °C, and e) vapour pressure in different gases.

a) Self-diffusion in	Grain	D [cm ² /s]	Reference
Pd	bulk	$3.5 * 10^{-13}$	[58]
Ni	bulk	$4.5 * 10^{-13}$	[58]
Pt	bulk	$1.5 * 10^{-13}$	[58]
Au	bulk	$1.2 * 10^{-9}$	[58]
b) Tracer-diffusion	Grain	D [cm ² /s]	Reference
Pt in Pd	bulk	$3.3 * 10^{-14}$	[62]
Pd in Au	bulk	$1.6 * 10^{-10}$	[58]s
Pt in Pd/Au (91/9 at. %)	bulk	$6.0 * 10^{-14}$	Calculated from Pt in Pd and
Pt in Pd/Au (50/50)	bulk	$1.1 * 10^{-12}$	Calculated from Pt in Pd and
Pt in Au	bulk	$3.4 * 10^{-11}$	[58]
(Pt in Au)	bulk	$(1.0 * 10^{-10})$	[58]
Pt in Pd	GB	$2.9 * 10^{-8}$	David Waller and present
c) Impurity diffusion	Grain	D [cm ² /s]	Reference
Ni in Pd/Ni (93.4/6.6)	bulk	$3.3 * 10^{-11}$ (1100 °C)	[72]
d) Oxygen properties	Grain	Value	Reference
O diffusion in Pd	bulk	$D = 6.2 * 10^{-8}$	[110]
O solubility in Pd	bulk	$c_0 = 2.4 \text{ at. \%}$	[110]
O diffusion in Pt	bulk	$D \approx 10^{-9}$	[173]
O solubility in Pt	bulk	$c_0 \approx 1 - 2 \text{ at. \%}$	[173]
O solubility in Au	bulk	Considered very low	[174]
O permeability in Au		2-7 orders of magnitude below other	[150]
e) Vapour pressure	Gas	Temperature [°C]	Mass loss / vapour pressure [mg/(cm ² * min)]
Pt [107]	Vacuum	1200	$5 * 10^{-8}$
Pt [107]	Air	1000	$1 * 10^{-5} - 3 * 10^{-4}$
Pt [107]	O ₂	1000	$2 * 10^{-5} - 2 * 10^{-3}$
Pd [107]	Vacuum	1000	$1 * 10^{-3}$
Pd [107]	Air	1000	$1 * 10^{-5} - 9 * 10^{-5}$
Pd [107]*	O ₂	1100	$1 * 10^{-2}$
Rh [107]	Vacuum	1200	$1 * 10^{-7}$
Rh [107]	Air	1000	$5 * 10^{-6}$
Ni [170]	O ₂ +H ₂ O	1200	$5 * 10^{-6} \text{ bar}$
Pt [109]	O ₂	1200	$2 * 10^{-3}$
Pt [109]	O ₂ +H ₂ O	1200	$1 * 10^{-3}$
Pd [109]	O ₂	1200	Not observable in 24h
Pd [109]	O ₂ +H ₂ O	1200	Not observable in 24h
		Formation enthalpy	
PdO		-170 kJ/mol	[44]
PtO ₂		-135 kJ/mol	[44]
Rh ₂ O ₃		-255 kJ/mol	[44]

*This data does not coincide with the observations by Opila [109].

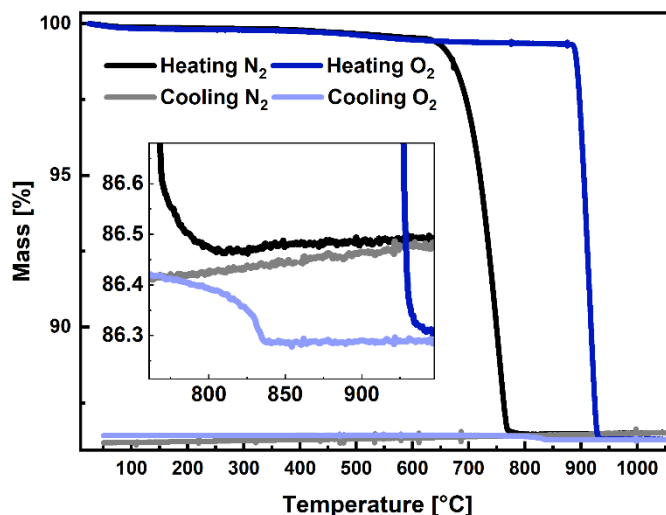


Figure A3. TG results for PdO (purchased from Sigma-Aldrich, purity 99.97 %, 520748, Lot # MKBR8359V) in 1 atm N₂ (N₂ 5.0 from AGA) and 1 atm O₂ (O₂ 5.0 from AGA) with a ramp rate of 10 °C per min and gas flow of 40 ml/min. Between the heating and cooling segment, the sample dwelled for 1 hour at 1050 °C. There is a large difference in the decomposition temperature of PdO depending on pO_2 . Pd metal re-oxidizes at ~830 °C upon cooling, which is quite significantly below the decomposition temperature of PdO. The experiments were performed using a NETZSCH STA 449 F1.

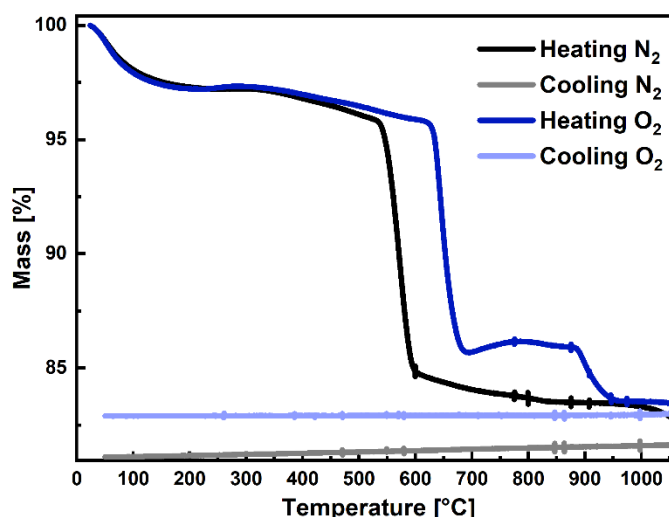


Figure A4. TG results for PtO₂ monohydrate (purchased from Sigma-Aldrich, purity 99.9 %, 229040, Lot # MKAA1564V) in 1 atm N₂ (N₂ 5.0 from AGA) and 1 atm O₂ (O₂ 5.0 from AGA) with a ramp of 10 °C per min and gas flow of 40 ml/min. Between the heating and cooling segment, the sample dwelled for 1 hour at 1050 °C. PtO₂ decomposes to Pt₃O₄ and Pt metal, and then further to only Pt metal. Notably, the mass of PtO₂ heated in O₂ is not equal to that heated in N₂ after the 1 hour dwell at 1050 °C, indicating that some oxygen remains in the sample heated in O₂. The experiments were performed using a NETZSCH STA 449 F1.

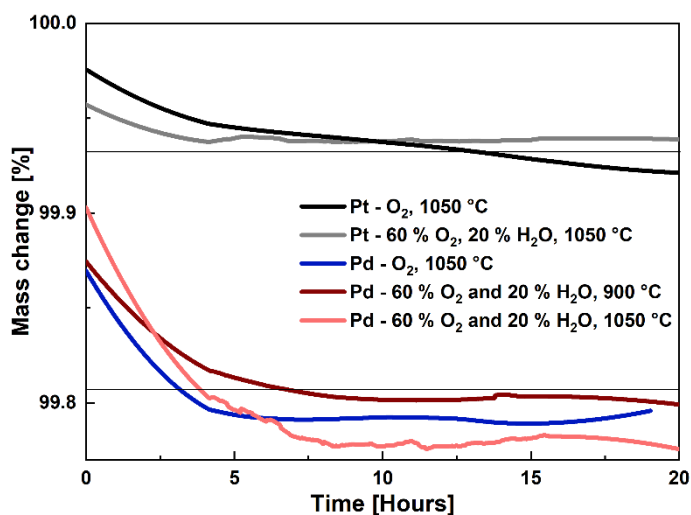


Figure A5. TG results at a high temperature dwell for Pt (99.9 %, Heraeus) and Pd (99.9 %, Koch-Light Laboratories LTD) metal in 1 atm O₂ (O₂ 5.0 from AGA) and in a combination of 60 % O₂, 20 % H₂O and 20 % N₂. Two horizontal lines are inserted to guide the eyes. The metal loss from Pt in O₂ show a linear decrease in mass, while the other measurements do not and are influenced by uncertainties. The experiments were performed using a NETZSCH STA 449 F1.

Table A1. Overview of the different perovskites with Pt which attempted to synthesize. The theoretical t -factor and qualitative analysis of the XRD of each sample are provided. The pyrochlore cif-file used to analyze the sample containing Y_2PtO_7 was of $Nd_2Pt_2O_7$ collected from Zabel *et al.* [159].

	t -factor*	Phases present and comment
LaNiO ₃	0.97	Phase pure LaNiO ₃
La ₂ NiPtO ₆	0.92	La ₂ NiPtO ₆ and small quantities of Pt-metal
La ₂ CoPtO ₆	0.91	La ₂ CoPtO ₆ and small quantities of Pt-metal
La ₂ FePtO ₆	0.90	Perovskite and large quantities of Pt-metal. Some Nd ₂ O ₃ .
Nd ₂ NiPtO ₆	0.88	Nd ₂ NiPtO ₆ and small quantities of Pt-metal
Nd ₂ CoPtO ₆	0.87	Nd ₂ CoPtO ₆ and small quantities of Pt-metal
Nd ₂ FePtO ₆	0.86	Perovskite and large quantities of Pt-metal. Some Nd ₂ O ₃ .
Y ₂ NiPtO ₆	0.83	Y ₂ O ₃ , NiO, Pt metal. Broader peak for Pt-metal than normal.
Y ₂ FePtO ₆	0.82	Pyrochlore (Y ₂ Pt ₂ O ₇) with some Fe at the Pt site (13 %), YFeO ₃ also present. Very little Pt-metal (1-2 %)
Y ₂ CoPtO ₆	0.81	Pyrochlore (Y ₂ Pt ₂ O ₇) with some Fe at the Pt site (17 %), YCoO ₃ also present. Very little Pt-metal (< 1 %)
LaSrNiPtO ₆	0.95	Perovskite with La ₂ O ₃ , NiO and Pt metal impurities. Impurities with Sr are not identified, but may be present.
LaSrCoPtO ₆	0.93	Perovskite with La ₂ O ₃ , Co ₃ O ₄ and Pt metal impurities. Impurities with Sr are not identified, but may be present.
LaSrFePtO ₆	0.93	Perovskite with 7 wt. % Pt. Low intensity of the ordering-peak at $Q = 1.38 \text{ \AA}^{-1}$, narrow main perovskite peak. No other impurities are observed.
YSrCoPtO ₆	0.91	Pt and Y-rich Pyrochlore (Y ₂ Pt ₂ O ₇) with 10-13 % Co and 12 % Sr from the refinements (home lab XRD data). SrCO ₃ and Co ₂ O ₃ impurities.
YSrFePtO ₆	0.90	Mainly Pt-metal, Y ₂ O ₃ (possibly with some Pt to form a pyrochlore), SrCO ₃ .

Table A2. Calculations of volume relations for $YM_{0.50}Rh_{0.50}O_3$. The ionic radii are collected from [133] and the cell volumes of the samples are collected from the ICSP data base at FIZ Karlsruhe [175]: LuRhO₃ [176], TbRhO₃ [123], YCoO₃ [177], YFeO₃ [178], YNiO₃ (P21/n) [179], YNiO₃ (Pnma, 653K) [88]. r is the radius of the indicated element and $c(A)$ is the coordination number of the A -cation. *The volume of YRhO₃ is estimated from the volume of LuRhO₃ and TbRhO₃.

Literature	Volume [\AA^3]	$r(A)$ [\AA]	$c(A)$ [\AA]	$r(B(III))$ [\AA]	$r(B(II)/B(IV))$
LuRhO ₃	220.85	1.032	9	0.665	
TbRhO ₃	230.17	1.095	9	0.665	
YRhO ₃ (est. *)	223.23	1.075	9	0.665	
YCoO ₃	205.04	1.075	9	0.610	0.6375
YFeO ₃	223.84	1.075	9	0.645	0.6825
Samples	Volume [\AA^3]	$r(A)$ [\AA]	$c(A)$ [\AA]	$r(B(III))$ [\AA]	$r(B(II)/B(IV))$
YFe _{0.50} Rh _{0.50} O ₃	227.2	1.075	9	0.655	0.69
YCo _{0.50} Rh _{0.50} O ₃	218.8	1.075	9	0.6375	0.6725
	Vol. calc. +III/+III [\AA^3]	Vol. calc. +II/+IV [\AA^3]	Degree of +III/+III	Degree of +II/+IV	
YFe _{0.50} Rh _{0.50} O ₃	223.54	235.48	69%	31%	
YCo _{0.50} Rh _{0.50} O ₃	214.14	225.89	60%	40%	

Appendix

Table A3. Atomic positions for $\text{YFe}_{0.50}\text{Rh}_{0.50}\text{O}_3$ (top) and $\text{YCo}_{0.50}\text{Rh}_{0.50}\text{O}_3$ (bottom) in space group *Pnma* obtained from Rietveld refinements using Topas [162]. Unit cell parameters are provided in Table 9.

Site	Element	Wyckoff site	x	y	z	Occupancy
Y	Y	4	0.432	0.25	0.018	1
Fe	Fe	4	0	0	0	0.5
Fe	Rh	4	0	0	0	0.5
O1	O	4	0.538	0.25	0.610	1
O2	O	8	0.194	0.058	0.307	1

Site	Element	Wyckoff site	x	y	z	Occupancy
Y	Y	4	0.423	0.25	0.019	1
Co	Co	4	0	0	0	0.5
Co	Rh	4	0	0	0	0.5
O1	O	4	0.548	0.25	0.618	1
O2	O	8	0.194	0.058	0.307	1

Table A4. List of chemicals used for syntheses of perovskite oxides.

Compound	Purity \geq [%]	Producer
La_2O_3	99.99	MolyCorp
Nd_2O_3	-	MolyCorp
Y_2O_3	99.9	Sigma-Aldrich
$\text{Sr}(\text{NO}_3)_2$	99.0	Sigma-Aldrich
$\text{Ni}(\text{NO}_3)_2 \times 6\text{H}_2\text{O}$	99.99	Sigma-Aldrich
$\text{Co}(\text{NO}_3)_2 \times 6\text{H}_2\text{O}$	98	Sigma-Aldrich
$\text{Fe}(\text{NO}_3)_2 \times 9\text{H}_2\text{O}$	99.99	Sigma-Aldrich
$\text{Rh}(\text{NO}_3)_2 \times x\text{H}_2\text{O}$	36 % trace metal basis	Sigma-Aldrich
Pt metal	99.9	Heraeus
Citric acid Monohydrate	98	Sigma-Aldrich

References

1. Hunt, L.B., *The Ammonia Oxidation Process for Nitric Acid Manufacture*. Platinum Metals Review, 1958. **2**(4): p. 129-134.
2. Brightling, J., *Ammonia and the fertiliser industry: The development of ammonia at Billingham*. Johnson Matthey technology review, 2018. **62**(1): p. 32-47.
3. Farcau, B.W., *The Ten-Cents War; Chile, Peru, and Bolivia in the War of the Pacific, 1879-1884*. 2000: Praeger Publishers. ISBN: 0-275-96925-8.
4. Franco, M.G.O.y. *Chincha guano islands*. Available from: https://commons.wikimedia.org/wiki/File:Chincha_guano_islands.JPG.
5. Connor, H., *Manufacture of nitric acid. Role of platinum alloy gauzes in the ammonia oxidation process*. Platinum Met. Rev., 1967. **11**(2): p. 60-9.
6. Smil, V., *Enriching the earth : Fritz Haber, Carl Bosch, and the transformation of world food production*. 2001, Cambridge, Mass: MIT Press. ISBN: 026219449X.
7. Hager, T., *The alchemy of air : a Jewish genius, a doomed tycoon, and the scientific discovery that fed the world but fueled the rise of Hitler*. 2008, New York: Harmony. ISBN: 978-0-307-4999-3.
8. BASF Corporate History, Ludwigshafen a.Rh./Germany. Web page: <https://www.basf.com/global/en/who-we-are/history/chronology.html>.
9. Olsen, K.A. and hydro, N., *Norsk Hydro gjennom 50 år : et eventyr fra realitetenes verden: 1905-1955*. 1955: Norsk Hydro.
10. Statistics Norway. 2021; Available from: <https://www.ssb.no/energi-og-industri/artikler-og-publikasjoner/vi-bruker-mindre-strom-hjemme>.
11. Yara, 2021, accessed on 30.06.21. Available from: <https://eng.heroya-industripark.no/about-hip/the-companies-in-the-industrial-park/yara-porsgrunn>.
12. Roser, M. and Ritchie, H. *Fertilizers*. 2013; Available from: <https://ourworldindata.org/fertilizers>.
13. Warner, M., *The Kinetics of Industrial Ammonia Combustion*. University of Sidney, 2013. PhD Thesis.
14. Hannevold, L., *Reconstruction of noble-metal catalysts during oxidation of ammonia*. University of Oslo, 2005. PhD Thesis.
15. Heywood, A.E., *Platinum Recovery in Ammonia Oxidation Plants*. Platinum Metals Review, 1973. **17**(4): p. 118-129.
16. Holzmann, H., *Platinum Recovery in Ammonia Oxidation Plants*. Platinum Metals Review, 1969. **13**(1): p. 2-8.
17. Holzmann, H., *Platin-Rückgewinnung bei der NH₃-Verbrennung an Platin/Rhodium-Netzkatalysatoren*. Chemie Ingenieur Technik, 1968. **40**(24): p. 1229-1237.
18. Hatfield, R.W., Beshty, B.S., Lee, H.C., Heck, R.M., and Hsiung, T.H., *Method for recovering platinum in a nitric acid plant*. 1994. Patent. EP0077121. Engelhard Corporation.
19. Nirisen, Ø., Waller, D., and Brackenbury, D.M., *The Development of a N₂O Abatement Catalyst: from Laboratory Scale to Plant Testing*. Topics in catalysis, 2018. **62**(17-20): p. 1113-1125.
20. Fjellvåg, A.S., *Struktur-egenskapsrelasjoner til perovskittoksidene LaNi_{1-x}M_xO₃, M = Rh, Pt og deres funksjon som katalysator for dekomponering av lystgass*. Master thesis, 2016, Department of Chemistry, University of Oslo.
21. Heywood, A.E., *Recovery of platinum from ammonia oxidation catalysts*. Platinum Metals Review, 1982. **26**(1): p. 28-32.

References

22. Fierro, J., Palacios, J., and Tomas, F., *Characterization of catalyst and catchment gauzes used in medium- and low-pressure ammonia oxidation plants*. Journal of Materials Science, 1992. **27**(3): p. 685-691.
23. Fierro, J.L.G., Palacios, J.M., and Tomás, F., *Morphological and chemical changes in palladium alloy gauzes used for platinum recovery in high-pressure ammonia oxidation plants*. Surface and Interface Analysis, 1989. **14**(9): p. 529-536.
24. Fierro, J.L.G., Palacios, J.M., and Tomás, F., *Redistribution of Platinum Metals within an Ammonia Oxidation Plant*. Platinum Metals Review, 1990. **34**(2): p. 62-70.
25. Ning, Y. and Yang, Z., *Platinum loss from alloy catalyst gauzes in nitric acid plants: The important role of the palladium component in metal capture during ammonia oxidation*. Platinum Metals Review, 1999. **43**(2): p. 62-69.
26. Ning, Y., Yang, Z., and Zhao, H., *Platinum recovery by palladium alloy catchment gauzes in nitric acid plants: The mechanism of platinum recovery*. Platinum Metals Review, 1996. **40**(2): p. 80-87.
27. Ning, Y., Yang, Z., and Zhao, H., *Structure Reconstruction in Palladium Alloy Catchment Gauzes*. Platinum Metals Review, 1995. **39**(1): p. 19-26.
28. Yang, Z., Ning, Y., and Zhao, H., *Changes of composition and surface state of palladium-nickel alloy gauzes used in ammonia oxidation apparatus*. Journal of Alloys and Compounds, 1995. **218**(1): p. 51-57.
29. Pura, J., Garbacz, H., Zdunek, J., Mizera, J., Gierej, M., and Laskowski, Z., *Analysis of two catalytic systems PtRhPd-PdAu and PtRh-PdAu after long-term exploitation*. Inżynieria Materiałowa, 2013. **4**(194): p. 358-362.
30. Pura, J., Kwaśniak, P., Jakubowska, D., Jaroszewicz, J., Zdunek, J., Garbacz, H., Mizera, J., Gierej, M., and Laskowski, Z., *Investigation of degradation mechanism of palladium-nickel wires during oxidation of ammonia*. Catalysis Today, 2013. **208**(Supplement C): p. 48-55.
31. Pura, J., Wicinski, P., Kwasniak, P., Zwolinska, M., Garbacz, H., Zdunek, J., Laskowski, Z., and Gierej, M., *Investigation of the degradation mechanism of catalytic wires during oxidation of ammonia process*. Appl. Surf. Sci., 2016. **388**(Part_B): p. 670-677.
32. Han, F. and Liu, X., *Comparison of Pt catchment between two Pd alloy in nitric acid catalyst gauze*. Guijinshu, 2017. **38**(1): p. 31-35.
33. Ivanovic, A., Trumic, B., Ivanov, S., Marjanovic, Sr., Zrilic, M.M., Volkov-Husovic, T., and Petkovic, B., *Optimisation of the Recrystallisation Annealing Regime of Pd-5Ni Alloy Using experimental design and statistical analysis to understand the metallurgical properties of palladium alloy for ammonia oxidation catchment gauze applications*, in Johns. Matthey Technol. Rev. 2016. p. 31-38.
34. Rdzawski, Z., Ciura, L., and Nikiel, B., *Metallographic examination of catalyst gauzes and catchment gauzes from platinum and palladium alloys*. Journal of Materials Processing Tech., 1995. **53**(1): p. 319-329.
35. Bishop, D.C. and Heywood, A.E., *Catchment packs*. 1988. Patent. CA 1240305, 469743. Canada.
36. McGrath, R.B. and Horner, B.T., *Catchment device for platinum recovery*. 1994. Patent. EP0 611 041 A1.
37. Waller, D., Brackenbury, D.M., and Evjedal, K., *Method and device for catchment of platinum group metals in a gas stream*. 2008. Patent. WO2008030106A1, Copyright (C) 2015 American Chemical Society (ACS). All Rights Reserved.: p. 17pp. Yara International Asa, Norway.
38. Holzmann, H., *Recovery of noble metals which are volatilized during catalytic reactions*. 1969. Patent. 3434826.

39. Beshty, B.S., Hatfield, R.W., Lee, H.C., Heck, R.M., and Hsiung, T.H., *Method for recovering platinum in a nitric acid plant*. 1985. Patent. 4526614, 6/403,997. Engelhard Corporation. USA.
40. Rudorfer, H., Wagner, A., Prammer, F., and Klausner, F., *Device For The Recovery Of Noble Metals*. 1977. Patent. 4022581, 05/653626. Chemie Linz Aktiengesellschaft. United States of America.
41. Stephenson, D.J., *Recovery Of Precious Metal*. 1985. Patent. 4511539, 06/590546.
42. Atkins, P.W. and Shriver, D.F., *Shriver & Atkins' inorganic chemistry*. 5th ed. 2010, Oxford: Oxford University Press. ISBN: 9780199236176.
43. Salman, A.u.R., Enger, B.C., Auvray, X., Lødeng, R., Menon, M., Waller, D., and Rønning, M., *Catalytic oxidation of NO to NO₂ for nitric acid production over a Pt/Al₂O₃ catalyst*. Applied Catalysis A: General, 2018. **564**: p. 142-146.
44. Bagot, P.A.J., Kruska, K., Haley, D., Carrier, X., Marceau, E., Moody, M.P., and Smith, G.D.W., *Oxidation and Surface Segregation Behavior of a Pt–Pd–Rh Alloy Catalyst*. The Journal of Physical Chemistry C, 2014. **118**(45): p. 26130-26138.
45. Bergene, E., Tronstad, O., and Holmen, A., *Surface Areas of Pt–Rh Catalyst Gauzes Used for Ammonia Oxidation*. Journal of Catalysis, 1996. **160**(2): p. 141-147.
46. Ivashenko, O., Johansson, N., Pettersen, C., Jensen, M., Zheng, J., Schnadt, J., and Sjøstad, A.O., *How Surface Species Drive Product Distribution during Ammonia Oxidation: An STM and Operando APXPS Study*. ACS Catalysis, 2021. **11**(13): p. 8261-8273.
47. Chmielarz, L. and Jabłońska, M., *Advances in selective catalytic oxidation of ammonia to dinitrogen: a review*. RSC Advances, 2015. **5**(54): p. 43408-43431.
48. Zakharchenko, N.I., *Recovery of platinum with calcium oxide sorbent in ammonia oxidation*. Russ. J. Appl. Chem., 2002. **75**(3): p. 402-407.
49. Chernyshov, V.I. and Kisil, I.M., *Platinum metals catalytic systems in nitric acid production. System optimization in non-concentrated acid plants*. Platinum Met. Rev., 1993. **37**(3): p. 136-43.
50. Ouchetto, K., Archaimbault, F., Choynet, J., and Et-Tabirou, M., *New ordered and distorted perovskites: the mixed platinates Ln₂MPtO₆ (Ln = La, Pr, Nd, Sm, Eu, Gd; M = Mg, Co, Ni, Zn)*. Mater. Chem. Phys., 1997. **51**(2): p. 117-124.
51. Kojima, T., Nomura, K., Miyazaki, Y., and Tanimoto, K., *Synthesis of Various LaMO₃ Perovskites in Molten Carbonates*. Journal of the American Ceramic Society, 2006. **89**(12): p. 3610-3616.
52. Sileo, E.E., Jobbágy, M., Paiva-Santos, C.O., and Regazzoni, A.E., *Thermal Decomposition of Crystalline Ni^{II}–Cr^{III} Layered Double Hydroxide: A Structural Study of the Segregation Process*. J. Phys. Chem. B, 2005. **109**(20): p. 10137-10141.
53. Tilley, R.J.D., *Understanding solids : the science of materials*. 2nd ed. 2013, Chichester: Wiley. ISBN: 9781118423288.
54. West, A.R., *Solid state chemistry and its applications*. 1984, Chichester: Wiley. ISBN: 0471903779.
55. Hull, A.W., *X-Ray Crystal Analysis of Thirteen Common Metals*. Physical Review, 1921. **17**(5): p. 571-588.
56. Hull, A.W., *A New Method of X-Ray Crystal Analysis*. Physical Review, 1917. **10**(6): p. 661-696.
57. Kittel, C. and McEuen, P., *Introduction to solid state physics*. 8th ed. 2005, Hoboken, N.J: Wiley. ISBN: 9780471415268.
58. Smithells, C.J., *Smithells metals reference book*. 8th ed. Metals reference book, ed. T.C. Totemeier and W.F. Gale. 2004, Amsterdam, Boston: Elsevier Butterworth-Heinemann. ISBN: 9780750675093.

References

59. Rakhtsaum, G., *Platinum Alloys: A Selective Review of the Available Literature*. Platinum Metals Review, 2013. **57**(3): p. 202-213.
60. Okamoto, H. and Massalski, T.B., *The Au–Pd (Gold-Palladium) system*. Bulletin of alloy phase diagrams, 1985. **6**(3): p. 229-235.
61. Chee, S.W., Wong, Z.M., Baraissov, Z., Tan, S.F., Tan, T.L., and Mirsaidov, U., *Interface-mediated Kirkendall effect and nanoscale void migration in bimetallic nanoparticles during interdiffusion*. Nature Communications, 2019. **10**(1): p. 2831.
62. Baheti, V.A., Ravi, R., and Paul, A., *Interdiffusion study in the Pd–Pt system*. Journal of Materials Science: Materials in Electronics, 2013. **24**(8): p. 2833-2838.
63. Zacharaki, E., Beato, P., Tiruvalam, R.R., Andersson, K.J., Fjellvåg, H., and Sjøstad, A.O., *From Colloidal Monodisperse Nickel Nanoparticles to Well-Defined Ni/Al₂O₃ Model Catalysts*. Langmuir, 2017. **33**(38): p. 9836-9843.
64. Haugrud, R., *On the high-temperature oxidation of nickel*. Corrosion Science, 2003. **45**: p. 211-235.
65. Anandprakash, K.P., *Effect of Tammann Temperature and Relative Humidity on Lead Chromate and Magnesium-Based Compositions*. Defence Science Journal, 1998. **48**: p. 303-308.
66. Liu, P.S. and Chen, G.F., *Chapter Two - Making Porous Metals*, in *Porous Materials*, P.S. Liu and G.F. Chen, Editors. 2014, Butterworth-Heinemann: Boston. p. 21-112.
67. Neukam, O., *Diffusionsüberzüge*. Galvanotechnik, 1970. **61**.
68. Debonte, W.J. and Poate, J.M., *Low temperature interdiffusion in the Au-Pd and Au-Rh thin film couples*. Thin Solid Films, 1975. **25**(2): p. 441-448.
69. Murakami, M., deFontaine, D., and Fodor, J., *X - ray diffraction study of interdiffusion in bimetallic Au/Pd thin films*. Journal of Applied Physics, 1976. **47**(7): p. 2850-2856.
70. Raub, E. and Wörwag, G., *Die Gold-Platin-Palladium-Legierungen*. Zeitschrift für Metallkunde, 1955. **46**(7): p. 513-515.
71. Kubaschewski, O. and Counsell, J.F., *Thermodynamische Eigenschaften des Systems Gold-Platin-Palladium*. Monatshefte für Chemie / Chemical Monthly, 1971. **102**(6): p. 1724-1728.
72. van Dal, M.J.H., Pleumeekers, M.C.L.P., Kodentsov, A.A., and van Loo, F.J.J., *Intrinsic diffusion and Kirkendall effect in Ni–Pd and Fe–Pd solid solutions*. Acta Materialia, 2000. **48**(2): p. 385-396.
73. Neumann, G., *Self-diffusion and impurity diffusion in pure metals : handbook of experimental data*. 1st ed, ed. C. Tuijn. Vol. v. 14. 2009, Amsterdam, Boston, London: Pergamon. ISBN: 9786611796242.
74. Greenwood, N.N., *Chemistry of the elements*. 2nd ed. ed, ed. A. Earnshaw. 1997, Amsterdam: Elsevier Butterworth-Heinemann. ISBN: 0750633654.
75. Dey, S., Bhattacharjee, S., Bose, R.S., and Ghosh, C.K., *Room temperature synthesis of hydrated nickel(III) oxide and study of its effect on Cr(VI) ions removal and bacterial culture*. Applied Physics A, 2015. **119**(4): p. 1343-1354.
76. Mukai, K., Sugiyama, J., Ikedo, Y., Aoki, Y., Andreica, D., and Amato, A., *Structural and Magnetic Nature for Fully Delithiated Li_xNiO₂: Comparative Study between Chemically and Electrochemically Prepared Samples*. The Journal of Physical Chemistry C, 2010. **114**(18): p. 8626-8632.
77. Li, D., Lee, K., Wang, B.Y., Osada, M., Crossley, S., Lee, H.R., Cui, Y., Hikita, Y., and Hwang, H.Y., *Superconductivity in an infinite-layer nickelate*. Nature, 2019. **572**(7771): p. 624-627.

78. Xu, Z., Jin, L., Backhaus, J.-K., Green, F., and Hayward, M.A., *Hole and Electron Doping of Topochemically Reduced Ni(I)/Ru(II) Insulating Ferromagnetic Oxides*. Inorganic Chemistry, 2021. **60**(19): p. 14904-14912.
79. Zhang, J., Chen, Y.-S., Phelan, D., Zheng, H., Norman, M.R., and Mitchell, J.F., *Stacked charge stripes in the quasi-2D trilayer nickelate $La_4Ni_3O_8$* . Proceedings of the National Academy of Sciences, 2016. **113**(32): p. 8945.
80. Crespin, M., Isnard, O., Dubois, F., Choynet, J., and Odier, P., *LaNiO₂: Synthesis and structural characterization*. Journal of Solid State Chemistry, 2005. **178**(4): p. 1326-1334.
81. Crespin, M., Levitz, P., and Gatineau, L., *Reduced forms of LaNiO₃ perovskite. Part 1.—Evidence for new phases: La₂Ni₂O₅ and LaNiO₂*. Journal of the Chemical Society, Faraday Transactions 2: Molecular and Chemical Physics, 1983. **79**(8): p. 1181-1194.
82. Carrillo, C., Johns, T.R., Xiong, H., DeLaRiva, A., Challa, S.R., Goeke, R.S., Artyushkova, K., Li, W., Kim, C.H., and Datye, A.K., *Trapping of Mobile Pt Species by PdO Nanoparticles under Oxidizing Conditions*. The Journal of Physical Chemistry Letters, 2014. **5**(12): p. 2089-2093.
83. Chen, X., Schwank, J.W., Fisher, G.B., Cheng, Y., Jagner, M., McCabe, R.W., Katz, M.B., Graham, G.W., and Pan, X., *Nature of the two-step temperature-programmed decomposition of PdO supported on alumina*. Applied Catalysis A: General, 2014. **475**: p. 420-426.
84. Lundgren, E., Gustafson, J., Mikkelsen, A., Andersen, J.N., Stierle, A., Dosch, H., Todorova, M., Rogal, J., Reuter, K., and Scheffler, M., *Kinetic Hindrance during the Initial Oxidation of Pd(100) at Ambient Pressures*. Physical Review Letters, 2004. **92**(4): p. 046101.
85. Kim, S.-J., Lemaux, S., Demazeau, G., Kim, J.-Y., and Choy, J.-H., *LaPdO₃: The First PdIII Oxide with the Perovskite Structure*. J. Am. Chem. Soc., 2001. **123**(42): p. 10413-10414.
86. Panin, R.V., Khasanova, N.R., Abakumov, A.M., Antipov, E.V., Van Tendeloo, G., and Schnelle, W., *Synthesis and crystal structure of the palladium oxides NaPd₃O₄, Na₂PdO₃ and K₃Pd₂O₄*. Journal of Solid State Chemistry, 2007. **180**(5): p. 1566-1574.
87. Matar, S.F., Demazeau, G., Möller, M.H., and Pöttgen, R., *Electronic structure and equation of state of PdO₂ from ab initio*. Chemical Physics Letters, 2011. **508**(4): p. 215-218.
88. Alonso, J.A., Martínez-Lope, M.J., Casais, M.T., García-Muñoz, J.L., Fernández-Díaz, M.T., and Aranda, M.A.G., *High-temperature structural evolution of RNiO₃ (R = Ho, Y, Er, Lu) perovskites: Charge disproportionation and electronic localization*. Physical Review B, 2001. **64**(9): p. 094102.
89. Jursic, I. and Rudtsch, S., *Thermal Stability of β -PtO₂ Investigated by Simultaneous Thermal Analysis and Its Influence on Platinum Resistance Thermometry*. International Journal of Thermophysics, 2014. **35**(6): p. 1055-1066.
90. Siegel, S., Hoekstra, H.R., and Tani, B.S., *The crystal structure of beta-platinum dioxide*. Journal of Inorganic and Nuclear Chemistry, 1969. **31**(12): p. 3803-3807.
91. Schwartz, K.B. and Prewitt, C.T., *Structural and electronic properties of binary and ternary platinum oxides*. Journal of Physics and Chemistry of Solids, 1984. **45**(1): p. 1-21.
92. Martin, N.M., Nilsson, J., Skoglundh, M., Adams, E.C., Wang, X., Velin, P., Smedler, G., Raj, A., Thompsett, D., Brongersma, H.H., Grehl, T., Agostini, G., Mathon, O., Carlson, S., Norén, K., Martinez-Casado, F.J., Matej, Z., Balmes, O., and Carlsson, P.-A., *Characterization of Surface Structure and Oxidation/Reduction Behavior of Pd–Pt/Al₂O₃ Model Catalysts*. The Journal of Physical Chemistry C, 2016. **120**(49): p. 28009-28020.
93. Shirako, Y., Wang, X., Tsujimoto, Y., Tanaka, K., Guo, Y., Matsushita, Y., Nemoto, Y., Katsuya, Y., Shi, Y., Mori, D., Kojitani, H., Yamaura, K., Inaguma, Y., and Akaogi, M., *Synthesis, Crystal Structure, and Electronic Properties of High-Pressure PdF₂-Type Oxides MO₂ (M = Ru, Rh, Os, Ir, Pt)*. Inorganic Chemistry, 2014. **53**(21): p. 11616-11625.

References

94. Hylland, K.T., Schmidtke, I.L., Wragg, D.S., Nova, A., and Tilset, M., *Synthesis of substituted (N,C) and (N,C,C) Au(III) complexes: the influence of sterics and electronics on cyclometalation reactions*. Dalton Transactions, 2022. **51**(13): p. 5082-5097.
95. Shi, H., Asahi, R., and Stampfl, C., *Properties of the gold oxides Au₂O₃ and Au₂O: First-principles investigation*. Physical Review B, 2007. **75**(20): p. 205125.
96. Moore, W.J. and Pauling, L., *The Crystal Structures of the Tetragonal Monoxides of Lead, Tin, Palladium, and Platinum*. Journal of the American Chemical Society, 1941. **63**(5): p. 1392-1394.
97. Hoekstra, H.R., Siegel, S., and Gallagher, F.X., *Reaction of Platinum Dioxide with Some Metal Oxides*, in *Platinum Group Metals and Compounds*. 1971, American Chemical Society. p. 39-53.
98. Range, K.J., Rau, F., Klement, U., and Heyns, A.M., *β -PtO₂: High pressure synthesis of single crystals and structure refinement*. Materials Research Bulletin, 1987. **22**(11): p. 1541-1547.
99. Muller, O. and Roy, R., *Formation and stability of the platinum and rhodium oxides at high oxygen pressures and the structures of Pt₃O₄, β -PtO₂ and RhO₂*. Journal of the Less Common Metals, 1968. **16**(2): p. 129-146.
100. Momma, K. and Izumi, F., *VESTA 3 for three-dimensional visualization of crystal, volumetric and morphology data*. J. Appl. Cryst, 2011. **44**(6): p. 1272-1276.
101. Li, T., Marquis, E.A., Bagot, P.A.J., Tsang, S.C., and Smith, G.D.W., *Characterization of oxidation and reduction of a platinum–rhodium alloy by atom-probe tomography*. Catalysis Today, 2011. **175**(1): p. 552-557.
102. Li, T., Bagot, P.A.J., Marquis, E.A., Tsang, S.C.E., and Smith, G.D.W., *Characterization of Oxidation and Reduction of a Palladium–Rhodium Alloy by Atom-Probe Tomography*. The Journal of Physical Chemistry C, 2012. **116**(7): p. 4760-4766.
103. Li, T., Bagot, P.A.J., Marquis, E.A., Edman Tsang, S.C., and Smith, G.D.W., *Atomic engineering of platinum alloy surfaces*. Ultramicroscopy, 2013. **132**: p. 205-211.
104. Hilaire, L., Guerrero, G.D., Légaré, P., Maire, G., and Krill, G., *A photoemission study of the oxidation of platinum in Pt-based alloys: Pt-Pd, Pt-Ru, Pt-Ir*. Surface Science, 1984. **146**(2): p. 569-582.
105. Farrauto, R.J., Lampert, J.K., Hobson, M.C., and Waterman, E.M., *Thermal decomposition and reformation of PdO catalysts; support effects*. Applied Catalysis B: Environmental, 1995. **6**(3): p. 263-270.
106. Chin, Y.-H., García-Diéguez, M., and Iglesia, E., *Dynamics and Thermodynamics of Pd–PdO Phase Transitions: Effects of Pd Cluster Size and Kinetic Implications for Catalytic Methane Combustion*. The Journal of Physical Chemistry C, 2016. **120**(3): p. 1446-1460.
107. Jehn, H., *High Temperature Behaviour of Platinum Group Metals in Oxidizing Atmospheres*. Journal of the Less-Common Metals, 1984. **100**: p. 321-339.
108. Alcock, C.B. and Hooper, G.W., *Thermodynamics of the Gaseous Oxides of the Platinum-Group Metals*. Proc. R. Soc. Lond. A, 1960. **254**(1279): p. 551-561.
109. Opila, E.J., *Unpublished work*. University of Virginia.
110. Gegner, J., Hörz, G., and Kirchheim, R., *Diffusivity and solubility of oxygen in solid palladium*. Full Set - Includes 'Journal of Materials Science Letters', 2009. **44**(9): p. 2198-2205.
111. Kondarides, D.I. and Verykios, X.E., *Interaction of Oxygen with Supported Ag–Au Alloy Catalysts*. Journal of Catalysis, 1996. **158**(2): p. 363-377.
112. Goodenough, J.B., Cooper, S.L., Egami, T., and Zhou, J.S., *Localized to Itinerant Electronic Transition in Perovskite Oxides*. 2001: Springer-Verlag Berlin and Heidelberg GmbH & Co. KG. ISBN: 978-3-540-45503-5.

113. Tilley, R.J.D., *Perovskites: Structure-Property Relationships*. 2016: Wiley. ISBN: 978-1-118-93566-8.
114. Abramov, Y.A., Tsirelson, V.G., Zavodnik, V.E., Ivanov, S.A., and Brown, I.D., *The chemical bond and atomic displacements in SrTiO₃ from X-ray diffraction analysis*. Acta Cryst. B, 1995. **51**(6): p. 942-951.
115. Li, B., Louca, D., Yano, S., Marshall, L.G., Zhou, J., and Goodenough, J.B., *Insulating Pockets in Metallic LaNiO₃*. Advanced Electronic Materials, 2016. **2**(2): p. 1500261.
116. Zhou, J.S., Marshall, L.G., and Goodenough, J.B., *Mass enhancement versus Stoner enhancement in strongly correlated metallic perovskites: LaNiO₃ and LaCuO₃*. Physical Review B, 2014. **89**(24): p. 245138.
117. Guan, L., Liu, B., Jin, L., Guo, J., Zhao, Q., Wang, Y., and Fu, G., *Electronic structure and optical properties of LaNiO₃: First-principles calculations*. Solid State Commun., 2010. **150**(41-42): p. 2011-2014.
118. Rajeev, K.P., Shivashankar, G.V., and Raychaudhuri, A.K., *Low-temperature electronic properties of a normal conducting perovskite oxide (LaNiO₃)*. Solid State Communications, 1991. **79**(7): p. 591-595.
119. Garcia-Munoz, J.L., Rodriguez-Carvajal, J., Lacorre, P., and Torrance, J.B., *Neutron-diffraction study of RNiO₃ (R = La, Pr, Nd, Sm): electronically induced structural changes across the metal-insulator transition*. Phys. Rev. B: Condens. Matter, 1992. **46**(8): p. 4414-25.
120. Zhou, J.S. and Goodenough, J.B., *Chemical bonding and electronic structure of RNiO₃, R= rare earth*. Physical Review B, 2004. **69**(15): p. 153105.
121. Lacorre, P., Torrance, J.B., Pannetier, J., Nazzari, A.I., Wang, P.W., and Huang, T.C., *Synthesis, crystal structure, and properties of metallic praseodymium nickel oxide (PrNiO₃): comparison with metallic neodymium nickel oxide (NdNiO₃) and semiconducting samarium nickel oxide (SmNiO₃)*. J. Solid State Chem., 1991. **91**(2): p. 225-37.
122. Zinkevich, M., Solak, N., Nitsche, H., Ahrens, M., and Aldinger, F., *Stability and thermodynamic functions of lanthanum nickelates*. Journal of Alloys and Compounds, 2007. **438**(1): p. 92-99.
123. Macquart, R.B., Smith, M.D., and zur Loye, H.-C., *Crystal Growth and Single-Crystal Structures of RERhO₃ (RE = La, Pr, Nd, Sm, Eu, Tb) Orthorhoidites from a K₂CO₃ Flux*. Crystal Growth & Design, 2006. **6**(6): p. 1361-1365.
124. Battle, P.D. and Vente, J.F., *Structural and Magnetic Characterization of La₂NiRhO₆*. J. Solid State Chem., 1999. **146**(1): p. 163-167.
125. Schinzer, C., *Spin-glass behavior of disordered perovskite LaNi_{1/2}Rh_{1/2}O₃*. J. Alloys Compd., 1999. **288**(1-2): p. 65-75.
126. Smith, A.E., Sleight, A.W., and Subramanian, M.A., *Electrical and magnetic properties of new rhodium perovskites: La₂MRhO₆, M=Cr, Fe, Cu*. Mater. Res. Bull., 2010. **45**(4): p. 460-463.
127. Shibasaki, S., Takahashi, Y., and Terasaki, I., *Thermoelectric properties of LaRh_{1-x}Ni_xO₃*. J. Phys.: Condens. Matter, 2009. **21**(11): p. 115501/1-115501/4.
128. Vasala, S. and Karppinen, M., *A₂B' B'' O₆ perovskites: A review*. Progress in Solid State Chemistry, 2015. **43**(1-2): p. 1-36.
129. Rao, C.N.R., Parkash, O.M., and Ganguly, P., *Electronic and magnetic properties of LaNi_{1-x}Co_xO₃, LaCo_{1-x}Fe_xO₃ and LaNi_{1-x}Fe_xO₃*. Journal of Solid State Chemistry, 1975. **15**(2): p. 186-192.
130. Asai, K., Sekizawa, H., Mizushima, K., and Iida, S., *Magnetic Properties of LaNi_{1-x}Co_xO₃ (0 ≤ x ≤ 0.5)*. Journal of the Physical Society of Japan, 1977. **43**(3): p. 1093-1094.

References

131. Bakke, I.M.B., *Struktur og magnetiske egenskaper til de perovskittliknende oksidene $ACo_{0.5}B_{0.5}O_3$ ($A = Y, La, Nd$; $B = Ti, Fe, Ni$)*. University of Oslo, 2018. Master thesis.
132. Li, J., Smith, A.E., Kwong, K.-S., Powell, C., Sleight, A.W., and Subramanian, M.A., *Lattice crossover and mixed valency in the $LaCo_{1-x}Rh_xO_3$ solid solution*. Journal of Solid State Chemistry, 2010. **183**(6): p. 1388-1393.
133. Shannon, R.D., *Revised effective ionic radii and systematic studies of interatomic distances in halides and chalcogenides*. Acta Crystallographica Section A, 1976. **32**(5): p. 751-767.
134. Lee, S., Lee, M.-C., Ishikawa, Y., Miao, P., Torii, S., Won, C., Lee, K., Hur, N., Cho, D.-Y., and Kamiyama, T., *Crystal and Magnetic Structures of La_2CoPtO_6 Double Perovskite*. ACS Omega, 2018. **3**(9): p. 11624-11632.
135. Beale, A.M., Jacques, S.D.M., Di Michiel, M., Mosselmans, J.F.W., Price, S.W.T., Senecal, P., Vamvakeros, A., and Paterson, J., *X-ray physico-chemical imaging during activation of cobalt-based Fischer-Tropsch synthesis catalysts*. Philos Trans A Math Phys Eng Sci, 2018. **376**(2110): p. 20170057-20170057.
136. Price, S.W.T., Geraki, K., Ignatyev, K., Witte, P.T., Beale, A.M., and Mosselmans, J.F.W., *In Situ Microfocus Chemical Computed Tomography of the Composition of a Single Catalyst Particle During Hydrogenation of Nitrobenzene in the Liquid Phase*. Angewandte Chemie International Edition, 2015. **54**(34): p. 9886-9889.
137. Price, S.W.T., Martin, D.J., Parsons, A.D., Sławiński, W.A., Vamvakeros, A., Keylock, S.J., Beale, A.M., and Mosselmans, J.F.W., *Chemical imaging of Fischer-Tropsch catalysts under operating conditions*. Science Advances, 2017. **3**(3): p. e1602838.
138. Sottmann, J., Di Michiel, M., Fjellvåg, H., Malavasi, L., Margadonna, S., Vajeeston, P., Vaughan, G.B.M., and Wragg, D.S., *Chemical Structures of Specific Sodium Ion Battery Components Determined by Operando Pair Distribution Function and X-ray Diffraction Computed Tomography*. Angewandte Chemie International Edition, 2017. **56**(38): p. 11385-11389.
139. Jørgensen, P.S., Ebbenhøj, S.L., and Hauch, A., *Triple phase boundary specific pathway analysis for quantitative characterization of solid oxide cell electrode microstructure*. Journal of Power Sources, 2015. **279**: p. 686-693.
140. Trini, M., De Angelis, S., Jørgensen, P.S., Hendriksen, P.V., Thornton, K., and Chen, M., *Towards the Validation of a Phase Field Model for Ni Coarsening in Solid Oxide Cells*. Acta Materialia, 2021. **212**: p. 116887.
141. Fjellvåg, A.S., Jørgensen, P.S., Waller, D., Wragg, D.S., Michiel, M.D., and Sjøstad, A.O., *Mechanism of grain reconstruction of Pd and Pd/Ni wires during Pt-catchment*. Materialia, 2022. **21**: p. 101359.
142. Goldstein, J.I., Newbury, D.E., Michael, J.R., Ritchie, N.W.M., Scott, J.H.J., and Joy, D.C., *Scanning Electron Microscopy and X-Ray Microanalysis*. 4th ed. 2017, New York: Springer. ISBN: 978-1-4939-6676-9.
143. Williams, D.B. and Carter, C.B., *Transmission Electron Microscopy: A Textbook for Materials Science*. 2nd ed. 2009, Boston: Springer. ISBN: 978-0-387-76502-0.
144. Geels, K., *Metallographic and Materialographic Specimen Preparation, Light Microscopy, Image Analysis and Hardness Testing*. 2006, ASTM International. ISBN: 9780803142657.
145. Kakihana, M., Okubo, T., Arima, M., Uchiyama, O., Yashima, M., Yoshimura, M., and Nakamura, Y., *Polymerized Complex Synthesis of Perovskite Lead Titanate at Reduced Temperatures: Possible Formation of Heterometallic (Pb,Ti)-Citric Acid Complex*. Chemistry of Materials, 1997. **9**(2): p. 451-456.
146. Als-Nielsen, J. and McMorrow, D., *Elements of modern X-ray physics*. 2nd ed. 2011, Oxford: Wiley-Blackwell. ISBN: 0-470-97395-1.

147. Willis, B.T.M., *Experimental neutron scattering*, ed. C.J. Carlile. 2009, Oxford: Oxford University Press. ISBN: 9780198519706.
148. Hessevik, J., Fjellvåg, A.S., Iveland, O., By, T., Skjelstad, J., Waller, D., Fjellvåg, H., and Sjøstad, A.O., *LaNiO₃ as a Pt catchment material in the ammonia oxidation process*. *Materials Today Communications*, 2022. **33**: p. 104084.
149. Fjellvåg, A.S., Sjøstad, A.O., Waller, D., and Skjelstad, J., *Grain Reconstruction of Pd and Pd/Ni Alloys for Platinum Catchment*. *Johnson Matthey Technology Review*, 2019. **63**(4).
150. Kawamura, K., Kajino, T., Nanko, M., and Maruyama, T., *Oxygen Permeability in Gold by Internal Oxidation of Gold Alloy*. *Electrochemical Society Proceedings*, 2003. **16**.
151. Chen, G., Guan, G., Kasai, Y., and Abudula, A., *Nickel volatilization phenomenon on the Ni-CGO anode in a cathode-supported SOFC operated at low concentrations of H₂*. *Int. J. Hydrogen Energy*, 2012. **37**(1): p. 477-483.
152. Håkonsen, S.F., Holme, B., and Waller, D., *An investigation of the limiting factors for Pt catchment in the Ostwald process*. To be published, 2022.
153. The MathWorks Inc., *Matlab*. [9.7.0.1247435 (2019b)].
154. Antolini, E., *Palladium in fuel cell catalysis*. *Energy & Environmental Science*, 2009. **2**(9): p. 915-931.
155. Lervold, S., Arnesen, K., Beck, N., Lødeng, R., Yang, J., Bingen, K., Skjelstad, J., and Venvik, H.J., *Morphology and Activity of Electrolytic Silver Catalyst for Partial Oxidation of Methanol to Formaldehyde Under Different Exposures and Oxidation Reactions*. *Topics in Catalysis*, 2019. **62**(7): p. 699-711.
156. Lee, M.-C., Sohn, C.H., Kim, S.Y., Lee, K.D., Won, C.J., Hur, N., Kim, J.Y., Cho, D.-Y., and Noh, T.W., *Stabilization of ferromagnetic ordering in cobaltite double perovskites of La₂CoIrO₆ and La₂CoPtO₆*. *Journal of Physics: Condensed Matter*, 2015. **27**(33): p. 336002.
157. Seinen, P.A., van Berkel, F.P.F., Groen, W.A., and Ijdo, D.J.W., *The ordered perovskite system Ln₂NiRuO₂*. *Materials Research Bulletin*, 1987. **22**(4): p. 535-542.
158. Meneghini, C., Ray, S., Liscio, F., Bardelli, F., Mobilio, S., and Sarma, D.D., *Nature of "Disorder" in the Ordered Double Perovskite Sr₂FeMoO₆*. *Physical Review Letters*, 2009. **103**(4): p. 046403.
159. Zabel, M., Rau, F., Steiner, C., and Range, K.J., *Crystal structure of neodymium platinum oxide (2/2/7), Nd₂Pt₂O₇*. *Zeitschrift für Kristallographie - Crystalline Materials*, 1997. **212**(2): p. 137-137.
160. Smrčok, L., *Rietveld refinement of Y₂O₃ using the Pearson VII profile shape function*. *Crystal Research and Technology*, 1989. **24**(6): p. 607-611.
161. Piir, I.V., Sekushin, N.A., Grass, V.E., Ryabkov, Y.I., Chezhina, N.V., Nekipelov, S.V., Sivkov, V.N., and Vyalikh, D.V., *Bismuth manganese titanate: Crystal structure and properties*. *Solid State Ionics*, 2012. **225**: p. 464-470.
162. Coelho, A.A., *TOPAS and TOPAS-Academic: an optimization program integrating computer algebra and crystallographic objects written in C++*. *Journal of Applied Crystallography*, 2018. **51**(1): p. 210-218.
163. Topwal, D., Sarma, D.D., Kato, H., Tokura, Y., and Avignon, M., *Structural and magnetic properties of Sr₂Fe_{1+x}Mo_{1-x}O₆ (1 ≤ x ≤ 0.25)*. *Physical Review B*, 2006. **73**(9): p. 094419.
164. Fjellvåg, A.S., Fjellvåg, Ø.S., Breard, Y., and Sjøstad, A.O., *Structural disorder and antiferromagnetism in LaNi_{1-x}Pt_xO₃*. *Journal of Solid State Chemistry*, 2021. **299**: p. 122181.

References

165. Barton, P.T., Seshadri, R., and Rosseinsky, M.J., *Electrical and magnetic properties of the complete solid solution series between SrRuO₃ and LaRhO₃: Filling t_{2g} versus tilting*. Phys. Rev. B: Condens. Matter Mater. Phys., 2011. **83**(6): p. 064417/1-064417/8.
166. Alonso, J.A., García-Muñoz, J.L., Fernández-Díaz, M.T., Aranda, M.A.G., Martínez-Lope, M.J., and Casais, M.T., *Charge Disproportionation in RNiO₃ Perovskites: Simultaneous Metal-Insulator and Structural Transition in YNiO₃*. Physical Review Letters, 1999. **82**(19): p. 3871-3874.
167. Fjellvåg, A.S., Fjellvåg, Ø.S., Kumar, S., Ruud, A., and Sjøstad, A.O., *Interplay of valence states and magnetic interactions in the perovskite system LaNi_{1-x}Rh_xO₃*. Journal of Solid State Chemistry, 2021. **298**: p. 122124.
168. Sadykov, V.A., Isupova, L.A., Zolotarskii, I.A., Bobrova, L.N., Noskov, A.S., Parmon, V.N., Brushtein, E.A., Telyatnikova, T.V., Chernyshev, V.I., and Lunin, V.V., *Oxide catalysts for ammonia oxidation in nitric acid production: properties and perspectives*. Applied Catalysis A: General, 2000. **204**(1): p. 59-87.
169. Stenzel, A., Fähsing, D., Schütze, M., and Galetz, M.C., *Volatilization kinetics of chromium oxide, manganese oxide, and manganese chromium spinel at high temperatures in environments containing water vapor*. Materials and Corrosion, 2019. **70**(8): p. 1426-1438.
170. Meschter, P.C., Opila, E.J., and Jacobson, N.S., *Water Vapor Mediated Volatilization of High Temperature Materials*. Annual Review of Materials Research, 2013. **43**: p. 559-88.
171. Johnson Matthey. Accessed on 12.06.22; Available from: platinum.matthey.com.
172. Woodward, P.M., Karen, P., Evans, J.S.O., and Vogt, T., *Solid State Materials Chemistry*. 2021, Cambridge: Cambridge University Press. ISBN: 9780521873253.
173. Velho, L.R. and Bartlett, R.W., *Diffusivity and solubility of oxygen in platinum and Pt-Ni alloys*. Metallurgical and Materials Transactions B, 1972. **3**(1): p. 65-72.
174. Toole, F.J. and Johnson, F.M.G., *The Solubility of Oxygen in Gold and in Certain Silver-Gold Alloys*. The Journal of Physical Chemistry, 1933. **37**(3): p. 331-346.
175. Bergerhoff, G. and Brown, I.D., *Crystallographic Databases*. F. H. Allen et al. (Hrsg.) Chester, International Union of Crystallography, 1987.
176. Yi, W., Liang, Q., Matsushita, Y., Tanaka, M., Hu, X., and Belik, A.A., *Crystal structure and properties of high-pressure-synthesized BiRhO₃, LuRhO₃, and NdRhO₃*. Journal of Solid State Chemistry, 2013. **200**: p. 271-278.
177. Knizek, K., Jirak, Z., Hejtmanek, J., Veverka, M., Marysko, M., Hauback, B.C., and Fjellvåg, H., *Structure and physical properties of YCoO₃ at temperatures up to 1000 K*. Phys. Rev. B: Condens. Matter Mater. Phys., 2006. **73**(21): p. 214443/1-214443/6.
178. du Boulay, D., Maslen, E.N., Streltsov, V.A., and Ishizawa, N., *A synchrotron x-ray study of the electron density in YFeO₃*. Acta Crystallogr., Sect. B: Struct. Sci., 1995. **B51**(6): p. 921-9.
179. Alonso, J.A., Martínez-Lope, M.J., Casais, M.T., García-Muñoz, J.L., and Fernández-Díaz, M.T., *Room-temperature monoclinic distortion due to charge disproportionation in RNiO₃ perovskites with small rare-earth cations (R = Ho, Y, Er, Tm, Yb, and Lu): A neutron diffraction study*. Physical Review B, 2000. **61**(3): p. 1756-1763.

Paper I



I

Grain Reconstruction of Palladium and Palladium-Nickel Alloys for Platinum Catchment

A. S. Fjellvåg, D. Waller, J. Skjelstad, A. O. Sjøstad

Johnson Matthey Technology Review, **2019**, 63, (4), 236

I

Grain Reconstruction of Palladium and Palladium-Nickel Alloys for Platinum Catchment

Effects on metal alloy composition at surface and in bulk when operated as a platinum catchment unit during high temperature ammonia oxidation

A. Slagtern Fjellvåg[#]

Centre for Materials Science and Nanotechnology, Department of Chemistry, University of Oslo, PO box 1126, Blindern, 0318 Oslo, Norway

D. Waller

Yara Technology Center, Herøya Research Park, Building 92, Hydrovegen 67, 3936 Porsgrunn, Norway

J. Skjelstad

K. A. Rasmussen, Birkebeinervegen 24, 2316 Hamar, Norway

A. Olafsen Sjøstad*

Centre for Materials Science and Nanotechnology, Department of Chemistry, University of Oslo, PO box 1126, Blindern, 0318 Oslo, Norway

Email: *a.o.sjastad@kjemi.uio.no,
[#]a.s.fjellvag@smn.uio.no

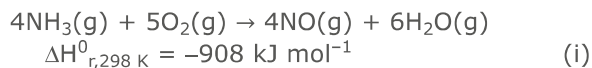
Platinum-rhodium gauzes are frequently used to catalyse the high temperature ammonia oxidation step for production of synthetic nitrogen-based fertilisers. The gauzes suffer from Pt loss in the form of platinum dioxide (PtO₂), due to the highly exothermic nature of the oxidation reaction. Industrially this is mitigated by installing one or more palladium-nickel catchment gauzes directly downstream of the combustion gauzes, to capture the lost Pt. The Pd-Ni catchment gauzes undergo severe structural modification during operation. In this study, we undertake a systematic study in a laboratory-scale furnace system to determine the role of each of the constituent gases O₂, H₂O and

PtO₂ on the structural changes of the Pd-Ni gauzes. In addition, some samples are exposed to real industrial conditions in an ammonia combustion pilot plant reactor. Fresh and spent catchment gauzes are analysed by means of scanning electron microscopy (SEM), energy dispersive X-ray spectroscopy (EDX), thermogravimetric analysis (TGA) and inductively coupled plasma mass spectroscopy/optical emission spectroscopy (ICP-MS/OES). By combining analysis of samples from furnace and pilot scale experiments, the main findings are that Pd-Ni gauzes undergo internal oxidation to nickel(II) oxide (NiO); which in the presence of steam results in Ni depletion and that PtO₂ vapour causes severe grain reconstruction. Furthermore, in laboratory-scale experiments no significant Pd loss is observed, which is in contrast to observations from the pilot plant where the samples are exposed to real post-ammonia oxidation conditions. Pd loss is likely attributed to some gas species contained in the real post-ammonia oxidation gas stream.

Introduction

Ammonia oxidation is one of the key reaction steps in the production of synthetic nitrogen-based fertilisers. Industrially, the reaction is typically carried out at 900°C and a pressure of 1–13 bar over metallic Pt-Rh catalytic gauzes (1). During operation, the Pt-Rh catalyst undergoes several structural changes, such as grain growth of the wire core, surface formation of so-called cauliflowers and enrichment of Rh on the wire surface, due to a significant loss of Pt (2, 3). The Pt is mainly lost as gaseous PtO₂ and it is anticipated to be caused by hot spots on the Pt-Rh gauze due to the extreme

exothermic nature of the oxidation of ammonia to NO (2) (selectivity ~96% (1)), Equation (i) (4):



Depending on plant conditions, the Pt loss is in the range of 0.05–0.4 g per tonne nitric acid (HNO₃) produced i.e., noble metal loss in a modern plant producing on average 1000 tonnes HNO₃ per day, represents a huge financial cost for the fertiliser industry (1). State of the art technology to reduce this cost proceeds *via* catchment of the formed PtO₂ vapour by Pd-Ni alloy gauzes, located just downstream of the Pt-Rh ammonia oxidation catalyst. The predecessor of this catchment technology, a palladium-gold (80:20 wt%) alloy gauze, was developed by Degussa in the late 1960s (5). The Pd-Au gauzes quickly outperformed other catchment systems, such as glass wool filters, Raschig rings and marble chips (6). Later, cheaper metals such as Ni and cobalt replaced Au in the Pd-Au alloy, as they gave an enhanced catchment efficiency in addition to lower costs (7). Still, the Pd-Ni catchment unit has several drawbacks. During operation, the Pd-Ni gauze wires reconstruct completely and swell in size. This results in a significant loss of mechanical strength and additionally, it is the dominant cause of a large pressure drop increase over the gauze pack during the campaign, see **Figure 1**. Furthermore, during operation, the gauze is depleted in Ni and depending on plant conditions, 0.2–0.4 g Pd is lost per gram Pt captured (6).

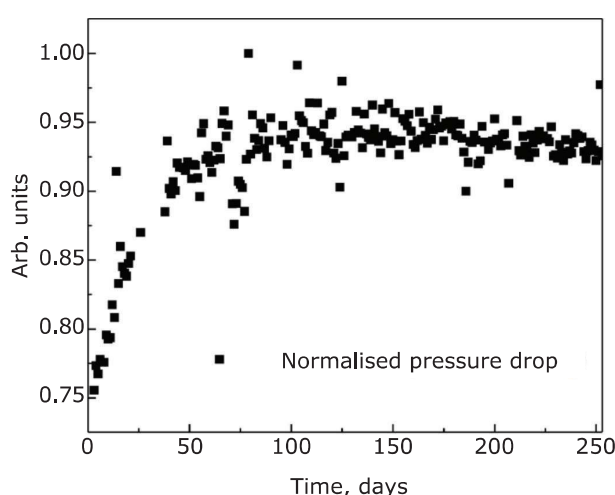


Fig. 1. Pressure drop from the Yara Technology Center industrial facility. Data points are normalised by dividing pressure by gas load to see the developing trend

Despite the fact that the aforementioned drawbacks of the Pd-Ni catchment system have been known for several decades, only a handful of studies related to this topic have been published in the last 50 years (5–18). Ning *et al.* (8) report on the surface reconstruction of the catchment gauze and both Fierro *et al.* (9) and Ning *et al.* (10) discuss the catchment mechanisms. Recently, Pura *et al.* (11) suggested that the alloying element Ni is not participating in the catchment process, but that grain boundary attack may be a mechanism responsible for grain reconstruction. This was further investigated by Pura *et al.* (18) suggesting that a rapid loss of Ni from grain boundaries causes the initial porosity in the wire. Still, sufficient understanding of the occurring reactions is not achieved and knowledge on how to improve or modify the Pd-Ni based catchment systems is still lacking. The common denominator between all the mentioned investigations is that they are based on gauzes used in industrial operation, where several different parameters such as temperature and gas composition are in play simultaneously. To the best of our knowledge, no or only minor focus has been put on systematic, single-parameter studies to unravel the underlying reasons for the grain reconstruction phenomena.

Here we report the results of systematic studies to understand the role of the individual constituents of the reaction gas mixture (O₂, H₂O and PtO₂ diluted in N₂) in the reconstruction of Pd-Ni gauzes, at conditions relevant for high-temperature ammonia oxidation. By exposing pure Pd and Pd-Ni wires and woven gauzes in a laboratory-scale furnace to the individual gas components in a systematic manner, we investigate which gas species cause reconstruction. We will also discuss the role of Ni with respect to Pt catchment, Ni loss and the existing Ni species during operation (metal, oxide and hydroxide). Finally, we compare the laboratory-scale results with two samples treated in a pilot plant at the Yara Technology Center facility (Herøya, Norway), where the samples experience the real conditions of high temperature ammonia oxidation in terms of gas mixture, linear gas velocity, temperature and pressure.

Experimental

Wires and woven gauzes of the industrial alloys Pd-Ni (95:5 wt%) and pure Pd were supplied by K. A. Rasmussen (wire diameters of 76 μm and 120 μm) which were used for the laboratory-scale experiments. In addition, pure Pd catchment gauzes

(76 μm) were used in pilot plant experiments with a pure Pt net and a lanthanum cobaltite (LaCoO_3)-based ammonia oxidation catalyst, the latter in the form of 3 mm cylindrical pellets. For the laboratory-scale furnace experiments, samples were heat treated in a six-zone furnace at 900–1050°C (ambient pressure) in a quartz tube (inner diameter = 6 mm) in various gas atmospheres containing synthetic air (5.0, Praxair, USA), steam and PtO_2 vapour. The composition of the water vapour mixture was 33 vol% H_2O , 14 vol% O_2 and 53 vol% N_2 . PtO_2 vapour was generated from a rolled up Pt gauze (~ 0.4 – 0.8 g) located upstream of the sample at 1050°C, producing a $p(\text{PtO}_2)$ of approximately 1×10^{-8} bar (2.5 mg Pt loss over 20 days in a flow of 1 l air per min). During heat treatment, samples were positioned perpendicular to the length direction of the quartz tube to enhance gas exposure to the gauze and wire in the gas flow. Samples from the Yara pilot plant were treated at 900°C and 5 bar in a gas mixture containing 10 vol% NH_3 in compressed air, before the ammonia oxidation combustion catalyst. This implies that the gas mixture contained approximately 9 vol% NO , 15 vol% H_2O and 6 vol% O_2 , 2000 ppm or 100 ppm N_2O (pure Pt or oxide catalyst) and the rest N_2 when exposed to the catchment alloy. The pilot plant samples were exposed to exactly the same conditions as industrial catchment gauzes and are compared with laboratory-scale samples (as described above) and industrial samples treated at 900°C at 5 bar for 47 days below an industrial Pt-Rh (95:5 wt%) catalyst in the industrial gas mixture (10 vol% NH_3 in compressed air).

Various sample surfaces and cross-sections were examined with a high-resolution Hitachi Regulus 8230 field-emission scanning electron microscope (FE-SEM). Images were obtained by collecting the secondary electrons produced by the electron beam with an acceleration voltage of 1 kV. Qualitative EDX analysis (mapping and point quantification) was performed on selected samples using an acceleration voltage of 30 kV. Samples were mounted with carbon tape on a copper plate or prepared for cross-section imaging by casting the wire in a conducting resin (PolyFast, Struers, UK) before grinding and polishing (1 μm diamond finish). Wet chemical etching of the polished sample was performed in HNO_3 (heat-treated gauze) or aqua regia (unreacted gauze) for 30 seconds at room temperature. Light microscopy was performed with a Zeiss Axio metallurgical microscope. ICP-MS/OES analysis was performed on selected samples by SINTEF Molab AS (Norway). Prior to analysis

samples were fully dissolved in aqua regia. The Pt content was determined by ICP-MS whereas Pd and Ni concentrations were determined by ICP-OES. The standard deviation was in the range of 1–2% of the measured value.

TGA was conducted with a NETZSCH (Germany) STA 449 F1 Jupiter[®], with an alumina TG-pin stage. The experiments were performed by stacking six (6) fresh Pd-Ni (or Pd) gauzes on top of each other and heating to 140°C to remove humidity and other surface species on the sample. Thereafter, the sample was ramped to 900°C ($10^\circ\text{C min}^{-1}$) before a 24 h dwell. After the experiment was completed, the same setup and temperature program was rerun with a fully oxidised sample for the background correction. In all experiments O_2 (5.0) and N_2 (5.0) from Praxair were used and the $p\text{O}_2$ was 0.2 bar over the sample.

Results and Discussion

As-Received Palladium-Nickel and Palladium Catchment Gauzes

Prior to exposing the as-received Pd-Ni and Pd wires to any gases, SEM and EDX analysis was performed on both wire surfaces and their cross-sections. In **Figure 2**, representative overview images of the wire surface (**Figure 2(a)**) and the cross-section (**Figure 2(b)**) of the 120 μm Pd-Ni alloy are shown. Overall, EDX analysis confirms the cross-sections of the alloys to contain minute quantities of oxygen, with slightly enhanced amounts at the surface, see **Table I**. In addition, EDX analysis of three randomly selected points on the Pd-Ni cross-section reveal the Ni content to be in the range from 4.4–5.0 wt%, close to the value provided by the supplier. EDX mapping did not reveal any obvious heterogeneities or impurities, neither within the grains nor along the grain boundaries. Based on this we conclude the Pd-Ni alloy to be a homogeneous solid-solution, of $\sim 95:5$ wt% Pd-Ni, within the uncertainty of the EDX analysis. Finally, it should be noted that light microscopy of chemically etched cross-sections reveal sharp grain boundaries and a grain size of 5–20 μm for 76 μm wires, of both Pd and the Pd-Ni alloy, see **Figure 2(c)** for the Pd-Ni alloy.

Effect of Oxygen

When the metallic Pd-Ni gauze (wire diameter 76 μm) is exposed to air in the TGA instrument at 900°C for 24 h, a mass gain of 1.47 wt% is

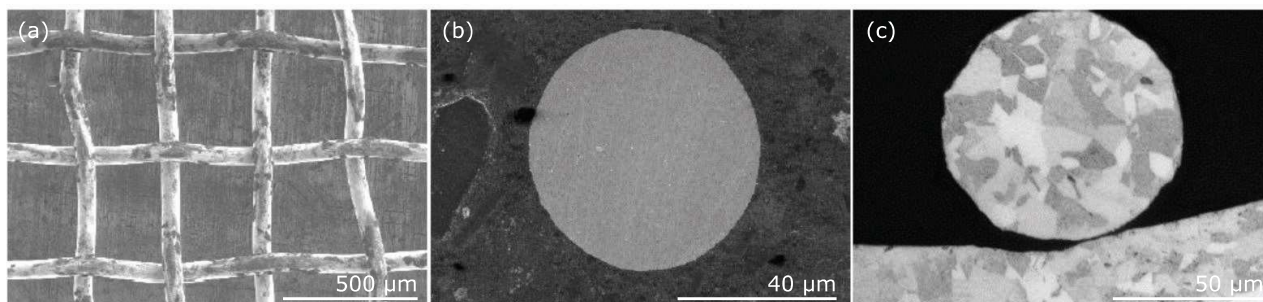


Fig. 2. (a) SEM image of the surface of a fresh 120 µm Pd-Ni wire; (b) SEM image of the cross-section of a fresh 120 µm Pd-Ni wire; (c) light microscope image of a 76 µm Pd-Ni wire after etching in aqua regia for 30 s

Table I Qualitative EDX Results of Fresh 120 µm Pd and Pd-Ni (95:5 wt%) Alloys

Sample	Area	Details	Pd, wt%	Ni, wt%	O, wt%
Pd-Ni	Surface	Large area	91.3	4.4	4.3
Pd-Ni	Cross section	Point, centre	95.0	5.0	0.0
Pd-Ni	Cross section	Point near centre	94.9	5.1	0.0
Pd-Ni	Cross section	Point off centre	94.5	4.4	1.1
Pd-Ni	Cross section	Point off centre	94.7	4.8	0.5
Pd	Surface	Large area	94.2	0.2 ^a	5.6
Pd	Cross section	Point, centre	100.0	0.0	0.0

^aPossibly overestimated value due to peak overlap between Ni and Cu (sample is mounted on Cu plate). Analysis certificate from K. A. Rasmussen shows a Ni content of <2 ppm in pure Pd wires

recorded, see **Figure 3(a)**. The observed mass gain is slightly larger than the theoretical value (1.36 wt%) for complete oxidation of Ni to NiO for a 95:5 wt% Pd-Ni alloy. When exposing the metallic Pd gauze to similar conditions, only a minor mass gain is observed (not shown). With reference to Ning *et al.* (10) and Gegner *et al.* (19), we assign the observed mass gain of the Pd gauze to a small oxygen solubility and formation of PdO on the Pd surface. The minor mass gain observed for pure Pd may indeed contribute in the slightly larger observed mass gain relative to theory for the Pd-Ni sample. The internal oxidation of the Pd-Ni alloy is shown visually in **Figure 3(b)–(d)**. Here, cross-sections of the Pd-Ni wire heated for 1 h and 4 h, analysed by SEM and EDX, show small precipitated particles approaching the wire centre with time. By EDX point analysis, the precipitated particles are found to consist of oxygen and nickel in an approximately 1:1 molar ratio, indicating NiO formation (**Figure 3(c)**).

As shown in **Figure 3(e)** and **Figure 3(f)**, chemical etching prior to SEM and EDX analysis reveals that the largest NiO precipitates are located

at the grain boundaries and that the grain size has increased to 10–30 µm. Additionally, the NiO precipitates are found at equal depth within the grains as in the grain boundaries, indicating that oxygen diffusion is approximately equally fast in grains and grain boundaries (**Figure 3(b)–(d)**). Notably, at the same time as oxygen diffuses towards the wire centre, EDX mapping show a distinct reduction in Ni concentration in the wire core (**Figure 3(b)–(d)**). EDX point analysis of the wire core indicate the Ni content to be 4.2 wt% and 2.7 wt% after 1 h and 4 h, respectively. This implies that during the oxidation process the Ni mobility is enhanced, causing a heterogeneous distribution of Ni with more NiO at the outer part of the wire. These observations coincide well with reports by Gegner *et al.* (19) on internal oxidation of alloys with a non-noble element in a solid solution with a more noble element. Finally, it should be noted that the initial grain growth is seen during the first 24 h, but no significant grain growth is observed after another 20–30 days of heat treatment (see Figure S1 in the Supplementary Information).

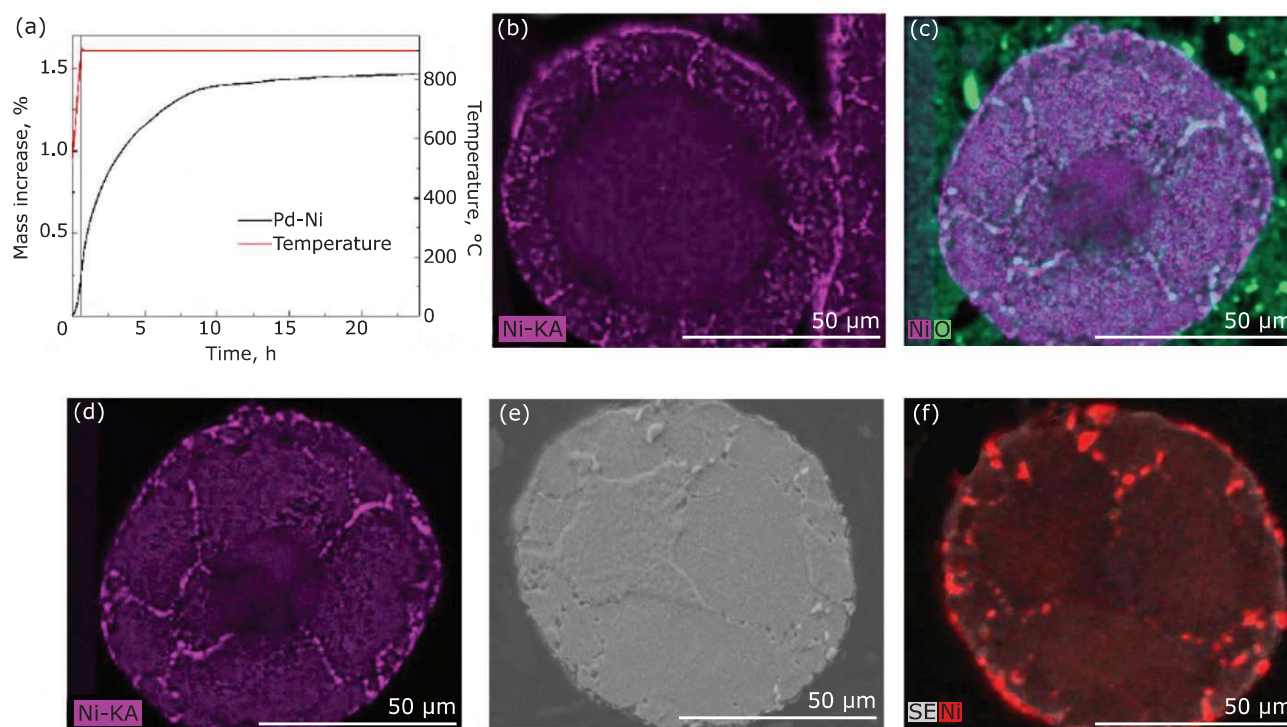


Fig. 3. (a) TGA of Pd-Ni gauze heated in air, heating rate $10^{\circ}\text{C min}^{-1}$ followed by a 24 h dwell at 900°C ; (b) EDX mapping of the Pd-Ni wire after 1 h exposure in the TGA experiment; (c)–(d) EDX mapping of the Pd-Ni wire after 4 h exposure in the TGA experiment; (e) SEM image of a $76\ \mu\text{m}$ Pd-Ni wire heated at 900°C for 30 days in a muffle furnace (air) and etched for 30 s in a HNO_3 before imaging; (f) EDX mapping of a $76\ \mu\text{m}$ Pd-Ni wire heated at 900°C for 30 days in a muffle furnace (air) and etched for 30 s in a HNO_3 before imaging

Palladium-Nickel Gauzes Exposed to Wet Air

When water vapour is included in the feed gas (wet air: 33 vol% H_2O , 14 vol% O_2 , 53 vol% N_2), the internal oxidation of Ni to NiO occurs in a similar manner as in dry air, see **Figure 4(a)**. However, based on gravimetry, the Pd-Ni gauze has lost 2.4 wt% of its initial mass after heat treatment for two weeks in wet air at 1050°C . ICP-MS analysis of the exposed gauze give a total Ni concentration of only 2.7 wt% relative to Pd, compared to 4.8 wt% on a comparable sample treated in dry air. In addition, SEM analysis reveal that the outer parts of the Pd-Ni wire is depleted in Ni (**Figure 4(b)**) and that some surface roughness has appeared (**Figure 4(c)**). The data also shows that only 0.1 wt% Pd is lost during two weeks' treatment in wet air; far below the industrial Pd loss observed during ammonia oxidation (see below). There is also no observed Pd loss in dry air. This correlates well with the work of Opila (20), which shows no Pd loss in wet or dry oxygen and Ar and other literature on Pd loss in dry air (21). Notably, these findings are in contradiction to the calculations of

Factsage (22, 23), which estimate a significant Pd loss as PdOH (22, 23) in wet gas and a smaller loss as PdO_2 and $\text{Pd}(\text{OH})_2$ (22, 23) (see Figure S2 in the Supplementary Information). This leads to the conclusion that the observed mass loss of Pd-Ni in wet air is due to NiO being hydrolysed by the wet air and forming volatile $\text{Ni}(\text{OH})_2$, which in turn causes Ni depletion. This observation is in line with Chen *et al.* (24).

Finally, after the two weeks' treatment in wet air the NiO precipitates are no longer seen at the grain boundaries. Unfortunately, chemical etching prior to SEM analysis has not revealed the exact position of the grain boundaries and thus the occurrence of grain growth is uncertain. In many ways the situation is similar to the grain growth observed during the initial oxidation process of Ni to NiO. During the initial oxidation, inwards/outwards diffusion of O-Ni increased the mobility of O-Ni, just as treatment in wet air may have increased Ni mobility by Ni diffusion towards the surface. The increased mobility may again contribute to grain growth. However, we are currently not in position to elaborate in detail on how grain growth is interwoven and connected to diffusion and the

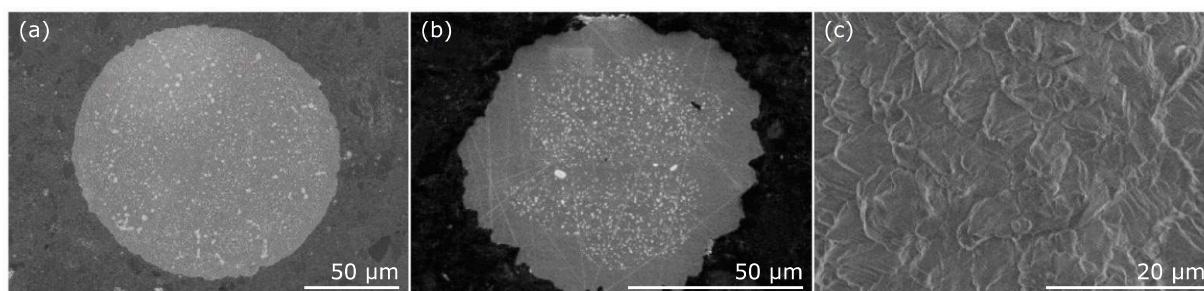


Fig. 4. (a) SEM image of the cross section of a Pd-Ni wire (120 μm) treated in wet air at 1050°C for 3 days; (b) cross section of a Pd-Ni gauze (76 μm) treated in wet air at 1050°C for 14 days; (c) surface of a Pd-Ni gauze (76 μm) treated in wet air at 1050°C for 14 days

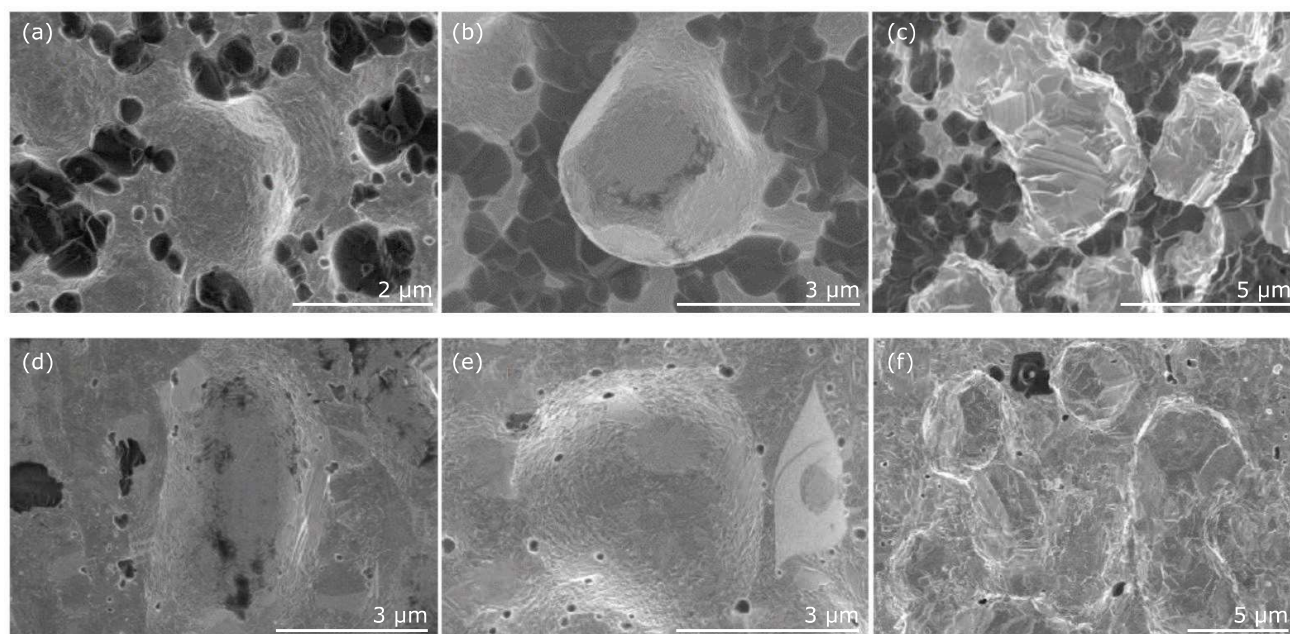


Fig. 5. SEM images of the Pd-Pt surface crystals observed on Pd-Ni (76 μm) gauzes after heat treatment at 1050°C in dry air with Pt upstream for: (a) 1 h; (b) 4 h; (c) 10 h. SEM images of the Pd-Pt surface crystals observed on Pd (120 μm) gauzes after heat treatment at 1050°C in dry air with Pt upstream for: (d) 1 h; (e) 4 h; (f) 10 h. The Pt content of the different Pd-Pt crystals are listed in [Table II](#)

oxidation process. We suggest this as a topic for future investigations.

Effect of Platinum Dioxide Vapour in Dry and Wet Air

The effect of exposing Pd and Pd-Ni wires to PtO_2 vapour in both dry and wet air is evaluated. First, we investigated if the presence of Ni in the catchment alloy would influence reactivity of PtO_2 toward Pd. Based on this, both materials were heat treated in dry air at 1050°C with Pt gauzes installed upstream. The results of exposing the two catchment materials to PtO_2 in dry air at 1 h, 4 h and 10 h are presented in [Figure 5](#). Both materials undergo an immediate

surface reaction and small Pd-Pt particles or crystals (size $\sim 2\text{--}3\ \mu\text{m}$) are already formed on the wire surfaces after 1 h exposure, as shown in [Figure 5\(a\)](#) and [Figure 5\(d\)](#). The crystals show roughness and have several small ladders on their sides, which increase in size from 4 h to 10 h ([Figure 5\(b\)–\(c\)](#) and [Figure 5\(e\)–\(f\)](#)). Notably, for Pd-Ni ([Figure 5\(a\)–\(c\)](#)), some smaller (1–2 μm) and more faceted crystals appear with a darker contrast in the SEM images. EDX mapping and point analysis of these crystals indicate NiO formation, in line with previous observations of Ni-oxidation in air. From the SEM images reported in [Figure 5](#), it appears as if Pd-Pt based crystals develop at a similar rate in both Pd-Ni and Pd ([Figure 5](#)). We

Table II Relative Increase in Wire Diameter and Qualitative EDX Results of Pt Concentrations in Pd-Pt Surface Crystals on Pd-Ni (120 μm) and Pure Pd (76 μm) Wires, After Heat Treatments at the Indicated Conditions^a

Temperature, °C	Time	Gas conditions	Wire swelling, %		Pt content, at %		Comment
			Pd-Ni	Pd	Pd-Ni	Pd	
1050	1 h	Dry air	–	–	1	–	Crystal as in Figure 5(a)
1050	4 h	Dry air	5	~0	–	6	On Pd-Pt crystal
1050	4 h	Dry air	–	–	–	4	Between Pd-Pt crystals
1050	10 h	Dry air	5	~0	3	4	On Pd-Pt crystals
1050	10 h	Dry air	–	–	–	2	Between Pd-Pt crystals
1050	16 h	Dry air	7	~0	12	–	Regular surface crystal
1050	1 d	Dry air	12	5	11	–	Regular surface crystal
1050	3 d	Dry air	25	15	15	19	Very exposed crystal ^b
1050	5 d	Dry air	37	25	14	14	Regular surface crystal
1050	10 d	Dry air	35–45	35	14	23	Regular surface crystal
1050	10 d	Dry air	–	–	28	41	Very exposed crystal ^b
1050	20 d	Dry air	45	45–60	16	22	Regular surface crystal
1050	20 d	Dry air	–	–	44	42	Very exposed crystal ^b
1050	30 d	Wet air	60–75	–	28	–	Regular surface crystal
900	19 d	Pilot plant, Pt catalyst	–	45–55	–	30	Regular surface crystal
900	19 d	Pilot plant, oxidation catalyst	–	45–60	–	0	Regular surface crystal
900	47 d	Industrial plant	–	45–50	30	–	Regular surface crystal

^aAll EDX measurements have an estimated uncertainty of ~10% of the measured value, while the values of swelling have an uncertainty of ~20% of the indicated value due to local variations in sample diameter

^bCrystal located on wire edge, making it subject to a large gas flow and PtO₂-concentration during laboratory scale experiments

therefore conclude that the NiO particles are not participating in the reconstruction and growth process of the Pd-Pt crystals.

With further heat treatment (≥ 1 day), the interior of the Pd and Pd-Ni wires become subject to the earliest stage of grain reconstruction and ladder-like growth, as if PtO₂ is penetrating sub surface from the formed Pt-Pd crystal layer reacting with more fresh metal on the wire, see **Figure 6(a)** and **Figure 6(b)**. At longer exposure time (≥ 3 days), the surface crystals show beautiful single crystal shapes. The ladders causing further crystal growth (from ~10–30 μm) are large, slowly growing over a face of an already existing crystal (**Figure 6(c)**). Prolonged exposure times (20 days) result in complete grain reconstruction to large surface crystals (~20–30 μm) (**Figure 6(d)–(f)**). The grain reconstruction and crystal formation also causes significant wire swelling; the wire diameter increases by up to 60% after 20 days, see **Figure 6(e)** and **Figure 6(f)** and **Table II**. Additionally, the grain reconstruction of the wire or gauze causes a significant reduction of mechanical strength.

Selected crystals on both the Pd-Ni and the Pd wires are analysed with respect to Pt content by means of EDX analysis and the results are summarised in **Table II**. Pt concentration in the average top-layered crystals increases rapidly the first day (~10–12 at%), followed by a slower accumulation. This observation goes hand in hand with the fact that the reconstruction starts to occur below the top layer of crystals, after one day on stream (**Figure 6(a)** and **Figure 6(b)**), indicating that Pt catchment is preferred on the Pd rich areas below the outermost Pd-Pt crystals. After 20 days on stream, the average surface crystals reach a Pt content of ~22 at% Pt, while the outermost exposed crystals reach a Pt content up to ~40 at% (65 wt%). This is similar to an industrial sample treated for 47 days, where the average Pd-Pt crystal on the wire surface has a Pt concentration of ~30 at%.

At this point it is worth commenting that the Pd-Pt crystal growth rate depends on how a specific part of the gauze or wire is directed toward the high velocity gas stream. The PtO₂ molecules have better access to such areas, which is reflected in a

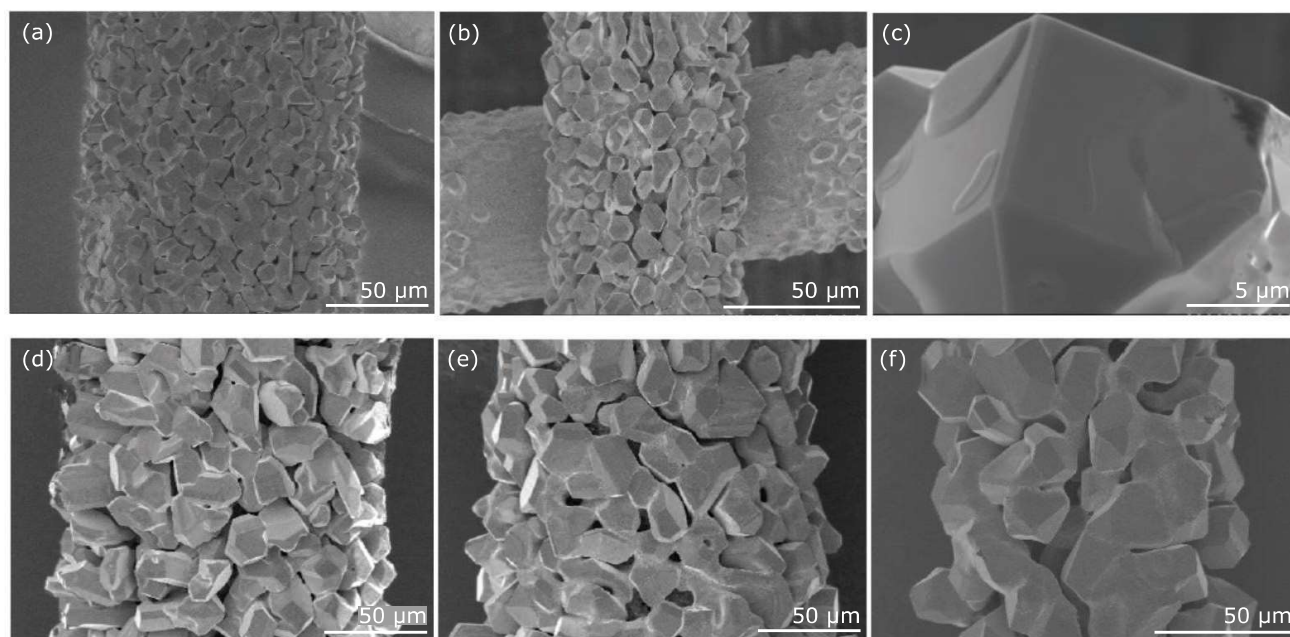


Fig. 6. SEM images of Pd (76 μm) and Pd-Ni (120 μm) gauzes heat treated at 1050°C with Pt upstream for 1–20 days: (a) Pd-Ni 1 day; (b) Pd 1 day; (c) Pd-Ni 3 days; (d) Pd-Ni 5 days; (e) Pd-Ni 20 days; (f) Pd 20 days

higher Pt content; more reconstruction and larger crystal facets (**Table II**). This is more prominent in laboratory-scale experiments, where the gas is not passing equally uniformly through the gauze as in the industrial or pilot plant. Correspondingly, on laboratory-scale samples, reconstruction is slower and Pt catchment lesser at the wire crossings and at the side(s) of the wire not directly exposed to the gas stream. These observations are applicable to both the Pd-Ni and the Pd catchment gauzes.

We can now combine the two previous experiments and perform a heat treatment with both wet air and PtO₂. If a Pd-Ni gauze is heated for two weeks at 1050°C in wet air with PtO₂, a mass increase of 6.5 wt% is observed. From ICP-MS/OES, the resulting Pd-Ni wire contains only 2.8 wt% Ni relative to Pd, at the same time as the gauze has reached a Pt content of 9.3 wt%. This indicates simultaneous Ni loss and Pt catchment. Furthermore, if the Pd-Ni gauze is heated for 30 days in total, the exterior of the wire becomes completely reconstructed, at the same time as the wire is almost fully depleted of Ni, see **Figure 7(a)** and **Figure 7(b)**. Only the wire core shows the presence of NiO particles. We therefore state that Ni-loss and grain reconstruction are individual effects, caused by the presence of water vapour and PtO₂, respectively.

Comparing with investigations by Pura *et al.* (18), we have also observed diffusion and segregation of NiO in the grain boundaries. However, this seems

not to cause grain reconstruction or porosity in dry or wet air. Our findings coincide well with the statement by Pura *et al.* (11), i.e. grain reconstruction is not caused by the presence of Ni or loss of Ni from the Pd-Ni alloy, but rather by catchment of Pt.

Pilot Scale Experiments – Testing at Industrial Conditions

Finally, two samples have been exposed in the ammonia oxidation pilot plant at the Yara Technology Center industrial facility. Here, NH₃ is included in the gas stream (10 vol% in air) and combusted over an ammonia oxidation catalyst just upstream of the catchment unit. Two scenarios were explored: (i) six pure Pt ammonia combustion gauzes and (ii) a bed of LaCoO₃-based ammonia oxidation catalyst pellets, positioned just upstream of a 76 μm pure Pd catchment gauze. As Ni does not significantly affect Pt catchment it was chosen to use pure Pd and not Pd-Ni gauzes in the pilot plant. The experiments were run for nineteen days at 900°C at total pressure of 5 bar, during which each combustion catalyst produced *ca.* 28 tonnes of nitric acid.

In the first case, when the ammonia oxidation catalyst was a pure Pt gauze, similar features occurred compared to samples heat-treated in the laboratory scale furnace in wet air with Pt upstream. This includes Pt catchment, grain

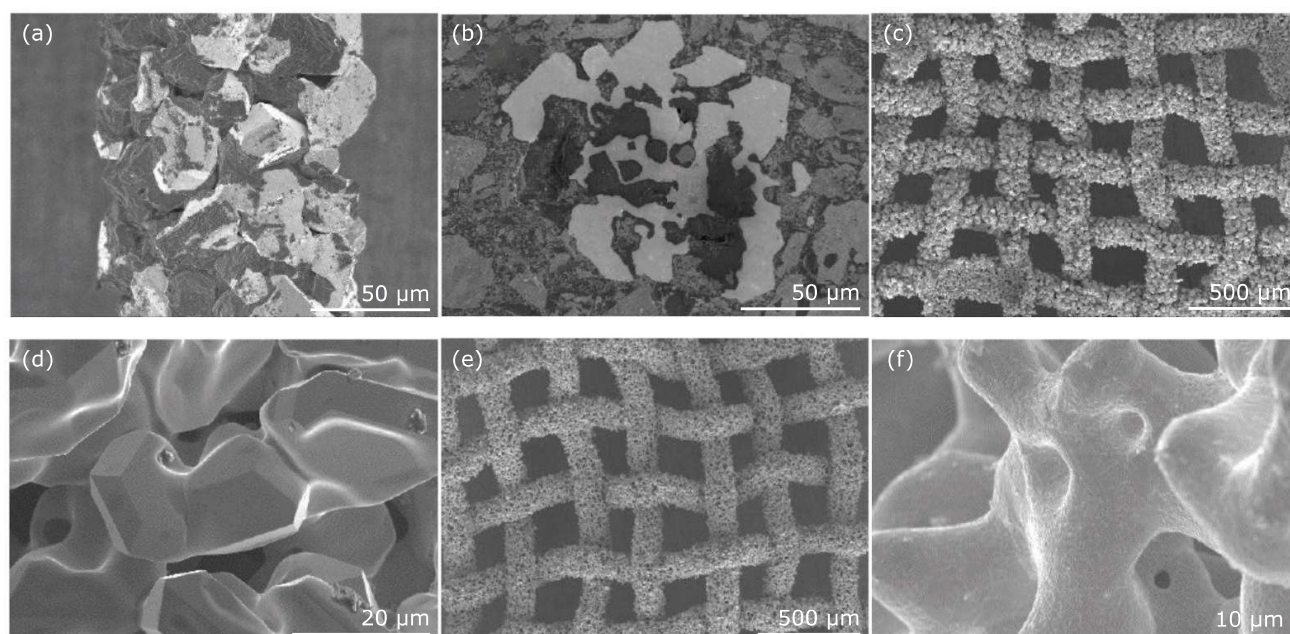


Fig. 7. SEM images of: (a) and (b) a Pd-Ni gauze (76 μm) heated for 30 days at 1050°C in wet air with PtO_2 ; (c) and (d) a Pd catchment gauze (76 μm) used in the pilot plant for 19 days with a pure Pt combustion catalyst at 900°C; (e) and (f) a Pd catchment gauze used in the pilot plant for 19 days with an LaCoO_3 -based combustion catalyst at 900°C

reconstruction and swelling, see **Figure 7(c)** and **Figure 7(d)**. The Pd-Pt crystals on the wire surface are in the range of 10–30 μm in size, with an average Pt concentration of ~ 30 at% (44 wt%), while the gauze in total had a Pt concentration of ~ 14 at% (23 wt%). The Pt concentration of the surface crystals obtained by EDX is similar to those found in samples treated in the laboratory scale furnace, confirming the validity of the laboratory scale experiments on Pt catchment. In contrast to our laboratory scale experiments, we now observe a significant Pd loss (0.036 g tonne^{-1} HNO_3), similar to reports by Holtzmann on Pd loss at real ammonia oxidation plant conditions (5).

In the second case, with the LaCoO_3 -based combustion catalyst, we can exclude effects by PtO_2 as it is not present in the gas stream. Still, the Pd catchment gauze is subject to swelling and pore formation, see **Figure 7(e)** and **Figure 7(f)**. However, the wire surface does not look similar to the Pd-Pt crystals observed previously (**Figure 7**) and there are no foreign elements present, hence there must be a different mechanism causing this pore formation. This means that the observed swelling of the Pd catchment gauze, which causes the increase in pressure drop across the gauze pack over time, happens regardless of Pt catchment. It is an intrinsic effect of the Pd gauze when placed in the ammonia oxidation reactor. The mechanism causing this porous structure is

still unknown and should be a relevant topic for future investigations.

More importantly, mass change studies and ICP-MS analysis reveal a significant Pd loss (0.033 g tonne^{-1} HNO_3 produced), very similar to the loss observed with a Pt combustion catalyst (see above). Since the Pd loss in the pilot plant occurs both with a Pt and LaCoO_3 combustion catalyst, it is unlikely to be connected to the Pt catchment or grain reconstruction caused by PtO_2 . In addition, there is no known thermal loss mechanism for Pd in wet or dry air that can explain such a large thermal Pd loss in the process gas (20). This leads to the conclusion that Pd loss is most probably caused by interaction with the demanding gas stream conditions of ammonia oxidation and thus by the gas constituents that were not present in the laboratory-scale experiments. Identifying the species or combination of species, present in the combusted process gas that lead to Pd loss is a very relevant topic for future investigations.

Conclusion

In this work we have observed that the Pd-Ni catchment system in a dry oxygen containing atmosphere is subject to internal oxidation of Ni to NiO. Further, in a wet oxygen enriched environment, Ni is also oxidised to NiO, but subsequently lost, most probably as Ni(OH)_2 . Furthermore, the presence of

PtO₂ vapour in wet or dry air causes severe grain reconstruction of both Pd and Pd-Ni wires, which in turn causes wire swelling and pore formation similar to industrial Pd-based catchment systems used during ammonia oxidation. In laboratory furnace experiments, no distinct Pd loss accompanies the Pt catchment. However, pilot-scale testing in an ammonia oxidation atmosphere show significant Pd loss, both with a Pt and LaCoO₃-based (non-Pt containing) combustion catalyst. In addition, a second type of pore formation is observed when using the LaCoO₃ catalyst in the pilot plant. Therefore, we suspect the Pd loss and the second type of pore formation to be related to gas species present only in the industrial gas mixture, not in our laboratory scale gas mixtures. We suggest this as a topic for further investigation.

Acknowledgements

The work is carried out in the industrial Catalysis Science and Innovation Centre (iCSI), which receives financial support from the Research Council of Norway (contract No. 237922). The authors appreciate fruitful discussions with the iCSI team, the support from Ole Bjørn Karlsen (UiO) in the initiation phase of the metallography work, and the assistance by Nibal Sahli on metallography and TGA (Yara Technology Center facility, Herøya, Norway).

References

1. M. Warner, 'The Kinetics of Industrial Ammonia Combustion', PhD Thesis, School of Chemical and Biomolecular Engineering, University of Sydney, Australia, May, 2013, 231 pp
2. O. Nilsen, A. Kjekshus and H. Fjellvåg, *Appl. Catal. A: Gen.*, 2001, **207**, (1–2), 43
3. Z. M. Rdzawski and J. P. Stobrawa, *J. Mater. Process. Technol.*, 2004, **153–154**, 681
4. G. Rayner-Canham and T. Overton, "Descriptive Inorganic Chemistry", 5th Edn., 2010, W. H. Freeman and Co, New York, USA, 723 pp
5. H. Holzmann, *Chemie Ing. Tech.*, 1968, **40**, (24), 1229
6. A. E. Heywood, *Platinum Metals Rev.*, 1973, **17**, (4), 118
7. B. S. Beshty, W. R. Hatfield, H. C. Lee, R. M. Heck and T. H. Hsiung, Engelhard Corporation, 'Method for Recovering Platinum in a Nitric Acid Plant', *US Patent 4,526,614*; 1985
8. Y. Ning, Z. Yang and H. Zhao, *Platinum Metals Rev.*, 1995, **39**, (1), 19
9. J. L. G. Fierro, J. M. Palacios and F. Tomás, *Surf. Interface Anal.*, 1989, **14**, (9), 529
10. Y. Ning, Z. Yang and H. Zhao, *Platinum Metals Rev.*, 1996, **40**, (2), 80
11. J. Pura, P. Kwaśniak, D. Jakubowska, J. Jaroszewicz, J. Zdunek, H. Garbacz, J. Mizera, M. Gierej and Z. Laskowski, *Catal. Today*, 2013, **208**, 48
12. Y. Ning and Z. Yang, *Platinum Metals Rev.*, 1999, **43**, (2), 62
13. Z. Yang, Y. Ning and H. Zhao, *J. Alloys Compd.*, 1995, **218**, (1), 51
14. A. E. Heywood, *Platinum Metals Rev.*, 1982, **26**, (1), 28
15. H. Holzmann, *Platinum Metals Rev.*, 1969, **13**, (1), 2
16. Z. Rdzawski, L. Ciura and B. Nikiel, *J. Mater. Proc. Tech.*, 1995, **53**, (1–2), 319
17. F. Han and X. Liu, *Guijinshu*, 2017, **38**, (1), 31
18. J. Pura, P. Wieceński, P. Kwaśniak, M. Zwolińska, H. Garbacz, J. Zdunek, Z. Laskowski and M. Gierej, *Appl. Surf. Sci.*, 2016, **388**, (Part B), 670
19. J. Gegner, G. Hörz and R. Kirchheim, *J. Mater. Sci.*, 2009, **44**, (9), 2198
20. E. J. Opila, Materials Science and Engineering, University of Virginia, USA, private communication, 1st August, 2016
21. H. Jehn, *J. Less Common Metals*, 1984, **100**, 321
22. C. W. Bale, E. Bělisle, P. Chartrand, S. A. Decterov, G. Eriksson, A. E. Gheribi, K. Hack, I.-H. Jung, Y.-B. Kang, J. Melançon, A. D. Pelton, S. Petersen, C. Robelin, J. Sangster, P. Spencer and M.-A. Van Ende, *Calphad*, 2016, **54**, 35
23. D. Cubicciotti, *J. Nucl. Mater.*, 1988, **154**, (1), 53
24. G. Chen, G. Guan, Y. Kasai and A. Abudula, *Int. J. Hydrogen Energy*, 2012, **37**, (1), 477

Supplementary

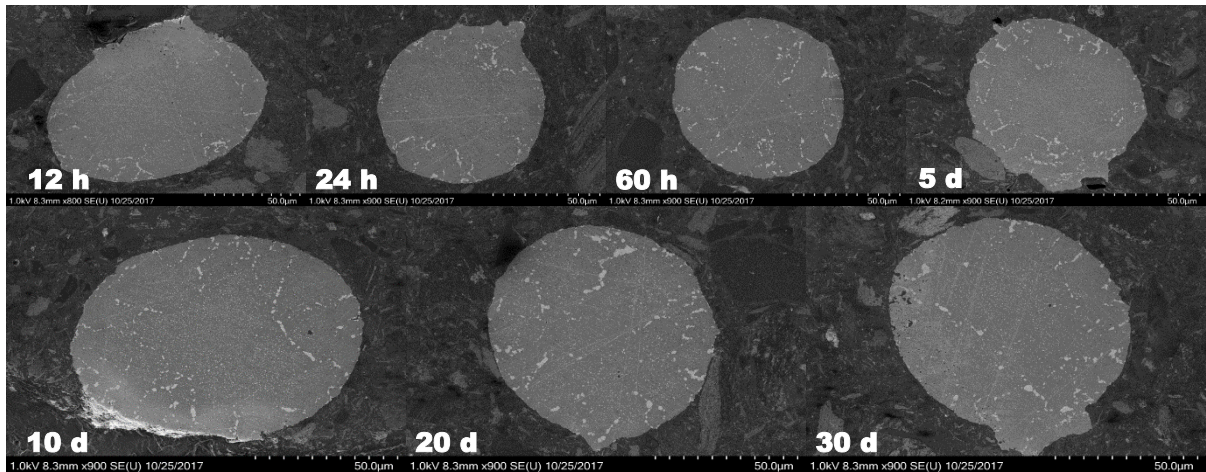


Figure S1. SEM cross section images of Pd/Ni (95/5 wt%) wires (76 μm) treated at 900 °C in a muffle furnace (air) for 12 hours to 30 days.

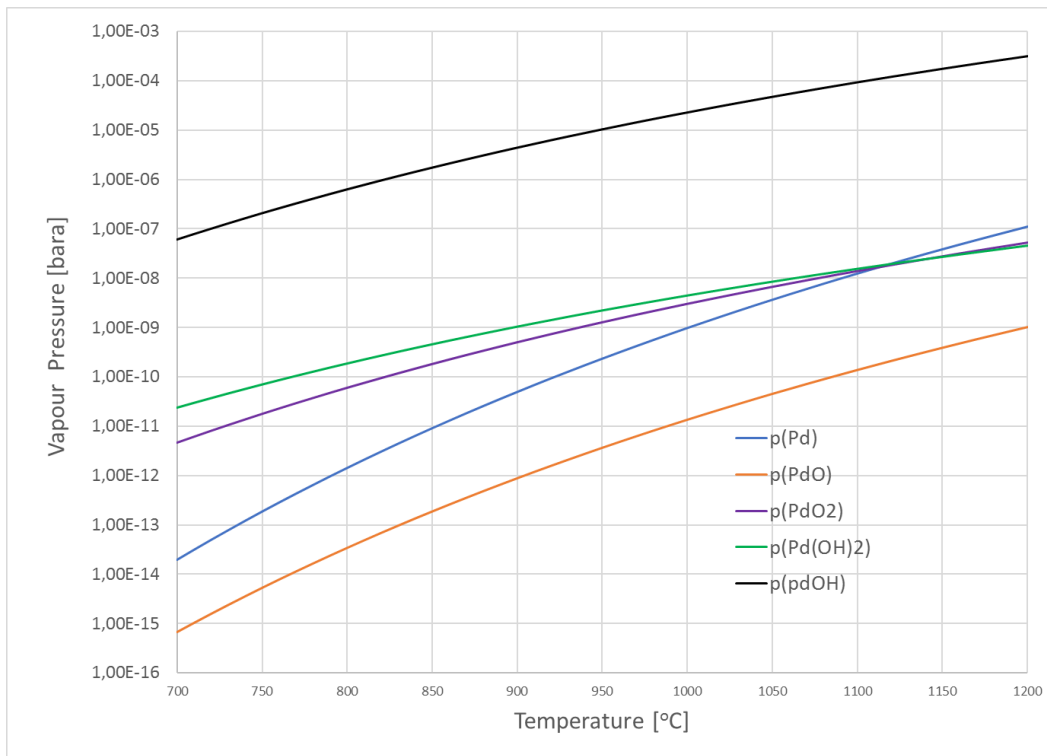


Figure S2. Calculations using Factsage estimating the vapor pressure of possible Pd-species present at pilot plant conditions.

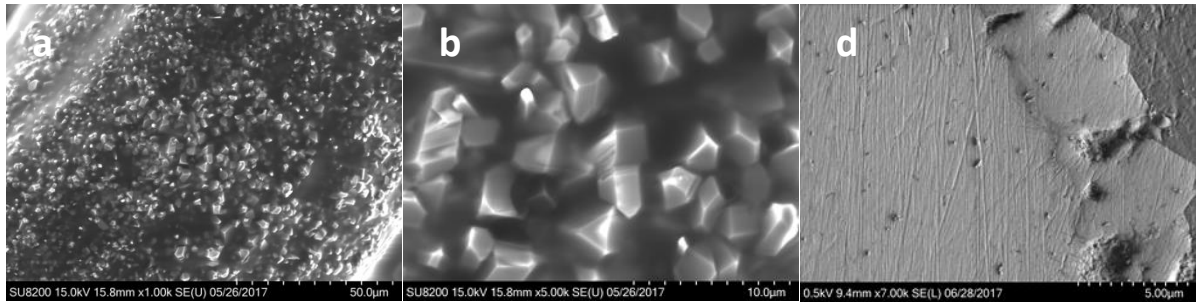


Figure S3. SEM-images of the surface (left and centre) and cross section (right) of a 76 μm Pd/Ni (95/5 wt%) wire heated in inert gas (N_2 5.0) for 6 days at 900 $^\circ\text{C}$.

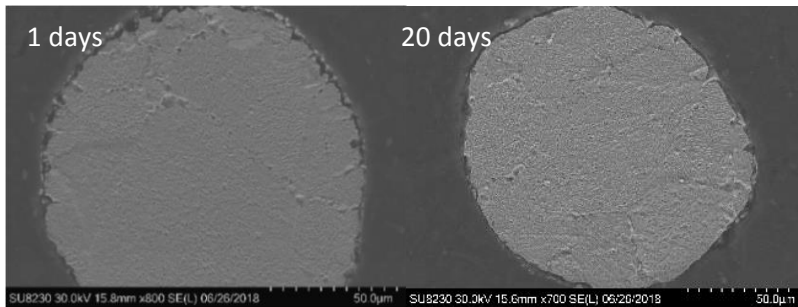


Figure S4. SEM cross section images of 120 μm Pd/Ni (95/5 wt%) wires heated in flowing air at 1050 $^\circ\text{C}$ for 1 and 20 days, after etching in aqua regia for 45 seconds.

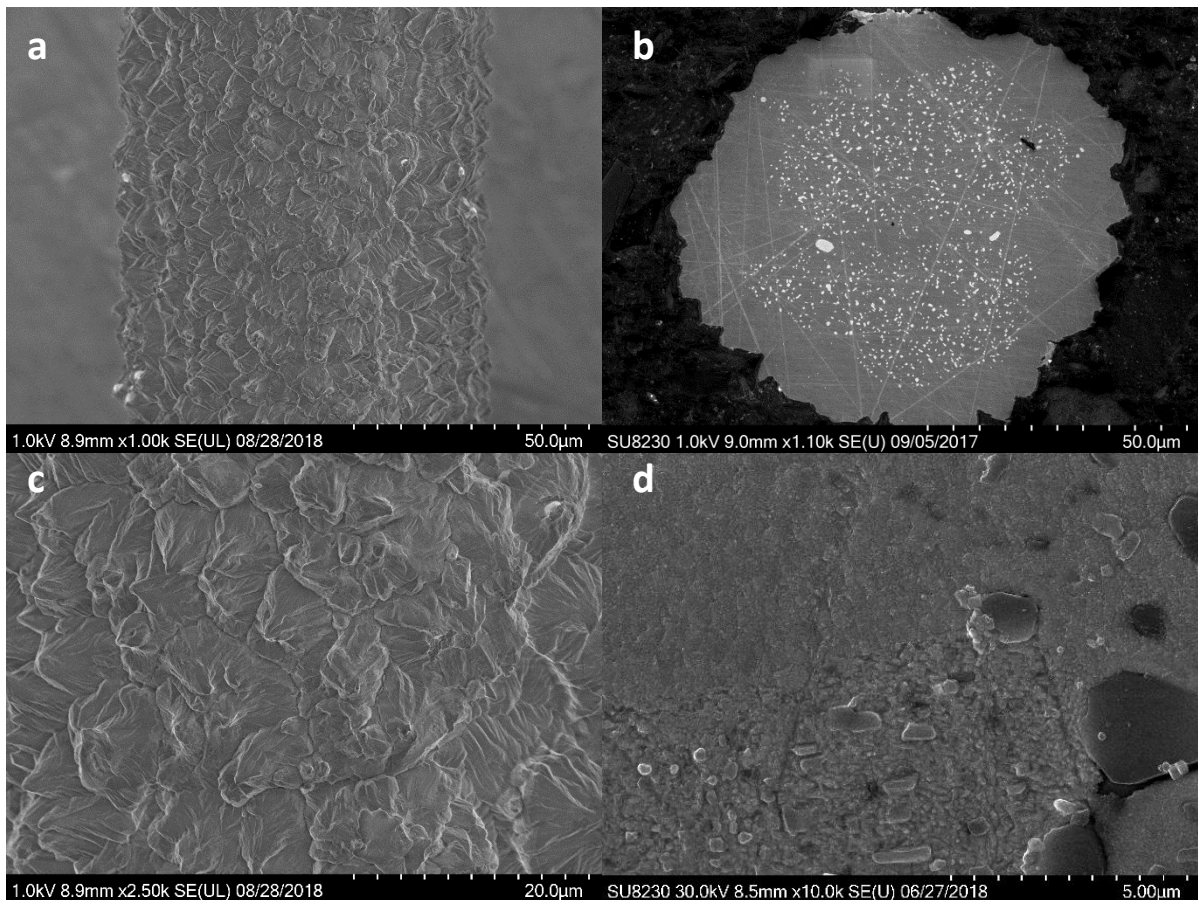


Figure S5. SEM images of 76 μm Pd-Ni wire heated for 4 weeks at 1050 $^\circ\text{C}$ in wet air (14 % O_2 , 33 % H_2O , balance N_2). The figure shows the surface (a, c), cross section (b) and cross section after etching in aqua regia for 10 seconds (d).

Paper II

Mechanism of grain reconstruction of Pd and Pd/Ni wires during Pt-catchment

A. S. Fjellvåg, P. S. Jørgensen, D. Waller, D. S. Wragg, M. D. Michiel,
A. O. Sjøstad
Materialia, 2022, 21, 101359



III



Mechanism of grain reconstruction of Pd and Pd/Ni wires during Pt-catchment

Asbjørn Slagtern Fjellvåg^{a,*}, Peter Stanley Jørgensen^b, David Waller^c, David Stephen Wragg^a, Marco Di Michiel^d, Anja Olafsen Sjøstad^{a,*}

^a Department of Chemistry, Centre for Materials Science and Nanotechnology, University of Oslo, Norway

^b Department of Energy Conversion and Storage, Technical University of Denmark, Fysikvej, 2800 Kgs. Lyngby, Denmark

^c Yara Technology Center, Herøya Research Park, Porsgrunn, Norway

^d ESRF, The European Synchrotron, 71 Avenue des Martyrs, Grenoble 38000, France

A B S T R A C T

We have investigated industrial Pd and Pd/Ni (91.3/8.7 at.%) wires and gauzes used for Pt-catchment during the ammonia oxidation process, focusing on the origin of the grain reconstruction phenomena. *In situ* X-ray absorption tomography experiments reveal severe reconstruction of polycrystalline Pd and Pd/Ni wires over the course of 10 days, caused solely by the presence of gaseous PtO₂ and dry air. A high partial pressure of PtO₂ results in higher Pt-catchment rates, which in turn causes more severe reconstruction of the Pd-based wire. Additionally, the Pt-catchment efficiency is reduced when the Pt-content on the wire surface increases. Scanning electron microscopy accompanied by energy dispersive X-ray analysis reveal that Pt diffuses rapidly into the wire core via grain boundaries already after 1 day of Pt catchment. However, quasi monocrystalline (pre-annealed) Pd and Pd/Ni samples show significantly less Pt-catchment and only a little reconstruction compared to the polycrystalline samples. With support from experiments and simulations, we conclude that bulk diffusion is one of the main limitations for Pt-catchment on both poly- and quasi monocrystalline Pd and Pd/Ni wires. The diffusion limitation causes a high surface concentration of Pt, which in turn limits further Pt-catchment due to a gas-surface equilibrium. The polycrystalline wire can overcome the diffusion limitation by utilizing a rapid grain boundary diffusion, transporting both Pt to the wire core and Pd to the wire surface. However, this transport process is also the cause of grain reconstruction.

1. Introduction

One of the most important products of the chemical industry today is nitrogen-based synthetic fertilizer, which is a necessity in order to feed the entire human population [1]. The production of fertilizers is largely based on producing ammonia using the Haber-Bosch process and nitric acid using the Oswald process. In the first step of the Oswald process, ammonia is oxidized to nitric oxide (NO) over a Pt/Rh gauze catalyst at high temperature (800–950 °C) and medium pressure (1–12 bar) [2,3]. Due to the demanding process conditions, significant quantities of platinum is lost (evaporated) in the form of PtO₂ vapour [2,3]. Industrially, the Pt-loss is mitigated by installing a number of Pd/Ni catchment gauzes downstream of the Pt/Rh catalytic gauzes. The Pd/Ni gauzes successfully capture Pt, and reach a Pt-concentration of ~50 wt.% during the campaign, but it is victim to severe degradation mechanisms. Due to a grain reconstruction process, the Pd/Ni wires swell in size and become completely porous, all within 20 days [4]. This give rise to a large pressure drop, limiting the number of Pd/Ni gauzes that can be installed for each campaign. This is particularly problematic for high pressure plants (10–12 bar), which have a high gas load and the highest Pt losses from the Pt/Rh combustion gauzes. In addition, the Pd/Ni alloy show complete Ni depletion and both Pd and Pd/Ni show a significant thermal loss of Pd [4].

Since the invention of the Pd-based gauzes for Pt-catchment in the late 1960s [5], several studies on their performance and degradation behaviour are reported [4,6–19]. Surprisingly, its behaviour is completely opposite to the expectations of a noble metal heated at high temperature; a huge increase in surface area is observed rather than sintering and grain growth (Fig. 1). During operation, it has been shown that wide angle grain boundaries in the Pd/Ni wires are severely etched, and that a deep recrystallization of the grain structure occurs [6,14]. However, this do not fully explain why the internal porosity appears. The surface of the Pd-based catchment gauze often contain beautiful clear faceted crystallites, which caused Ning et al. [7] to suggest that a re-alloying and recrystallization process is the cause for the change in morphology. Recently, Fjellvåg et al. [4] showed that the porosity which appears in the Pd/Ni gauzes, when installed for the ammonia oxidation reaction, is caused by two different phenomena: (1) interaction between Pd/Ni and the aggressive NO_x/NH₃/H₂O/O₂ gas mixture and high process temperature (900 °C), which give rise to a rounded shape of the crystallites on the surface (Fig. 1b, c); and (2) grain reconstruction caused by Pt-catchment, resulting in crystallites on the surface with well-developed facets and an edged shape (Fig. 1e, f), similar to the crystallites observed by Ning et al. [7]. By closely viewing the industrial sample in Fig. 1d, one may believe that both the rounded and the edged shapes characterize the sample treated at real industrial conditions. Finally, it is generally agreed that Ni does not participate actively in the grain reconstruction process. However, it diffuses to the grain boundaries (GBs),

* Corresponding authors.

E-mail addresses: a.s.fjellvag@smn.uio.no (A.S. Fjellvåg), a.o.sjastad@kjemi.uio.no (A.O. Sjøstad).

<https://doi.org/10.1016/j.mta.2022.101359>

Received 26 November 2021; Accepted 7 February 2022

Available online 7 February 2022

2589-1529/© 2022 Acta Materialia Inc. Published by Elsevier B.V. All rights reserved.

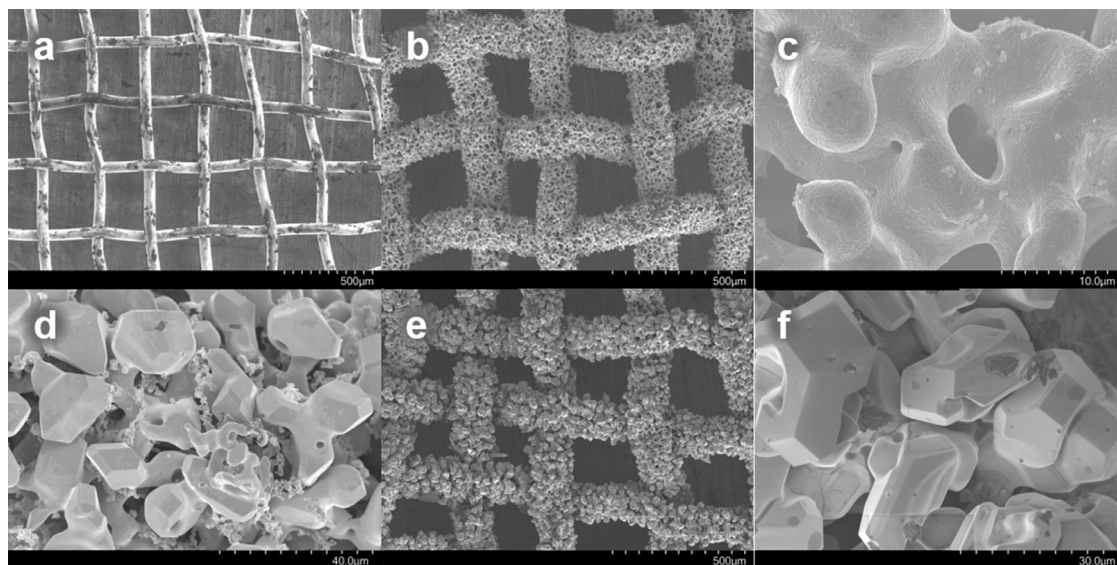


Fig. 1. SEM images of (a) a fresh Pd/Ni (91.3/8.7 at.%) net, (b, c) a pure Pd net after operation in an ammonia oxidation reactor using an oxide catalyst, *i.e.* no Pt-catchment possible (point 1 in text), (d) a Pd/Ni net after operation in a full scale industrial plant, and (e, f) a pure Pd net after operation in an ammonia oxidation reactor using a pure Pt catalyst (point 2 in text). The images were collection in relation to a previously published investigation [4].

become oxidized to NiO and is subsequently lost to the gas stream as gaseous Ni(OH)₂ [4].

PtO₂ plays a key role in the grain reconstruction process (point 2 in the text above). During simple Pt-catchment experiments on Pd and Pd/Ni wires in air, PtO₂ alone is able to transform a solid Pd-based metal wire into a porous mass [4]. Although the system appears chemically simple (only 4 elements present) the changes in morphology and composition are complex, and detailed investigations of the wire life cycle are needed to understand the mechanisms involved. This has stimulated us to apply *in situ* X-ray absorption computed tomography (absorption-CT), a technique that has proven fruitful in recent investigations of different catalysts [20–22]. Visualized by a series of 3D images we are able to follow the development of Pd and Pd/Ni wires in real time during Pt catchment experiments, and study local changes in the chemical composition and morphology; as well as average variations in the radial and axial directions of reasonably large samples.

To support the findings from *in situ* absorption-CT, we have investigated the same samples with scanning electron microscopy (SEM), energy dispersive X-ray spectroscopy (EDX) and inductively coupled plasma optical emission spectroscopy (ICP-OES). The results obtained on the polycrystalline wires are complemented by laboratory experiments on quasi monocrystalline Pd and Pd/Ni wires, to compare the effect of different grain structures. Inspired by different corrosion studies [23–28], we investigate the role of grain boundaries (GB) in the grain reconstruction process, and use a diffusion model to explain our findings.

2. Experimental details

All Pd and Pd/Ni (91.3/8.7 at.%) wire samples used in the absorption-CT or in the home laboratory experiments are originating from the same source of polycrystalline wires; produced by K. A. Rasmussen (purity > 99.9%) with a wire diameter of 76 μm and grain size diameter of approximately 5 μm. For some selected home laboratory experiments, the polycrystalline sample wires were transformed into quasi monocrystalline wires (grain size in the range of 20–200 μm) by annealing for 7 days at 1100 °C in a double quartz ampoule, with both ampoules evacuated during sealing.

In situ Synchrotron radiation X-ray absorption-CT experiments were performed at beamline ID15A, ESRF, Grenoble, France [29]. The technique is based on radiography (2D-imaging). A series of radiographs of

the object from several different angles are used to reconstruct a 3D image. Six different *in situ* absorption-CT experiments, each with a duration of 10–12 h, were carried out on polycrystalline Pd and Pd/Ni wires (Table 1). In these experiments, a tomogram was collected every 10 min. In order to investigate samples at later stages of the grain reconstruction process [4], some samples were pre-treated in our dedicated furnace system located at University of Oslo [4] before the *in situ* absorption-CT experiments. Both Pd and Pd/Ni samples were aged for 1, 4, 7 and 10 days at 1000 °C, with a rolled-up Pt-net (~340 mg; purity > 99.9%; supplied by K. A. Rasmussen) upstream; also at 1000 °C. A gas flow of 1 L/min in a 6 mm inner diameter (ID) quartz tube (gas velocity: 0.59 m/s) was used. We estimate a $p(\text{PtO}_2)$ of 5×10^{-8} atm based on mass loss from the Pt net. In addition to the *in situ* absorption-CT experiment, *ex situ* tomograms of all samples were collected at room temperature.

The experimental setup used for the *in situ* absorption-CT experiments is shown schematically in Fig. S1. A short piece of the aged Pd or Pd/Ni wire (~3 mm long) was mounted between two pieces of quartz wool in the end of a sapphire tube (2 mm outer diameter (OD), 1 mm ID). The length of the Pd or Pd/Ni wire was positioned along the length of the sapphire tube. The end-pieces of quartz wool were squeezed tightly together to make it sufficiently strong to allow a high gas flow, and to stabilize the sample position. Just below the sample (upstream with respect to gas flow), ~130 mg of Pt-wire was packed between two more pieces of quartz wool as the PtO₂ (g) source. We estimate that the $p(\text{PtO}_2)$ was approximately the same as in the home lab experiments, based on a similar gas flow, temperature and amount of Pt stacked in the tube relative to the tube size ($p(\text{PtO}_2)$ of $\sim 5 \times 10^{-8}$ atm). The packed sapphire tubes were mounted on a 1/16" Swagelok T-coupling using Teflon ferrules. The T-coupling was screwed in to a Huber 1001-goniometer mounted on a rotation stage. During the experiments, a prototype 12 × 10 × 10 cm³ furnace system (produced by Entech Energiteknik AB, Sweden) with two orthogonal cylindrical open tubes was used. The sapphire tube with the sample was inserted vertically into the furnace (from below), while the X-ray beam passed through the horizontal opening in the furnace. The furnace system was optimized to ensure a uniform temperature around the Pd (Pd/Ni) wire and the rolled up Pt-wires. The furnace was calibrated to keep the sample position at 1000 °C. The temperature at 12.5 mm from the centre of the furnace was 1019 °C and at 27.5 mm from the centre it was 986 °C. The gas flow through the sapphire tube (synthetic air 5.0 (21% O₂

Table 1

List of samples used for the *in situ* absorption-CT experiments with information on pre-treatment conditions and duration of the *in-situ* experiments. All experiments were carried out at 1000 °C in a flow of synthetic air.

Sample name	Composition	Pre-treatment	<i>In situ</i> exp. time	Number of tomograms
Pd 0–12h	Pure Pd	0 h	12 h	72
Pd 24–34h	Pure Pd	24 h	10 h	55
Pd/Ni 0–12h	Pd/Ni (91.3/8.7 at.%)	0 h	12 h	73
Pd/Ni 24–36h	Pd/Ni (91.3/8.7 at.%)	24 h	12 h	48*
Pd/Ni 4–4.5d	Pd/Ni (91.3/8.7 at.%)	4 days	12 h	71
Pd/Ni 7–7.3d	Pd/Ni (91.3/8.7 at.%)	7 days	4 h	37

*The synchrotron X-ray beam was down two times during this experiment, resulting in fewer tomograms.

in N₂) provided by Air Liquide) was regulated by a Brooks GF40 mass flow controller controlled using a Lab View program [30].

When starting the experiment, the sapphire tube was mounted on the stage at room temperature and the gas flow was set to 1 mL/min. When the furnace reached 1000 °C, the gas flow was slowly increased to 28 mL/min, to replicate the linear gas velocity of 0.59 m/s, used in the home laboratory experiments (1 L/min in a 6 mm ID-tube). It was necessary to keep a low flow during the heating phase, to ensure no movement of the quartz wool, Pd-wire or the rolled up Pt net. During the experiments, when operated at 1000 °C, the overpressure inside the sapphire tube was ~0.4 bar.

To capture the tomograms, a monochromatic beam with an energy of 37.5 keV was used. The detector was a PCO Edge camera positioned at a distance of 300 mm from the sample. To calibrate for the background, 100 frames of dark field images (no beam) and 100 frames of flat field images (beam, but no sample) were captured for every tomogram. When imaging the sample, 900 frames were captured in 10 s, while the sample was rotated by 180°. The image size collected was 1.8 mm × 1.5 mm, with a voxel size of 0.7 μm. A small vibration/wobbling of the sapphire tube caused a slight reduction of the data quality and resolution for some of the samples. The reconstruction of radiographs to tomograms was carried out using Matlab [31], with the filtered back projection algorithm [32]. Matlab was also used for the mathematical analysis of the absorption-CT results [33], see supplementary for further descriptions (Section S.1.2).

Additional Pt-catchment experiments on the quasi monocrystalline Pd and Pd/Ni wires (mentioned above) were performed in the home laboratory using our furnace system. The wire samples were heated for 10 days at 900 °C in a flow of air (1 L/min in a 6 mm ID tube), with a Pt-net (~340 mg) located upstream at a temperature of 1000 °C. Extra samples presented in the supplementary section were heated for 3.5 days using 76 μm wire diameter samples and a high gas flow (1 L/min in a 4 mm ID tube) and for 20 days using 120 μm wire diameter samples with normal gas flow (1 L/min in a 6 mm ID tube).

Additional examination of selected samples from the absorption-CT and the home laboratory annealing experiments was carried out with SEM/EDX and ICP-OES analyses. SEM/EDX was performed with a high-resolution Hitachi SU8230 field-emission scanning electron microscope (FE-SEM). Images were obtained by collecting the secondary electrons produced by the electron beam with an acceleration voltage of 1 kV. EDX analysis (mapping and point quantification) was performed using an acceleration voltage of 30 kV. For surface analysis, samples were mounted with carbon tape on a copper plate. For imaging of wire cross sections, samples were cast in a conducting resin (PolyFast, Struers, Denmark) before grinding and polishing (1 μm diamond finish).

ICP-OES analyses were carried out by Mikrolab Kolbe (Fraunhofer Institute in Oberhausen, Germany). Acid digestion was performed by Mikrolab Kolbe to dissolve the samples. The samples were measured with an ICP-OES Spectro Arcos from Spectro, and checked with an AAS Contra800 from AnalytikJena. The estimated error of the measurement is 0.015% absolute for Ni, 0.025% absolute for Pt in samples with more

than 15% Pt, 0.04% absolute for Pt in samples with less than 15% Pt, and 0.055% absolute for Pd. Diffusion experiments were performed by heating a Pd single crystal (111-orientation) and polycrystalline Pd-disc at 900 °C in a flow of air with a Pt filament upstream, with the sample located in a 45° angle to the gas flow. The Pt filament was resistively heated a little beyond the furnace temperature to obtain a higher $p(\text{PtO}_2)$, but the exact $p(\text{PtO}_2)$ is not determined. The single crystal was annealed for 23 h, while the polycrystalline disc were annealed for 4 h and 35 min. Diffusion profiles were obtained using sputtered neutral mass spectroscopy (SNMS) performed by MATS (UK) Ltd.

3. Results

3.1. *In situ* X-ray absorption-CT

3.1.1. Qualitative comparison of Pd and Pd/Ni wires from 0 to 1.5 days

The grain reconstruction process of Pd and Pd/Ni wires are in this work studied with *in situ* absorption-CT using an experimental set-up which allows a PtO₂ containing gas flow and high temperature (1000 °C). The complete grain reconstruction of Pd and Pd/Ni is known to take approximately 10–20 days [4]. To capture as much of the process as possible, the absorption-CT experiments were therefore split into different experiments, each with a duration of ~12 h, utilizing a pre-treatment performed prior to the experiment (see Experimental details and Table 1).

Fig. 2 shows the visual development of the pure Pd and Pd/Ni wires during the first 0–12 and 24–34 h of Pt catchment, extracted from the *in situ* absorption-CT data. Before visualizing the tomograms, the data is segmented based on the measured attenuation coefficient, to find the contributions from the different constituent (Pd, Pt, Ni, NiO, air/voids), as heavier elements have a higher attenuation of the X-ray beam (Section S.1.2.1). The result is the volume rendering of the wires shown in Fig. 2, where anything considered as air/voids is removed from the figure. We assume the metal wire is completely dense after production, *i.e.* that there is no internal porosity in the fresh wire. After 1.5 h, surface roughness is already apparent for both wires, which develops into small crystallites which grow with time. The surface crystallization develops in a similar manner for both wires, and after 34 h the largest surface crystallites are up to 10 μm in diameter.

Additionally, after 1.5 h, some dark line-shaped features are visible just below the surface of the Pd/Ni wire (Fig. 2, «NiO in GBs»). These are not present in the pure Pd wire, suggesting that they are NiO precipitates appearing as a result of internal oxidation of Ni to NiO in the Pd/Ni alloy. The line-like features occur because NiO precipitates mainly inside the grain boundaries, as reported by Gegner et al. [34]. After 4 h, the volume of the Pd/Ni wire has increased by ~4.6%, very close to the expected volume increase for complete oxidation of the 8.7 at.% Ni to NiO (~4.6%; see Supplementary Section S.1.3). The values are nearly equal, however, the internal oxidation should not be completed after only 4 h [4]. We can therefore assume that we have both Pt catchment and internal oxidation of Ni, at this stage of the experiment.

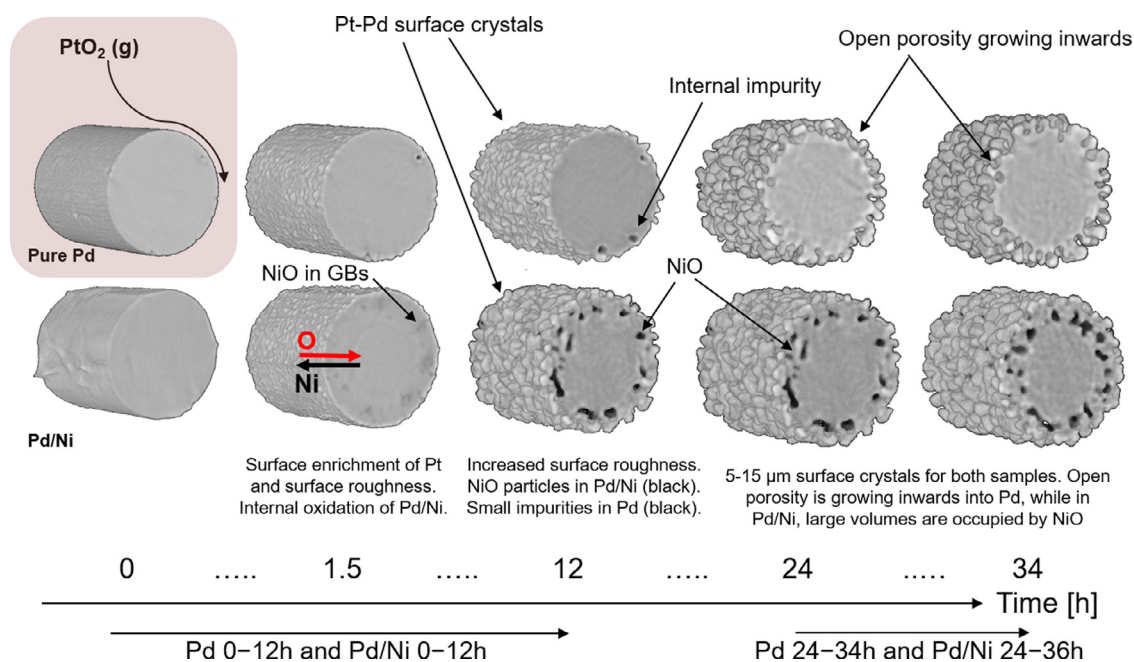


Fig. 2. Schematic illustration of the morphological changes and chemical dynamics of Pd and Pd/Ni (91.3/8.7 at.%) wires after 0, 1.5, 12, 24 and 34 h of Pt catchment at 1000 °C during *in situ* absorption-CT experiments in synthetic air with $p(\text{PtO}_2) \approx 5 \times 10^{-8}$ bar. The large NiO particles and the impurities inside the Pd/Ni and Pd wires, respectively, are manually coloured black. An EDX image showing the NiO distribution in the cross section of an oxidized Pd/Ni wire is shown in Fig. S3c.

After 12 h, NiO has assembled into larger particles inside the Pd matrix (black regions in Fig. 2, «NiO»), with a diameter of 3–7 μm . The volume of the black regions (Fig. 2, «NiO») in the Pd/Ni-wire is ~7–8% of the wire volume after 12 h (Fig. S6e), while we expect that NiO should make up a volume of 10.7% after complete oxidation (Supplementary Section S.1.3). The remaining NiO particles are probably small and mixed with the Pd-matrix, and does not appear as separate particles in the tomogram, meaning they are smaller than the resolution of the experiment. This causes the overall tomogram intensity to be lower for Pd/Ni compared to pure Pd (Table S1). Unfortunately, there is an issue with too low contrast between NiO and void/space to separate them in the analysis, preventing quantitative analysis of Ni/NiO in Pd (extended description in Supplementary Section S.1.2.2). Because of this, we have carried out quantitative analysis only for the pure Pd wires.

Notably, in the pure Pd wire, a few circular shapes of low density appear over the first 12 h, with a volume of ~0.6% of the wire volume. We ascribe this to impurities in the Pd-sample, shown as black shapes in Fig. 2 («Internal impurity»).

3.1.2. Quantitative analysis of Pd-wires from 0 to 1.5 days

Time dependent development. For the first two *in situ* experiments on Pd (named Pd 0–12 h and Pd 24–34 h in figures), we see several trends (calculations are explained in Supplementary Section S.1.2.4). Firstly, there is a volume increase with time (Fig. S6a), which we ascribe to Pt-catchment. This correlates well with the fact that the average intensity of the tomogram increases with time (Fig. S6b), as expected when the sample incorporates an element (Pt) that attenuates X-rays more strongly. From the volume increase we calculate the Pt-concentration (Fig. 3a) to reach ~1.2 at.% Pt after 12 h. The Pt-content is only slightly higher for the Pd 24–34 h sample, but this is probably related to the amount of Pt captured during the pre-treatment of this sample. The Pd 24–34 h sample has a linear increase in Pt-content, which increases with the approx. same rate as the Pd 0–12 h sample from 8 to 12 h.

Analysis of the absorption-CT data shows furthermore that the increase in Pt content is accompanied by an increase in the surface area (Fig. 3b). The increase in surface area is seen visually by a change in

surface morphology and growth of small crystallites on the wire surface (Fig. 2). The surface crystals are in the range of 2–10 μm in diameter, and increases in both size and quantity with time (Fig. 3d). The intensity of the surface crystals in the tomograms ranges from the Pd bulk intensity to a value well above the theoretical Pt-intensity (Supplementary Section S.1.4.3), but is on average close to the theoretical Pt-intensity (Fig. S8). However, SEM/EDX indicate that the surface crystallites are not solely composed of Pt, instead they are rather rich in Pd (Section 4.3.1).

Notably, as the wire grows outwards, porosity is developing inwards. The degree of porosity within the original radius of the wire (38 μm) is just above 1% after 12 h and almost 6% after 34 h (Fig. 3c). Interestingly, the degree of porosity and surface area is much larger for the Pd 24–34 h sample compared to Pd 0–12 h, even though the Pt-concentration does not show the same evolution.

Radius dependent analysis. In Fig. 4 we compare the degree of porosity and the average intensity *versus* radius. As described above, the sample is growing in size, porosity is developing inwards and the intensity increases with time. From 0 to 12 h, the porosity develops to a depth of 30 μm from the sample centre, but with a low degree of porosity (~10% at 35 μm). After 34 h, the porosity has only developed slightly deeper into the sample (~28 μm), but the degree of porosity is much larger (~30–35% at 35 μm). The intensity of both samples are very high near the sample surface, and is reduced radially inwards to the centre of the wires. After 12 h, the intensity approaches the bulk Pd-intensity at approximately the same radial point as the degree of porosity goes to zero, while after 34 h, the elevated intensity reaches slightly deeper into the sample compared to the degree of porosity. This indicates that Pt has not penetrated far into Pd, only slightly below the porosity. This correlates well with the EDX results to be presented in Section 4.3.

Length dependent analysis. In the experimental setup, the reaction gas mixture was flowing along the length of the Pd wire, allowing us to analyse differences in Pt catchment from the reactor inlet to the outlet. When Pt is captured, the Pt concentration in the gas stream is reduced, causing a lower $p(\text{PtO}_2)$ towards the gas outlet. In the experiment from 0 to 12 h, the largest volume increase is at the gas inlet-end of the Pd-wire,

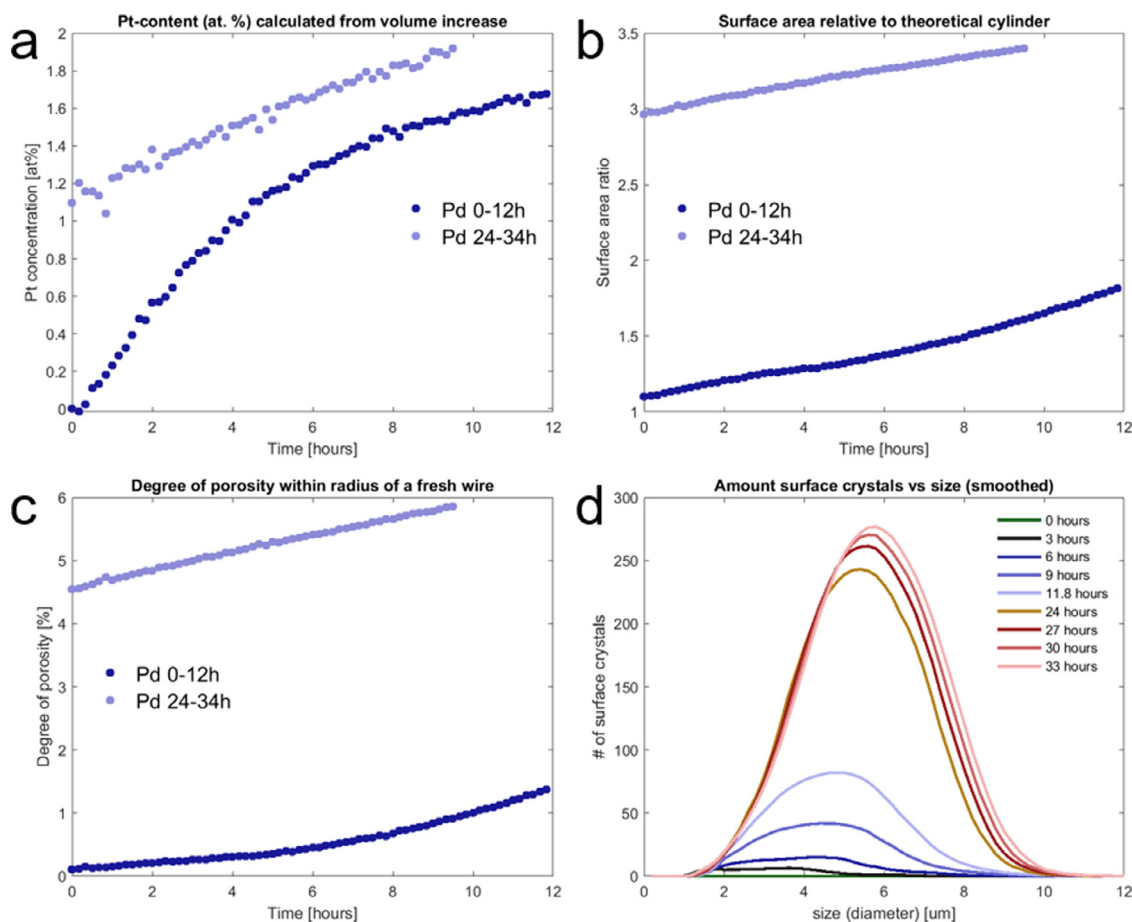


Fig. 3. Results from quantitative analysis of pure Pd wires during *in situ* absorption-CT experiments from 0 to 12 h and 24 to 34 h at 1000 °C in synthetic air with $p(\text{PtO}_2) \approx 5 \times 10^{-8}$ bar. (a) Pt-content [at.%] calculated from volume increase of the wires, (b) calculated surface area, relative to a cylinder of the same dimensions as the Pd-wire (76 μm diameter), (c) calculated degree of porosity within the radius of a fresh wire (38 μm), and (d) distribution of surface crystals *versus* size at selected time points. The mathematics behind the calculations are explained in Supplementary Section S.1.2.4.

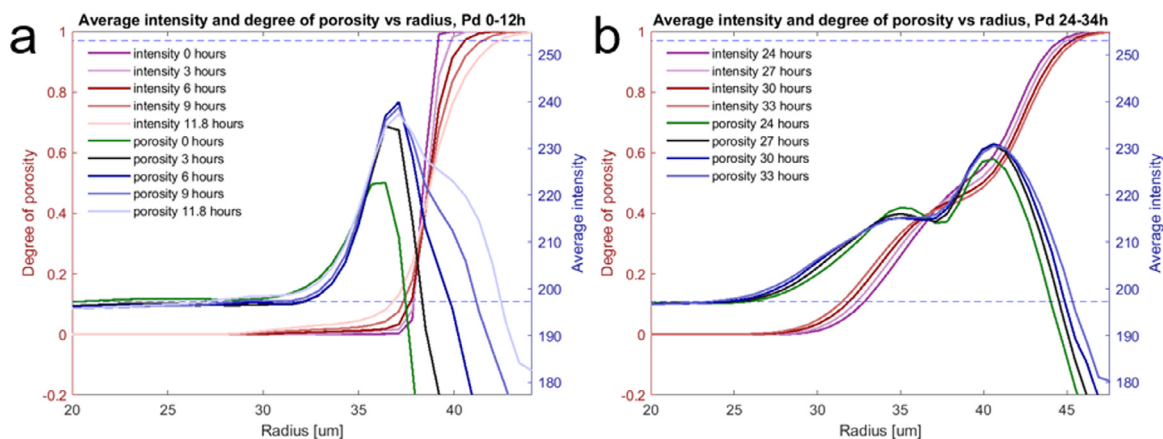


Fig. 4. Plot of radius dependence of degree of porosity (magenta-red, left axis) and intensity (green-blue, right axis), for (a) pure Pd from 0 to 12 h (Pd 0–12 h) and (b) pure Pd from 24 to 34 h (Pd 24–34 h). The time stamp for each line is indicated in the figure. The dotted lines indicate the theoretical intensity corresponding to pure Pd (lower intensity) and pure Pt (higher intensity). The original wire radius is 38 μm .

see Fig. 5a. This is probably due to faster and more extensive Pt catchment at the inlet-end where the $p(\text{PtO}_2)$ is higher, and less Pt catchment at the outlet-end where the $p(\text{PtO}_2)$ is lower.

By recalculating volume increase to Pt-content and comparing with the Pt-concentration calculated from the $p(\text{PtO}_2)$ (see calculation in Supplementary Section S.1.5), we obtain the percentage of Pt captured from the gas stream along the wire length, see Fig. 5b. After 3 h, the graph has a non-linear trend, indicating that the Pt catchment efficiency is faster

near the reactor inlet and reduces along the wire length. This correlates well with a reduction in $p(\text{PtO}_2)$ from the inlet to the outlet, as would be expected under Pt catchment conditions. Furthermore, the catchment efficiency reduces from $\sim 42\%$ after 3 h to $\sim 19\text{--}22\%$ after 12 or more hours. During both experiments (Pd 0–12 h and Pd 24–34 h), the trend is reducing Pt-catchment efficiency with time. This shows that the pristine Pd wire has a significantly higher catchment rate compared to the wire where the surface already contains Pt in addition to Pd. It can also be

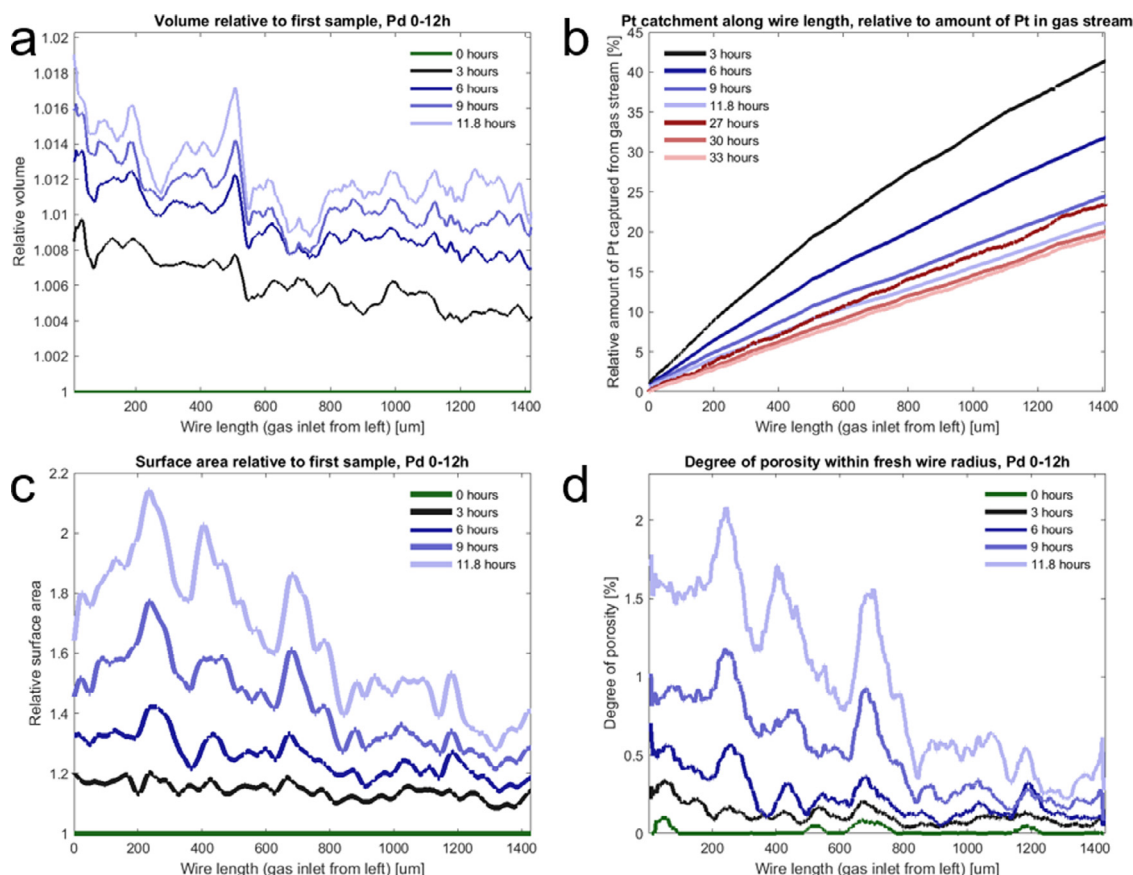


Fig. 5. (a) Volume increase along the wire length relative to the Pd-wire at $t = 0$, (b) total catchment efficiency along wire length calculated from volume increase and the $p(\text{PrO}_2)$ in the gas stream, (c) change in surface area relative to the Pd wire at $t = 0$, and (d) degree of porosity along the wire length. Time is indicated by the colour scheme in the figure.

noted that the surface area increases more at the inlet end (Fig. 5c), and the porosity is much higher near the inlet end (Fig. 5d). However, there is no similar correlation to the intensity along the wire length (Fig. S7a). This is probably related to the fact that the intensities in this experiment are not quantitatively reliable, and we have more confidence in the volume calculations. For the Pd 24–34 h sample, no significant change in the volume and surface area along the wire length is observed (Fig. S7d,e). For the Pd/Ni 0–12 h sample, there is also a larger increase in radius near the gas inlet (Fig. S7c). Based on the observations of the Pd 0–12 h sample during Pt-catchment conditions, we believe that a higher $p(\text{PrO}_2)$ causes increased Pt-catchment, which correlates with more severe morphological changes. Additionally, a surface with both Pt and Pd does not capture Pt equally well as a pure Pd surface.

3.1.3. In situ absorption-CT of Pd/Ni wires from 0 to 7 days

We have also investigated several Pd/Ni wires with *in situ* absorption-CT (Table 1). Despite the poor contrast between NiO and void/space, we take notice of several trends. Volume, radius, surface area and pore depth generally increase between and during all experiments. This shows that a steady grain reconstruction process occurs in a similar manner for both pure Pd and Pd/Ni, in line with previous studies [4]. More information on the Pd/Ni wires can be found in the supplementary information Section S.1.4.

3.2. Qualitative analysis of Pd/Ni and pure Pd wires from 0 to 10 days

In Fig. 6 we compare *ex situ* tomograms collected at room temperature for both Pd and Pd/Ni wires after Pt catchment experiments performed in our home laboratory furnace. The initial surface roughness

develops with time into large crystallites. The combination of crystallites on the surface and porosity developing inwards causes a complete wire reconstruction over the course of 10 days. We can see that the development of the wires is very similar for Pd and Pd/Ni (Fig. 6a and c).

The sample intensity (excluding the pores) initially increases near the surface for both materials (Fig. 6b and d), indicating similar Pt catchment. With time (≥ 7 days), the Pd and Pd/Ni wires show an elevated intensity also near the centre, indicating that Pt is incorporated in the entire wire. After the recrystallization process has propagated through the entire wire (~ 10 days), the largest crystallites are located far from the wire centre, leaving behind significant voids inside the sample. This is clearly seen from the cross section of the Pd-wires in Fig. 6e.

3.3. Additional experiments to support absorption-CT data

3.3.1. ICP-OES and SEM/EDX analyses of exposed *in situ* absorption-CT samples

In order to determine the total quantity of Pt the wires captured during the *in situ* absorption-CT experiments, ICP-OES analyses were performed on selected Pd and Pd/Ni samples. The ICP-OES results (Table 2) show that the Pt content increase with increasing PtO_2 exposure times for both samples. However, the Pt-content on the Pd/Ni alloy after 4 days is lower than that after 1 day. We believe this is simply due to the fact that the piece of wire sent for ICP-OES was located close to the rear end of the wire during heating, and did thus not capture as much Pt as the first wire. Still, the wire had significantly larger degree of reconstruction after 4 days compared to 1 day (Fig. 6). Additionally, it appears as the Pd/Ni wire captured more Pt than the pure Pd wire after

Table 2
ICP-OES analysis of Pd and Pd/Ni (91.3/8.7 at.%) wires after *in situ* absorption-CT experiments at 1000 °C in a flow of air with Pt upstream. Elemental compositions are reported in at.%.

Sample	Time [d]	Pd [at.%]	Pt [at.%]	Ni [at.%]	Pt/(Pd+Pt+Ni)	Pt/(Pd+Pt)	Ni/(Ni+Pd)
Pd-Ni	1	85.6	4.6	9.8	4.6	5.1	10.3
Pd-Ni	4	87.6	3.7	8.7	3.7	4.0	9.0
Pd-Ni	7	80.5	10.5	9.0	10.5	11.6	10.0
Pure Pd	1	96.7	3.3	–	–	3.3	–
Pure Pd	2.5	95.1	4.9	–	–	4.9	–
Pure Pd	4	93.6	6.4	–	–	6.4	–
Pure Pd	7	86.1	13.9	–	–	13.9	–
Pure Pd	10	79.9	20.1	–	–	20.1	–

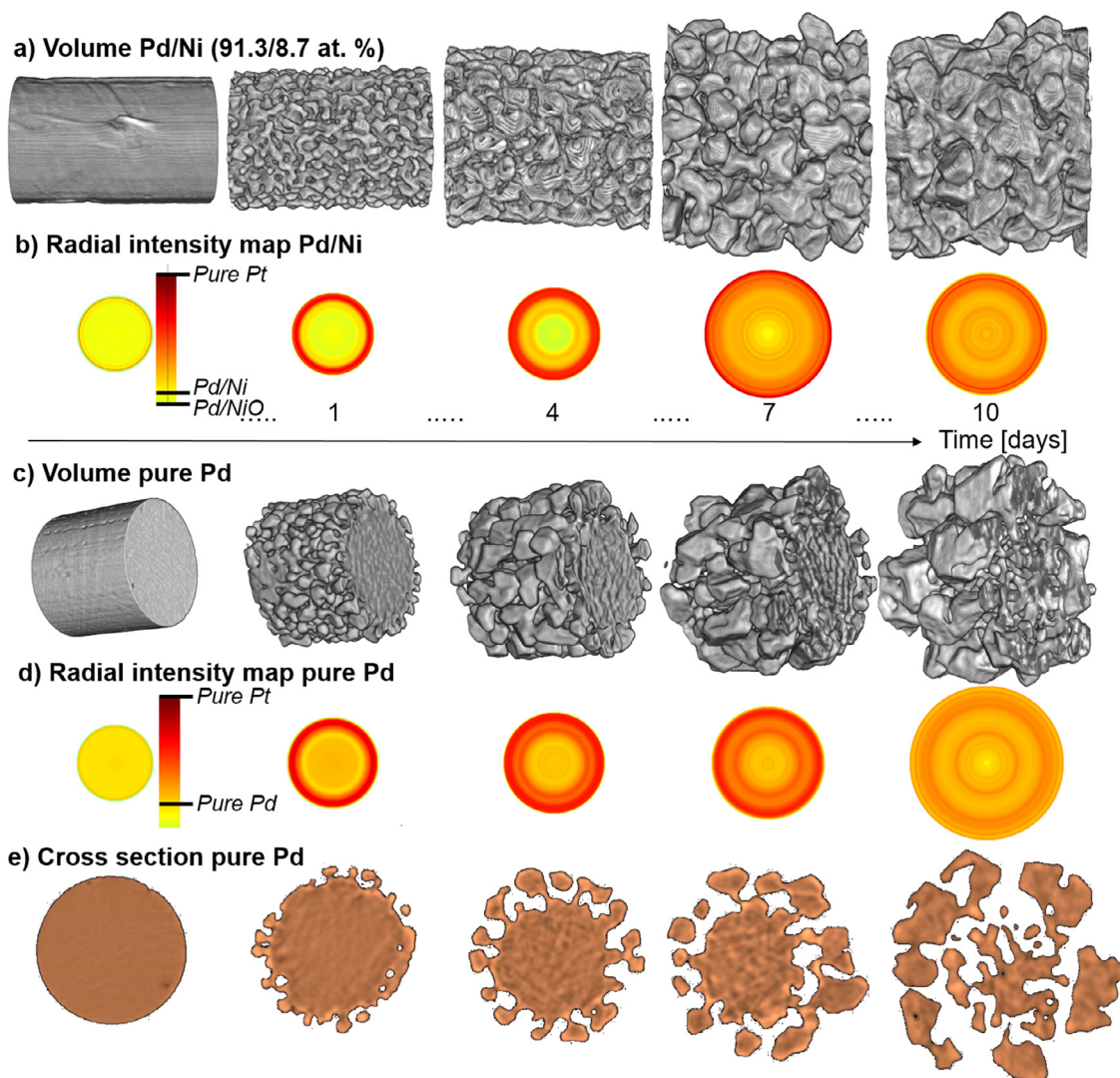


Fig. 6. Illustration comparing the time development of (a–b) Pd/Ni (91.3/8.7 at.%) and (c–e) pure Pd. The figure shows (a) volume rendering and (b) radial intensity map of the sample (excluding pores) of Pd/Ni (91.3/8.7 at.%). It further shows (c) volume rendering, (d) radial intensity map of the sample (excluding pores) and (e) cross section of pure Pd. The Pd/Ni samples are viewed only from the side due to missing contrast between voids and NiO in the sample cross section.

1 day, while after that, the Pd wire is slightly faster. We interpret these minor differences to be within the uncertainty of the experimental Pt-catchment setup and the ICP-OES measurements, and conclude that Pd and Pd/Ni wires captures Pt with similar rates.

Since ICP-OES only give information on the overall Pt content, additional SEM/EDX analyses were carried out to get more detailed insight into the atomic distribution of Pt in the Pd and Pd/Ni samples, see Fig. 7 and Table 3. The Pt-concentration in the wires increases with time, and

it increases slightly faster for pure Pd compared to Pd/Ni (Table 3). Additionally, in the pure Pd-wire, Pt has diffused into the core of the wire via the grain boundaries, forming a complete grain boundary network through the wire (Fig. 7a). This is not the case for the Pd/Ni wire, where only a weak grain boundary pattern is seen close to the surface (Fig. 7b). The same effect is present in the wires after 4 days (Fig. 7c,d). The darker areas inside the pure Pd wire heated for 4 days (Fig. 7c) have a smaller Pt-content compared to the surrounding areas, which is

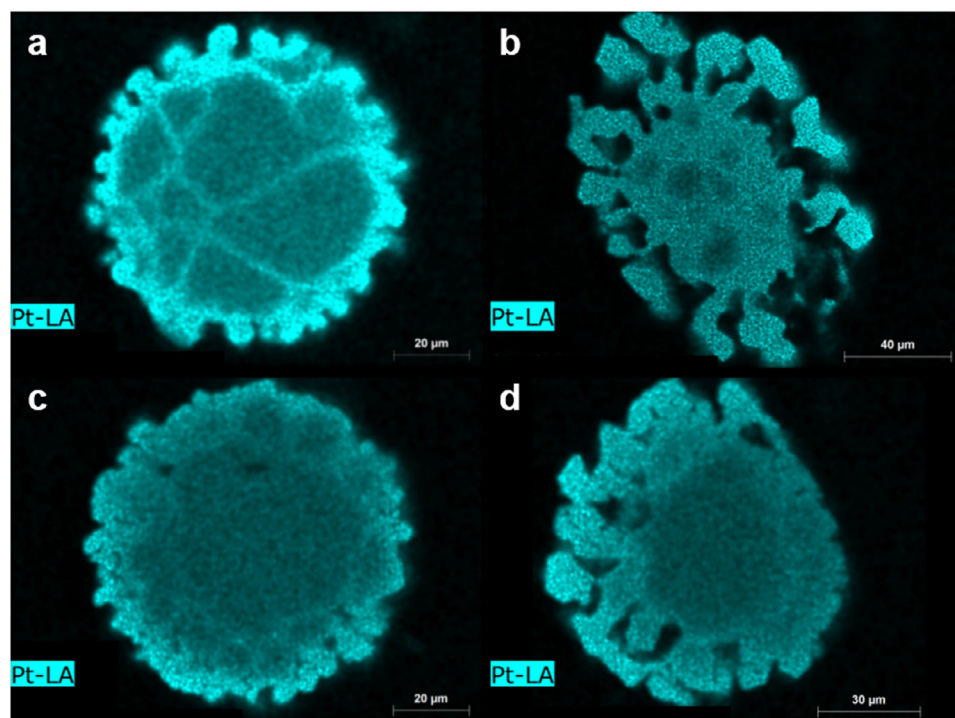


Fig. 7. EDX-maps of samples pre-treated for the *in situ* absorption-CT experiment. (a) Pure Pd treated for 1 day, (b) pure Pd treated for 4 days, (c) Pd/Ni (91.3/8.7 at.%) treated for 1 day and (d) Pd/Ni treated for 4 days.

Table 3

Quantitative EDX-values from the surface and cross section of the Pd/Ni (91.3/8.7 at.%) and pure Pd wires. Data is collected from the cross sections shown in Figs. 7 and S11.

Pt/(Pd+Pt)	Time [days]	Surface crystal [at.%]	1–2 μm from surface [at.%] [*]	Centre [at.%] [*]
Pd/Ni	1.0	4.7	5.0	0.0
Pd/Ni	2.5	3.8	3.4	0.0
Pd/Ni	4.0	10.9	5.7	0.1
Pd/Ni	7.0	14.5	12.8	1.7
Pd/Ni	10.0	15.0	11.0	0.1
Pure Pd	1.0	7.3	5.1	0.0
Pure Pd	2.5	6.3	4.0	0.0
Pure Pd	4.0	11.5	12.5	3.2 / 1.4 ^{**}
Pure Pd	7.0	22.9	11.0	4.4 / 2.7 ^{**}
Pure Pd	10.0	26.5	22.5	13.1

^{*} Obtained from sample cross section.

^{**} two different values are found for the Pt-content in the core. The high (low) value is the bright (dark) regions in Fig. 7.

probably the centre of the grains. These areas contain ~ 2 at.% less Pt than the surrounding Pt-rich areas (Table 3). An additional reason for the higher Pt-concentration in the core of the pure Pd wire heated for 4 days could be because it reconstructs more heavily than the Pd/Ni wire, allowing Pt to diffuse more easily into the wire centre due to a shorter diffusion path.

Comparing the EDX analysis (Table 3) to the ICP-OES results (Table 2), we see similar trends in increased Pt-content with time. The Pt-content in the two samples is very similar in the ICP-OES measurements, but from EDX, the pure Pd sample is more rich in Pt. This is most probably because the Pt-exposure varies significantly through the length of a wire, and the piece investigated with EDX may be slightly different from that investigated by ICP-OES. Because ICP-OES averages a larger piece in the analysis, it is reasonable to believe that pure Pd and Pd/Ni captures Pt approximately equally fast.

3.3.2. Pre-treated samples prior to lab scale Pt-catchment experiments

In order to supplement the *in situ* absorption-CT experiments, additional catchment experiments were performed in our laboratory scale

furnace system at UiO. In this case, we wanted to explore the effect of Pt-catchment without the presence of grain boundaries in the wire, *i.e.* a quasi monocrystalline wire. This was achieved by pre-annealing Pd and Pd/Ni nets, identical to those used in the absorption-CT experiments, for 7 days in vacuum at 1100 °C. The new grain structure of the Pd and Pd/Ni nets are nicely seen in Fig. 8a and g, where it is possible to see grain boundaries crossing the wire every ~ 20 – $200 \mu\text{m}$. After 10 days of Pt-catchment at 900 °C, the mass increase reveal that the Pd/Ni net contains ~ 2.6 at.% Pt, and the pure Pd net contains ~ 2.3 at.% Pt. Relative to a polycrystalline net, where Pt-contents of 20–30 at.% is expected after a 10 days' experiment, this is a very low level of catchment.

SEM/EDX investigation of the quasi monocrystalline samples (Fig. 8) show only minor morphological changes of the wire shape at some locations. This contrasts the observations on the polycrystalline wires (Fig. 2), where complete grain reconstruction is observed after 10 days. Still, several small surface crystals have appeared on the surface of the Pd/Ni wires (Figs. 8j and S12f), which occurs to a lower extent for the pure Pd wires (Fig. 8b and d). Viewing the wire cross sections, the Pd/Ni wire surfaces are rougher than for pure Pd (Fig. 8e and h). From qualita-

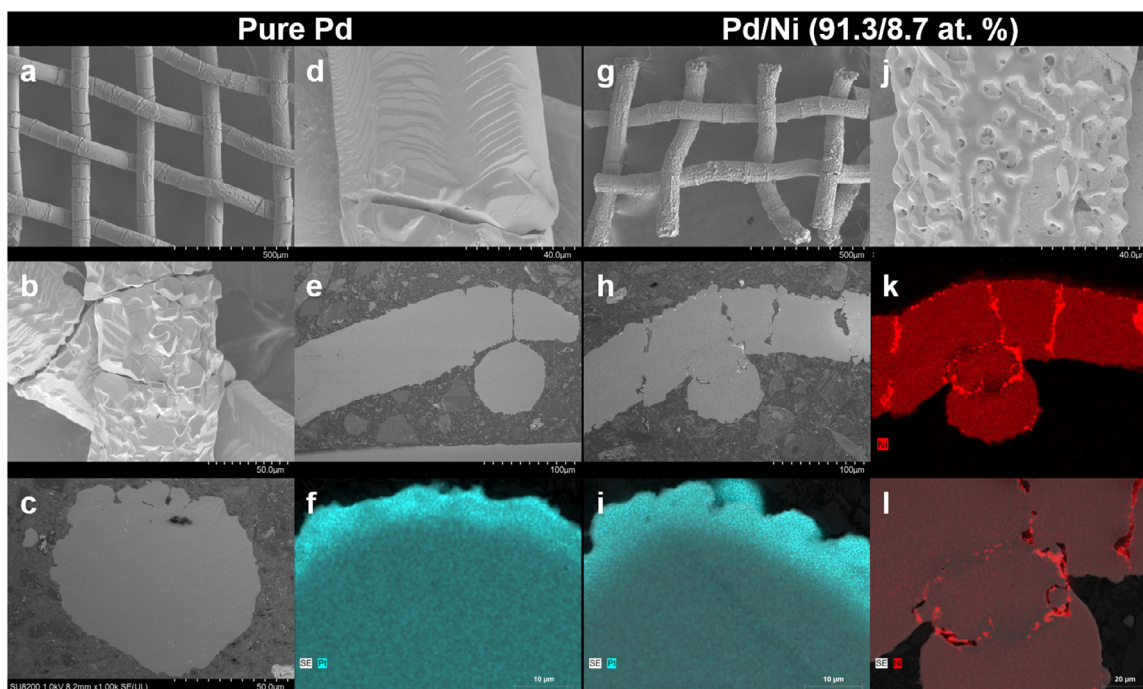


Fig. 8. SEM/EDX images of the surface and cross section of 76 μm quasi monocrystalline (pre-annealed) pure Pd (left; a–f) and Pd/Ni (91.3/8.7 at.%) (right; g–l) wires after a 10-day Pt-catchment experiment at 900 $^{\circ}\text{C}$. The cyan coloured EDX maps show Pt, while the red EDX maps show Ni. More SEM/EDX data is shown in Figs. S12 and S13.

tive EDX mapping, the Pt-distribution close to the surface is similar for the two samples (Fig. 8f and i). Pt is located close to the surface, and has penetrated $\sim 10\ \mu\text{m}$ into the wire. For the two EDX maps with Pt shown in Fig. 8 (f and i), the pure Pd wire contains 6 at.% Pt (10 wt.%) at the points richest in Pt, and the Pd/Ni wire contains 11 at.% Pt (18 wt.%). EDX analysis of the wire surfaces show similar Pt-contents, however slightly larger, ranging from 10 to 20 at.% Pt for both samples. The low amount of Pt captured on the quasi monocrystalline Pd and Pd/Ni samples may suggest a lack of transport of Pt into the wire core, and that mainly the wire surface is enriched in Pt during Pt-catchment.

The degree of surface reconstruction varies significantly with location, which is seen both from SEM/EDX analysis of these samples (Fig. 8; additional data in Figs S12 and S13) as well as on the additional Pt-catchment experiments presented in the supplementary section (Section S.2.2). Certain regions of the samples show a significantly higher surface reconstruction compared to other regions located only a few hundred μm away (Fig. S15), which is likely due to a much higher gas exposure for the highly reconstructed regions. It is fair to assume that the reconstruction is more severe at locations exposed to a higher gas flow, simply because it is then exposed to more PtO_2 .

The grain boundaries are distinct in the wire cross section for both samples, where pores/voids have formed at several locations (Fig. 8e and h). At some locations, the pores go through the entire wire cross section, or just partly into the wire cross section, or pores/voids are present inside the wire (more images in Figs. S12–S17). It is hard to say if these pores/voids are located within the wire volume, or if it is open porosity connected to the air around the sample. On rare occasions, pores/voids are also found on locations not looking like a GB, *i.e.* in the bulk grains. For most of the samples, EDX mapping show carbon in the pores/voids, indicating that the casting material has entered the pores during sample preparation for SEM/EDX, and that the pores are open. However, the casting method applied for sample preparation uses extensive force, and we cannot rule out or confirm if internal voids are present. We recommend that a more delicate analysis of the presence of internal voids are performed in dedicated experiments.

For the Pd/Ni wire, NiO particles are also present inside the sample. Several NiO particles are located near/in the pores/voids (Fig. 8k,l), and these NiO particles are generally larger than average. It is previously reported that the largest NiO precipitates are formed in the GBs [4]. However, it is difficult to conclude if NiO moved to the pores/voids after the pores/voids appeared, or if the pores/voids appear as a result of the presence of the large NiO particles. As this analysis is based only on a few 2D images of the sample, the exact characteristics of the pores/voids and NiO in the quasi monocrystalline wires remain unexplained.

3.4. Grain boundary diffusion coefficient of Pt in Pd

Two diffusion experiments were performed to investigate the diffusion coefficient of Pt in Pd, using a single crystal (111) and a polycrystalline disc of pure Pd. The bulk diffusion coefficient is well known from literature, and in our experiment we find that the bulk diffusion coefficient from both the single crystal and polycrystalline disc fits very well with literature reports ($D_{\text{Pt}} = 3.26 \times 10^{-14}\ \text{cm}^2/\text{s}$ [35]), see Fig. 9a. The polycrystalline disc was annealed for 4 h and 35 min, while the single crystal was annealed for 23 h. To compare the results, the data for the polycrystalline disc was normalized to that of the single crystal, see Fig. 9b (calculation shown in Supplementary Section S.2.3). When plotting $\log(\text{Pt-concentration})$, it becomes clear that the deepest part of the diffusion profile of the polycrystalline disc is different from that of the single crystal (inset in Fig. 9b). The mathematical fit follows the data for the single crystal, and does not fit the tail of the polycrystalline data deeper into the wire than $\sim 1.5\ \mu\text{m}$, a region which corresponds to grain boundary diffusion. Following the procedure from Le Claire [36] (see Supplementary Section S.2.3), a linear fit was obtained from the tail of the diffusion profile when plotting the natural logarithm against depth to the power of 6/5 (Fig. 9c). A different value is obtained from the original and normalized data set, but with a small difference. Trusting the original (non-normalized) data set, the obtained GB diffusion coefficient for Pt in Pd is $D_{\text{GB}} = 2.9 \times 10^{-8}\ \text{cm}^2/\text{s}$.

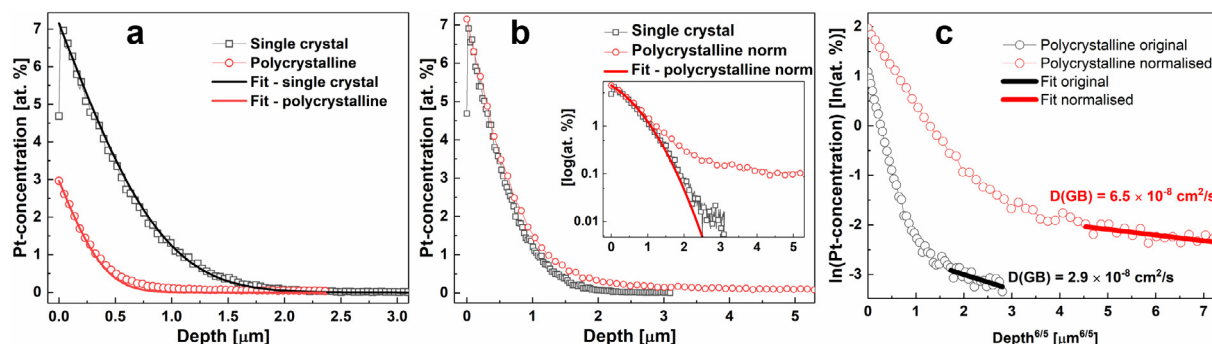


Fig. 9. (a) Raw data diffusion profiles of the Pd single crystal and polycrystalline Pd disc, with a fit calculated from $D_{Pt} = 3.26 \times 10^{-14} \text{ cm}^2/\text{s}$. (b) Comparison of the data for the single crystal and polycrystalline disc after normalising the data for the polycrystalline disc. (c) $\ln(\text{Pt-concentration})$ versus $\text{depth}^{5/6}$ and the linear fits obtained for the two versions of the data set for the polycrystalline disc. The obtained GB diffusion coefficients are included in figure c.

4. Discussion

4.1. Tomography

The propagation of the grain reconstruction process that occurs during Pt-catchment on Pd-based alloys is poorly understood. In this study, we have combined *in situ* absorption-CT, with several *ex situ* techniques to understand the fate of the Pd and Pd/Ni wires during Pt-catchment. The main advantage of tomography is the possibility to visualize both the surface morphology and bulk content of a 3D object. Standard experiments with e.g. SEM of cross sections yield only one image slice, compared to thousands of slices for each sample in tomography.

Technically, performing an *in situ* X-ray tomography experiment requires several challenges to be addressed; to ensure spatial resolution, elemental contrast (quantitative information if possible) and time resolution. Additionally, the requirements above must be met while using both high temperature (1000 °C) and gas flow. Several different techniques can be used to obtain tomography images. One possibility is to use μ -beam CT, which uses a beam with a narrow cross section to scan through the sample. By using X-ray diffraction (XRD), X-ray absorption spectroscopy (XAS) or X-ray fluorescence (XRF) as contrast, one obtains a spectrum for each voxel, which in turn is analyzed to yield quantitative information. A collective name for these techniques is physio-chemical imaging, which have been successfully applied to several catalyst investigations [20–22]. However, μ -beam CT requires time to scan through the sample (~5–50 min), which means the materials in question should not change in the time scale of the measurement, or the chemical reaction should be paused during data collection. Additionally, at high temperature (1000 °C), it may be difficult to ensure that the material does not move or vibrate during the measurement, which will affect the resolution. μ -beam CT is therefore best suited for *ex situ* experiments, or in experiments where the chemical reaction is paused during the data collection.

In our case with 76 μm noble metal wires, high temperature, and medium rapid changes, absorption-CT is the best possible technique, which allows data collection in the range of 10 s. The only drawback is the non-quantitative intensities, which may cause low elemental contrast for multi-component systems (Section S.1.2.2). However, this could be overcome by using different beam energies in different parts of the experiment, to provide optimal contrast between the different components of the sample, while maintaining high resolution.

4.2. On the grain reconstruction process

In this study, we have found that the Pd and Pd/Ni wires undergo a large increase in volume and surface area during Pt-catchment experiments, which is caused by surface crystallites growing on the wire surface and porosity developing inwards into the wire (Fig. 6). We also

find that the Pt-catchment rate depends on both the $p(\text{PtO}_2)$ above the wire and the Pt-concentration on the wire surface (Fig. 5), and that morphological changes correlate with high Pt catchment. Long duration also causes more grain reconstruction, *i.e.* a long experiment with low $p(\text{PtO}_2)$ can cause equally or more reconstruction than a short experiment with high $p(\text{PtO}_2)$ (Fig. 3). Polycrystalline samples show Pt-penetration through the entire wire, enabled by rapid GB diffusion (Fig. 7), which is not possible for the quasi monocrystalline samples (Fig. 8). However, this also shows that the GBs are a prerequisite for the large degree of reconstruction, which occurs for the polycrystalline samples.

The Pt-catchment phenomena has only been investigated in a handful of studies [4–18], and the coupled Pt-catchment – Pd-reconstruction process is barely addressed. Ning et al. [7] suggested that a re-alloying and recrystallization process causes the morphological changes of the Pd-based wire, and Pura et al. [6,14] concluded that deep recrystallization occurs, along with etching of wide angle grain boundaries. Though the most recent publication, from 2019, confirms the cause-effect relation between Pt-catchment and grain reconstruction in laboratory experiments [4], the mechanism remains unexplained. Actually, similar morphological changes and recrystallization phenomena as we observe are described in several different corrosion studies [23–25]. Severe surface recrystallization is reported during the oxidation of Mn-containing IF steel [24,25], and the appearance of internal porosity is reported during the oxidation of Ni metal [23]. In such investigations on metal alloy oxidation, oxygen is often the key diffusing species [37]. To understand the underlying mechanism, it is also important to identify the rate determining step in the corrosion process.

During Pt catchment experiments, both PtO_2 and O_2 are present in the gas phase, but PtO_2 is the key constituent causing grain reconstruction. The rate-limiting step in this process is likely to be either (1) transport of PtO_2 from the gas phase to the wire surface, accompanied by the transformation of PtO_2 into Pt, or (2) the diffusion of Pt into the Pd-wire. We therefore address the journey of PtO_2 from the gas phase and into the Pd wire, as visualized in Fig. 10.

4.3. Transport of Pt from the gas phase to the wire surface

Let us first consider the transport of Pt from the gas phase to the surface, *i.e.* $\text{PtO}_2(\text{g}) \rightarrow \text{Pt}(\text{s}) + \text{O}_2(\text{g})$. When Pt arrives on the surface and forms a solid solution with Pd, the oxygen content in the wire is low [4], and we can say that it is a metallic alloy. We therefore believe that oxygen acts mainly as a spectator in the grain reconstruction process, and that the active species are Pt and Pd.

During the first 3 h of the *in situ* absorption-CT experiment on pure Pd, the Pt catchment efficiency is ~42% (Fig. 5). This is quite high considering that maximally 50 ppb of PtO_2 is present in the gas phase. The gas velocity (0.59 m/s) tells us that Pt only has a contact time of ~2.5

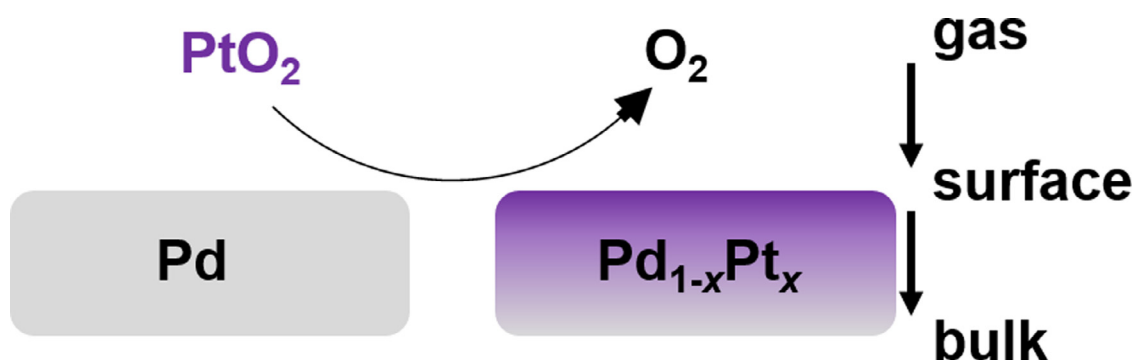


Fig. 10. Schematics of the steps in the Pt-catchment process. Pt travels from the gas phase and into the bulk, via the surface.

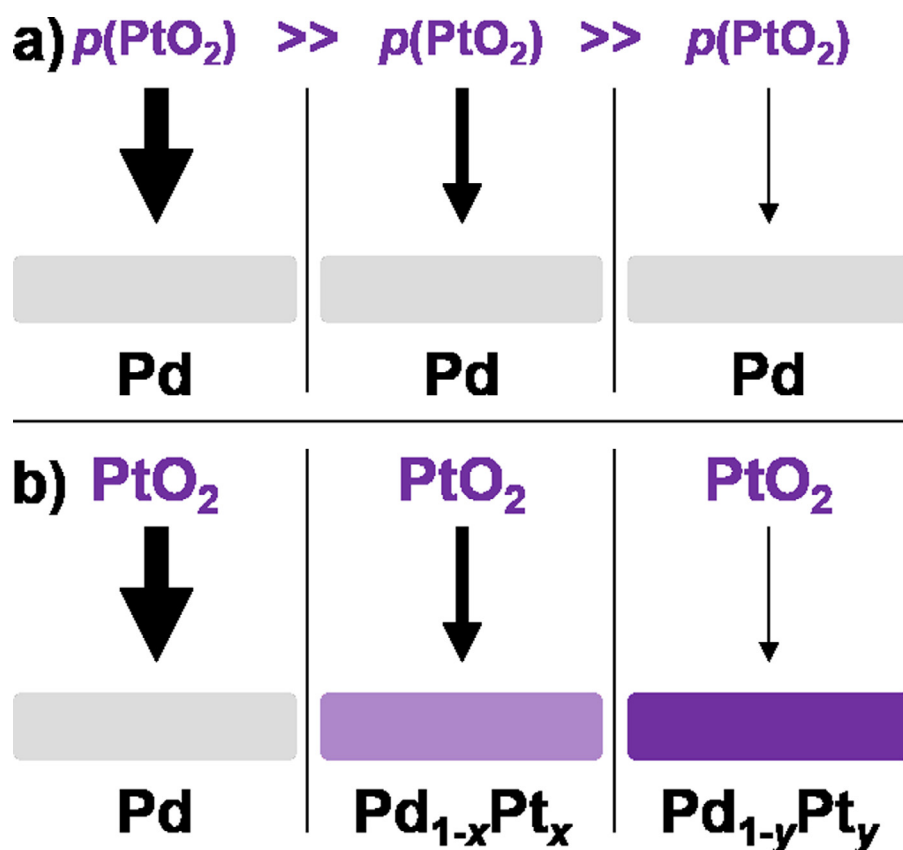


Fig. 11. (a) Schematic illustrating how high/low $p(\text{PtO}_2)$ causes more (thick arrow) and less (thin arrow) Pt-catchment onto a Pd-surface, (b) schematic illustrating the slower Pt-catchment rate of a Pd sample which is already enriched in Pt, where the more purple samples contain more Pt ($y > x$).

milliseconds for it to be absorbed on the 1.5 mm wire piece used in the absorption-CT experiments. This narrow time window combined with a quite high catchment rate indicates fast kinetics for the Pt-deposition. After 12 h on stream, the catchment efficiency is reduced to ~18–22% (Fig. 5), *i.e.* a small addition of Pt to a pristine Pd-surface significantly reduces the catchment efficiency, even though the surface area has almost doubled. This correlates well with the low catchment abilities of the quasi monocrystalline Pd-wires, which has a high surface concentration of Pt and reaches a catchment limitation (Fig. 8). This leads us to conclude that less Pt is captured on a surface which is already enriched in Pt, as illustrated in Fig. 11. This is reasonable considering that a nm-thin layer of Pt dominates the surface of a Pd/Pt (31/69 at.%) alloy at temperatures above the stability temperature of PdO [38].

The rapid kinetics for Pt-catchment imply that the Pt deposition (gas \rightarrow surface) is sufficiently fast to not be the rate-limiting step. But the surface concentration of Pt has a significant impact on the Pt deposition rate. It is more likely that the properties of the bulk

wire, *i.e.* diffusion and the surface concentration, are the limiting factors.

4.4. Diffusion in Pd

In the situation just after Pt is captured on the Pd wire surface, a gradient in Pt-concentration will span from the surface and into the wire core. This gradient in chemical potential causes Pt and Pd to diffuse towards each other and mix, because there is an energetic gain in mixing ($E_{\text{mix,Pt-Pd}} = -2.9$ kJ/mol) relative to formation of separate phases [39]. This is also evident from the Pd-Pt binary phase diagram, where the two components are completely miscible over the entire compositional range at high temperature [40]. *I.e.*, there is a chemical drive toward inward diffusion of Pt, and outwards diffusion of Pd.

From Baheti et al. [35], Pd diffusion in bulk Pd is slightly faster than Pt diffusion in bulk Pd, and the dominating diffusion mechanism is vacancy diffusion. Additionally, for Pd with 3.5 at.% Pt, the diffu-

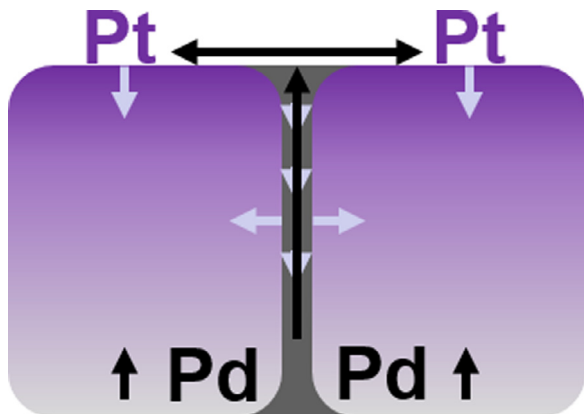


Fig. 12. Schematic illustration of the different diffusion paths in the Pt catchment process. Two grains are positioned next to each other, separated by a GB. Pt is diffusing into the grains from the surface and the GB, while Pd is diffusing towards Pt in the bulk and via the GBs.

tion coefficient of Pd is ~ 2 order of magnitude higher than that of Pt (Table S4). This imply that Pd-diffusion should be slightly faster than Pt-diffusion during Pt-catchment experiments. However, for both constituents, it is likely that GB diffusion is significantly faster. We have found that the GB diffusion coefficient for Pt in Pd (Fig. 9) is ~ 5 orders of magnitude higher than that reported in bulk at 900 °C. The rapid GB diffusion coefficient also manifests itself clearly in Fig. 7, where Pt has been transported to the centre of the wire core via the GBs already after 24 h. It is also reasonable that Pd has a similarly high GB diffusion coefficient as Pt. This leads to a series of different diffusion paths, which are illustrated in Fig. 12. In this scenario, where GB diffusion is significantly faster than bulk diffusion, bulk diffusion could be the rate-limiting step.

4.5. Simulated diffusion model

To understand the role of diffusion, in both bulk and in the GBs, a simple 2D diffusion model was constructed using matlab [31] (see Supplementary Section S.3 for a complete explanation). The model is based on a circular sample, which simulate the cylindrical shape of the Pd-wire. Diffusion is considered from the wire surface, using a bulk diffusion coefficient of $D_{Pt} = 3.26 \times 10^{-14}$ cm²/s and our obtained grain boundary diffusion coefficient of $D_{GB} = 2.9 \times 10^{-8}$ cm²/s (Table S4). The input parameters were chosen with the purpose to replicate the relevant Pt-catchment conditions ($T = 900\text{--}1000$ °C, $p(\text{PtO}_2) = 5 \times 10^{-8}$ bar).

Previous work by Håkonsen et al. [41] has showed that the maximal Pt-concentration, which can be obtained on the surface of Pd-Pt alloys during Pt-catchment experiments, is near 35 at.%, and depend on the partial pressure of PtO₂ ($p(\text{PtO}_2)$) in the experiment. We therefore limited the maximal surface concentration to two different values in two different sets of simulations, to see the effect of a limiting surface concentration; 35 and 20 at.%. In addition, we perform the simulation both for a scenario of a polycrystalline and a monocrystalline sample at three different temperatures, which becomes 12 different data sets. The model also includes a limiting rate of Pt-catchment, based on the results from the *in situ* absorption-CT experiment, where a linear increase in the volume of the Pd wire was observed over the first 4 h for pure Pd (1.0% after 4 h, Fig. S6a). The simulations were run for three different scenarios/models:

- (1) *Monocrystalline Pd-wire.* This model displays the simplest scenario, considering Pt diffusion into a monocrystalline Pd-wire, using only the bulk diffusion coefficient for Pt in Pd. A radial diffusion profile is obtained for simulations using this model (Fig. 13).
- (2) *Filling of the grain boundaries.* This model takes into account both bulk- and GB diffusion. During the simulation, the GBs are rapidly

filled up with Pt, much faster than Pt is transported into the bulk (Fig. S24). During the initial 200–500 s of Pt-catchment, the model shows that this is the time needed to almost completely fill the GB with Pt (Fig. S25).

- (3) *Polycrystalline Pd-wire.* This model includes diffusion from both the GBs and the surface, but uses only the bulk diffusion coefficient. The model considers the GBs as surface, and adds Pt equally fast to both the surface and the GBs, i.e. the GBs act as a surface with respect to being a source of Pt available for diffusion. In this way, only the bulk diffusion coefficient is taken into account. This is perhaps an overestimation of the diffusion in the polycrystalline wire, but may also be realistic considering that the polycrystalline sample reconstructs and obtains a much higher surface area during Pt-catchment. It is also a necessary assumption to reduce the computational time. We can then follow the expected development of the Pt-concentration in a polycrystalline Pd-wire over a 10-day diffusion simulation (Fig. 13).

The diffusion model (Figs. 13 and S27) show that inwards diffusion of Pt is inherently slow in the monocrystalline samples, and that temperature has a significant impact on the quantity of Pt which can be absorbed by bulk diffusion (3% at 900 °C versus 12% at 1000 °C), along with the maximal Pt-concentration on the surface. The polycrystalline sample is limited in a similar way, but not to the same extent due to a much smaller grain size, and thus a shorter diffusion distance. Still, it is only at 950 °C and above that the polycrystalline wire absorb the quantity of Pt obtained in Pt-catchment experiments at 1000 °C (ICP-OES data, Table 2). The diffusion model for the monocrystalline sample at 900 °C correlate well with the quasi monocrystalline sample treated at 900 °C (Section 4.3.2).

Overall, there are two main limitations for the quantity of Pt which can be absorbed by diffusion; the diffusion constant and the surface concentration of Pt. A third limitation for the total catchment/absorption of Pt is the rate of Pt which can be captured from the gas phase by the Pd wire as function of time. In the beginning of the diffusion simulation, the Pt-catchment abilities of the Pd-wire is the limitation (Fig. 13, linear region with a dark red dashed line), which we have included because of the linear increase in Pt-concentration the first 4 h of Pt-catchment (Fig. 3a), before the Pt-catchment rate is reduced. This also correlates with our observations that a pristine Pd-wire captures Pt significantly faster than a wire that is already enriched in Pt (Fig. 5).

After the initial phase of the Pt-catchment experiment, the surface is nearly saturated with Pt due to a limited bulk diffusion. At this point, the second regime limiting Pt-catchment takes over, which is the reduced Pt-deposition onto the surface (Fig. 13, bright red and blue dashed lines). For lower temperatures and slower bulk diffusion, and larger grain size, the diffusion limitation strikes earlier in the experiment, and the transition from the first (maximal Pt-catchment possible) to second (diffusion/Pt-deposition) limitation occurs earlier (Fig. S27). The fact that the surface concentration of Pt develops gradually during real experiments means that the transition between these two regions is gradual. In our physical diffusion experiment (Section 4.4), the real surface concentration is only 7 at.% after 23 h, meaning that different surface concentrations will indeed affect the quantity of Pt absorbed by diffusion. From these results, we find it probable that bulk diffusion is the rate-limiting step in the Pt catchment process on Pd, at least after the initial hours of Pt-catchment.

4.6. Diffusion limitation – deposition limitation

With basis in the findings from the diffusion simulations (Supplementary Section 5.5), we can now ask, what is the result of the bulk diffusion limitation in Pd? The bulk diffusion limitation causes an elevated Pt-concentration on the surface, which again causes reduced deposition of Pt from the gas phase onto the wire. The diffusion limitation is therefore dictating the Pt catchment efficiency. This is probably due to an equilibrium between the Pt on the sample surface and the PtO₂ in the

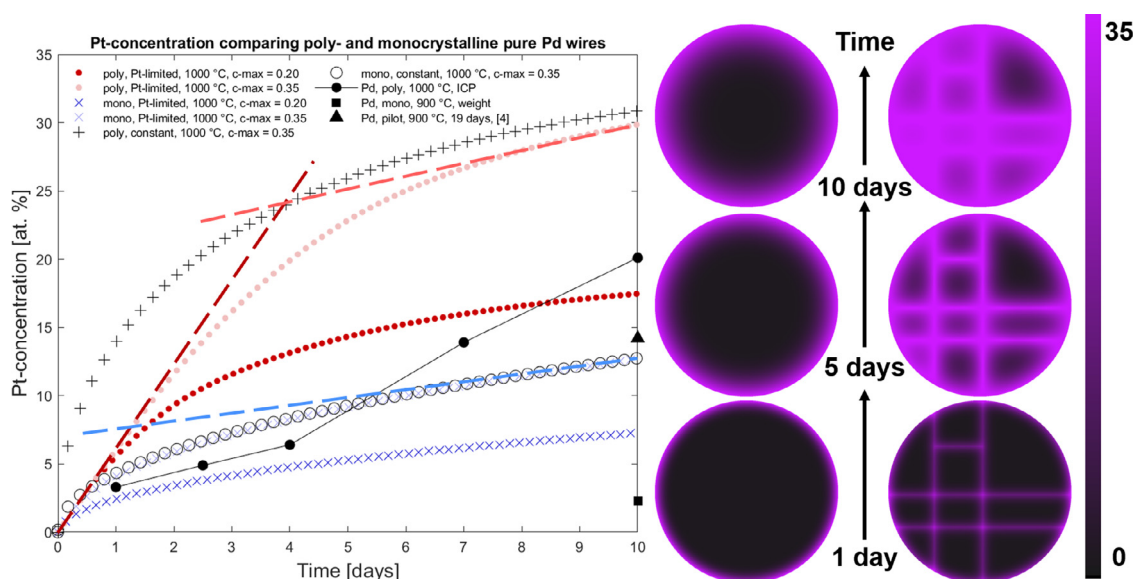


Fig. 13. Left: Pt-concentrations *versus* time calculated using the diffusion model for the poly- and quasi monocrystalline wires at 1000 °C, Pt-content for the investigated polycrystalline samples collected with ICP-OES and for the quasi monocrystalline sample collected by mass changes, and Pt-content in the pilot plant sample from Fjellvåg et al. [4]. The model with a limited Pt-catchment based on absorption-CT results is denoted “poly/mono limit”, while the model denoted “poly/mono” used the constant surface concentration (*c*-max) throughout the simulation. The dashed straight lines indicate the two different limiting regions during Pt-catchment. Right: Colour map showing the 2D diffusion profile of Pt (dark purple) into Pd (black) for the mono- (left) and polycrystalline (right) samples at 1000 °C for the indicated time. A colour bar is shown on the far right. The results from the diffusion model at 900 and 950 °C are presented in Fig. S27.

gas phase, *i.e.* re-evaporation of Pt during catchment, which results in no net Pt-catchment (the so-called “issue of a limiting Pt-concentration during Pt-catchment”, studied by Håkonsen et al. [41]). This correlates well with the results by Holzmann, where a pure Pt catchment gauze did not capture any Pt during pilot testing of different catchment gauzes [5].

Bringing back the analogy of base metal oxidation, in some cases, the inwards diffusion of oxygen is the rate-limiting step, causing the outwards diffusion of metal to be faster than the inwards diffusion of oxygen. This leads to a special scenario where metal atoms diffuse out to the surface. This is the case for oxidation of bulk Ni to NiO, where the outwards Ni-diffusion is faster than the inwards O-diffusion, through the NiO layer that forms during oxidation [23,42]. It is also the case for the Mn-containing IF steel investigated by Zhang et al. [24,25], where inwards oxygen diffusion was the limiting factor. This caused Mn to diffuse through the GBs, to the surface, and cause a recrystallization on the surface. In our Pd-Pt (Pd/Ni-Pt) system, multiple diffusion paths are available, as illustrated by Fig. 12. The inwards Pt-diffusion is limited, as described by the diffusion model above. However, outwards Pd-diffusion, especially through the grain boundaries, is important in this system for two main reasons:

- (1) There is a driving force for diffusion of Pd to the surface, to mix with the incoming Pt from the gas phase ($E_{mix, Pt-Pd} = -2.9$ kJ/mol [39]).
 - (i) This is driven strongly by the fact that Pt does not continue to deposit on the surface unless the Pt-concentration on the surface is sufficiently low (dependent on temperature and $p(PtO_2)$).
- (2) The bulk diffusion coefficient for Pd is higher than for Pt.
 - (i) $D_{Pt} = 3.26 \times 10^{-14}$ cm²/s and $D_{Pd} = 2.85 \times 10^{-13}$ cm²/s [35] at 900 °C.

Due to these factors, there is probably a large flux of Pd diffusing outwards of the Pd-wire and towards the surface to mix with Pt. If the outward Pd-diffusion occurs as vacancy hopping, a large flux of vacancies diffuses in the opposite direction of Pd, *i.e.* into the wire. Along with these vacancies, diffusion of Pt occurs. However, since the diffusion coefficient for Pt is lower than that of Pd [35], the outwards flux of Pd is likely to be higher than the inwards flux of Pt and result in a net inwards diffusion of vacancies. A high concentration of vacancies inside the wire

may in turn cause formation of porosity, as occurs in several other diffusion systems [26–28]. This would correlate well with our observed results of porosity developing inwards into the wire samples during Pt-catchment (Fig. 5). However, we have only been able to document that pores are present in the samples, and not if they are in fact voids formed within the sample as a result of agglomeration of vacancies. It is also possible that the GB Kirkendall effect can cause porosity in the GBs [43,44], which is where the rapid inwards diffusion of Pt (and outwards diffusion of Pd) occurs in the polycrystalline wire (Fig. 7), and where the main selection of pores/voids are formed in the quasi monocrystalline wire (Fig. 8).

Also the quasi monocrystalline wires show some reconstruction under sufficient gas flow of PtO₂ (high $p(PtO_2)$), indicating that the Kirkendall effect and internal porosity could be a pathway to reconstruction also of these samples. Both the $p(PtO_2)$ and temperature may therefore be important factors that determine how the mechanism for reconstruction proceeds. Because our system is not an interdiffusion system, but captures Pt from the gas phase molecule PtO₂, Kirkendall voids may not appear in the same manner as in other systems. However, that does not exclude the Kirkendall effect from participating in the reconstruction mechanism. We cannot conclude if the mechanism for porosity stems from a surface recrystallization similar to that of the Mn-containing IF steels [24,25], which forces the GBs to crack open due to significant GB diffusion, or if internal (sub-surface) voids are formed first, similar to the oxidation of solid nickel [23,26,42]. We recommend the topic of internal voids and the Kirkendall effect during Pt-catchment as a topic for future investigations.

4.7. Mechanism for grain reconstruction due to Pt-catchment

In summary, the Pd-based catchment unit is victim to a bulk grain diffusion limitation. This is evident from experiments with a quasi monocrystalline Pd-wire (Fig. 8), which captures small amounts of Pt that are unable to diffuse deep into the bulk, along with our simulated diffusion model (Fig. 13). In turn, the diffusion limitation causes a low Pt-catchment due to the equilibrium between surface Pt and gas phase PtO₂ (Fig. 5) [41]. The polycrystalline wires partially overcomes this

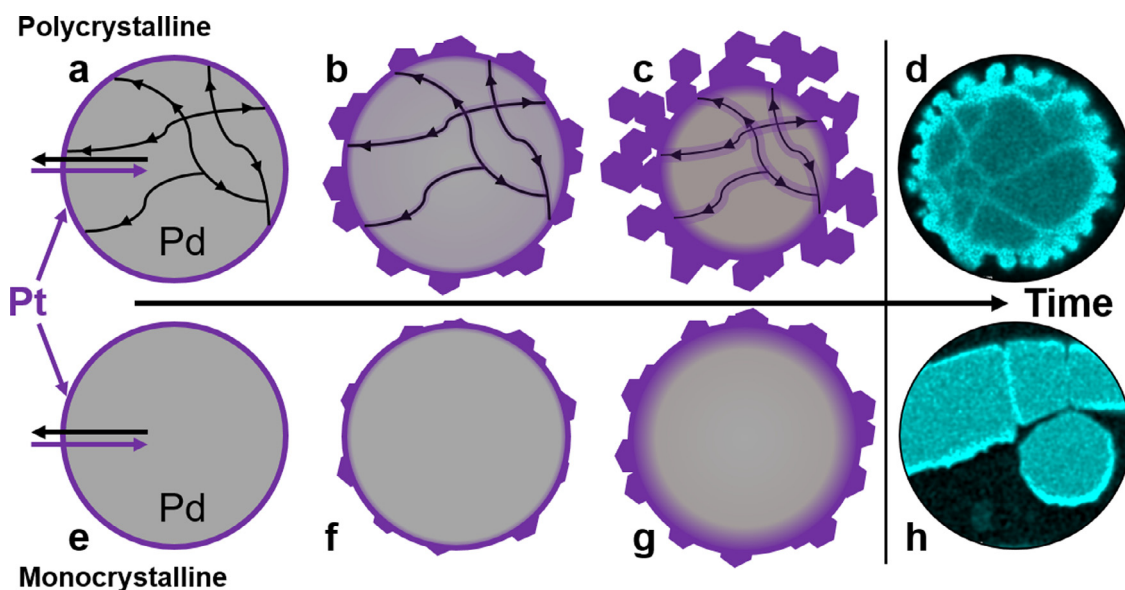


Fig. 14. Schematic illustration of suggested mechanism for grain reconstruction in Pd-based alloys caused by Pt-catchment. The top half show the mechanism for a polycrystalline wire, while the bottom illustrates the mechanism for a quasi monocrystalline wire. The right hand side of the figure compare the illustration with SEM and EDX images. The description for the mechanism is provided in the text above.

issue by rapid GB diffusion (Fig. 7), providing Pd with a rapid diffusion path into the wire core, which again causes more Pt to be captured because of a lower surface concentration of Pt. However, this also results in grain reconstruction.

With basis in the current discussion related to the Pt transport in form of the gas phase molecule PtO_2 , its deposition onto the surface and the subsequent solid state diffusion of Pt and Pd, we propose a mechanism for the grain reconstruction/recrystallization of polycrystalline Pd-based wires during Pt-catchment. A schematic of the process is given in Fig. 14. The process proceeds as the following:

Polycrystalline Pd and Pd/Ni wires

- (1) The wire is rapidly covered with Pt (first ~ 1 h, Fig. 14a).
- (2) Pt diffuses into the wire, and toward the wire core via the GBs (Fig. 14d), while Pd is transported outward to the wire surface via GBs. Here, Pt and Pd mix, which results in the formation of small surface crystals (Fig. 14b). After ~ 1 day, the surface is covered with Pd-Pt crystallites of $5\text{--}10\ \mu\text{m}$ in size.
- (3) The surface is covered in Pd-Pt crystallites, but the core is still intact (Fig. 14c). The grain boundaries in the remaining core continue to transport Pd-atoms to the surface, which causes more Pt-catchment and a continuation of the grain reconstruction process ($\sim 1\text{--}4$ days). See comparison with SEM/EDX in Fig. 14d.
- (4) With more time, the process continues until the entire wire is completely reconstructed and consists only of $\sim 10\text{--}20\ \mu\text{m}$ crystals ($\sim 7\text{--}10$ days for $76\ \mu\text{m}$ wire). The grain reconstruction is like a self-repeating process for the polycrystalline Pd-wire, which begins near the surface and continues until the entire wire is completely reconstructed.

Quasi monocrystalline Pd and Pd/Ni wires

- (1) The wire is rapidly covered with Pt (first ~ 1 h, Fig. 14e).
- (2) Pt diffuses into Pd, and the two elements mix. Small crystallites are formed at some locations to minimize the surface energy (Fig. 14f).
- (3) Slow inwards Pt-diffusion results in a high surface concentration of Pt, causing low Pt-catchment compared to the polycrystalline wire. Because of the diffusion limitation, the wire core remains as pure Pd for short experiments (< 10 days, Fig. 14g). See comparison with SEM/EDX in Fig. 14h.

- (4) Extra-long exposure times and/or heavy exposure to PtO_2 can over time cause some reconstruction also of the quasi monocrystalline wires.

For a polycrystalline sample, the mechanism describes that if the incoming amount of Pt is higher than the amount that can be absorbed by bulk diffusion, grain reconstruction will occur. If the wire is (quasi) monocrystalline, the wire can only capture the amount that can be absorbed by bulk diffusion, which is very low for the Pd-rich alloys. In order to maximize Pt-catchment, the Pd-wire should therefore be polycrystalline, even though this may result in grain reconstruction.

4.8. Suggestions for improvements of current technology

A way to reduce the grain reconstruction could be to either manipulate the relative diffusion rate between the bulk and grain boundary catchment unit, e.g. by increasing the temperature as in the diffusion model (Section 4.5), or switch to a different catchment system with enhanced bulk diffusion properties. Though a temperature increase over the catchment unit may reduce the diffusion limitation for a Pd-based catchment system, it may go at the cost of the efficiency of ammonia oxidation process, which is the primary reason for choosing specific conditions in the reactor. Alternatively, one can imagine that if the Pd-wire had a very small grain size ($< 1\ \mu\text{m}$), and no grain growth occurred during operation, it could significantly improve the diffusional properties of the system by better exploiting the GB-diffusion, which would hopefully not result in severe grain reconstruction.

The mechanism proposed above applies for Pd-based alloys, both with and without addition of small amounts of secondary elements, such as Ni. The effect of adding 8.7 at.% (5 wt.%) Ni is minimal on the Pt-catchment abilities and the grain reconstruction process. However, additions of various elements could reduce the grain reconstruction issue. We have observed that Ni oxidizes to NiO, and is mainly located in the grain boundaries. This is, to a certain extent, hindering grain boundary diffusion, as seen in Fig. 7. We recommend further investigation of different alloys to fully understand the effect of different compositions and different grain structures; to see if possible additives can reduce the grain reconstruction by improving the overall diffusion or by reducing GB-diffusion relative to bulk diffusion. It may also help to maintain a small grain size of the system during operation. This may be performed

by aid of an advanced diffusion model including all realistic parameters, especially the surface concentration and deposition of Pt onto the surface. This can e.g. be obtained by performing molecular dynamics simulations, by which one can also study the kinetics for the reaction between PtO₂ and the surface of different alloys, and understand the role of oxygen in the system.

5. Conclusions

We have investigated Pd and Pd/Ni (91.3/8.7 at.%) samples in different Pt-catchment experiments in order to understand the grain reconstruction phenomena, which is caused by catchment of Pt from the gaseous molecule PtO₂. *In situ* absorption-CT experiments of polycrystalline Pd and Pd/Ni wires show rapid morphological changes during Pt-catchment, and that a higher $p(\text{PtO}_2)$ causes more severe morphological changes. However, time is also a highly important factor for the grain reconstruction, in addition to the $p(\text{PtO}_2)$. A pristine Pd-surface has a significantly higher Pt-catchment rate compared to a mixed Pt-Pd surface, resulting in reduced Pt-catchment efficiency during a Pt-catchment experiment. Due to rapid GB diffusion, Pt is able to reach the core of the Pd and Pd/Ni wires within one day, causing these parts of the wire core to be more rich in Pd than the centre of the grains. The effect of adding 8.7 at.% (5 wt.%) Ni to the Pd alloy prior to catchment experiments have only a minor effect on the Pt catchment abilities and the grain reconstruction phenomena.

There is a clear difference for Pt-catchment on quasi monocrystalline samples; the Pt-catchment efficiency is significantly lower and Pt is solely detected near the surface of the wire samples. In addition, the surface reconstruction is low compared to the polycrystalline samples. Quasi monocrystalline Pd/Ni (91.3/8.7 at.%) reconstructs slightly more than pure Pd, which may be related to the internally located NiO particles. However, a high exposure to PtO₂ has a significantly higher effect on the reconstruction of the quasi monocrystalline samples than the composition.

The low Pt-catchment rates for the quasi monocrystalline samples are caused by slow bulk diffusion, hindering Pt from diffusing deep into the Pd- and Pd/Ni-wires. In turn, the diffusion limitation results in less Pt-deposition onto to the wire surface. This is due to the interaction/equilibrium between Pt on the wire surface and PtO₂ in the gas phase, i.e. the diffusion limitation is indirectly causing less Pt catchment. The polycrystalline Pd- and Pd/Ni-wire can overcome the diffusion limitation by utilizing rapid GB diffusion to transport Pd out to the wire surface and ensure further Pt-deposition in the surface. However, this also results in grain reconstruction. We speculate if the GB and/or bulk Kirkendall effect contributes in forming internal voids in both the poly- and quasi monocrystalline Pd and Pd/Ni wires, which in turn causes the observed reconstruction. We strongly recommend this topic for future investigations. In short, we can say that grain reconstruction is a corrosion process caused by gas phase platinumation. In an applied perspective (e.g. operational use in ammonia oxidation) a polycrystalline Pd-wire may be preferred in order to maintain a high Pt-catchment rate, even at the cost of grain reconstruction.

Declaration of Competing Interest

The authors declare that they have no known competing financial interests or personal relationships that could have appeared to influence the work reported in this paper.

Acknowledgments

The authors would like to thank Thomas By (K. A. Rasmussen) and Dr. Susmit Kumar (University of Oslo) for discussions on the topic of diffusion in metals, and Dr. Øystein Slagtern Fjellvåg (Institute for Energy technology, Norway) and Dr. Bruno Gonano (University of Oslo)

for help with experimental data collection. We also appreciate discussions with the entire iCSI centre, the Catchment Team in iCSI, and the research group NAFUMA (University of Oslo). We would also like to acknowledge the expertise and advanced instrumentation of the European Synchrotron Radiation Facility, especially beamline ID15A, and the expertise of Patrick Springer and MikroLab Kolbe in ICP-OES/MS analysis. Thanks to the Interreg project ESS & MAX IV: Cross Border Science and Society for financial support for the UiO-DTU collaboration, and thanks to the kind people of DTU Energy for hospitality during visits. The project was financed by the Research Council of Norway through the project iCSI (project no. 237922).

Supplementary materials

Supplementary material associated with this article can be found, in the online version, at doi:10.1016/j.mta.2022.101359.

References

- [1] V. Smil, *Enriching the Earth: Fritz Haber, Carl Bosch, and the Transformation of World Food Production*, MIT Press, 2001.
- [2] M. Warner, *The Kinetics of Industrial Ammonia Combustion*, University of Sydney, 2013.
- [3] L. Hannevold, *Reconstruction of Noble-Metal Catalysts During Oxidation of Ammonia*, *Reconstruction of Noble-Metal Catalysts During Oxidation of Ammonia*, Department of Chemistry, Faculty of Mathematics and Natural Sciences, University of Oslo Unipub: Oslo, 2005.
- [4] A.S. Fjellvåg, A.O. Sjøstad, D. Waller, J. Skjelstad, Grain reconstruction of Pd and Pd/Ni alloys for platinum catchment, *Johns. Matthey Technol. Rev.* 63 (4) (2019).
- [5] H. Holzmann, Platin-rückgewinnung bei der NH₃-verbrennung an platin/rhodium-netzkatalysatoren, *Chem. Ing. Tech.* 40 (24) (1968) 1229–1237.
- [6] J. Pura, P. Kwaśniak, D. Jakubowska, J. Jaroszewicz, J. Zdunek, H. Garbac, J. Mizera, M. Gierej, Z. Laskowski, Investigation of degradation mechanism of palladium–nickel wires during oxidation of ammonia, *Catal. Today* 208 (2013) 48–55 Supplement C.
- [7] Y. Ning, Z. Yang, H. Zhao, Structure reconstruction in palladium alloy catchment gauzes, *Platin. Met. Rev.* 39 (1) (1995) 19–26.
- [8] J. Fierro, J. Palacios, F. Tomás, Characterization of catalyst and catchment gauzes used in medium- and low-pressure ammonia oxidation plants, *J. Mater. Sci.* 27 (3) (1992) 685–691.
- [9] J.L.G. Fierro, J.M. Palacios, F. Tomás, Redistribution of platinum metals within an ammonia oxidation plant, *Platin. Met. Rev.* 34 (2) (1990) 62–70.
- [10] J.L.G. Fierro, J.M. Palacios, F. Tomás, Morphological and chemical changes in palladium alloy gauzes used for platinum recovery in high-pressure ammonia oxidation plants, *Surf. Interface Anal.* 14 (9) (1989) 529–536.
- [11] Y. Ning, Z. Yang, Platinum loss from alloy catalyst gauzes in nitric acid plants: the important role of the palladium component in metal capture during ammonia oxidation, *Platin. Met. Rev.* 43 (2) (1999) 62–69.
- [12] Y. Ning, Z. Yang, H. Zhao, Platinum recovery by palladium alloy catchment gauzes in nitric acid plants: the mechanism of platinum recovery, *Platin. Met. Rev.* 40 (2) (1996) 80–87.
- [13] Z. Yang, Y. Ning, H. Zhao, Changes of composition and surface state of palladium–nickel alloy gauzes used in ammonia oxidation apparatus, *J. Alloy. Compd.* 218 (1) (1995) 51–57.
- [14] J. Pura, P. Wicinski, P. Kwasniak, M. Zwolinska, H. Garbac, J. Zdunek, Z. Laskowski, M. Gierej, Investigation of the degradation mechanism of catalytic wires during oxidation of ammonia process, *Appl. Surf. Sci.* 388 (2016) 670–677 Part B.
- [15] J. Pura, H. Garbac, J. Zdunek, J. Mizera, M. Gierej, Z. Laskowski, Analysis of two catalytic systems PtRhPd-PdAu and PtRh-PdAu after long-term exploitation, *Inż. Mater.* 4 (194) (2013) 358–362.
- [16] A.E. Heywood, Recovery of platinum from ammonia oxidation catalysts, *Platin. Met. Rev.* 26 (1) (1982) 28–32.
- [17] A.E. Heywood, Platinum recovery in ammonia oxidation plants, *Platin. Met. Rev.* 17 (4) (1973) 118–129.
- [18] F. Han, X. Liu, Comparison of Pt catchment between two Pd alloy in nitric acid catalyst gauze, *Guojinshu* 38 (1) (2017) 31–35.
- [19] A. Zakrzewska, M. Rubel, A. Skalski, The change in the surface topography of Pd Au getter gauzes used in the ammonia oxidation process, *Mater. Sci. Eng.* 75 (1) (1985) L5–L8.
- [20] S.W.T. Price, K. Geraki, K. Ignatyev, P.T. Witte, A.M. Beale, J.F.W. Mosselmanns, *In situ* microfocus chemical computed tomography of the composition of a single catalyst particle during hydrogenation of nitrobenzene in the liquid phase, *Angew. Chem. Int. Ed.* 54 (34) (2015) 9886–9889.
- [21] S.W.T. Price, D.J. Martin, A.D. Parsons, W.A. Sławiński, A. Vamvakeros, S.J. Keylock, A.M. Beale, J.F.W. Mosselmanns, Chemical imaging of Fischer-Tropsch catalysts under operating conditions, *Sci. Adv.* 3 (3) (2017) e1602838.
- [22] A.M. Beale, S.D.M. Jacques, M. Di Michiel, J.F.W. Mosselmanns, S.W.T. Price, P. Senecal, A. Vamvakeros, J. Paterson, X-ray physico-chemical imaging during activation of cobalt-based Fischer-Tropsch synthesis catalysts, *Philos. Trans. A Math. Phys. Eng. Sci.* 376 (2110) (2018) 20170057–20170057.

- [23] R. Haugsrud, On the high-temperature oxidation of nickel, *Corros. Sci.* 45 (2003) 211–235.
- [24] Y.I. Zhang, Y.Y. Zhang, F.H. Yang, Z.T. Zhang, Effect of alloying elements (Sb, B) on recrystallization and oxidation of Mn-containing IF steel, *J. Iron Steel Res. Int.* 20 (3) (2013) 39–56.
- [25] Z.T. Zhang, Y.Y. Zhang, Simultaneous recrystallization and oxidation behavior of Mn-containing IF steel, *J. Iron Steel Res. Int.* 19 (8) (2012) 67–74.
- [26] D.J. Young, *High Temperature Oxidation and Corrosion of Metals*, Corrosion series, 1, Jordan Hill: Elsevier Science & Technology, Jordan Hill, 2008 Vol.
- [27] C.U. Kim, *Electromigration in Thin Films and Electronic devices: Materials and reliability*, Woodhead Publishing, 2011 Kim, C.U., Editor.
- [28] D. Kim, J.h. Chang, J. Park, J.J. Pak, Formation and behavior of Kirkendall voids within intermetallic layers of solder joints, *J. Mater. Sci. Mater. Electron.* 22 (7) (2011) 703–716.
- [29] G.B.M. Vaughan, R. Baker, R. Barret, J. Bonnefoy, T. Buslaps, S. Checchia, D. Duran, F. Fihman, P. Got, J. Kieffer, S.A.J. Kimber, K. Martel, C. Morawe, D. Mottin, E. Papillon, S. Petitdemange, A. Vamvakeros, J.P. Vieux, M. Di Michiel, ID15A at the ESRF - a beamline for high speed operando X-ray diffraction, diffraction tomography and total scattering, *J. Synchrotron Radiat.* 27 (2) (2020) 515–528.
- [30] R. Bitter, T. Mohiuddin, M. Nawrocki, *LabVIEW: Advanced Programming Techniques*, CRC Press, 2006.
- [31] MATLAB. 9.7.0.1247435 (R2019b). Natick, Massachusetts: The MathWorks Inc.; 2019.
- [32] N. Chetih, Z. Messali, Tomographic image reconstruction using filtered back projection (FBP) and algebraic reconstruction technique (ART), in: *Proceedings of the 3rd International Conference on Control, Engineering & Information Technology (CEIT)*, 2015.
- [33] P.S. Jørgensen, K.V. Hansen, R. Larsen, J.R. Bowen, High accuracy interface characterization of three phase material systems in three dimensions, *J. Power Sources* 195 (24) (2010) 8168–8176.
- [34] J. Gegner, G. Hörz, R. Kirchheim, Diffusivity and solubility of oxygen in solid palladium, *J. Mater. Sci. Lett.* 44 (9) (2009) 2198–2205.
- [35] V.A. Baheti, R. Ravi, A. Paul, Interdiffusion study in the Pd–Pt system, *J. Mater. Sci. Mater. Electron.* 24 (8) (2013) 2833–2838.
- [36] A.D. Le Claire, The analysis of grain boundary diffusion measurements, *Br. J. Appl. Phys.* 14 (6) (1963) 351–356.
- [37] B. Foss, D.S. McPhail, B. Shollock, Oxidation and oxygen transport in a commercial polycrystalline Ni-based superalloy under static and loading conditions, Oxidation and oxygen transport in a commercial polycrystalline Ni-based superalloy under static and loading conditions, Imperial College London, 2013 Editors.
- [38] T. Li, P.A.J. Bagot, E.A. Marquis, S.C. Edman Tsang, G.D.W. Smith, Atomic engineering of platinum alloy surfaces, *Ultramicroscopy* 132 (2013) 205–211.
- [39] E. Antolini, Palladium in fuel cell catalysis, *Energy Environ. Sci.* 2 (9) (2009) 915–931.
- [40] G. Rakhtsaum, Platinum alloys: a selective review of the available literature, *Platin. Met. Rev.* 57 (3) (2013) 202–213.
- [41] S.F. Håkonsen, B. Holme, D. Waller, An investigation of the limiting factors for Pt catchment in the ostwald process, To be published (2022).
- [42] E. Zacharaki, P. Beato, R.R. Tiruvalam, K.J. Andersson, H. Fjellvåg, A.O. Sjøstad, From colloidal monodisperse nickel nanoparticles to well-defined Ni/Al₂O₃ model catalysts, *Langmuir* 33 (38) (2017) 9836–9843.
- [43] L. Klinger, E. Rabkin, Theory of the Kirkendall effect during grain boundary interdiffusion, *Acta Mater.* 59 (4) (2011) 1389–1399.
- [44] E. Rabkin, L. Klinger, T. Izyumova, V.N. Semenov, Diffusion-induced grain boundary porosity in NiAl, *Scr. Mater.* 42 (11) (2000) 1031–1037.

Supplementary

S.1. *In situ* X-ray absorption-CT experiment and analysis

S.1.1. Experimental setup

A detailed description of the experimental setup is given in the experimental section. Here we provide an illustration of the furnace used for the absorption-CT experiment and how the sample was mounted, see Figure S1.

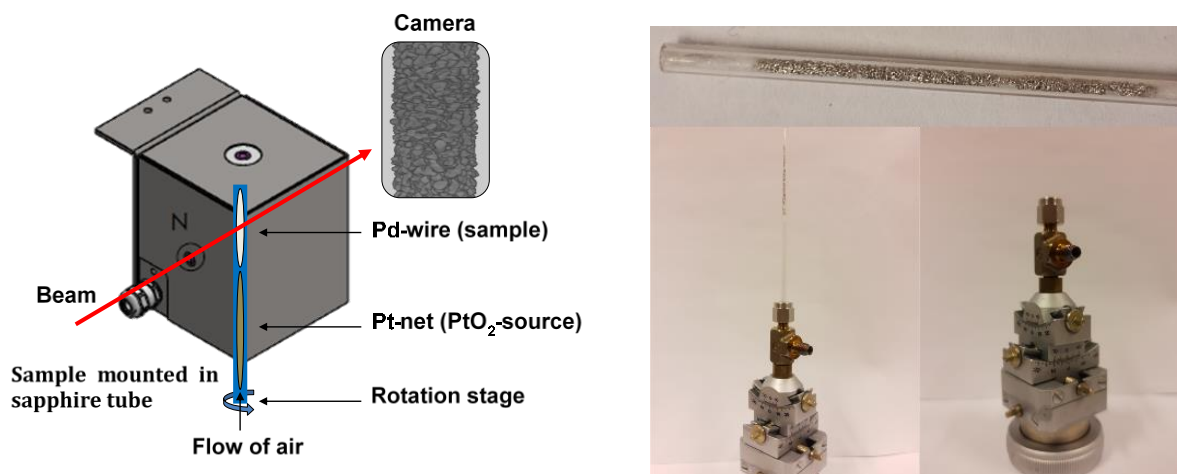


Figure S1. Left: illustration of the experimental setup, right: picture of sample mounting in sapphire tube, and mounting on goniometer.

S.1.2. Mathematical analysis of absorption-CT data using matlab

S.1.2.1. Intensity segmentation

The mathematical analysis of the absorption-CT data was performed using matlab [31]. First we identify the intensity that the different elements (Pd, Ni, NiO, Pt, air/voids) appear with in the tomograms collected. This is done to segment out the volumes related to the different elements. This is done based on the histogram showing the relative distribution of the different intensities, see Figure S2.

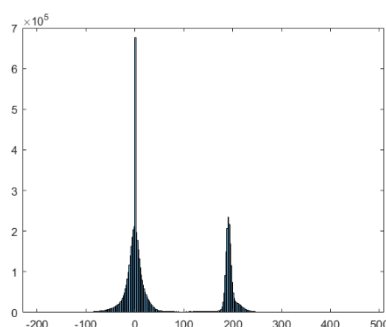


Figure S2. Histogram of the pure Pd sample at time $t = 0$, showing the distribution of the different intensities.

The intensity for the elements in the tomogram is given by the absorption coefficient (μ), which is highly dependent on the density (ρ) of the material. Theoretical values for μ/ρ are well known and reported by NIST [45]. However, though the obtain values are represented by the absorption

coefficient, the data is only qualitatively reliable due to how the attenuated X-ray beam is measured by the camera, which does not preserve the quantitative nature of X-ray absorption experiment. We therefore only determine relative changes between samples. This implies that we find the expected intensity of the pure materials from calibration samples, see Table S1. The obtained values are the average intensity near the wire core (cylinder with 10 μm radius). We use these experimental values to estimate compositional changes in the wire during the experiment. However, in the experiments, the voxel intensity varies from values far below the expected intensity of Pd to values far above the expected intensity of Pt. The intensities can therefore not be used to calculate reliable atomic fractions of the elements, only give a qualitative indication of change.

Table S1. Intensity (μ) obtained from calibration wire samples after correcting for thermal expansion for the *in situ* absorption-CT experiments at 1000 °C. The samples are from the same batch of samples used in the experiment.

	μ (calibration)
Pd	197
Pt	253
Pd/Ni (91.3/8.7 at. %)	190
Pd/NiO (91.3/8.7 at. %)	182

S.1.2.2. Artefact intensity (materials phase contrast artefact)

We would like to mention an issue with a *materials phase contrast artefact* affecting the voxel intensities in the tomograms. Regions of low density (*e.g.* NiO (6.67 g/cm^3) or air) which are located near regions of high density (*e.g.* Pd (11.9 g/cm^3)) obtain an artificially low intensity (Figure S3), because the two phases have very different density. This occurs both for NiO and voids located inside the Pd matrix, and air located around the sample. This causes NiO and air to be indistinguishable in the tomogram. Several regions show an intensity well below -200 (Figure S3), while the expected minimum intensity in the experiment is 0, in the case of vacuum (zero density). The intensity value of this region is an artefact, but the fact that there is contrast in the tomogram, *i.e.* a difference in intensity, is real. The regions of NiO in the Pd/Ni wire (Figure S3a) look like they are connected to the surface at some locations. However, this is because NiO is located in large crystallites in the grain boundaries close to the surface, which is clearly seen from the EDX-map in Figure S3c. For the pure Pd wire, we have not been able to find any porosity by SEM investigations of the wire cross section, and we therefore believe that the internal regions of low density are impurities from the wire production.

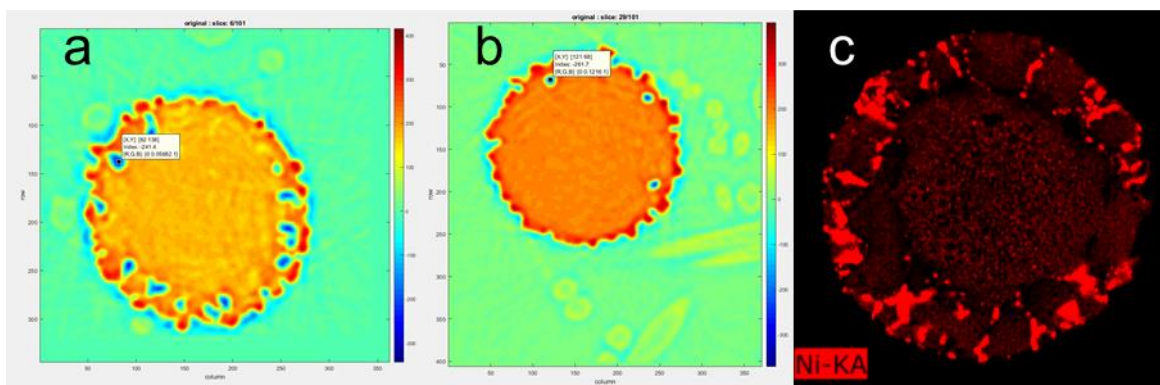


Figure S3. Raw data tomograms of (a) Pd/Ni and (b) pure Pd wires, which both display the *phase contrast artefact* effect. (c) EDX map of the Pd/Ni wire after 1 day of pre-treatments. The regions of negative intensity are influenced by artefacts (*phase contrast artefact*), and this occurs both inside and outside both wires.

A similar effect occurs for the interface between the air and surface of the Pd/Ni and pure Pd wires, causing an overestimation of the wire intensity near the wire surface (Figure S4a). A radial intensity profile showing the intensity overestimation of a fresh Pd wire is shown in Figure S4b. We have not been able to successfully correct for this artefact without introducing other artefacts in the analysis, and the readers should be prepared to know that because of this issue, the intensity near the wire surface and of several of the surface crystals on both Pd and Pd/Ni wires are overestimated.

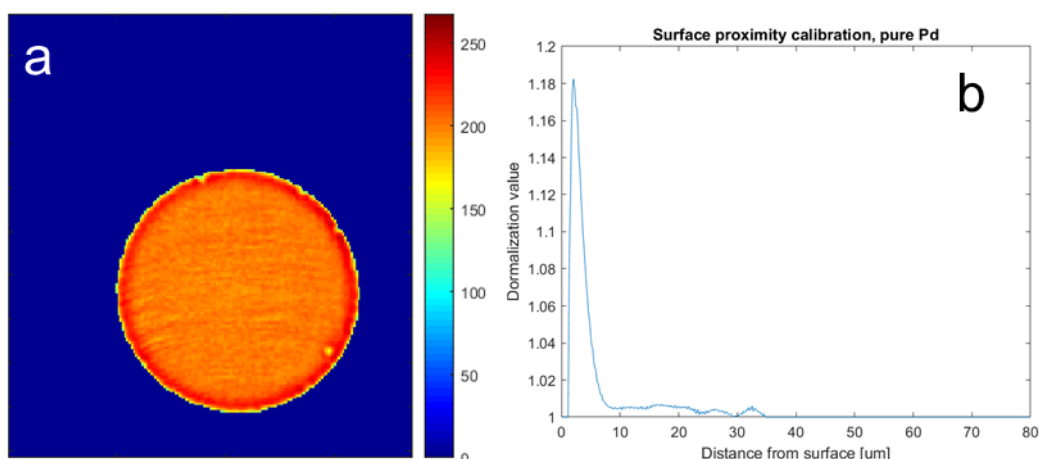


Figure S4. Pure Pd wire before heat treatment showing how the surface of the wire has an overestimated intensity. Profile showing the calculated overestimation of the intensity in a regular Pd/Ni wire (a) and pure Pd sample (b).

S.1.2.3. Volume of NiO inside Pd/Ni and voids/pores inside pure Pd

As seen in Figure S3, regions of low density appear inside both the Pd/Ni and pure Pd samples. The volume of these regions relative to the total volume of the wire (Pd + NiO/voids inside) is shown in Figure S5a. This value is calculated from only the regions which are located inside the Pd-matrix, *i.e.* is not connected to the surface. For Pd/Ni, the volume of these regions is therefore smaller than the total volume of NiO, as some of it is connected to the surface. Considering all volume seen within the radius of a fresh Pd/Ni wire, the total volume of regions of low density is $\sim 5\%$ (Figure S5b). Most probably, large amounts of this volume is NiO. Additionally, some NiO may be located in small particles which are not visible as separate particles, but mixed with the intensity of Pd in the tomogram, giving a lower intensity value compared to pure Pd.

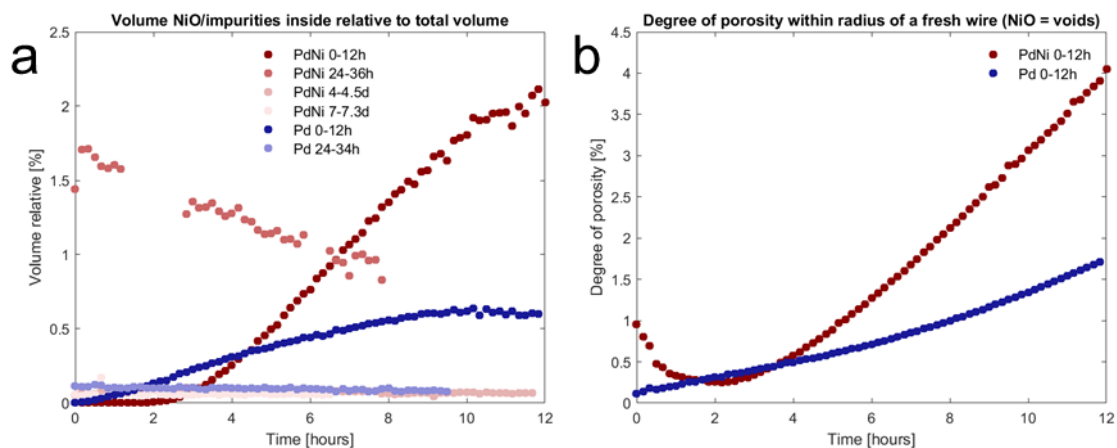


Figure S5. (a) Volume of regions with low density located inside wire, i.e. not connected to the surface for all wires. (b) Volume of all regions of low density within the radius of a fresh wire for Pd 0-12h and Pd/Ni 0-12h. For Pd-wires, the volume located inside the wire is most probably impurities. The porosity near the surface of the Pd-wire is most probably voids. For Pd/Ni, the volume is most probably NiO.

S.1.2.4. Calculations behind the absorption-CT figures reported in the main text

After understanding the impact of the *materials phase contrast artefact*, we analyse the tomograms to extract as much information as possible. The wire volume was segmented out using a lower intensity limit of 130. This implies that all Ni/NiO with real or artefact intensities (far below 0) is segmented out of the sample volume, leaving mainly Pd in the tomogram. The reason why such a high limit is chosen is to avoid any quartz nearby the wire (as seen in the background of Figure S3) to be included in the calculation. Furthermore, knowing that the internal phase of low density is NiO in Pd/Ni and impurities in pure Pd, the regions which are physically located inside the wire, i.e. those regions without a connection to the surface, are considered as part of the wire in the calculations. This is because we know they are not voids, which is supported by the fact that the internal voids are located quite homogeneously along the wire length. The regions of low density which are located near the wire surface is still considered as voids.

The centre of the wire in each slice was defined from the size of the wire in x- and y-directions. The wire volume was calculated from the amount of voxels which make up the entire wire, where each voxel has a size of $0.7 \times 0.7 \times 0.7 \mu\text{m}^3$. The Pt-content was calculated assuming that all volume increase relative to the pristine Pd-wire at $t = 0$ is caused by Pt-catchment. This is done by using the density and atomic weight of Pd and Pt metal to recalculate the volume increase to at. % Pt. The degree of porosity was calculated from the volume of pores within the threshold radius ($76 \mu\text{m}$) relative to a cylinder of this size. The radius was defined as the radius where the degree of porosity exceeded 95%. The surface area is calculated using a polygonization method as introduced by Jørgensen *et al.* [33].

Radius and length dependent properties are in general calculated using the same approach as described for Pt-content and volume increase above. The only difference is that the calculation iterates through the wire radius using a circular mask to identify the properties at a given radius, and uses the slice number in z-direction for the properties along the length. Several length-dependent properties are smoothed along the wire length up to $50 \mu\text{m}$ before plotting.

The surface crystals in the tomograms are located by calculating a depth map from the surface of the wire and inwards, i.e. showing the distance from the surface to each voxel in the wire. Voxels found as

a local maximum by the imregionalmax-function in matlab are then considered as the centre of a surface crystal. The radius of the surface crystal is the value of the voxel in the depth-map used to find the surface crystal. The intensity of the surface crystal is the average intensity of a sphere of the same radius drawn around the centre voxel in the surface crystal, disregarding any porosity.

S.1.3. Volume of NiO in Pd/Ni (91.3/8.7 at. %), calculation

The molar density of NiO:

$$\frac{74.69 \text{ g/mol}}{6.67 \text{ g/cm}^3} = 11.21 \text{ cm}^3/\text{mol}$$

The molar density of Ni:

$$\frac{58.69 \text{ g/mol}}{8.91 \text{ g/cm}^3} = 6.59 \text{ cm}^3/\text{mol}$$

The molar density of Pd:

$$\frac{106.42 \text{ g/mol}}{11.9 \text{ g/cm}^3} = 8.94 \text{ cm}^3/\text{mol}$$

The volume expansion of Ni going to NiO is therefore:

$$\frac{11.21 \text{ cm}^3/\text{mol}}{6.59 \text{ cm}^3/\text{mol}} = 1.70$$

Relative volume of 8.7 at. % Ni in Pd

$$\frac{0.087 \times 6.59 \text{ cm}^3/\text{mol}}{0.087 \times 6.59 \text{ cm}^3/\text{mol} + (1 - 0.087) \times 8.94 \text{ cm}^3/\text{mol}} = 6.56 \%$$

Relative volume of 8.7 at. % NiO in Pd

$$\frac{0.087 \times 11.21 \text{ cm}^3/\text{mol}}{0.087 \times 11.21 \text{ cm}^3/\text{mol} + (1 - 0.087) \times 8.94 \text{ cm}^3/\text{mol}} = 10.67 \%$$

Expected volume increase of Pd/Ni (91.3/8.7 at. %) wire when Ni is oxidized to NiO

$$\frac{0.087 \times 11.21 \text{ cm}^3/\text{mol}}{0.087 \times 6.59 \text{ cm}^3/\text{mol} + (1 - 0.087) \times 8.94 \text{ cm}^3/\text{mol}} - 6.56 \% = 4.60 \%$$

The volume increase of Pd/Ni corresponds well to the expected volume increase during internal oxidation. The volume of NiO after internal oxidation is significantly higher than the volume of low density regions found inside the wire surface. This causes an issue with identifying the difference between voids and NiO.

S.1.4. Additional *in situ* absorption-CT results

S.1.4.1. Time-dependent analysis of Pd from 0 to 1.5 days and Pd/Ni from 0 to 7.3 days

Additional data which have not been presented in the main text is reported here. We provide additional figures for the pure Pd wires and a short analysis of the Pd/Ni wires. Several *in situ* experiments were performed for the Pd/Ni wires (Pd/Ni 0-12h, Pd/Ni 34-36h, Pd/Ni 4-4.5d and Pd/Ni

7-7.3d). However, we limit ourselves in the analysis due to uncertainties in the obtained data. The *materials phase contrast artefact* causes NiO and voids to be indistinguishable in the absorption-CT analysis. This implies that we consider the results only as semi-quantitative, but we can still extract certain trends during Pt-catchment on Pd/Ni.

For the first *in situ* experiment with Pd/Ni (Pd/Ni 0-12h), internal oxidation of Ni to NiO occurs during the experiment, causing a strange development of the volume (Figure S6a). First, the volume expands due to absorption of oxygen, and then it reduces due to the *phase contrast artefact* causing NiO to be considered as voids. A similar trend is observed for the average intensity (Figure S6b), which is reduced during the first 4 hours during the oxidation process, and then it increases for the rest of the experiment, probably due to Pt-catchment. This also causes a swift increase in radius for the Pd/Ni 0-12h wire during the first 2 hours, before a steady increase of the radius throughout the experiment (Figure S6c). However, for the next *in situ* experiments (Pd/Ni 34-36h, Pd/Ni 4-4.5d and Pd/Ni 7-7.3d), all NiO is already oxidized, which implies that no sudden changes in volume or intensity should occur. For these samples, both the volume, intensity and radius increase between each *in situ* experiment in addition to a slight increase during each *in situ* experiment. This corresponds well with an increase in surface area and pore depth. The fact that the radius, surface area and pore depth changes steadily during the experiments is a clear indication that the Pt catchment is accompanied by morphological changes in a steady tempo. The process occurs in a very similar way for both pure Pd and Pd/Ni.

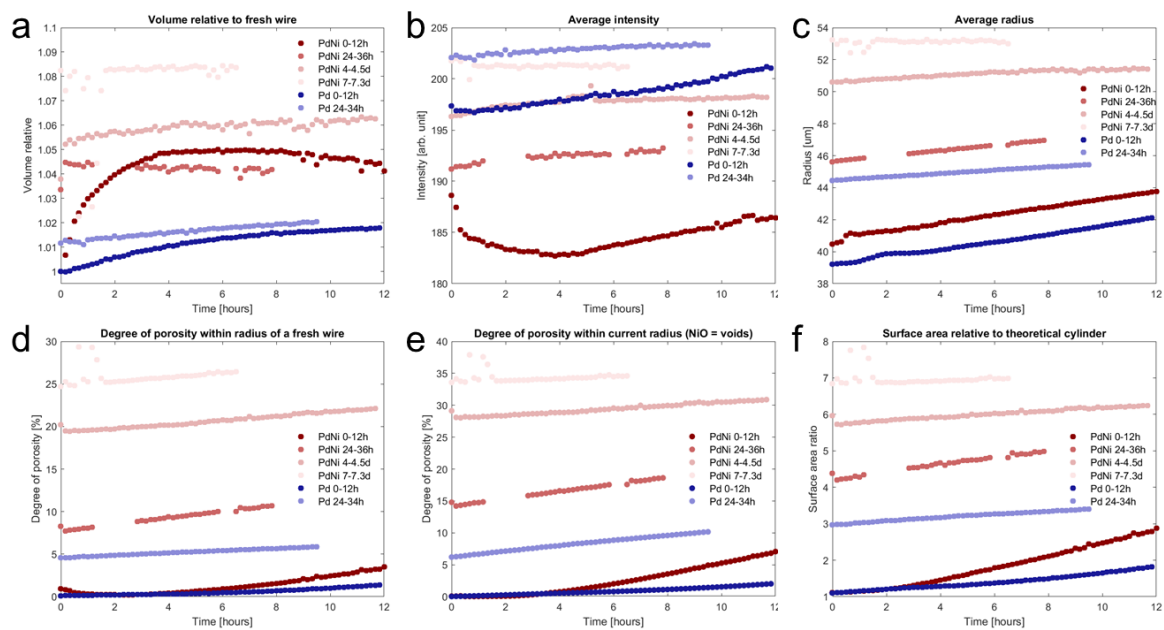


Figure S6. Time dependent plots of several properties calculated from *in situ* absorption-CT data collected at 1000 °C of pure Pd from 0 to 0.5 and 1 to 1.5 days, and of Pd/Ni (91.3/8.7 at. %) from 0 to 0.5, 1 to 1.5, 4 to 4.5 and 7 to 7.3 days. The figure shows a) volume relative to a fresh wire, b) average intensity, c) average radius, d) degree of porosity within the radius of a fresh wire (38 μm), e) degree of porosity within current radius (radius of Figure S6c), and f) surface area relative to a theoretical cylinder. Be aware that due to the missing contrast between NiO and voids, there is an overestimation of the surface area (up to $\sim 25\%$ error), pore depth (up to $\sim 5\ \mu\text{m}$ overestimation) and degree of porosity (up to $\sim 25\%$ error).

S.1.4.2. Length dependent analysis of Pd from 0 to 34 hours and Pd/Ni from 0 to 12 hours

Additional length dependent analysis of the pure Pd wires are provided in Figure S7, in addition to the radius of the Pd/Ni 0-12h sample in Figure S7c. The radius is the only property of the Pd/Ni wires along the length that is not influenced by artefacts.

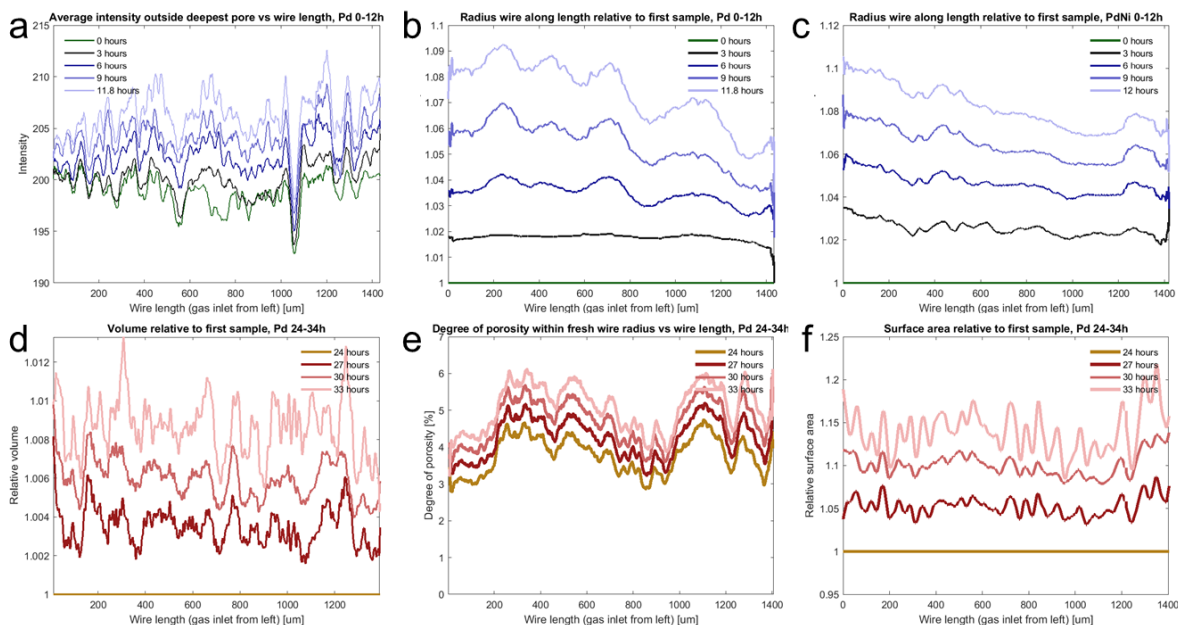


Figure S7. Different plots along wire length: a) average intensity on the part of the wire outside the deepest pore for Pd 0-12h, b) radius of Pd 0-12h, c) radius of Pd/Ni 0-12h, d) change in volume relative to sample after 24 hours for Pd 24-34h, e) degree of porosity within the radius of a fresh wire (38 μm) for Pd 24-34h, and f) change in surface area relative to the sample after 24 hours for Pd 24-34h.

S.1.4.3. Surface crystals on Pd from 0 to 34 hours

A significant effect of Pt-catchment is the growth of surface crystals on the Pd wire surface. The surface crystals have a size, intensity and position (versus radius and length) (Figure S8). From 0 to 12 hours, there is a large increase in amount of surface crystals with time. Most of the crystals are located near the original radius of the wire, $38 \pm 4 \mu\text{m}$. After 24 hours, the amount of surface crystals has increased significantly, but the size and intensity distribution is very similar to before. Still, there is a distinct growth in the size of the surface crystals from 24 to 34 hours.

The general trends for the surface crystals from 0 to 34 hours are that small surface crystals typically have a high intensity and are located at a large radius, i.e. they are the crystals located outermost on the wire. These are probably enriched in Pt. The crystals with low intensity are located below the outermost crystals, and these may also be larger than the outmost crystals, but exists in very few amounts. These are probably crystallites which appear when porosity grows inwards into the wire.

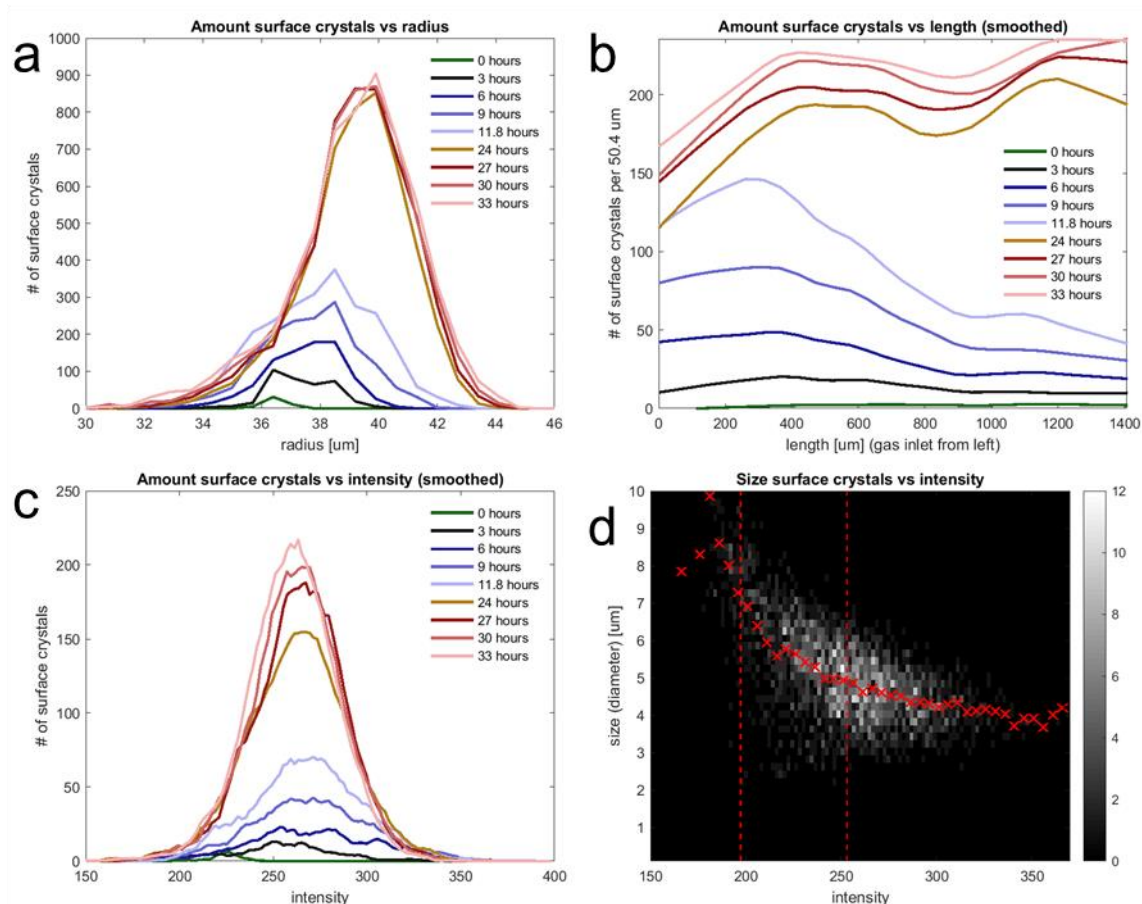


Figure S8. Amount of surface crystals on Pd from 0 to 34 hours versus (a) radius, (b) along the wire length and (c) intensity. (d) Show size versus intensity after 12 hours, where the background is a 2D histogram of size versus intensity (scale shown in the right) and the red crosses are the average. The red dotted lines show the intensity corresponding to pure Pd and pure Pt, respectively.

S.1.4.4. Surface crystals on Pd/Ni from 0 to 7.3 days

There are seemingly a few more surface crystals on the Pd/Ni wires compared to pure Pd. However, by examining Figure 6a and c, they look very similar. The amount of surface crystals may be overestimated due to regions of NiO inside Pd/Ni which are interpreted as voids. The distribution along the wire radius show that Pd/Ni have several more crystals located at slightly lower radius, as expected from the misinterpretation of NiO considered as voids. The size of the surface crystals is very similar for both Pd/Ni and pure Pd from 0 to 1.5 days. With more time (4-4.5 and 7-7.3 days), Pd/Ni samples show an increase in the size of surface crystals, up to a ~ 15 μm diameter of the surface crystals, but the total amount of crystals is approximately the same.

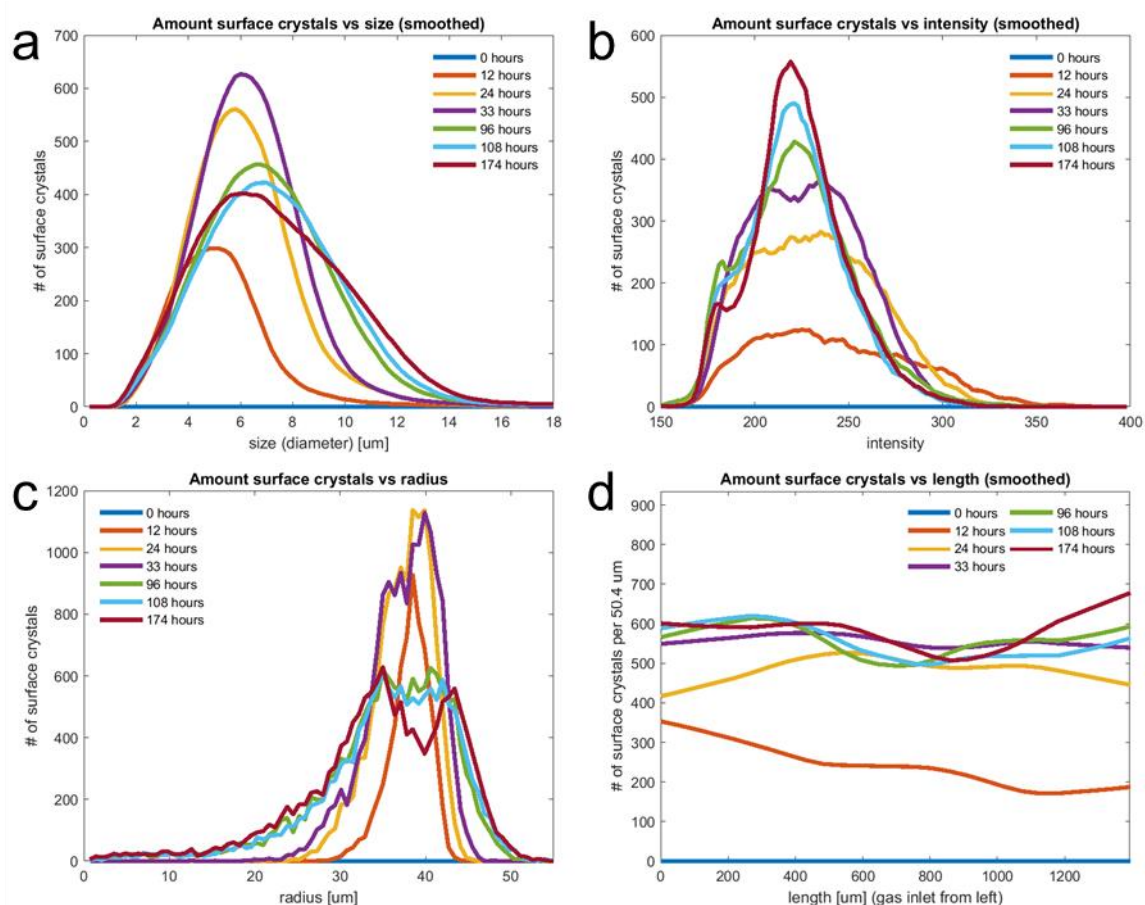


Figure S9. Surface crystals on Pd/Ni wires at selected time points indicated in the figure. a) amount surface crystals versus size, b) amount surface crystals versus intensity, c) amount surface crystals vs radius, and d) amount surface crystals versus length.

S.1.4.5. Example of raw data for selected samples

The raw data of Pd and Pd/Ni wires are shown in Figure S10. A colour map is used to show the reader the issue with similar intensity of NiO/voids inside and around the wires. As seen in several samples, the intensity near the sample surface and areas inside the samples are similar. For Pd/Ni samples, blue areas inside the samples are in several occasions NiO, while in Pd, we believe them to be voids.

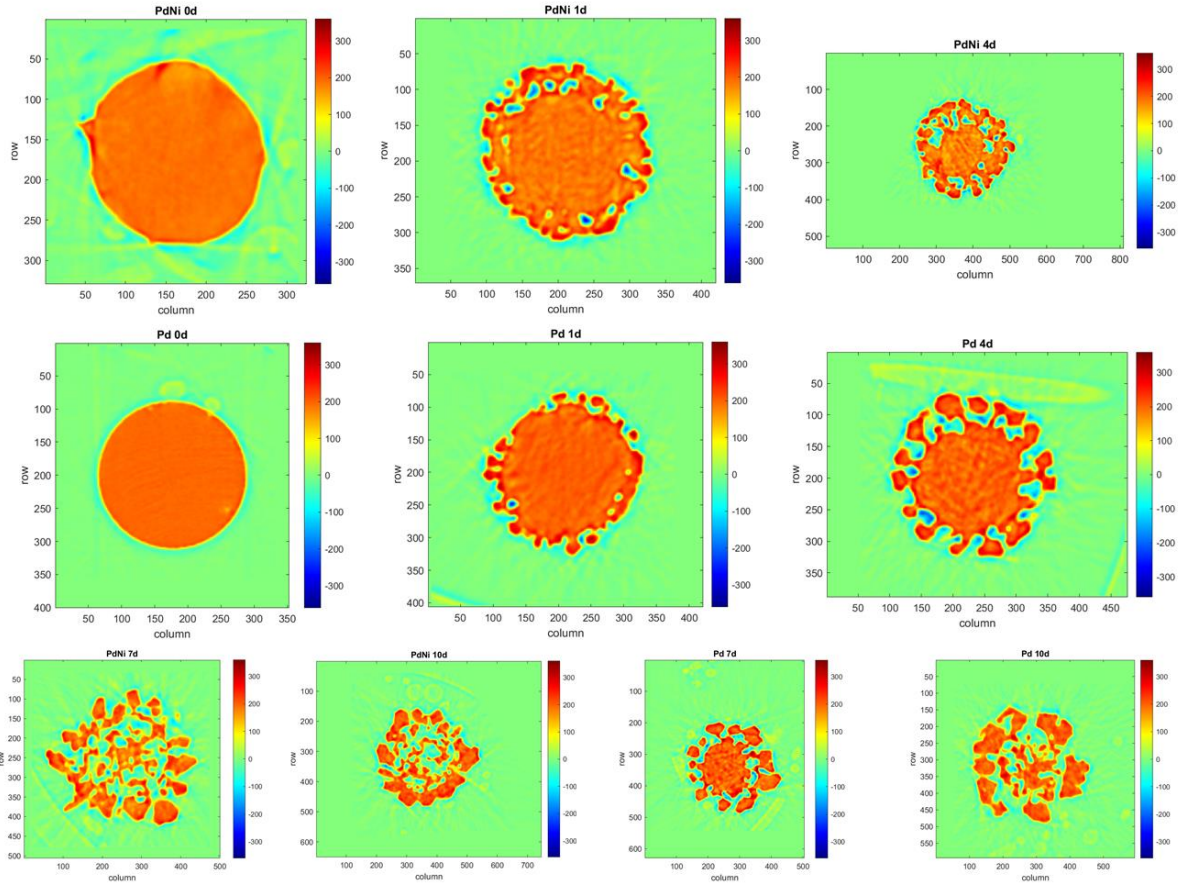


Figure S10. Raw data of Pd/Ni and Pd samples, showing a colour map of the intensities.

S.1.5. Calculation of PtO_2 concentration in gas phase, and how it changes along wire length in the *in situ* absorption-CT experiment

In the *in situ* absorption-CT experiments, a large amount of Pt-wires were packed in the upper section of the sapphire tube used for the experiments, and we can therefore assume that the gas is saturated with $PtO_2(g)$. Through comparisons with home lab experiments we estimate the PtO_2 concentration in the gas stream.

In home lab experiment, we use the same gas velocity as in the experiments (0.59 m/s). With a gas flow of 1L/min of air in a 6 mm ID tube, we obtain a $p(PtO_2)$ of approx. 5×10^{-8} bar. The mass of Pt lost from the Pt source in the *in situ* experiment is therefore:

Flow of Pt atoms in grams per 12 hours:

$$5 * 10^{-8} \times \frac{0.028 \text{ L/min}}{24 \frac{\text{L}}{\text{mol}}} \times 60 \text{ min} \times 12 \text{ hours} \times 195.1 \frac{\text{g}}{\text{mol}} = 8.2 \times 10^{-6} \text{ g(Pt)/12 hours}$$

After 12 hours, the pure Pd sample has had a volume increase of $8.39 \times 10^4 \mu\text{m}^3$. Assuming this volume increase is caused by Pt catchment, we use a density for platinum of 20.6 g/cm^3 [46] to calculate the weight of Pt which is captured

$$8.39 \times 10^4 \times (10^{-4})^3 \text{ cm}^3 \times 20.6 \frac{\text{g}}{\text{cm}^3} = 1.73 \times 10^{-6} \text{ g(Pt)/12 hours}$$

This is the volume increase for the measured part of the wire, which is approx. 1.5 mm. In the sample setup, approx. 3 mm sample was installed.

S.2. Other experimental data and calculations

S.2.1. EDX analysis of pre-treated samples for the *in situ* absorption-CT experiment

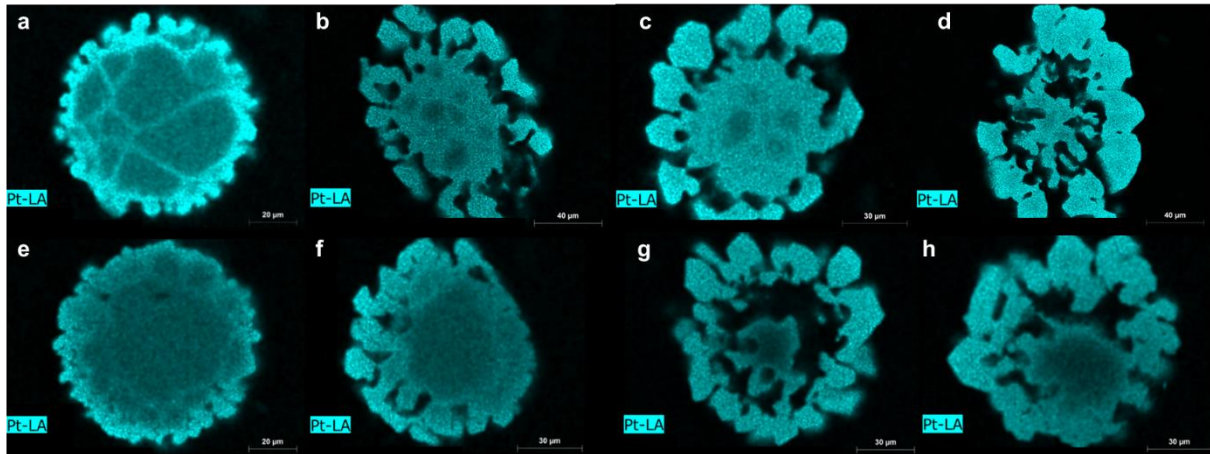


Figure S11. EDX map of the wire samples pre-treated for the *in situ* absorption-CT experiment. a) Pure Pd after 1 day, b) pure Pd after 4 days, c) pure Pd after 7 days, d) pure Pd after 10 days, e) Pd/Ni after 1 day, f) Pd/Ni after 4 days, g) Pd/Ni after 7 days, and h) Pd/Ni after 10 days.

S.2.2. SEM/EDX analysis of quasi monocrystalline Pd and Pd/Ni wires

This section contains a selection of additional SEM/EDX data which are not presented in the main part of the paper. Both data from the sample presented in the main part of the paper (Pd and Pd/Ni, 76 μm wire diameter, 10 days Pt-catchment, Figure 8) and additional samples are shown here. This is presented to provide the reader with a wider insight into the behaviour of the quasi monocrystalline Pd and Pd/Ni wires during Pt-catchment.

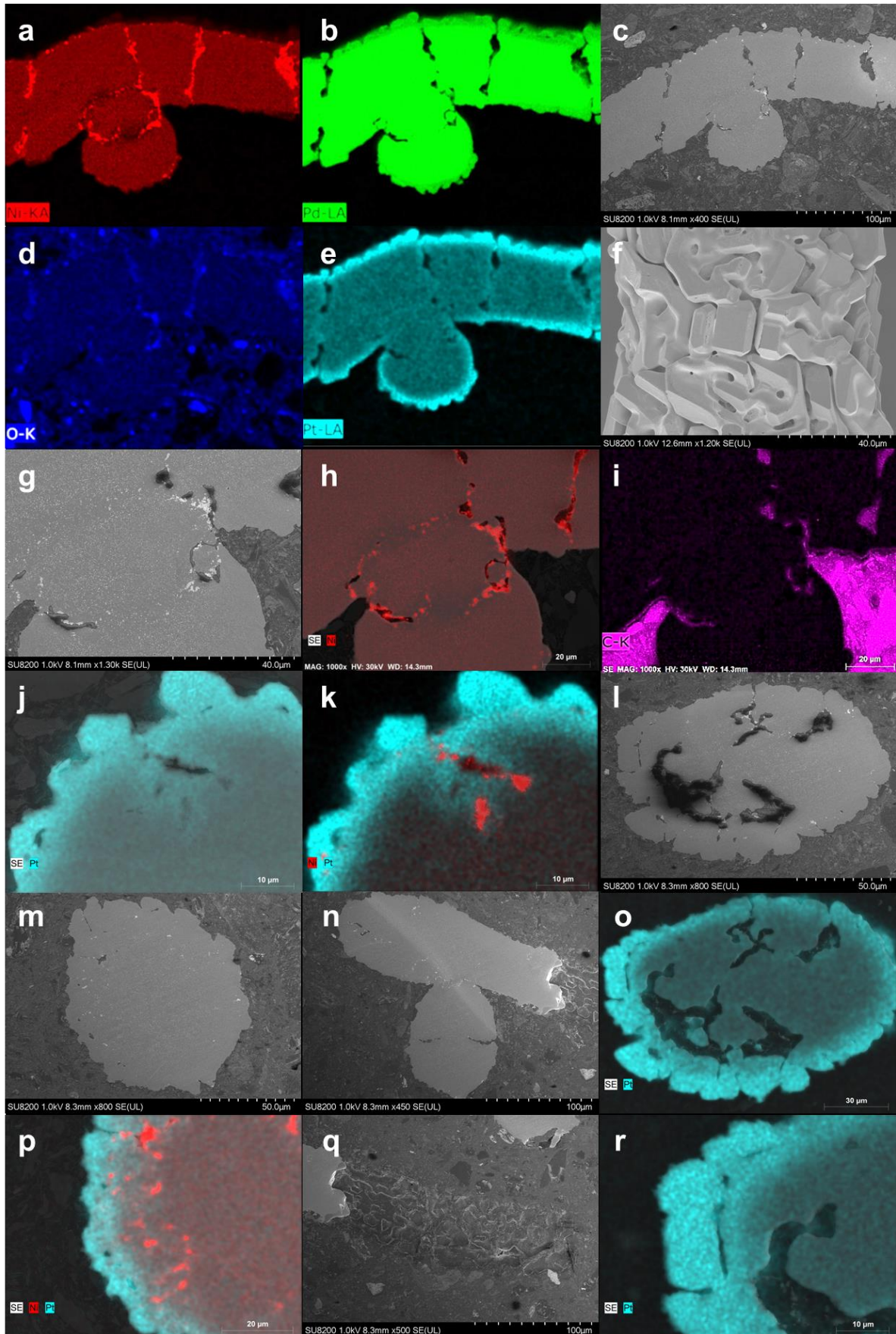


Figure S12. Additional SEM/EDX of the quasi monocrystalline Pd/Ni (91.3/8.7 at. %) sample (76 μm wire diameter) treated for Pt-catchment for 10 days, which is also presented in Figure 8.

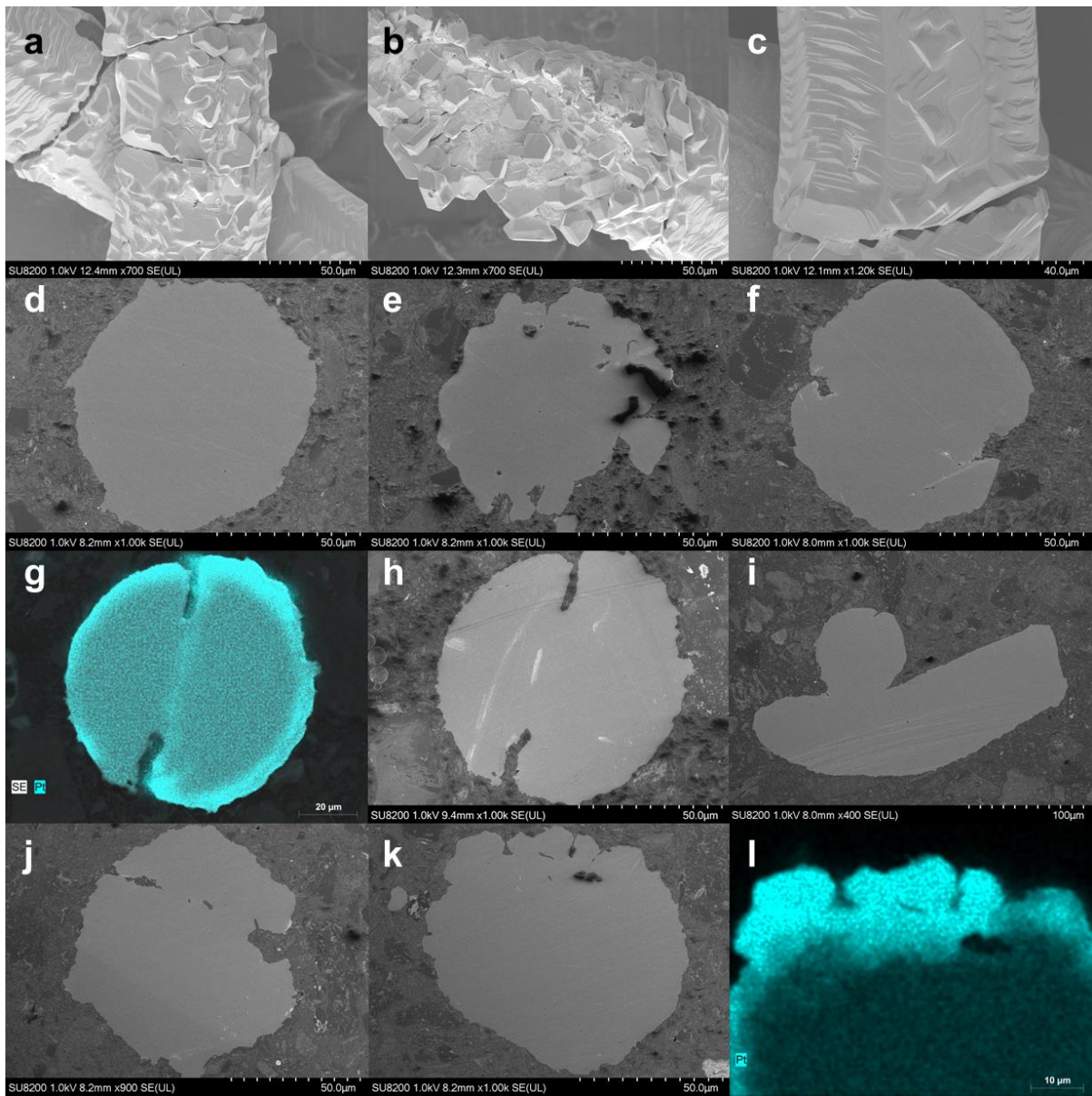


Figure S13. Additional SEM/EDX of the quasi monocrystalline Pd sample (76 μm wire diameter) treated for Pt-catchment for 10 days, which is also presented in Figure 8.

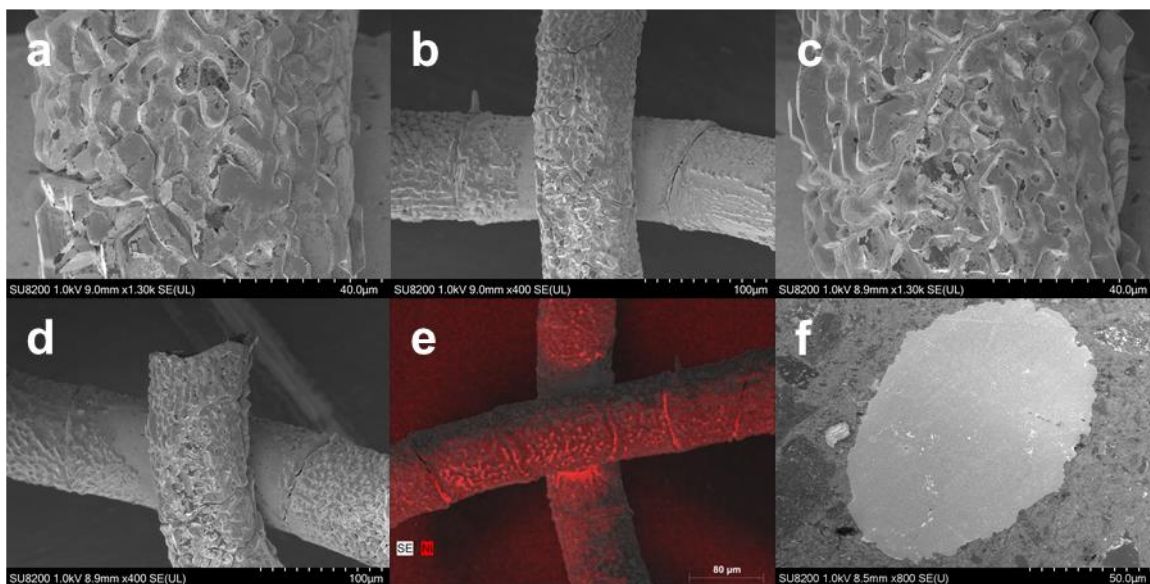


Figure S14. SEM/EDX analysis of a 76 μm quasi monocrystalline Pd/Ni (91.3/8.7 at. %) wire treated for Pt-catchment for 3.5 days in extra-large flow (1 L/min in a 4 mm ID tube) of gas and PtO_2 ($p(\text{PtO}_2) = 8.1 \times 10^{-8}$ bar).

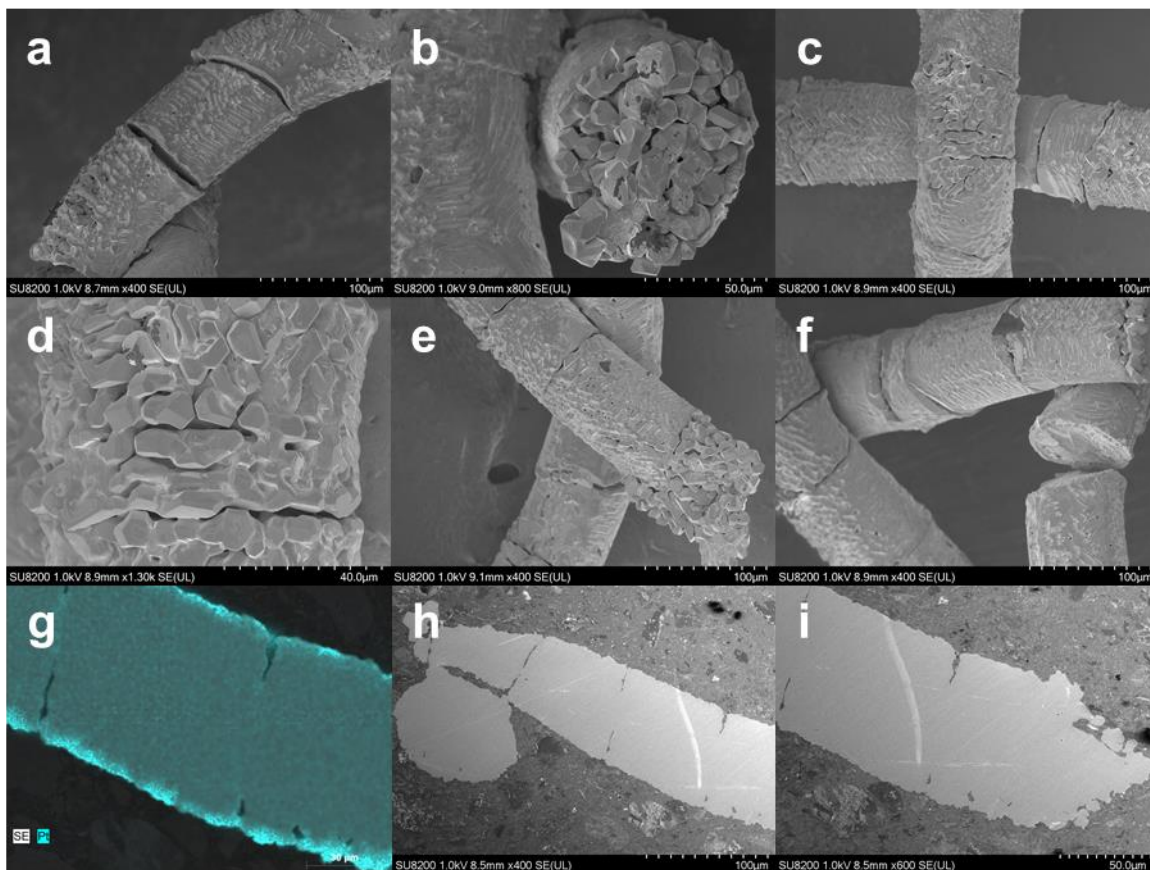


Figure S15. SEM/EDX analysis of a 76 μm quasi monocrystalline Pd wire treated for Pt-catchment for 3.5 days in extra-large flow of gas (1 L/min in a 4 mm ID tube) and PtO_2 ($p(\text{PtO}_2) = 6.8 \times 10^{-8}$ bar). Quantitative EDX of the sample in Figure S15g is presented in Table S2.

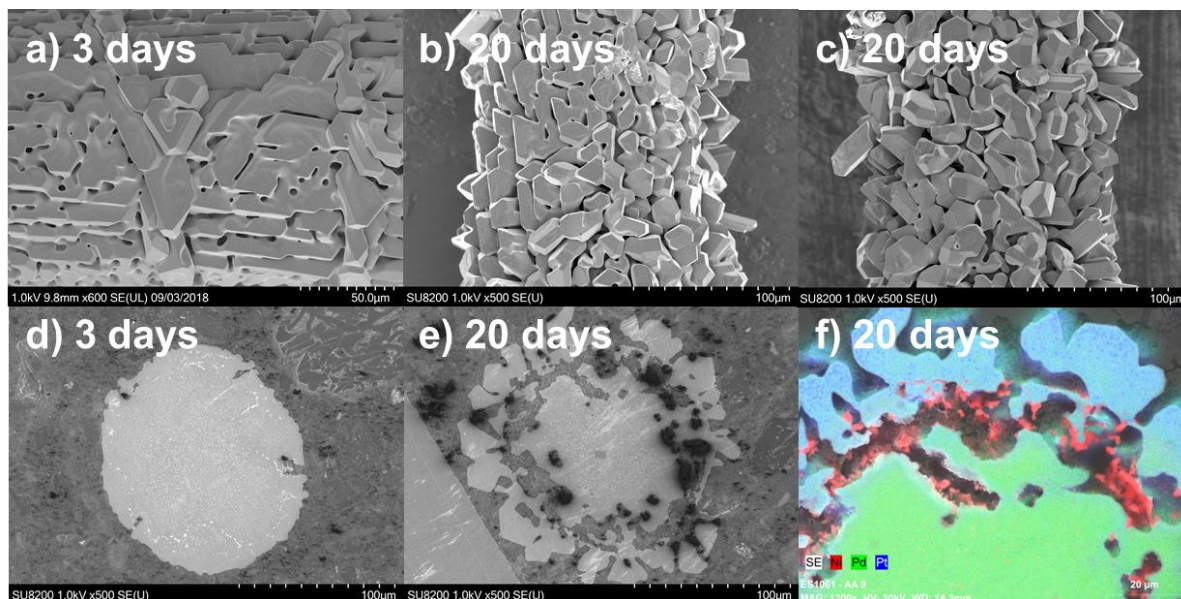


Figure S16. SEM/EDX analysis of a 120 μm quasi monocrystalline Pd/Ni (91.3/8.7 at. %) wire treated for Pt-catchment for 20 days with normal flow of gas and PtO_2 ($p(\text{PtO}_2) = 4.3 \times 10^{-8}$ bar), but with sample positioning giving very high exposure to the investigated part of the sample.

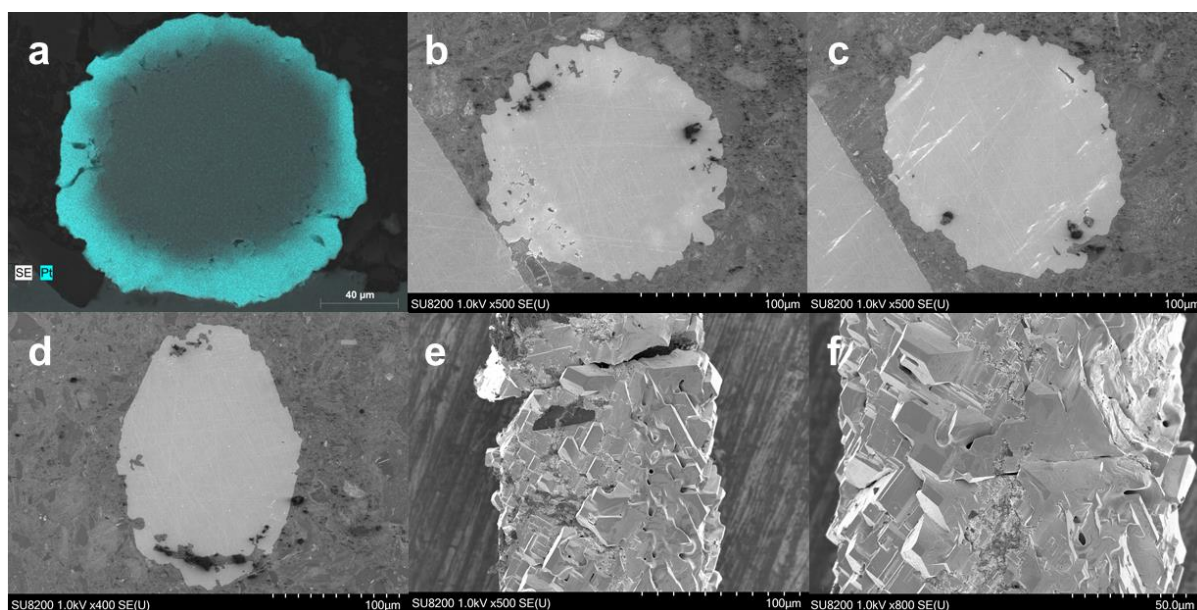


Figure S17. SEM/EDX analysis of a 120 μm quasi monocrystalline Pd wire treated for Pt-catchment for 20 days with normal flow of gas and PtO_2 ($p(\text{PtO}_2) = 4.2 \times 10^{-8}$ bar), but with sample positioning giving very high exposure to the investigated part of the sample.

Table S2. Quantitative EDX analyses [at. %] of the cross section of a) a 120 μm quasi monocrystalline Pd-wire tested for Pt-catchment for 20 days and b) a 76 μm quasi monocrystalline Pd-wire tested for Pt-catchment for 3.5 days. The locations are selected to be on the in- or out-side small pores/voids in the Pd wires. Figure S18 shows the locations (point P) of each point analysed.

a) pure Pd (120 μm) quasi monocrystalline wire treated for Pt-catchment for 20 days (Figure S17)

Point (P)	Pt	Pd	Ni	O	Pt/(Pd+Pt)	Depth (μm)
1	26.3	72.5	0.1	0.0	27 %	2
2	15.3	70.3	0.1	13.5	18 %	15
3	0.4	89.9	0.0	9.0	0 %	25

4	25.1	74.4	0.1	0.0	25 %	2
5	5.4	94.3	0.0	0.0	5 %	15
6	0.1	88.6	0.0	11.0	0 %	30
7	28.2	70.6	0.1	0.0	29 %	2
8	14.7	84.9	0.1	0.0	15 %	13
9	0.3	99.2	0.0	0.0	0 %	30
10	19.9	79.6	0.1	0.0	20 %	2
11	5.0	94.4	0.1	0.0	5 %	15
12	0.1	98.8	0.2	0.0	0 %	30

b) pure Pd (76 μm) quasi monocrystalline wire treated for Pt-catchment for 3.5 days (Figure S15)						
Point (P)	Pt	Pd	Ni	O	Pt/(Pd+Pt)	Depth (μm)
1	90.8	6.4	0.1	0.0	7 %	2
2	98.9	0.3	0.0	0.0	0 %	12
3	85.9	8.3	0.1	0.0	9 %	2
4	84.3	9.9	0.1	0.0	10 %	3
5	97.6	0.4	0.2	0.0	0 %	12
6	85.6	11.3	0.1	0.0	12 %	3
7	91.9	5.5	0.0	0.0	6 %	4
8	89.5	0.3	0.1	8.4	0 %	12
9	98.2	0.0	0.2	0.0	0 %	12
10	95.9	0.5	0.1	0.0	1 %	10

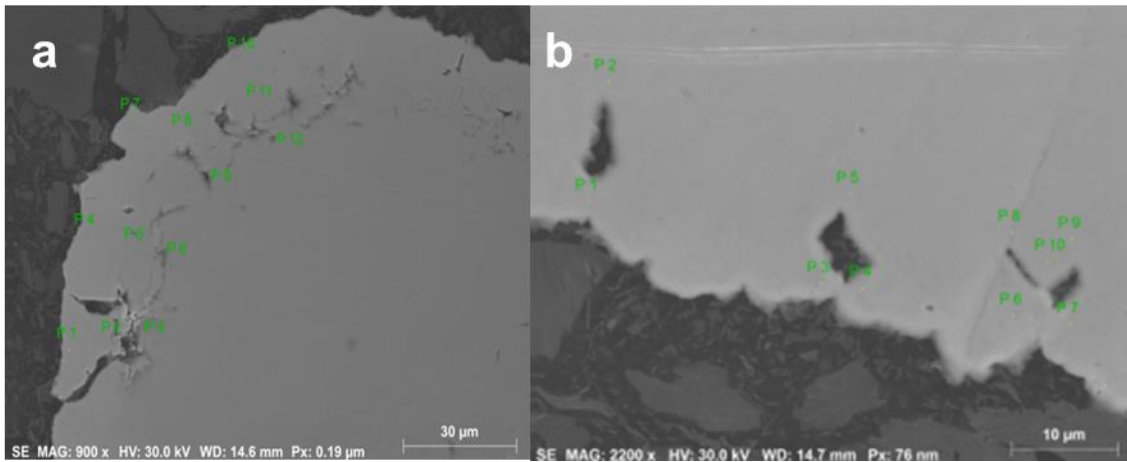


Figure S18. Image showing the points of the quasi monocrystalline Pd samples analysed with quantitative EDX in Table S2. a) 120 μm sample treated for 20 days and b) 76 μm sample treated for 3.5 days.

S.2.3. Calculation of grain boundary diffusion coefficient

In the experiment, a gas flow of PtO_2 is used above the diffusion sample. The solution of the diffusion equation is in this scenario given by the solution with an open plate and gas flow above the sample [47]

$$\frac{c_x - c_o}{c_s - c_o} = \text{erfc}\left(\frac{x}{2\sqrt{Dt}}\right)$$

Assuming c_o (concentration in the gas phase above the surface) is 1

$$c_x = c_s \times \operatorname{erfc}\left(\frac{x}{2\sqrt{Dt}}\right)$$

This provides a good fit with the obtained results in Figure 9.

To compare the data for the polycrystalline disc (4.58 hours anneal) with the single crystal (23 hours anneal) we normalise the data by setting the same maximal surface concentration for the polycrystalline disc as that of the single crystal, i.e. $c_s^{\text{polycrystalline}} = c_s^{\text{single crystal}}$. We increase all the values in the profile accordingly, so that

$$c_x^{\text{polycrystalline norm}} = c_x^{\text{polycrystalline}} * (c_s^{\text{single crystal}} / c_s^{\text{polycrystalline}})$$

Assuming diffusion in one dimension can be described simply by $D_{1D} = x^2/t$, where x is distance and t is time, two different experiments with the same diffusion constant can be described as

$$D = \frac{x_1^2}{t_1} = \frac{x_2^2}{t_2} \rightarrow x_2 = x_1 \sqrt{\frac{t_2}{t_1}}$$

We therefore multiply the depth of the diffusion profile for the polycrystalline disc with $x\sqrt{t_2/t_1}$, so that $depth_{norm} = depth \times \sqrt{23/4.58}$. This corresponds to the Pt-concentration values of $c_x^{\text{polycrystalline norm}}$.

To analyse the grain boundary diffusion coefficient, the solution from Le Claire [36] is used

$$D_{GB} \times s \times \delta = 1.322 \sqrt{\frac{D_{Pt}}{t}} \left(-\frac{\partial \ln \bar{c}}{\partial y^{6/5}} \right)^{-\frac{5}{3}}$$

where D_{GB} is the grain boundary diffusion coefficient for Pt in Pd, s is the segregation factor, δ is the grain boundary width, D_{Pt} is the bulk diffusion coefficient of Pt in Pd, t is the time, \bar{c} is the average concentration profile and y is the depth. The segregation factor can be assumed to be 1 [48] and we assume δ to be 1 nm. This should not be an underestimation of the GB width [49].

We use the original data set with the sample annealed at 4.58 hours to calculate the grain boundary diffusion. In the analysis, we find the slope of the concentration when plotting against depth^{6/5} to be -3055.5 cm^{6/5}, providing a $D_{GB} = 2.9 \times 10^{-8} \text{ cm}^2/\text{s}$.

S.3. 2D diffusion model combining bulk and grain boundary diffusion

In this section, details related to the diffusion model used to show the diffusion limitation in the Pd-wire used for Pt-catchment is explained. Key aspects to consider in these calculations, such as the combination of the different diffusion rates, how the grain boundary structure is described, and how the addition of Pt is solved.

S.3.1. General information about the diffusion model

The diffusion model is developed in matlab [31]. To simulate diffusion, we use Ficks second law [47].

$$\frac{dc}{dt} = D \frac{d^2c}{dx^2}$$

The model is 2-dimensional (2D), which imply that each point is a pixel in an image, and the concentration of Pt is in the range of 0 and 1. When there is a difference in concentration through a pixel, Pt will be moved in this direction. We first create a circle where the area inside the circle is Pd (Figure S19a), while the area outside the wire will work at the Pt-source for diffusion into the wire (Figure S19b). At $t = 0$, the Pt-content is zero inside the sample.

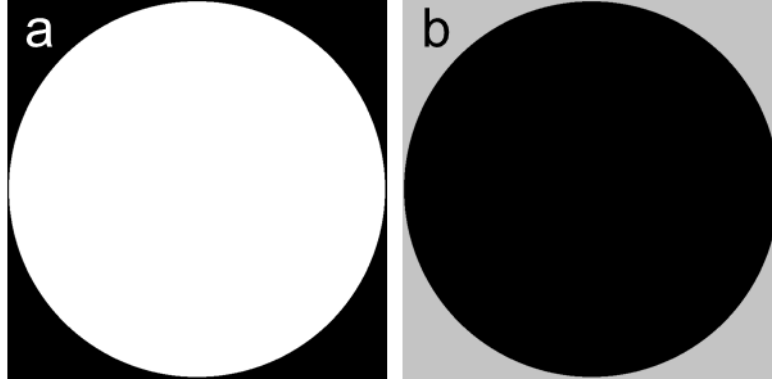


Figure S19. a) Area coloured white is Pd, representing the sample. b) area coloured in black is the sample, while area in grey around the sample is Pt on the wire surface that can diffuse into the sample.

The concentration gradient is calculated through a pixel by considering the concentration, c , in a pixel with c_{ij} relative to $c_{i(j-1)}$ and $c_{i(j+1)}$ in the vertical direction of the image, as in the equation

$$dc_{ij}^{vertical} = D_{ij}[(c_{i(j-1)} - c_{ij}) - (c_{ij} - c_{i(j+1)})]dt$$

The same relation is used in the horizontal direction, cross direction from left to right, and cross direction from right to left. In this way, the Pt can move any direction within the defined frame/image. We then define a diffusion coefficient in the same way inside a circle, which is simulating the Pd-sample. This causes the diffusion simulation to only allow diffusion inside the area defined as the sample originally, as in Figure S19a. To facilitate this, the pixels that contain a diffusion coefficient at the boundary of the sample also depends on the four directions, as with the concentration gradient. The magnitude of the diffusion coefficient will depend on the material type and on the temperature. The temperature used in the experiment is therefore only selected through the value of the diffusion coefficient used in the diffusion simulation.

Furthermore, the diffusion between two pixels must be equal in the sense that all Pt that exits pixel ij in order to enter $i(j + 1)$, must also enter $i(j + 1)$. This imply that these two operations must have the same diffusion coefficient, i.e. the diffusion coefficient does not exist inside each pixel, but between two pixels, see Figure S20.

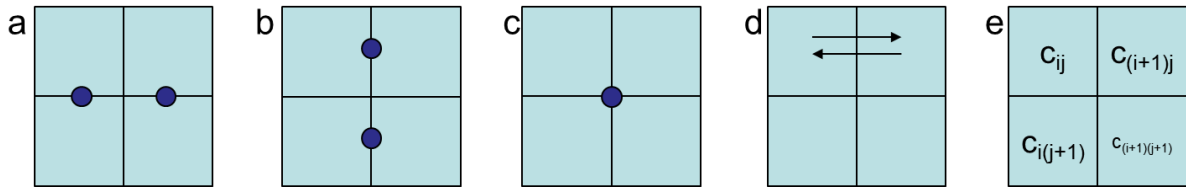


Figure S20. The points mark the location of the diffusion coefficient in the vertical (a), horizontal (b) and cross (c) directions. This is in order to maintain the same movement of Pt out of one pixel and into the other, as shown with arrows in (d). The concentrations exist inside each pixel, as in (e).

It is now necessary to define two additional parameters, which strongly affects the computational time for the diffusion calculation; the pixel size and the time step (dt). In order to save time, we do not use a constant time step, but calculate the highest possible time step based on the calculated gradient (dc_{ij}) by the relation

$$dt = 0.001 / \max(dc_{ij})$$

where $\max(dc_{ij})$ is the highest absolute value in the gradient (dc_{ij}). This ensures that the change in concentration during iterations do not become so high that it introduced artefacts, simultaneously as the computational time is limited. The dt calculated above is directly affected by the diffusion coefficient, and then also the pixel size. Reducing the pixel size from 1000 to 100 nm causes the diffusion coefficient to increase by a factor of 100 inside each pixel, because it has unit $[distance^2/second]$. This occurs because the movement is 10 times shorter, and will reduce the dt in the equation above, and increase the amount of necessary iterations. Additionally, a small pixel size, such as 10 nm, requires a lot of memory to run calculations for a 76 μm diameter circle, which would then be 7600x7600 pixels. A large pixel size will in this way save computational time. We have used 100 nm pixel size in our final calculations.

S.3.2. Surface concentration of Pt

We now need to account for the supply of Pt to the Pd-wire, as in a real Pt-catchment experiment. The Pd sample is a circle (Figure S21a), and the supply of Pt is approximated by maintaining a constant concentration of Pt outside the sample through all the iterations, as in Figure S21b. The diffusion coefficient exists only in the innermost layer of Pt around the sample.

In our SEM investigations (section 4.3), we found at most a Pt-concentration of 26.5 at. %. However, from Fjellvåg *et al.* [4] we know that the surface concentration of Pt at the highest and absolutely most exposed can reach ~ 45 at% after 20 days, while more common surface concentrations are in the range of $\sim 30 - 35$ at%. We therefore use a maximum Pt-concentration of 0.35 in our diffusion model, which is in line with the findings of Håkonsen *et al.* [41].

S.3.3. First diffusion calculation, monocrystalline Pd-wire

We are now ready to run a diffusion calculation of Pt into Pd. This scenario corresponds to a monocrystalline Pd-wire. The 2D diffusion profile calculated for a temperature of 960 °C is shown in Figure S21 (corresponds to 1000 °C after calibrating for temperature section S.3.5). We see that there is diffusion of Pt in a circular manner inwards into the wire.

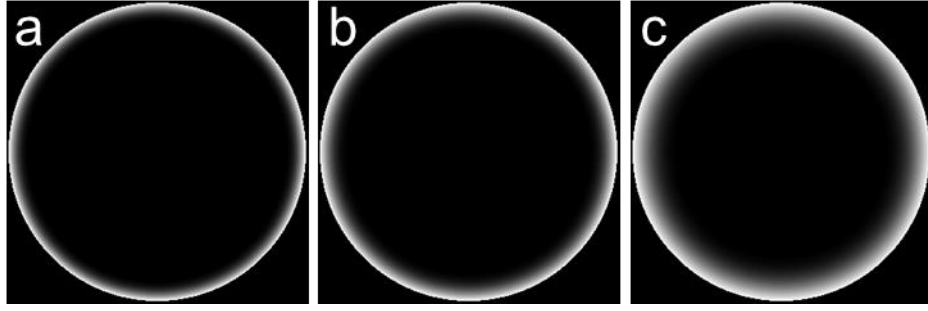


Figure S21. Result from diffusion model. Diffusion into monocrystalline Pd-wire using a temperature of 960 °C after a) 1 day, b) 5 days and c) 10 days.

We can also compare the Pt-diffusion at different temperatures. The 2D diffusion profile after 10 days is shown for selected temperatures between 900 and 1000 °C in Figure S22, showing that the inwards Pt-diffusion is significantly faster at higher temperatures.

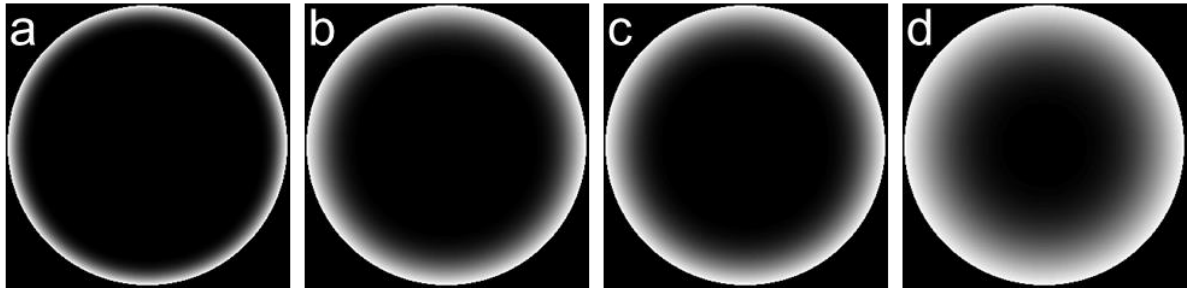


Figure S22. Simulated Pt-diffusion into a monocrystalline Pd-wire after 10 days at different temperatures; a) 900 °C, b) 950 °C, c) 960 °C and d) 1000 °C.

S.3.4. Normalization

First though, a normalization is introduced in order to compensate for the volume increase associated with Pt-catchment. For each iteration, the density in each pixel is calculated using tabulated values for the density of Pd and Pt. Based on the ratio of density before/after the iteration, the concentration profile is accordingly reduced. This is done as follows:

$$volume_i = \left(C_{Pt}^i * \frac{M_{Pt}}{\rho_{Pt}} \right) + \left((1 - C_{Pt}^i) * \frac{M_{Pd}}{\rho_{Pd}} \right)$$

$$volume_{i-1} = \left(C_{Pt}^{i-1} * \frac{M_{Pt}}{\rho_{Pt}} \right) + \left((1 - C_{Pt}^{i-1}) * \frac{M_{Pd}}{\rho_{Pd}} \right)$$

$$V_{expansion} = \frac{volume_i}{volume_{i-1}}$$

$$C_{Pt}^i(updated) = \frac{C_{Pt}^i}{V_{expansion}}$$

Where M_{Pt} and M_{Pd} is the formula weight (atomic weight) of Pt and Pd, respectively, and ρ_{Pt} and ρ_{Pd} is the density of Pt and Pd, respectively. Because $\rho_i > \rho_{i-1}$, the normalization compensates for the volume increase caused by the diffusion of Pt into the sample. The Pt-content in the 2D diffusion

profile is then summed up to obtain the total Pt-concentration, which is plotted versus time in Figure S23.

S.3.5. Compare diffusion model to analytical solution of the diffusion equation

We can now compare the data in Figure S22 with an analytical solution to the diffusion equation for a cylindrical sample, in order to see how realistic the created diffusion model is. It is especially important to know if the model realistically reproduces the expected diffusion profile at a given temperature, alternatively to calibrate for temperature. We compare with the analytical solution of the diffusion equation for a cylindrical sample with an infinite Pt-source on the surface of the sample, as in the situation where a material is deposited in the surface. The equation for the diffusion profile is given below [50]

$$c(r, t) = c_s \left(\frac{a^{\frac{1}{2}}}{r^{\frac{1}{2}}} \right) \operatorname{erfc} \left(\frac{a - r}{2\sqrt{Dt}} \right)$$

where a is the radius of the cylindrical sample (38 μm), D is the diffusion constant, t is time, r is distance, c_s is the surface concentration of Pt and c is the concentration profile. The diffusion profile calculated from this equation is integrated to obtain the total Pt-content in the entire sample, C_{Pt} . The Pt-concentration is then normalized by updating the radius (a) during the calculation of the solution to the analytical diffusion equation, as follows:

$$a_{updated} = \sqrt{\left(\frac{\left(C_{Pt} \frac{M_{Pt}}{\rho_{Pt}} + (1 - C_{Pt}) \frac{M_{Pd}}{\rho_{Pd}} \right)}{\frac{M_{Pd}}{\rho_{Pd}}} \right) * a_{original}^2}$$

The simulated diffusion model (Figure S21) is already normalized (section S.3.4), and the two models are compared in Figure S23 with different temperature. The simulated diffusion model overestimates the inwards diffusion of Pt with approximately 40 °C. When using 960 °C in the simulation, our model is close to the analytical solution at 1000 °C. We therefore use 960 °C as the standard temperature to obtain the correct diffusion at 1000 °C, giving a slight overestimation of the diffusion. When 1000 °C is written in the main text of this paper, it corresponds to calculations using 960 °C as the input temperature in the simulated diffusion model. The similar shape of the Pt-concentration profiles from the calculations indicate that the current diffusion model calculates the diffusion correctly.

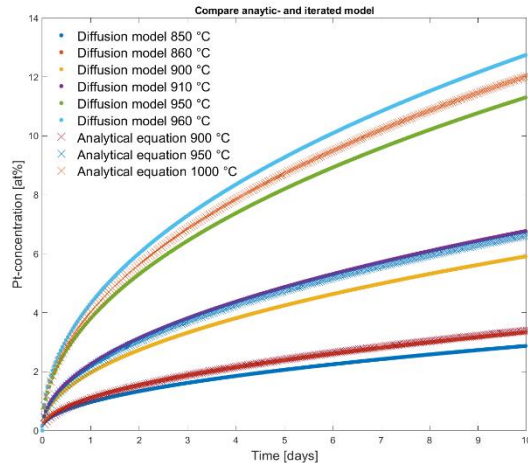


Figure S23. Comparison between analytical solution to diffusion equation for a cylindrical sample and the current model for a monocrystalline wire, at different temperatures, which are indicated in the figure.

S.3.6. Introduction of grain boundaries and grain boundary diffusion

In order to simulate a real polycrystalline Pd-wire used for Pt-catchment, we need to introduce grain boundaries (GB). This is done by changing the diffusion coefficient in some channels through the sample, as in Figure S24a. The length of the GBs introduced is slightly more than the circumference of the wire, corresponding to the length of GBs the observed in Figure 7a. The width of the GBs should preferably be realistic, which means a GB width of approximately 10 nm. However, this is difficult to obtain because the high diffusion coefficient in the GBs forces the time step, dt , to be much shorter for these calculations, meaning many more iterations. The pixel size is instead twice that used in the other calculations (5 pixels per μm). The calculation is still not fast enough to run realistically long calculations (10 days), but we can see the effect of the GBs during the first 500 seconds of diffusion of Pt into Pd. The result of introducing GBs to the system is that they rapidly fill up with Pt in the range of minutes (Figure S24b-d). Already after 60 seconds, the centre of the GBs contain 9 at. % Pt, while after 500 seconds the centre of the GBs contain 31 at. % Pt, and are in practice full of Pt. The Pt-concentration in the GBs near the wire core is shown in Figure S25.

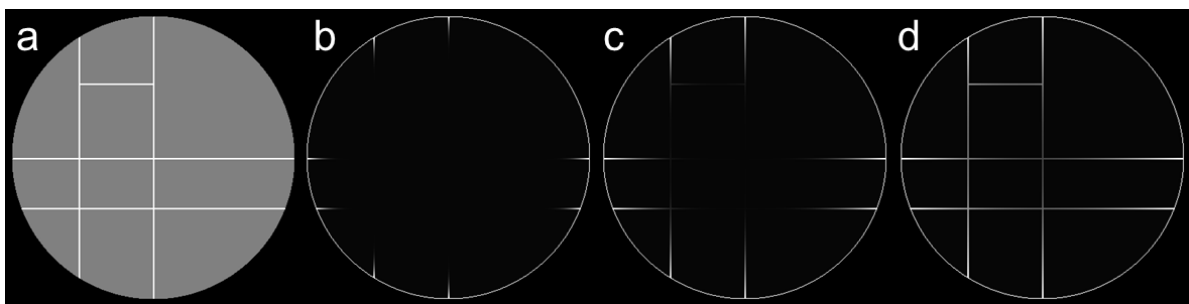


Figure S24. a) Diffusion coefficient for a wire sample containing grain boundaries (white corresponds to GBs, grey to bulk), b) Pt-concentration after 1 second, c) Pt-concentration after 10 seconds, and d) Pt-concentration after 60 seconds.

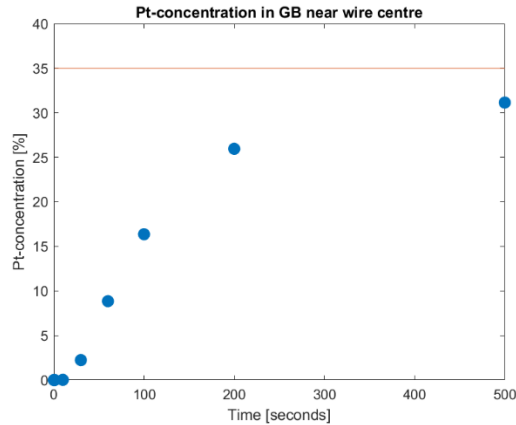


Figure S25. Pt-concentration in the GB near the wire centre versus time for the model showing filling of the GBs. The straight red line correspond to the limiting Pt-concentration of 35 at. % Pt.

S.3.7. Approximating a diffusion system for polycrystalline wire

The calculation above (section S.3.6) cannot be run for long time because of the small time step needed, causing an extremely long computational time even at a supercomputer. This is due to the fact that this calculation has to be run as a serial job, not a parallel job. However, we see that the effect of introducing GBs is that they rapidly fill up with Pt, transporting Pt into the core of the wire. This is similar to the EDX maps shown in Figure 7. We can therefore approximate the system by placing a concentration of Pt inside the GBs already from the beginning of the calculation, and maintain a constant concentration of Pt in the GBs through all the iterations. In this way, we can remove the GB diffusion coefficient from the system, and use only the bulk diffusion coefficient. This allows for a similar time step as in the model for a monocrystalline wire. The GBs will now act like a surface, and the evolution of the Pt-concentration over 10 days is shown in Figure S26.

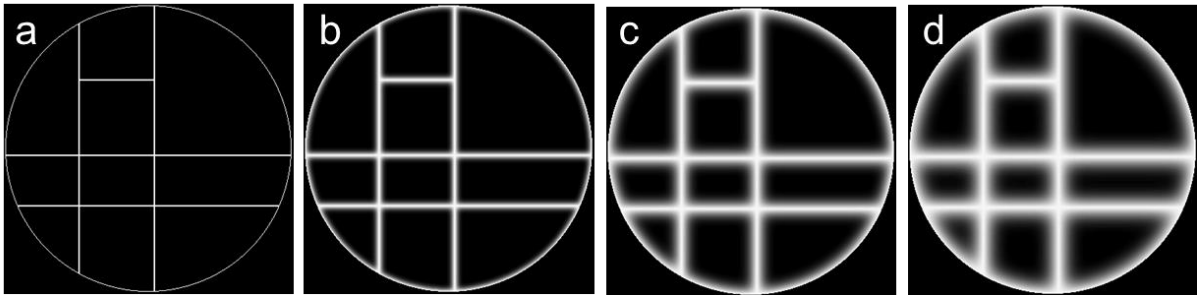


Figure S26. Model for diffusion in polycrystalline Pd. a) the concentration profile after 1 hour, b) the concentration profile after 1 day, c) the concentration profile after 5 days, and d) the concentration profile after 10 days.

S.3.8. Adding Pt-catchment limitation based on tomography results

In order to make the diffusion model more realistic, a limit to the surface concentration of Pt was introduced. In the *in situ* absorption-CT experiment, a linear increase in volume was observed for the first 4 hours of the Pt-catchment experiment on pure Pd, with a 1.0 % volume increase (Figure S6). This limitation is introduced by gradually increasing the Pt-content in the first layer of pixels on the wire surface, corresponding to the correct Pt-content to be introduced in each time window, dt . The result from the Pt-catchment limited diffusion model is shown in Figure S27, where the results are also compared with the non-Pt-limited diffusion model and experimental results.

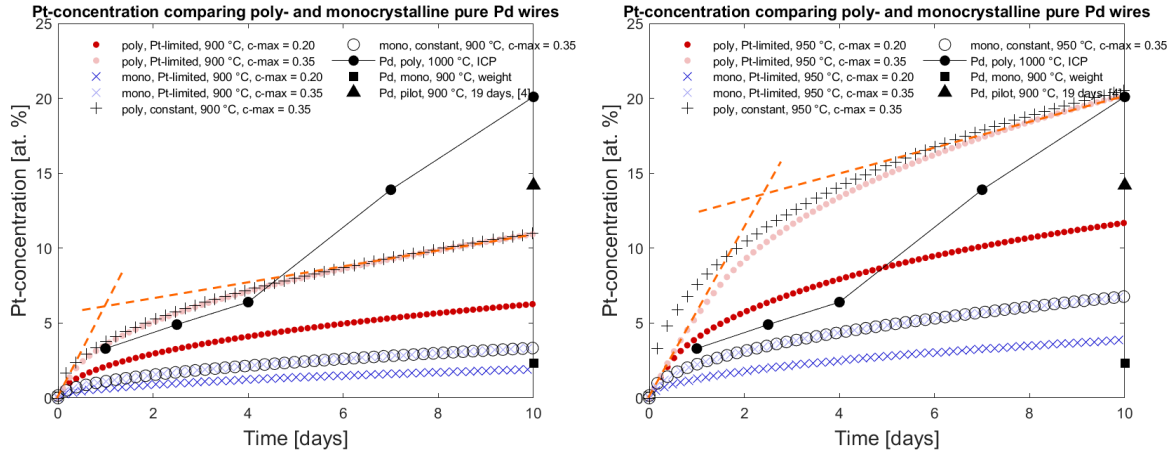


Figure S27. Pt-concentration versus time for the model including the Pt-limitation. Experimental data is also included in the figure. The data at 900 °C (860 °C in the model) is shown to the left, 950 °C (910 °C in the model) is shown to the right and data at 1000 °C (960 °C in the model) is shown in Figure 13.

S.3.9. Summary of important variables and parameters

The variables which are used in the different calculations are summarized in Table S3 and diffusion constants for the Pd-Pt system are summarized in Table S4.

Table S3. Table of different values relevant for the diffusion model, and general diffusion properties considered in this investigation. The abbreviations used are $D_{diffusing\ element}^{sample\ information}$

Diffusion model	Time calc.	dt [s]	D_{Pt}^{bulk} $\left[\frac{cm^2}{s}\right]$	D_{Pt}^{GB} $\left[\frac{cm^2}{s}\right]$	Pixel size [nm]	GB width [nm]	T [°C]	c_0 [at. %]
GB-filling	500 s	0.0001 / $\max(dc_{ij})$	3.26×10^{-14}	2.9×10^{-8}	200	400	960	0.35
Mono	10 d	0.001 / $\max(dc_{ij})$	3.26×10^{-14}	-	100	-	860, 910, 960	0.20, 0.35
Poly	10 d	0.001 / $\max(dc_{ij})$	3.26×10^{-14}	-	100	100	860, 910, 960	0.20, 0.35

Table S4. Diffusion coefficients collected from Baheti *et al.* [35], and the GB-diffusion coefficient from the current investigation.

	Pure Pd	Pure Pt	Pd with 3.5 at. % Pt
D_{Pd} [cm ² /s]	2.84×10^{-13}	3.30×10^{-14}	4.39×10^{-13}
D_{Pt} [cm ² /s]	3.26×10^{-14}	6.33×10^{-14}	4.47×10^{-15}
D_{Pt}^{GB} [cm ² /s]	2.9×10^{-8}		

References

- National Institute of Standards and Technology (NIST) and U.S. Department of Commerce. *X-Ray Mass Attenuation Coefficients*. [cited 2021 03.02.21]; Available from: <https://physics.nist.gov/PhysRefData/XrayMassCoef/tab3.html>.


46. Smithells, C.J., *Smithells metals reference book = Metals reference book*, in *Metals reference book*, Totemeier, T.C. and Gale, W.F., Editors. 2004, Elsevier Butterworth-Heinemann: Amsterdam Boston.
47. Tilley, R.J.D., *Understanding solids : the science of materials*. 2nd ed. ed. 2013, Chichester: Wiley.
48. Schwarz, S.M., Kempshall, B.W., Giannuzzi, L.A., and Stevie, F.A., *Utilizing the SIMS technique in the study of grain boundary diffusion along twist grain boundaries in the Cu(Ni) system*. *Acta Materialia*, 2002. **50**(20): p. 5079-5084.
49. Prokoshkina, D., Esin, V.A., Wilde, G., and Divinski, S.V., *Grain boundary width, energy and self-diffusion in nickel: Effect of material purity*. *Acta Materialia*, 2013. **61**(14): p. 5188-5197.
50. Watson, E.B., Wanser, K.H., and Farley, K.A., *Anisotropic diffusion in a finite cylinder, with geochemical applications*. *Geochimica et Cosmochimica Acta*, 2010. **74**(2): p. 614-633.

Paper III

Platinum catchment using Pd/Au alloys: Effect of enhanced diffusion

A. S. Fjellvåg, D. Waller, T. By, A. O. Sjøstad

Submitted to *Industrial & Engineering Chemistry Research*



III

Paper IV

Structural disorder and antiferromagnetism in $\text{LaNi}_{1-x}\text{Pt}_x\text{O}_3$

A. S. Fjellvåg, Ø. S. Fjellvåg, Y. Breard, A. O. Sjøstad

Journal of Solid State Chemistry, **2021**, 299, 122181



IV

IV

Structural disorder and antiferromagnetism in $\text{LaNi}_{1-x}\text{Pt}_x\text{O}_3$ A.S. Fjellvåg^{a,*}, Ø.S. Fjellvåg^b, Y. Breard^c, A.O. Sjøstad^{a,*}^a Department of Chemistry, Centre for Materials Science and Nanotechnology, University of Oslo, Norway^b Department for Neutron Materials Characterization, Institute for Energy Technology, PO Box 40, NO-2027, Kjeller, Norway^c Laboratoire CRISMAT, UMR 6508 CNRS ENSICAEN, 6 bd du Maréchal Juin, 14050, Caen Cedex 4, France

ARTICLE INFO

Keywords:

Crystal structure
B-site ordering
Disorder
Domains
Magnetism
Antiferromagnetism

ABSTRACT

We report on the B-site substitution of Pt for Ni in the system $\text{LaNi}_{1-x}\text{Pt}_x\text{O}_3$. The system can only be synthesized between $x \leq 0.50$, with LaNiO_3 ($x = 0.00$) and the stoichiometric double perovskite $\text{La}_2\text{NiPtO}_6$ ($x = 0.50$) as the end members. Higher Pt-contents ($x > 0.50$) are unachievable due to the preference of Pt to being in oxidation state +IV in octahedral coordination. Upon introducing Pt into LaNiO_3 , a phase transformation from rhombohedral ($R\bar{3}c$) to monoclinic ($P2_1/n$) symmetry is observed for $0.075 \leq x \leq 0.125$, where all monoclinic samples are B-site ordered, and Pt show a strong preference for the Pt-site (2c-site) for all compositions ($x \geq 0.20$). Powder X-ray diffraction analysis reveal disorder of the Pt-distribution in several of the non-equimolar samples ($0.20 \leq x \leq 0.40$), which point toward cluster formation with domains of high and low Pt-content within each sample. $\text{La}_2\text{NiPtO}_6$ further show an antiferromagnetic transition at ~ 40 K. A similar transition is observed for all monoclinic samples ($x \geq 0.20$), however, the transition is less pronounced for lower x . This is explained in terms of the structural disorder, *i.e.* by the coexistence of antiferromagnetic domains with long range order and paramagnetic domains dominated by short range antiferromagnetic interactions.

1. Introduction

Platinum, one of the most stable noble metals, has been utilized for applications for centuries, *e.g.* in crucibles for high temperature heat treatments and in thermocouples. This has led to the discovery of several different Pt containing oxides [1], through unexpected side reactions. Pt has preference for oxidation state 0, +II and +IV, as seen from the stability of Pt metal at low partial pressures of oxygen ($p\text{O}_2$), Pt_3O_4 at intermediate temperature and $p\text{O}_2$, and PtO_2 at higher $p\text{O}_2$ [1]. The stability of the +II and +IV oxidation states of Pt can be rationalized by the square planar coordination with a d^8 -configuration (+II) and an octahedral coordination with a d^6 low spin configuration (+IV).

In double perovskites, such as $\text{La}_2\text{CoPtO}_6$, Pt adopts the +IV oxidation state. The compound is insulating and weakly ferromagnetic at low temperature ($T < \sim 50$ K) [2]. Compared with $\text{La}_2\text{CoIrO}_6$, the magnetic interaction between Co(II, high spin) and Pt(IV) is weak [2], explained through a hybridization mechanism first applied on Cr-based double perovskites [3]. In these 5d-systems, spin orbit coupling may also affect the magnetic interactions. The synthesis procedure for the similar compound, $\text{La}_2\text{NiPtO}_6$, has previously been reported [4], but its magnetic properties are so far unrevealed. Additionally, neither $\text{LaCo}_{1-x}\text{Pt}_x\text{O}_3$ nor

$\text{LaNi}_{1-x}\text{Pt}_x\text{O}_3$ have been tried synthesized and investigated for non-equimolar compositions ($x \neq 0.50$).

It is well-known that LaNiO_3 is a Pauli paramagnetic metal, which upon B-site substitution turn insulating. The magnetic properties of LaNiO_3 are highly dependent on structural distortions induced by substitution, the choice of substituent element, and the consecutive internal redox processes; the result is varying ferro- (FM) and antiferromagnetic (AFM) interactions [5–10]. In $\text{Sr}_2\text{FeMoO}_6$, the grain structure and degree of B-site ordering has been shown to strongly influence both magnetoresistance and magnetic properties [11,12], also for non-equimolar compositions [13]. By applying various synthesis protocols, different degree of long range Fe–Mo ordering can be achieved. However, the short range Fe–Mo ordering is still present, regardless of the degree of long range ordering. For B-site substituted LaNiO_3 , long range ordering is only achieved by substitution with 4d- or 5d-elements which obtain a +IV oxidation state, reducing Ni to +II [14]. The subsequent order-disorder phenomena and the effect on magnetic properties in LaNiO_3 , in both equimolar and non-equimolar compositions, has so far attracted little attention.

Herein we investigate the structure and magnetic properties of $\text{LaNi}_{1-x}\text{Pt}_x\text{O}_3$, $0 \leq x \leq 0.50$. Inspired by the studies on $\text{Sr}_2\text{FeMoO}_6$, we

* Corresponding authors.

E-mail addresses: a.s.fjellvag@smn.uio.no (A.S. Fjellvåg), a.o.sjastad@kjemi.uio.no (A.O. Sjøstad).

pay special attention to the structural disorder of non-equimolar compounds in the system $\text{LaNi}_{1-x}\text{Pt}_x\text{O}_3$. We further evaluate magnetic properties below room temperature, and correlate low temperature magnetic ordering to structural disorder.

2. Experimental

$\text{La}(\text{NO}_3)_3 \times 6\text{H}_2\text{O}$ (99.9 %) and $\text{Ni}(\text{NO}_3)_2 \times 6\text{H}_2\text{O}$ (99 %) were purchased from Alfa and KEBO Lab, respectively, whereas Pt metal (99.9 %) was purchased from Heraeus and citric acid ($\text{C}_6\text{O}_7\text{H}_8 \times \text{H}_2\text{O}$; 98 %) was purchased from Sigma-Aldrich. The La and Ni nitrate salts were dissolved in water and the accurate salt concentrations (mol/g) of the solutions were determined by thermogravimetry. All samples were synthesized using a citric acid complexation method. Stoichiometric amounts of La- and Ni nitrate solutions and Pt metal were weighed out, before the Pt metal was dissolved in aqua regia (1 part HNO_3 , 3 parts HCl, VWR Chemicals). The two solutions were mixed, and 50 g of citric acid was added per gram of targeted oxide product. The solution was boiled until complete loss of water and nitrate in form of nitrous gasses, followed by overnight heat treatment at 180 °C. The samples were subsequently calcined at 400 °C in air for 12 h before pelletizing and high temperature heat treatment. For the first annealing step, samples with $x \geq 0.30$ were annealed at 1000 °C in sealed quartz ampoules with 7 bar O_2 for 12 h, using Ag_2O (KEBO Lab, 99 %) as the oxidizing agent, which releases O_2 during the heating sequence whereas samples with $x \leq 0.25$ were annealed at 850 °C in a flow of O_2 (from AGA, 5.0 quality) for 12 h. In the second annealing step, all samples were annealed at 1000 °C for 12 h in a flow of O_2 . For LaNiO_3 ($x = 0$), the high temperature heat treatment was performed twice at 850 °C in a flow of O_2 for 48 h. The synthesis conditions are expected to provide O-content near 3.0 in LaNiO_3 [15]. Prior to the magnetic measurements, samples with compositions $x = 0.20$, $x = 0.30$ and $x = 0.40$ were annealed again for 2 weeks at 1000 °C in a flow of O_2 , in order to improve the homogeneity of the samples.

Powder X-ray diffraction (XRD) were performed for all samples in the home laboratory using a Siemens Bruker-AXS D5000 diffractometer with $\text{Cu K}\alpha 1$ radiation ($\lambda = 1.5406 \text{ \AA}$) and transmission flat-plate geometry. Powder synchrotron X-ray diffraction data for selected samples ($x = 0.00, 0.05, 0.20, 0.30, 0.40, 0.50$) were collected at beam line BM01B at the Swiss-Norwegian Beam Lines (SNBL), European Synchrotron Radiation Facility (ESRF) in Grenoble, France [16]. Synchrotron XRD experiments were performed using a 2D DEXELA detector and wavelength $\lambda = 0.50506 \text{ \AA}$ for $x = 0.00$, $\lambda = 0.50467 \text{ \AA}$ for $x = 0.05$, $x = 0.20$, $x = 0.30$ and $x = 0.40$, while for $x = 0.50$, a high-resolution detector with six Si(111) analyzer crystals and $\lambda = 0.50506 \text{ \AA}$ was used. The data was collected after the initial $2 \times 12 \text{ h}$ heat treatment. The $x = 0.50$ sample was mixed with MgO to reduce absorption. One additional dataset (Fig. S5b) of synchrotron XRD of $\text{LaNi}_{0.70}\text{Pt}_{0.30}\text{O}_3$ were collected after the sample were annealed for two additional weeks. The data were collected at BM01, SNBL (ESRF), using $\lambda = 0.71490 \text{ \AA}$ and a PILATUS 2 M detector. Obtained data were reduced with the Bubble software [17], and the 2D diffraction patterns were visualized with the ALBULA software. Structural analysis was performed by Rietveld refinements using the software TOPAS [18]. For all datasets, we refined scale factor, background polynomial, Gaussian and Lorentzian peak shape and zero error. For the structures, the lattice parameters, atomic positions, thermal displacement factors and occupancies were refined. The occupancies of Ni(II), Ni(III) and Pt(IV) were restricted to yield charge neutrality and the nominal composition in total for all refinements. Identical atomic positions were used in the refinements for both structures in the two-phase (domain) model, while the scale factor, lattice parameters and peak profile was refined individually.

Magnetic measurements were performed using a Quantum Design physical properties measurement system (QD-PPMS). Samples for DC magnetization were measured from 4 to 300 K using a 2000 Oe external DC-field. In AC magnetization mode, samples were measured from 4 to 60 K both with and without a 2000 Oe external DC field, and with a 10

and 15 Oe AC field with frequencies of 117, 1117, 1997, 4997 and 9997 Hz. Field dependent DC magnetization measurements were performed at 4 K with a DC field varying between -9 and 9 T.

3. Results

3.1. Synthesis and phase relations

In this work, we have investigated LaNiO_3 , $\text{La}_2\text{NiPtO}_6$ and $\text{LaNi}_{1-x}\text{Pt}_x\text{O}_3$ for $0 \leq x \leq 0.70$. LaNiO_3 is a rhombohedral ($R\text{-}3c$) perovskite (Fig. 1a), while $\text{La}_2\text{NiPtO}_6$ is a monoclinic ($P2_1/n$) double perovskite with B -site ordering and a β -angle very close to 90° (Fig. 1b). Attempts to synthesize Pt containing samples by a solid-state route using Pt metal as precursor proved unsuccessful, as the metallic Pt did not oxidize completely, and Pt metal impurities were present in the products. As an alternative, we turned to the citric acid complexation synthesis route, where the precursor elements are mixed in a solution to ensure good atomic distribution. Combined with a high $p\text{O}_2$ during annealing, we avoid that platinum nucleates to Pt metal particles during synthesis. Correspondingly, we find all samples in the range $0 \leq x \leq 0.40$ to be phase pure (Fig. S1), while for $x = 0.50$, $< 0.50 \text{ mol \% Pt}$ is present. For $x = 0.60$ and $x = 0.70$, $\text{La}_2\text{NiPtO}_6$ is formed, in addition to significant quantities of Pt and La_2O_3 impurities. We believe a higher Pt-content than $x = 0.50$ cannot be stabilized in this system since Pt is unable to adopt lower oxidation states than +IV in the perovskite, and Ni will not go below +II under regular synthesis conditions.

Upon the introduction of Pt into LaNiO_3 , forming $\text{LaNi}_{1-x}\text{Pt}_x\text{O}_3$, a phase transformation from $R\text{-}3c$ to $P2_1/n$ occurs, and a structural two-phase region is observed for $0.075 \leq x \leq 0.125$ (Fig. 1c). This imply that only a small solid solution range is associated with Pt-substitution for Ni ($6b$ -site, Table S1) in LaNiO_3 , without causing a phase transformation. However, a much larger substitutional range is possible with Ni-substitution for Pt ($2c$ -site, Table S2) in $\text{La}_2\text{NiPtO}_6$, as in $\text{La}_2\text{Ni}_{1-2x}\text{Pt}_{2x}\text{O}_6$ ($0.20 \leq x \leq 0.50$). At the phase boundary, the unit cell volume of the monoclinic phase is $\sim 2.6 \%$ larger than the rhombohedral phase (Fig. 1c). Comparing the cell parameters of the monoclinic cell (c -axis is divided by $\sqrt{2}$), we observe that the three axis lengths become very similar ($a \approx b \approx c/\sqrt{2}$) (Fig. 1c), i.e. there is no strong anisotropic distortion induced by the Pt-substitution. In addition, we note the trend of expansion for the unit cell parameters and volume (Fig. 1c) with increasing Pt content (x). When entering the regime $x \geq 0.50$, the unit cell parameters and volume flatten out, consistent with unsuccessful introduction of Pt into the compound beyond $\text{La}_2\text{NiPtO}_6$ ($x = 0.50$).

3.2. Structural details for $\text{LaNi}_{1-x}\text{Pt}_x\text{O}_3$ ($0.20 \leq x \leq 0.50$)

The $P2_1/n$ space group and structure of $\text{La}_2\text{NiPtO}_6$ includes B -site ordering [4], while a B -site disordered perovskite is better described in the $Pnma$ space group. For the higher symmetry perovskite LaNiO_3 ($R\text{-}3c$), B -site ordering is not allowed by symmetry. In the space group $P2_1/n$, long-range B -site ordering is indicated by the intensity of a low angle peak at $Q \approx 1.37 \text{ \AA}^{-1}$ [11]. Due to the large difference in atomic number between Ni and Pt, we can expect strong intensity of the peak if the B -site is ordered. The peak consists of the (101), (10 $\bar{1}$) and (011) Bragg reflections, which all relate to layers with alternating stacking of the two different B -site cations (Fig. S3). The peak is also allowed in the $Pnma$ space group [as (011)], but it always show minimal intensity for disordered perovskites. In this way, the peak is a fingerprint of the long-range ordering of B -site cations in perovskites, similar to the descriptions by Meneghini et al. [11] on the B -site ordering in $\text{Sr}_2\text{FeMoO}_6$.

Rietveld refinements of synchrotron XRD data of $\text{La}_2\text{NiPtO}_6$ give a good fit using the reported structure model [4] with space group $P2_1/n$ (Fig. S1). The cell parameters and volume are very close to the reported values [4]. Refinements of the degree of B -site ordering show almost complete B -site ordering for $\text{La}_2\text{NiPtO}_6$ (Table S3). Ni and Pt are further

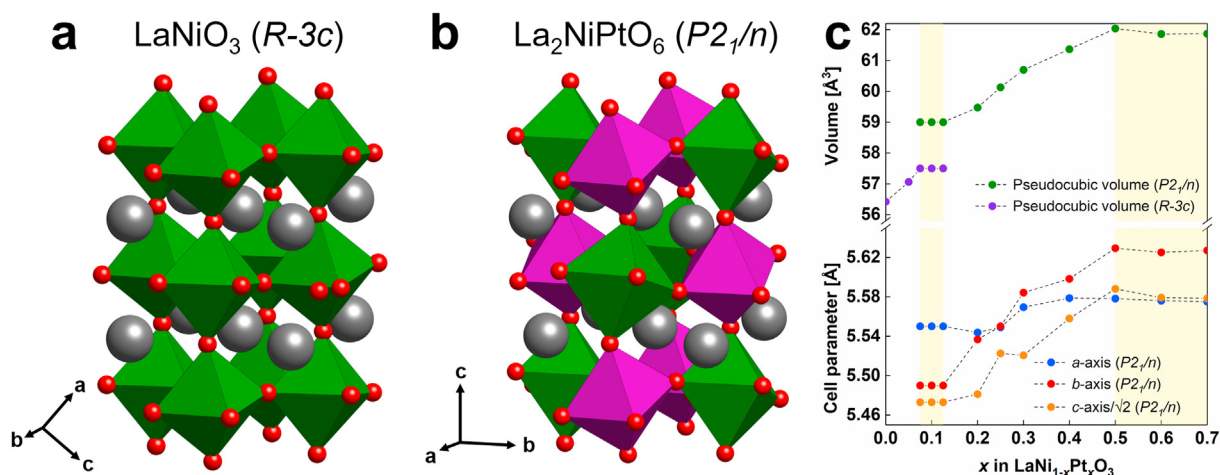


Fig. 1. Crystal structure of (a) LaNiO_3 ($R-3c$) and (b) $\text{La}_2\text{NiPtO}_6$ ($P2_1/n$). (c) Cell parameters and pseudocubic cell volume for the $\text{LaNi}_{1-x}\text{Pt}_x\text{O}_3$ system, where the c -axis of the monoclinic phase is divided by $\sqrt{2}$ for direct comparison. The rhombohedral lattice parameters (low x) are excluded for clarity (Fig. S2). The white areas are compositions with single phase, while for the beige areas, multiple phases are present.

expected to adopt the oxidation states +II and +IV, respectively, as reported in the literature [2,4]. This is reasonable considering that the structure is ordered, and in compliance with the empiric rule that B -site ordering will only occur if the B -elements obtain different oxidation states [14]. Additionally, our magnetic measurements support this conclusion, see below.

Among the monoclinic non-equimolar compositions ($0.20 \leq x \leq 0.40$), the refinements are performed using the same monoclinic structure as $\text{La}_2\text{NiPtO}_6$ ($P2_1/n$), however, with replacing an amount of Pt with Ni, as in the substitutional system $\text{La}_2\text{Ni}_{2-2x}\text{Pt}_{2x}\text{O}_6$ ($0.20 \leq x \leq 0.50$). For all the monoclinic samples ($0.20 \leq x \leq 0.50$), the analysis provides clear indications of B -site ordering (Fig. S1), indicated by the intensity of the low angle peak at $Q \approx 1.37 \text{ \AA}^{-1}$ (Fig. 2). In the $\text{LaNi}_{1-x}\text{Pt}_x\text{O}_3$ sample with $x = 0.05$, the low angle peak at $Q \approx 1.37 \text{ \AA}^{-1}$ is absent, but the presence of B -site ordering could still be visible through peak broadening or peak splitting. This would be the case if an improved Rietveld refinement fit is obtained with space group $P2_1/n$ compared to $R-3c$. We find that introducing 5 % Pt into LaNiO_3 slightly changes the intensities of some of the peaks, but no peak broadening is observed, and the refinements provide similar R_{wp} value for both space group $R-3c$ and $P2_1/n$. We therefore conclude that $x = 0.05$ is best described in $R-3c$ with the absence of B -site ordering.

Upon comparing the synchrotron XRD data of the monoclinic samples ($0.20 \leq x \leq 0.50$; Fig. 2), several trends can be seen with increasing the

Pt-content. (1) The intensity of the ordering-peaks ($Q \approx 1.37$ and 2.64 \AA^{-1}) increases, (2) all peaks shift towards lower Q , *i.e.* larger interatomic distances, (3) the main perovskite peak ($Q \approx 2.26 \text{ \AA}^{-1}$) has a much larger shift towards lower Q compared to the ordering-peaks, and (4) the peak shape for the main perovskite peak changes significantly. Furthermore, in the Rietveld refinements of the monoclinic samples ($0.20 \leq x \leq 0.50$), the peaks which indicate B -site ordering ($Q \approx 1.37 \text{ \AA}^{-1}$ and $Q \approx 2.64 \text{ \AA}^{-1}$), are not well fitted by the structural model. The two peaks are located at a lower Q than the average structure calculated during Rietveld refinements, *i.e.* they correspond to scattering from a region with a larger unit cell volume than the average structure. A different feature is observed for the main perovskite peak, which for a low Pt-content (low x) have an asymmetric tail extending towards higher Q , *i.e.* smaller interatomic distances. In this way, it appears as domains of different size contributes differently to the different peaks; *large unit cell domains* contribute to the B -site ordering peaks, while *small unit cell domains* contribute to a tail in the main perovskite peak.

Intuitively, the *large unit cell domains* should contain large Pt-contents and mimic the double perovskite $\text{La}_2\text{NiPtO}_6$, and therefore give a strong scattering contribution to the ordering peaks ($Q \approx 1.37$ and 2.64 \AA^{-1}). Correspondingly, the *small unit cell domains* may therefore be Ni-rich domains, which contribute to the tail of the main perovskite peak. These factors make it challenging to achieve satisfactory Rietveld

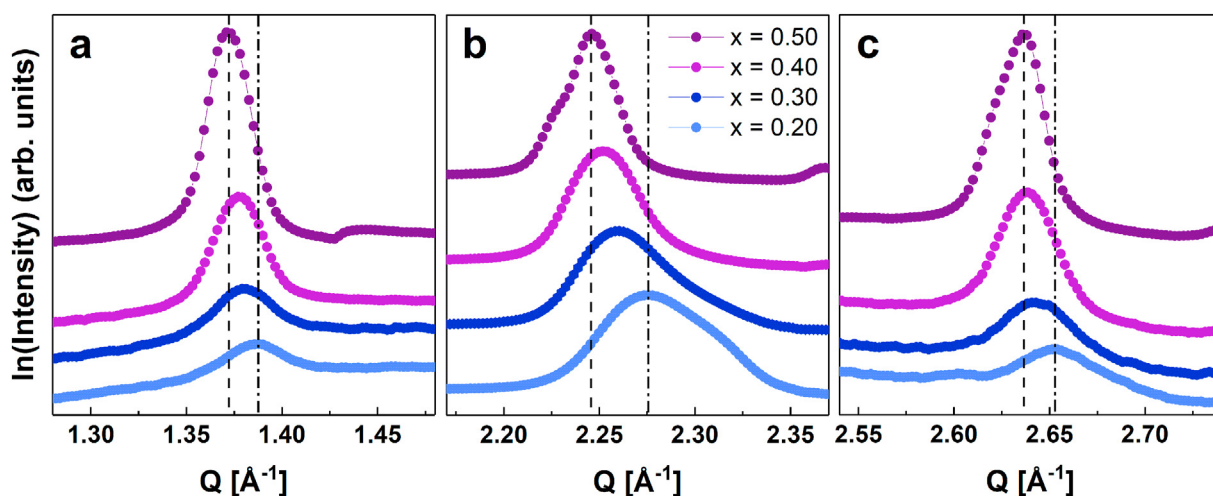


Fig. 2. Comparison of low angle peak indicating (a) ordering peak with hkl indices (101), (10 $\bar{1}$) and (011), (b) main perovskite peak with hkl indices (020), (112) and (200) and (c) a higher angle ordering peak with hkl indices (121), (013), (211) and (103). The compositions are indicated in the figure. The black dashed and dashed dot lines show the position of the maximum of the peaks for $x = 0.50$ and $x = 0.20$, respectively.

refinement fits with a one-structure model. The effect is most prominent for $x = 0.30$, but also strong in $x = 0.20$ and $x = 0.40$, i.e. all the monoclinic non-equimolar compositions.

To handle this situation, we expand the structural model for Rietveld refinements into a two-phase (domain) model with one *large* and one *small* unit cell (Table S3), mimicking a composite material with different degrees of Ni/Pt content and ordering. In a first approximation, these two phases (domains) were considered to only differ with respect to unit cell parameters. This significantly improved the fit of the asymmetric peak shape and the fit of the position of the ordering peaks, see Fig. 3. Subsequent refinements of the B-site occupation indicate that the Pt-content is higher in the *large* cell and lower in the *small* cell, consistent with our expectations (Fig. 3c). We also find that the β -angle is larger for the *small* cell and samples with a low Pt-content. The two-phase (domain) model significantly improves the Rietveld refinement fit, which is clearly seen for the main perovskite peak ($Q \approx 2.25 \text{ \AA}^{-1}$) when evaluating the difference curve (Fig. 3b). The domain-model is best suited for the samples with $0.20 \leq x \leq 0.40$, while for $x = 0.50$, the single phase model is well suited. Though dependable quantification is difficult to obtain, we believe that the qualitative information gathered is reliable. The refinements show that Pt has a very strong preference for the Pt-site (2c-site), while Ni occupies both B-atom sites (2c and 2d sites) (Table S3). For samples with a lower Pt-content ($x \leq 0.40$), a lower degree of B-site ordering is observed, corresponding to the reduced intensity of the peak at $Q \approx 1.37 \text{ \AA}^{-1}$.

We believe the *large* and *small* domains originate from inhomogeneous distribution of Pt. Pt-rich domains contain a more ordered Ni-Pt sub-lattice compared to the average structure, while regions poor in Pt are much less B-site ordered. The Pt-rich regions are expected to have larger unit cell parameters and volume in view of the trends shown in Fig. 3c. The fact that the samples are synthesized from a wet chemical citric acid-based route indicates a homogenous phase with atomic distribution of the elements during phase formation.

For the DC-magnetization measurements (see below), we performed an extended two weeks long heat treatment in order to obtain less noisy data. By performing this treatment, the XRD pattern for the $x = 0.30$ sample is only slightly changed (Fig. S4). The peak width of the main perovskite peak ($Q \approx 2.2 \text{ \AA}^{-1}$) is slightly reduced, but the peak asymmetry, with a tail extending towards higher angles, is still present throughout the diffraction pattern. Though a small difference can be observed in the 1D diffraction pattern (Fig. S4), the Debye-Scherrer cones in the 2D-diffraction pattern are smooth, both before and after the two

weeks extended heat treatment (Fig. S5). This shows that the sample was homogeneous also before the extended heat treatment, and that the treatment mainly affected macro/microstructural properties. Rietveld refinements after the extended heat treatment (Table S3) show that the domain model still describes the system significantly better than a single-phase model, indicating that the material is still dominated by Pt-rich and Pt-depleted domains. This shows that the described domain-feature is an intrinsic feature of the system, and not a consequence of limited diffusion in the synthesis process. It should again be emphasized that the citric acid method was used for synthesis, which ensure good atomic mixing and short diffusion pathways. The Pt-clustering is therefore believed to occur in small nm-sized domains inside grains, similar to the ordering phenomena well described by Meneghini *et al.* for $\text{Sr}_2\text{FeMoO}_6$ [11]. In $\text{Sr}_2\text{FeMoO}_6$, different degree of long-range ordering of Fe and Mo can be achieved by different synthesis protocols. However, the short-range ordering of Fe and Mo is always present, regardless of long-range order observed by XRD. For $\text{LaNi}_{1-x}\text{Pt}_x\text{O}_3$, we may have a very similar situation. The main differences are that (1) Pt has a very high preference for the Pt-site (2c-site) in the structure, and (2) we are additionally considering disorder in non-equimolar compounds.

Based on the current findings, we can now prepare a model of the microstructure of $\text{LaNi}_{1-x}\text{Pt}_x\text{O}_3$ in the ionic approximation. For $\text{La}_2\text{NiPtO}_6$, a Ni atom located next to a Pt(IV)-octahedra will adopt a +II oxidation state, and the oxygen in between them -II. When a Pt(IV) atom is replaced by a Ni atom, this Ni atom will adopt an oxidation state of +III. To keep charge neutrality, another Ni(III) must also be generated by oxidation of another Ni(II) to Ni(III). Thus, we find it more appropriate to describe the system by the formula $\text{La}_2\text{Ni}_y^{\text{II}}\text{Ni}_{2-2y}^{\text{III}}\text{Pt}_y^{\text{IV}}\text{O}_6$, $0 \leq y \leq 1$, with end members $\text{LaNi}^{\text{III}}\text{O}_3$ ($y = 0$) and $\text{La}_2\text{Ni}^{\text{II}}\text{Pt}^{\text{IV}}\text{O}_6$ ($y = 1$). Consequently, Ni(III)-O-Ni(II) segments are present in the structure for the non-equimolar compositions ($0.20 \leq x \leq 0.40$), and the oxygen atom located between them will be uncompensated in terms of charge. Therefore, there are three different oxygen atoms depending on which elements they are positioned between; Ni(III)-O-Ni(III), Ni(II)-O-Pt(IV) or Ni(II)-O-Ni(III), see Fig. 4a. The Ni(II)-O-Ni(III) segment deviate from the ionic approximation and the oxygen atoms of these segments will interact with its nearby Ni-atoms to find the most appropriate charge distribution.

To minimize the energy of the system, the number of uncompensated oxygen atoms must be reduced as much as possible. By evaluating both a clustering of Pt atoms (Fig. 4b) and random distribution (Fig. 4c), we observe that the number of uncompensated oxygen atoms can be reduced

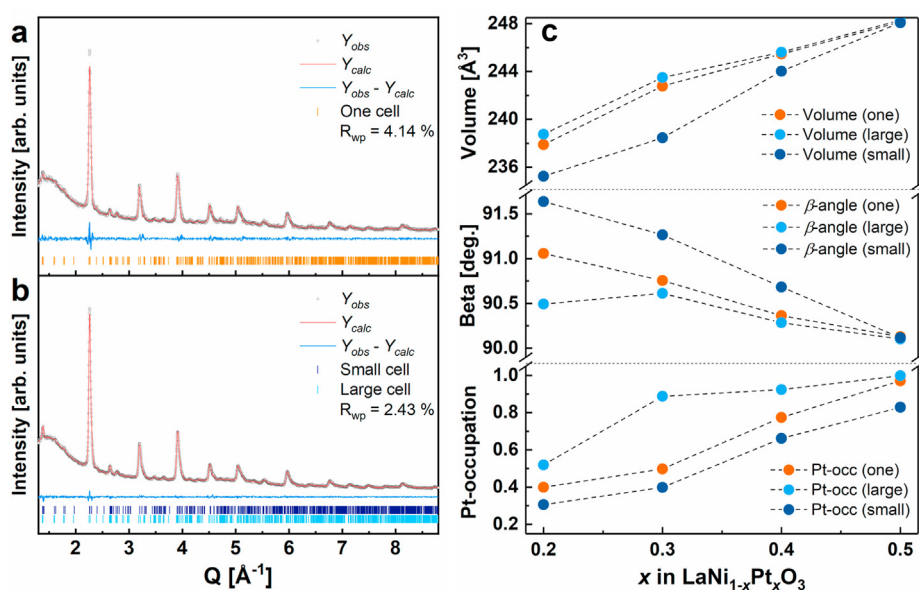


Fig. 3. Rietveld refinements of $\text{LaNi}_{0.70}\text{Pt}_{0.30}\text{O}_3$ ($P2_1/n$) using (a) a structure model with a single unit cell and (b) using the two-phase (domain) structure model described in the text, which also refine the B-site occupancy of Ni and Pt. The fit of the two-phase (domain) model prove superior to reproduce the experimental diffraction pattern (Table S3). The large bump below 2 \AA^{-1} is background from the instrumental setup. (c) Unit cell volume, β -angle and Pt-occupation from Rietveld refinements with the one- and two-unit cell model.

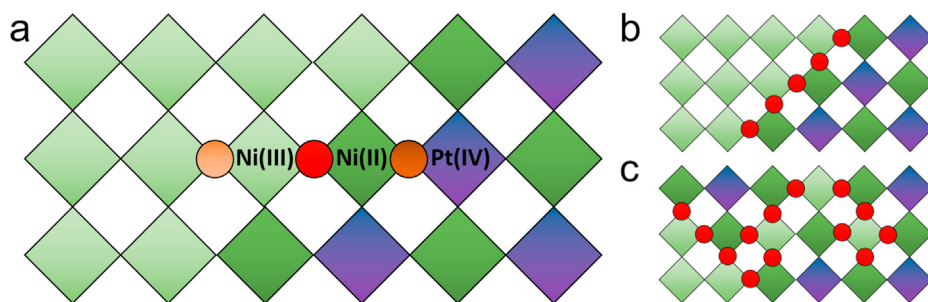


Fig. 4. (a) Illustration of the different “type” of octahedral corner sharing oxygen ions (the circles) in $\text{LaNi}_{1-x}\text{Pt}_x\text{O}_3$. The bright orange oxygen ions are positioned between two Ni(III) ions, the red is positioned between one Ni(II) and one Ni(III) ion, and the brown is positioned between one Ni(II) and one Pt(IV) ion. (b) Illustration of the number of uncompensated O-ions in the case of clustering and (c) random Pt-distribution. (For interpretation of the references to colour in this figure legend, the reader is referred to the Web version of this article.)

by forming clusters. The Pt rich clusters can in this way form boundaries of uncompensated oxygen atoms, which supports the observed phase separation in the system, simply by an energy minimization. The energy gain for clustering must therefore be significant. On the other hand, if the energy gain was substantial, we would have expected a wider immiscibility gap, with low solubility of Pt into LaNiO_3 and of Ni into $\text{La}_2\text{NiPtO}_6$. However, the observed two-phase region is narrow ($0.075 \leq x \leq 0.125$), indicating that the driving force for clustering is strong at a local scale, but not as strong on a long-range scale. The origin behind the phenomena of local ordering and clustering of Pt-rich regions remains to be explained, and local probes such as transmission electron microscopy, total scattering analysis and X-ray absorption spectroscopy, along with other average structure techniques such as neutron diffraction, may be needed to understand it.

3.3. Magnetic properties

3.3.1. Paramagnetic region ($T > 100$ K)

LaNiO_3 is found to be Pauli paramagnetic in the temperature interval 4–300 K (Fig. S6), in compliance with earlier reports on LaNiO_3 powders [19]. Upon substituting Pt into LaNiO_3 , as in $\text{LaNi}_{1-x}\text{Pt}_x\text{O}_3$, the Pauli paramagnetic behaviour changes to regular temperature dependent paramagnetism for $x = 0.05$, as well for all other samples (Fig. 5 and Fig. S7). At elevated temperature (~ 100 –300 K), these samples follow a linear Curie-Weiss relationship (Fig. S8). For the $x = 0.20$, 0.30 and 0.40 samples prepared, after following only the initial synthesis protocol (2×12 hou heat treatment), the Curie-Weiss region deviated slightly from linear behaviour. After extended heat treatments (two additional weeks),

the susceptibility is slightly lowered, and the Curie-Weiss region is more pronounced (Fig. S9). We suggest that macro/microstructural changes caused by the heat treatment is the origin of this effect, as the structural domain model still describes the system best also after the extended heat treatment (see above).

Curie-Weiss analysis further yields a highly negative θ -value for all analysed compositions, and a paramagnetic moment in the range of 2.4–3.1 μ_B , see Table 1. The paramagnetic moment is approximately unchanged through the compositional series, i.e. it is almost invariant with respect to the Pt-content. Based on the proposed chemical formula from the ionic approximation (see above), $\text{La}_2\text{Ni}_y^{\text{II}}\text{Ni}_{2-2y}^{\text{III}}\text{Pt}_y^{\text{IV}}\text{O}_6$, and assuming Ni(III) is in the low spin state, the electronic configuration at the B-site for $0 \leq y \leq 1$ ($0 \leq x \leq 0.50$) will be:

$$y\text{Ni}^{\text{II}} + (2 - 2y)\text{Ni}^{\text{III}} + y\text{Pt}^{\text{IV}} \rightarrow y(t_{2g}^6 e_g^2) + (2 - 2y)(t_{2g}^6 e_g^1) + y(t_{2g}^6 e_g^0)$$

We see that the average number of unpaired electrons at the B-site will always be one. In the spin-only approximation [20], this results in a minimal change in the paramagnetic moment through the compositional series (Table 1), and comply well with our observation of a similar paramagnetic magnetic moment for all compositions.

Notably, all compositions show a slightly higher magnetic moment than the spin-only approximation, especially $x = 0.05$, 0.25 and 0.50 (Table 1). The elevated magnetic moment may have several origins, such as small amounts of magnetic impurities, an unexpected high-spin state of Ni(III), spin orbit coupling, or microstructural effects (surfaces-/interfaces). Firstly, magnetic impurities are unlikely. The only impurity observed with XRD is Pt-metal for $x = 0.50$, which does not contribute to the Curie-Weiss paramagnetic moment as Pt is a Pauli paramagnetic metal. The spin state of Ni or spin orbit coupling could in combination explain the elevated magnetic moment, but our experimental data cannot confirm either scenario.

With respect to structural effects, both the degree of B-site ordering [12] and the existence of surface states [21] are known to affect magnetic properties. In $\text{LaNi}_{1-x}\text{Pt}_x\text{O}_3$, the local Ni–Pt ordering inside domains, and the interface between domains, may therefore induce magnetic phenomena not possible to describe by this simple approximation. We have clearly seen the effect of extended heat treatments on the magnetic susceptibility (Table 1 and Fig. S9), and believe the sample homogeneity and macro/microstructure is related to the observed magnetic moment. We therefore conclude that the spin-only approximation describes well the paramagnetic moments of these samples, and that the microstructure

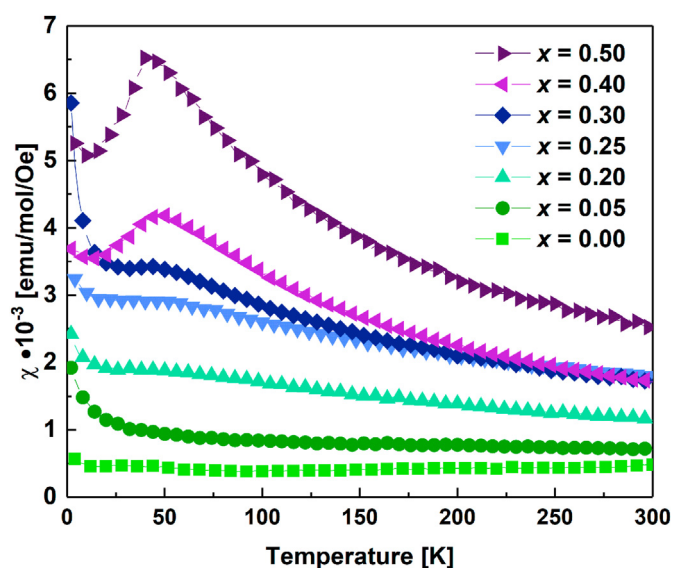


Fig. 5. Zero field cooled (ZFC) DC magnetization measurements of $\text{LaNi}_{1-x}\text{Pt}_x\text{O}_3$ ($0 \leq x \leq 0.50$) using a 2000 Oe external DC-field. The sample compositions are indicated in the figure.

Table 1

Experimental magnetic moment and the θ -value calculated using the Curie-Weiss relation, and the theoretical magnetic moment calculated from the spin-only approximation [20].

x	0.05	0.20 ^a	0.20 ^b	0.25	0.30	0.40	0.50
$m(\text{exp.})$	2.7	2.7	2.4	3.1	2.6	2.4	2.9
$m(\text{theory})$	1.76	1.84	1.84	1.87	1.90	1.95	2.00
θ [K]	−1027	−350	−322	−354	−194	−111	−130

^a Standard heat treatment procedure.

^b Sample heated for two additional weeks.

contributes with minor additional effects.

3.3.2. Antiferromagnetic transition at low temperature

For $\text{La}_2\text{NiPtO}_6$, the DC magnetic susceptibility show a clear drop below ~ 40 K, consistent with long-range antiferromagnetic ordering (Fig. 5). The transition also occurs for all monoclinic samples ($x \geq 0.20$), i.e. with *B*-site ordering, but not for $x = 0.05$. However, the transition gets much less pronounced with reducing Pt-content, and for $x \leq 0.30$ the transition is visible only as a small step in the susceptibility. This is probably due to a significant paramagnetic contribution upon further cooling, resulting from the fact that the non-equimolar samples contain less of the long-range Ni–Pt structural ordering. Still, the transition temperature (T_N) is seemingly unaffected and changes very little with Pt-content (Fig. 5). The fact that $x = 0.05$ is structurally described by *R*-3c indicates that this sample could still be metallic [22], and it may not be dominated by the same mechanisms as the other samples.

To understand the low temperature magnetic properties of this system, field dependent DC magnetic measurements were performed at 4 K, see Fig. 6a. The magnetization is low for all samples, and the lowest magnetization is observed for samples with low x (low Pt-content). It is therefore likely that an AFM ground state dominates all samples, with some differences depending on the Ni/Pt content. This correlates well with the negative theta value from the Curie-Weiss analysis (Table 1), which showed increasingly negative values for samples with a low x (low Pt-content). Additionally, the field dependent magnetization measurements show an upswing at high magnetic fields for several of the compositions, most prominent for $x = 0.40$ and $x = 0.50$ (Fig. 6a). This is evident from the derivative of the magnetization (Fig. 6b), which for these samples increases for fields above 1 T. The phenomenon is quite weak, show no signs of saturation up to 9 T, and its origin is unknown. It could simply come from the fact that we transition from a strong ($x = 0.05$; short range interactions) to weak ($x = 0.50$; long range ordered) antiferromagnet with increasing Pt-substitution, causing the Pt-rich samples to be more affected by the external field. Additionally, if there is a small degree of disorder, e.g. a few percent mixing in Ni–Pt ordering, structural strain, inter-grain effects, or magnetostriction, this could cause different canting of the spins in the magnetic field, resulting in varying effects in the field dependent magnetization. We find it unlikely that this effect is coming from changes in magnetic interactions or electron configuration.

To further investigate the AFM transition at ~ 40 K, AC magnetic measurements was performed for two compositions, $x = 0.25$ and $x = 0.50$, see Fig. 7. For $\text{La}_2\text{NiPtO}_6$, χ' show similar behaviour as the DC magnetization; there is a drop in the susceptibility below ~ 42 K and the AFM transition show no frequency dependence. χ'' is generally noisy and close to zero, but a weak peak is observed above the transition temperature. This indicates that the AFM transition may start at a higher

temperature than indicated from χ' . However, we still believe that $\text{La}_2\text{NiPtO}_6$ is near being a pure antiferromagnet. For $x = 0.25$, χ' show an increase in susceptibility below T_N (Fig. 7), while χ'' is noisy and close to zero. The behaviour contrasts that of $\text{La}_2\text{NiPtO}_6$, especially the different behaviour of χ' (Fig. 7), indicating a deviation from pure antiferromagnetism for $x = 0.25$. In this way, all the non-equimolar compositions may be different compared to the equimolar $\text{La}_2\text{NiPtO}_6$ ($x = 0.50$).

4. Discussion

We have shown how Pt-substitution causes disorder in the non-equimolar compositions in $\text{LaNi}_{1-x}\text{Pt}_x\text{O}_3$ ($0.20 \leq x \leq 0.40$), and that a domain-structure appears with Pt-rich domains, with large degree of *B*-site ordering, and Pt-depleted domains, with low degree of *B*-site ordering. The present investigation draws similarities to the structural disorder in $\text{Sr}_2\text{FeMoO}_6$ [11]. Locally, Ni–Pt ordering is favoured in a similar way as Fe–Mo ordering is favoured, a property that has strong influence on the magnetic interactions in the systems. As presented above, the most evident antiferromagnetism exists in $\text{La}_2\text{NiPtO}_6$, which becomes less pronounced for samples with lower Pt content. The samples with less Pt ($x \leq 0.40$) consist of local domains of high Pt-content and *B*-site ordering, which are probably dominated by the same AFM interactions as $\text{La}_2\text{NiPtO}_6$. The magnetization decreases from high ($x = 0.50$) to low ($x = 0.05$) Pt-content in the field dependent magnetization (Fig. 6), indicating a reduced ability of the Pt-depleted samples to become magnetized. As the AFM transition becomes less evident with lower Pt-content (Fig. 5), we suggest that the Pt-depleted domains remain in a paramagnetic state, but with short-range AFM interactions. The susceptibility for $0.20 \leq x \leq 0.40$ can thus be considered as a combination of the paramagnetic $x = 0.05$ and antiferromagnetic $x = 0.50$ samples (Fig. S11), as if the antiferromagnetic ordering of $x = 0.50$ is simply diluted by the Pt-depleted domains. This indicates that the magnetic interactions are unchanged through the system; there is only a change in the quantity depending on the Pt-content in the samples. If the system showed a trend with changing oxidation states, such as in $\text{LaNi}_{1-x}\text{Rh}_x\text{O}_3$ [23], a change in magnetic interaction mechanism should have occurred. The results therefore correlate well with the structural domain model, showing that ordered antiferromagnetic domains (Pt-rich domains) coexist with paramagnetic domains (Pt-depleted domains) for $0.20 \leq x \leq 0.40$, where the latter is dominated by short-range AFM interactions.

Regarding the magnetic interactions in $\text{La}_2\text{NiPtO}_6$, there are several similarities between the two stoichiometric double perovskites $\text{La}_2\text{NiPtO}_6$ and $\text{La}_2\text{NiTiO}_6$ [24]; both are weakly antiferromagnetic at low temperature, and the second *B*-site elements have very similar electronic configurations: $t_{2g}^0 e_g^0$ for Ti(IV) and $t_{2g}^6 e_g^0$ for Pt(IV). We speculate if the full t_{2g} -orbitals of Pt(IV) are participating or not with

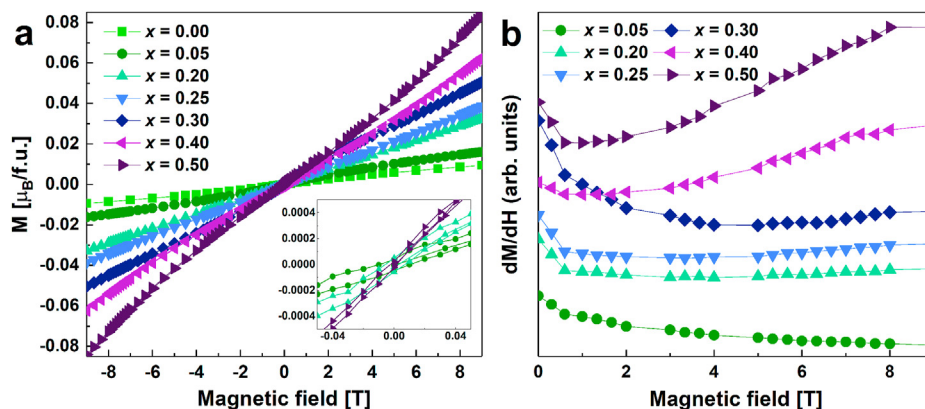


Fig. 6. (a) Field dependent DC magnetic measurements from -9 to 9 T at 4 K, and (b) the derivative of the magnetization ($x = 0.00$ is included in Fig. S10). The formula unit (f.u.) used is $\text{LaNi}_{1-x}\text{Pt}_x\text{O}_3$ for all samples. The increase in derivative towards $H = 0$ T is due to a slight non-linearity near $H = 0$ T.

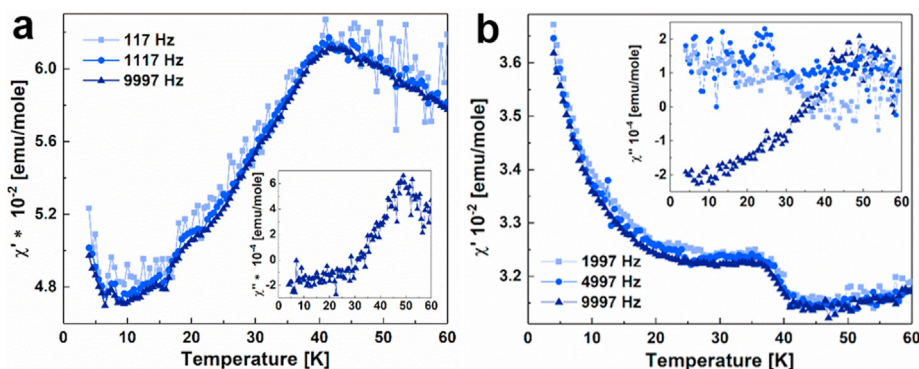


Fig. 7. AC magnetization measurements of a) $\text{La}_2\text{NiPtO}_6$ using a 10 Oe AC field, and b) of $\text{LaNi}_{0.75}\text{Pt}_{0.25}\text{O}_3$ using a 15 Oe AC field. The real component of the susceptibility (χ') is shown in the main figure, and the imaginary component of the susceptibility (χ'') is shown in the inset.

respect to magnetic interactions in $\text{La}_2\text{NiPtO}_6$. If there is no interaction of the full t_{2g} -orbitals of Pt, the two compounds should be dominated by similar magnetic interactions, namely the super-super exchange interaction between the e_g - and p -orbitals through Ni–O–(Ti/Pt)–O–Ni, as in $\text{La}_2\text{NiTiO}_6$ [24]. However, in $\text{La}_2\text{CoPtO}_6$ [2] a hybridization mechanism is suggested for the interaction between Co(II) high-spin ($t_{2g}^5 e_g^2$) and the full t_{2g} -orbital of Pt(IV) [2]. Here, the t_{2g} -orbital of Co(II) is only partially filled, allowing the unpaired t_{2g} -electron of Co(II) to hybridize with the Pt(IV) t_{2g} -orbital. Because the Pt(IV) t_{2g} -orbital is full, both FM and AFM coupling with Co(II) is possible, resulting in a weak magnetic interaction and low ordering temperature [2]. This shows that even though the t_{2g} -orbital of Pt(IV) is full, it can participate in magnetic interactions when the neighbouring element have unpaired t_{2g} -electrons. Unlike $\text{La}_2\text{CoPtO}_6$, in the scenario with Ni(II) ($t_{2g}^6 e_g^2$)/Ti(IV) ($t_{2g}^0 e_g^0$) and Ni(II) ($t_{2g}^6 e_g^2$)/Pt(IV) ($t_{2g}^6 e_g^0$), both B -site elements have full/empty t_{2g} -orbitals, and the t_{2g} -orbitals are much less likely to participate in magnetic interactions. It is therefore plausible that the magnetic interactions dominating $\text{La}_2\text{NiPtO}_6$ are more similar to that of $\text{La}_2\text{NiTiO}_6$, with mainly super-super exchange interactions through the e_g - p -orbitals, resulting in an AFM ground state for both compounds.

Assuming that the super-super exchange interaction above is the dominating magnetic interaction in $\text{La}_2\text{NiPtO}_6$, it should also dominate the Pt-rich domains with large degree of B -site ordering in $\text{LaNi}_{1-x}\text{Pt}_x\text{O}_3$ ($0.20 \leq x \leq 0.40$). With respect to the Pt-depleted domains dominated by strong short-range AFM interactions, Ni(III) is the dominating species, which is heavily investigated in both metallic and insulating nickelates [22,25,26]. At low temperatures, the insulating YNiO_3 is reported to be antiferromagnetic with a charge disproportionation of Ni(III) to Ni(III + δ) and Ni(III – δ), resulting in a monoclinic structure and two different Ni-sites [25]. Charge disproportionation of Ni(III) is also relevant for our compounds, as it shows how Ni(III) is intrinsically unstable in an insulating oxide matrix. Upon Pt-substitution in $\text{LaNi}_{1-x}\text{Pt}_x\text{O}_3$, the same charge disproportionation of Ni(III) may occur once the compound turns insulating. One can imagine that Ni-atoms located at the Pt-site (2c-site) will exist as Ni(III + δ). Correspondingly, Ni(III – δ) must be present at the Ni-site (2d-site). Such an electronic disproportionation is not limited to insulating nickelates, but is also reported for metallic nickelates, as shown by Li et al. [27], who described insulating pockets in LaNiO_3 using PDF. In order to understand these systems, one certainly needs to look well beyond any ionic approximation. Local structure investigations (TEM, PDF, XAS) may be a necessity to understand how the electronic landscape is changed by introducing dopants, and how that affects both insulating and metallic nickelates.

5. Conclusions

We have demonstrated that the system $\text{LaNi}_{1-x}\text{Pt}_x\text{O}_3$ ($0 \leq x \leq 0.50$) undergoes a change in oxidation states upon Pt-substitution, causing the system to be better described by the formula $\text{La}_2\text{Ni}_y^{\text{II}}\text{Ni}_{2-2y}^{\text{III}}\text{Pt}_y^{\text{IV}}\text{O}_6$, $0 \leq y \leq 1$. Because Pt has a strong preference for the Pt-site (2c-site) in the monoclinic structure of $\text{La}_2\text{NiPtO}_6$ ($P2_1/n$), and adopts only the +IV oxidation state, it becomes unfavourable to randomly distribute Pt at the B -site for the non-equimolar compositions in $\text{LaNi}_{1-x}\text{Pt}_x\text{O}_3$ ($0.20 \leq x \leq 0.50$) due to issues of charge balance on the nearby Ni- and O-atoms. Although a wet-chemical synthesis route is used, clustering of Pt-rich and Pt-depleted domains occurs inside the sample, also after an additional two weeks long heat treatment, demonstrating that the domain structure is an energetically favourable state. Only the Pt-rich samples with a large degree of structural long-range order show a distinct antiferromagnetic transition at low temperature ($T_N \approx 40$ K). For $0.20 \leq x \leq 0.40$, the magnetization decreases from high to low Pt-content simultaneously as the Néel-point (~ 40 K) becomes less pronounced, as if the antiferromagnetism of $x = 0.50$ is diluted by paramagnetic Pt-depleted domains with short-range AFM interactions. The electronic configuration of this system draws clear similarities to that of $\text{La}_2\text{NiTiO}_6$, indicating that both systems may be dominated by the same antiferromagnetic interaction (super-super-exchange). This would explain why the Pt-rich samples show the most distinct Néel-point.

CRediT authorship contribution statement

A.S. Fjellvåg: Conceptualization, Methodology, Validation, Formal analysis, Investigation, Writing – original draft, Writing – review & editing, Visualization. **Ø.S. Fjellvåg:** Validation, Methodology, Formal analysis, Writing – original draft, Writing – review & editing, Visualization. **Y. Breard:** Formal analysis, Investigation, Writing – original draft, Writing – review & editing. **A.O. Sjøstad:** Conceptualization, Methodology, Writing – original draft, Writing – review & editing, Supervision, Project administration, Funding acquisition.

Declaration of competing interest

The authors declare that they have no known competing financial interests or personal relationships that could have appeared to influence the work reported in this paper.

Acknowledgements

The authors would like to acknowledge the help of Dr. Susmit Kumar with magnetic measurements and discussions on this topic, along with

Associate Professor Björn Martin Valldor. We also acknowledge the expertise of the Swiss-Norwegian Beam Lines at ESRF, Grenoble. In addition, we greatly appreciate discussions on structure-property relations in the NAFUMA group at the University of Oslo. The project was financed by the Research Council of Norway through the projects RID-SEM (project no. 272253) and iCSI (project no. 237922).

Appendix A. Supplementary data

Supplementary data to this article can be found online at <https://doi.org/10.1016/j.jssc.2021.122181>.

References

- [1] K.B. Schwartz, C.T. Prewitt, Structural and electronic properties of binary and ternary platinum oxides, *J. Phys. Chem. Solid.* 45 (1) (1984) 1–21.
- [2] M.-C. Lee, C.H. Sohn, S.Y. Kim, K.D. Lee, C.J. Won, N. Hur, J.Y. Kim, D.-Y. Cho, T.W. Noh, Stabilization of ferromagnetic ordering in cobaltite double perovskites of $\text{La}_2\text{CoRhO}_6$ and $\text{La}_2\text{CoPtO}_6$, *J. Phys. Condens. Matter* 27 (33) (2015) 336002.
- [3] H. Das, P. Sanyal, T. Saha-Dasgupta, D.D. Sarma, Origin of magnetism and trend in Tc in Cr-based double perovskites: interplay of two driving mechanisms, *Phys. Rev. B* 83 (10) (2011) 104418.
- [4] K. Ouchetto, F. Archaimbault, J. Choisnet, M. Et-Tabirou, New ordered and distorted perovskites: the mixed platinates Ln_2MPTO_6 (Ln = La, Pr, Nd, Sm, Eu, Gd; M = Mg, Co, Ni, Zn), *Mater. Chem. Phys.* 51 (2) (1997) 117–124.
- [5] J.S. Zhou, J.B. Goodenough, B. Dabrowski, Exchange Interaction in the insulating Phase of RNiO_3 , *Phys. Rev. Lett.* 95 (12) (2005) 127204.
- [6] J. Androulakis, J. Giapintzakis, Magnetoresistance in $\text{LaNi}_{1-x}\text{Co}_x\text{O}_3$ ($0.3 \leq x \leq 0.6$), *Physica B* 405 (1) (2010) 107–112.
- [7] C. Schinzer, Spin-glass behavior of disordered perovskite $\text{LaNi}_{1/2}\text{Rh}_{1/2}\text{O}_3$, *J. Alloys Compd.* 288 (1–2) (1999) 65–75.
- [8] P.D. Battle, J.F. Vente, Structural and magnetic Characterization of $\text{La}_2\text{NiRhO}_6$, *J. Solid State Chem.* 146 (1) (1999) 163–167.
- [9] K. Asai, H. Sekizawa, K. Mizushima, S. Iida, Magnetic Properties of $\text{LaNi}_{1-x}\text{Fe}_x\text{O}_3$ ($0 \leq x \leq 0.2$), *J. Phys. Soc. Jpn.* 45 (4) (1978) 1417–1418.
- [10] N.Y. Vasanthacharya, P. Ganguly, J.B. Goodenough, C.N.R. Rao, Valence states and magnetic properties of $\text{LaNi}_{1-x}\text{Mn}_x\text{O}_3$ (for $0 \leq x \leq 0.2$ and $x = 0.5$), *J. Phys. C Solid State Phys.* 17 (15) (1984) 2745–2760.
- [11] C. Meneghini, S. Ray, F. Liscio, F. Bardelli, S. Mobilio, D.D. Sarma, Nature of “Disorder” in the ordered double perovskite $\text{Sr}_2\text{FeMoO}_6$, *Phys. Rev. Lett.* 103 (4) (2009), 046403.
- [12] D.D. Sarma, S. Ray, K. Tanaka, M. Kobayashi, A. Fujimori, P. Sanyal, H.R. Krishnamurthy, C. Dasgupta, Intergranular Magnetoresistance in $\text{Sr}_2\text{FeMoO}_6$ from a magnetic tunnel barrier Mechanism across grain boundaries, *Phys. Rev. Lett.* 98 (15) (2007) 157205.
- [13] D. Topwal, D.D. Sarma, H. Kato, Y. Tokura, M. Avignon, Structural and magnetic properties of $\text{Sr}_2\text{Fe}_{1+x}\text{Mo}_{1-x}\text{O}_6$ ($1 \leq x \leq 0.25$), *Phys. Rev. B* 73 (9) (2006), 094419.
- [14] S. Vasala, M. Karppinen, $\text{A}_2\text{B}'\text{B}''\text{O}_6$ perovskites: a review, *Prog. Solid State Chem.* 43 (1–2) (2015) 1–36.
- [15] R.A. Budiman, S.i. Hashimoto, T. Nakamura, K. Yashiro, K. Amezawa, T. Kawada, Oxygen nonstoichiometry and electrochemical properties of $\text{LaNiO}_{3-\delta}$, *ECS Trans.* 66 (2) (2015) 177–183.
- [16] W. van Beek, O.V. Safonova, G. Wiker, H. Emerich, SNBL, a dedicated beamline for combined in situ X-ray diffraction, X-ray absorption and Raman scattering experiments, *Phase Transitions* 84 (8) (2011) 726–732.
- [17] V. Dyadkin, P. Pattison, V. Dmitriev, D. Chernyshov, A new multipurpose diffractometer PILATUS@SNBL, *J. Synchrotron Radiat.* 23 (3) (2016) 825–829.
- [18] A.A. Coelho, TOPAS and TOPAS-Academic: an optimization program integrating computer algebra and crystallographic objects written in C++, *J. Appl. Crystallogr.* 51 (1) (2018) 210–218.
- [19] J.S. Zhou, L.G. Marshall, J.B. Goodenough, Mass enhancement versus Stoner enhancement in strongly correlated metallic perovskites: LaNiO_3 and LaCuO_3 , *Phys. Rev. B* 89 (24) (2014) 245138.
- [20] R.J.D. Tilley, *Understanding Solids : the Science of Materials*, second ed., Wiley, Chichester, 2013.
- [21] J.Q. Yan, J.S. Zhou, J.B. Goodenough, Ferromagnetism in LaCoO_3 , *Phys. Rev. B* 70 (1) (2004), 014402.
- [22] J.S. Zhou, J.B. Goodenough, Chemical bonding and electronic structure of RNiO_3 , R= rare earth, *Phys. Rev. B* 69 (15) (2004) 153105.
- [23] A.S. Fjellvåg, Ø.S. Fjellvåg, S. Kumar, A. Ruud, A.O. Sjøstad, Interplay of valence states and magnetic interactions in the perovskite system $\text{LaNi}_{1-x}\text{Rh}_x\text{O}_3$, *J. Solid State Chem.* (2021) 122124.
- [24] M. Karolak, M. Edlmann, G. Sangiovanni, Nickel-titanium double perovskite: a three-dimensional spin-1 Heisenberg antiferromagnet, *Phys. Rev. B* 91 (7) (2015).
- [25] J.A. Alonso, J.L. García-Muñoz, M.T. Fernández-Díaz, M.A.G. Aranda, M.J. Martínez-Lope, M.T. Casais, Charge Disproportionation in RNiO_3 perovskites: simultaneous metal-Insulator and structural Transition in YNiO_3 , *Phys. Rev. Lett.* 82 (19) (1999) 3871–3874.
- [26] J.A. Alonso, M.J. Martínez-Lope, M.T. Casais, J.L. García-Muñoz, M.T. Fernández-Díaz, M.A.G. Aranda, High-temperature structural evolution of RNiO_3 (R = Ho, Y, Er, Lu) perovskites: Charge disproportionation and electronic localization, *Phys. Rev. B* 64 (9) (2001), 094102.
- [27] B. Li, D. Louca, S. Yano, L.G. Marshall, J. Zhou, J.B. Goodenough, Insulating Pockets in metallic LaNiO_3 , *Adv. Electron. Mater.* 2 (2) (2016) 1500261.

Supplemental data and information

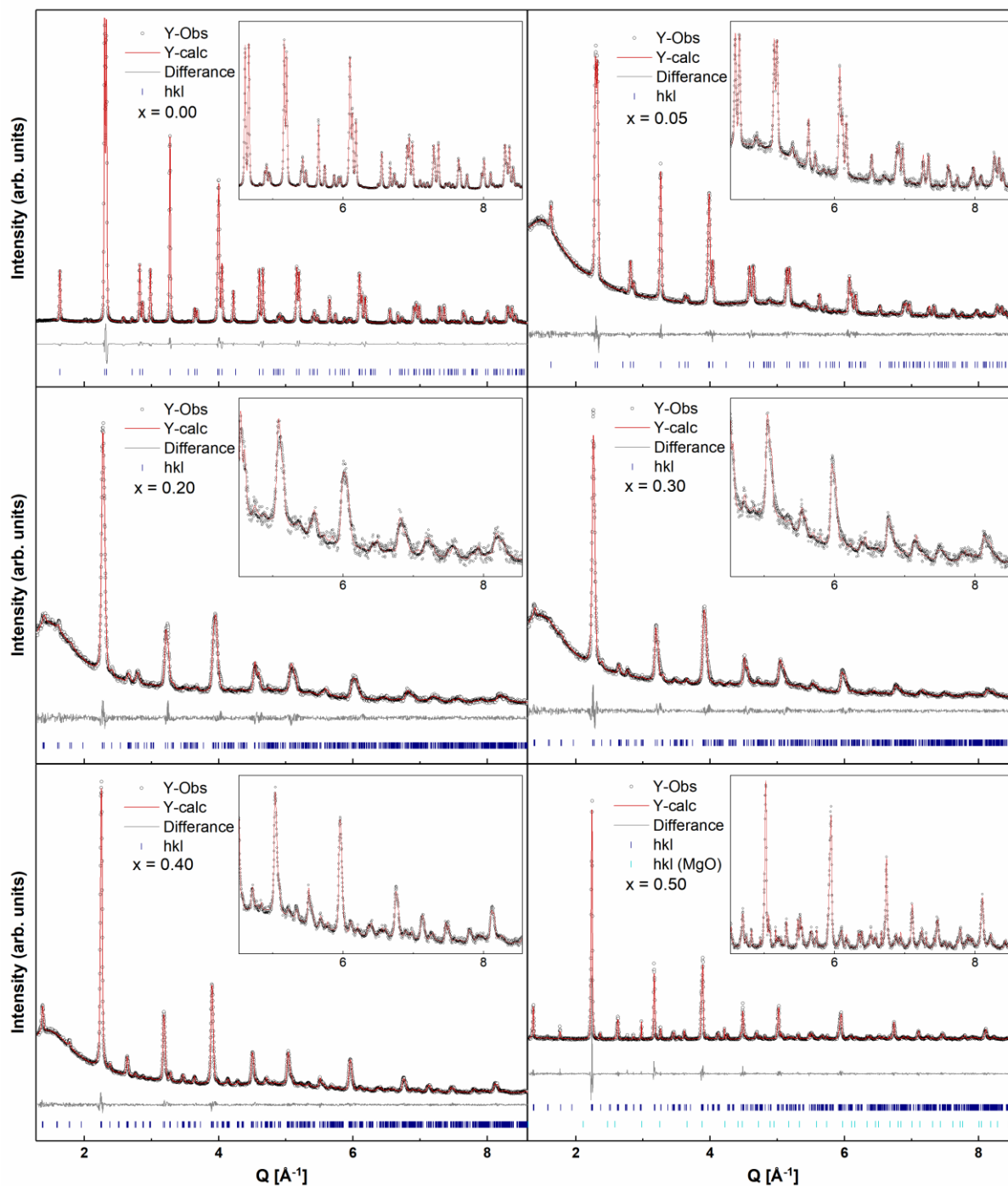


Figure S1. Rietveld refinement of $\text{LaNi}_{1-x}\text{Pt}_x\text{O}_3$ using the single phase model and space group $R-3c$ for $x = 0.00$ and $x = 0.05$ and $P2_1/n$ for $x \geq 0.20$; $\lambda = 0.50506 \text{ \AA}$ for $x = 0.00$ and $x = 0.50$ and $\lambda = 0.50467 \text{ \AA}$ for $x = 0.05, 0.20, 0.30$ and 0.40 . Dark blue ticks represent Bragg reflections from $\text{LaNi}_{1-x}\text{Pt}_x\text{O}_3$ ($R-3c$ or $P2_1/n$), and cyan ticks represent Bragg reflections from MgO ($Fm-3m$), which was used to reduce absorption for $\text{La}_2\text{NiPtO}_6$.

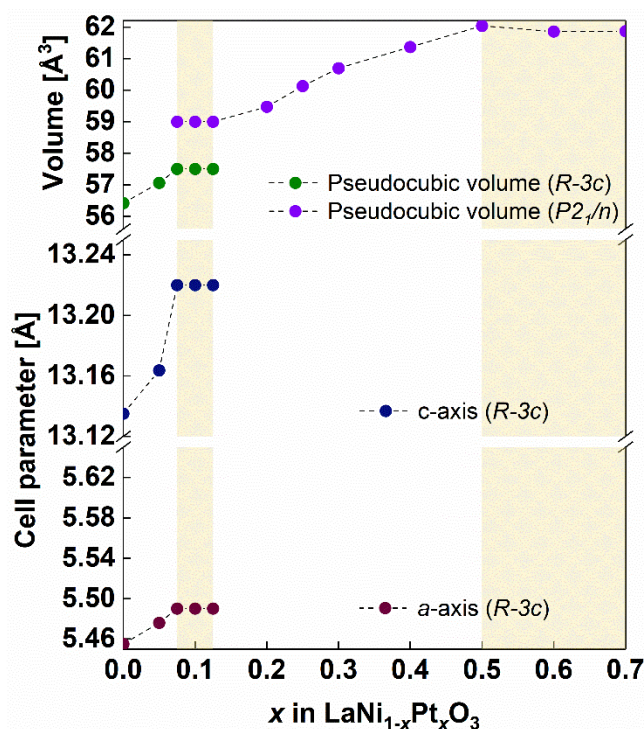


Figure S2. Cell parameters for the rhombohedral samples in $\text{LaNi}_{1-x}\text{Pt}_x\text{O}_3$, along with the pseudocubic volume.

Table S1. Crystallographic information for $\text{LaNi}_{0.95}\text{Pt}_{0.05}\text{O}_3$ obtained from Rietveld refinements of XRD data with a one-unit cell model, with $a = b = 5.476 \text{ \AA}$, $c = 13.164 \text{ \AA}$ and $\gamma = 120^\circ$ in $R-3c$.

Site	Atom	Wyckoff	x	y	z	Occ	B_{iso}
La1	La3	6a	0	0	0.25	1	1.170(13)
Ni1_1	Ni3	6b	0	0	0	0.9	0.420(17)
Ni1_2	Ni2	6b	0	0	0	0.05	0.420(17)
Ni1_3	Pt4	6b	0	0	0	0.05	0.420(17)
O1	O-2	18e	0.4601(15)	0	0.25	1	2.90(17)

Table S2. Crystallographic information for $\text{La}_2\text{NiPtO}_6$ obtained from Rietveld refinements of XRD data with a one-unit cell model, with $a = 5.578 \text{ \AA}$, $b = 5.629 \text{ \AA}$, $c = 7.903 \text{ \AA}$ and $\beta = 90.13^\circ$ in $P2_1/n$.

Site	Atom	Wyckoff	x	y	z	Occ	B_{iso}
La1	La3+	4e	0.5027(6)	0.5449(2)	0.2498(3)	1	0.76(3)
Ni1_1	Ni2+	2d	0.5	0	0	0.972(3)	0.41(6)
Ni1_2	Ni3+	2d	0.5	0	0	0	0.41(6)
Ni1_3	Pt4+	2d	0.5	0	0	0.028(3)	0.41(6)
Pt1_1	Pt4+	2c	0	0.5	0	0.972(3)	0.464(18)
Pt1_2	Ni3+	2c	0	0.5	0	0.028(3)	0.464(18)
O1	O2-	4e	0.223(4)	0.219(4)	0.950(4)	1	0.4(2)
O2	O2-	4e	0.285(4)	0.696(4)	0.961(4)	1	0.4(2)
O3	O2-	4e	0.401(6)	0.999(3)	0.246(3)	1	0.4(2)

Table S3. Results from structural analysis and Rietveld refinements of selected members in the $\text{LaNi}_{1-x}\text{Pt}_x\text{O}_3$ series. The Pt-occupancy is the occupancy of Pt on the $2c$ -site in $P2_1/n$ and $6b$ -site in $R-3c$, while the rest of the B -atom are occupied by Ni (Ni-site in $P2_1/n$ is $2d$ -site). For $x = 0.50$, the two structures in the domain

model have very similar dimensions. This shows that the model is best suited only for the non-equimolar compositions. Due to broad peaks, the crystallite sizes are calculated without subtracting the instrumental peak broadening. Additionally, as the peak broadening may originate from sub-particle domains, the calculated crystallite size is mainly appropriate to describe the domain size, not the particle size.

x, domain model	Unit cell size	Phase fraction	a [Å]	b [Å]	c [Å]	beta [°]	Volume [Å ³]	Rwp	Cry. Size [nm]	Pt-occ (theory)	Pt-occ (exp)
0.05	"large"	56 %	5.482		13.183		343.1		18	0.05	0.03
0.05	"small"	44 %	5.469		13.145		340.5	2.4	25	0.05	0.07
0.20	"large"	44 %	5.572	5.535	7.742	90.5	238.7		15	0.40	0.52
0.20	"small"	56 %	5.519	5.500	7.753	91.6	235.2	3.1	12	0.40	0.31
0.30 (regular)	"large"	41 %	5.581	5.580	7.821	90.6	243.5		18	0.60	0.89
0.30 (regular)	"small"	59 %	5.545	5.556	7.742	91.3	238.5	2.4	10	0.60	0.40
0.30 (annealed)	"large"	55 %	5.573	5.595	7.812	90.6	243.6		22	0.60	0.65
0.30 (annealed)	"small"	45 %	5.571	5.561	7.749	91.6	240.0	7.5	14	0.60	0.55
0.40	"large"	52 %	5.575	5.603	7.863	90.3	245.6		24	0.80	0.92
0.40	"small"	48 %	5.560	5.603	7.835	90.7	244.0	2.7	10	0.80	0.66
0.50	"large"	76 %	5.574	5.636	7.905	90.1	248.3		34	1.00	1.00
0.50	"small"	24 %	5.596	5.615	7.894	90.1	248.1	13.2	57	1.00	0.83
x, simple model	Unit cell size	Phase fraction	a [Å]	b [Å]	c [Å]	beta [°]	Volume [Å ³]	Rwp	Cry. Size [nm]	Pt-occ (theory)	Pt-occ (exp)
0.05	avg	1	5.476		13.164		341.8	2.9	43	0.05	
0.20	avg	1	5.544	5.537	7.752	91.1	237.9	4.6	22	0.40	0.40
0.30 (regular)	avg	1	5.569	5.584	7.807	90.8	242.8	4.1	37	0.60	0.51
0.30 (annealed)	avg	1	5.579	5.585	7.813	90.7	243.4	9.9	16	0.60	0.60
0.40	avg	1	5.579	5.598	7.860	90.4	245.5	2.8	81	0.80	0.78
0.50	avg	1	5.578	5.629	7.903	90.1	248.1	16.3	155	1.00	0.97

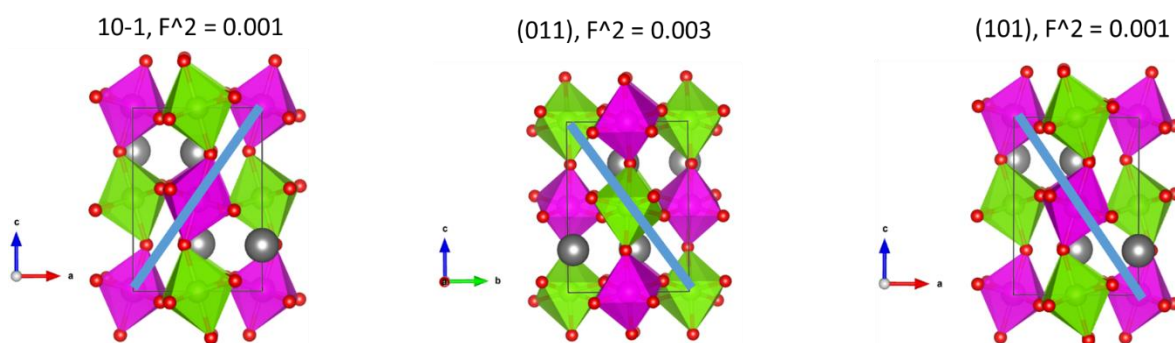


Figure S3. Example of crystallographic planes associated with *B*-site ordering in the double perovskite $\text{La}_2\text{NiPtO}_6$ ($P2_1/n$).

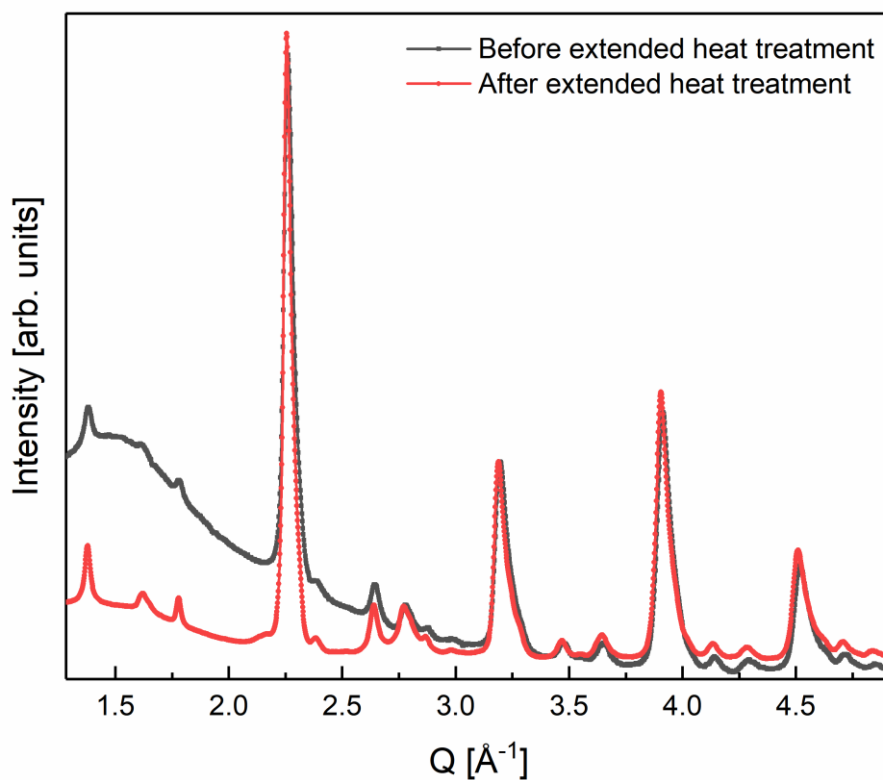


Figure S4. Synchrotron XRD of $\text{LaNi}_{0.70}\text{Pt}_{0.30}\text{O}_3$ before and after the extended two weeks long heat treatment. $\lambda = 0.50467 \text{ \AA}$ (before heat treatment) and $\lambda = 0.71490 \text{ \AA}$ (after heat treatment). The difference in background at low scattering angle is from the different experimental setups.

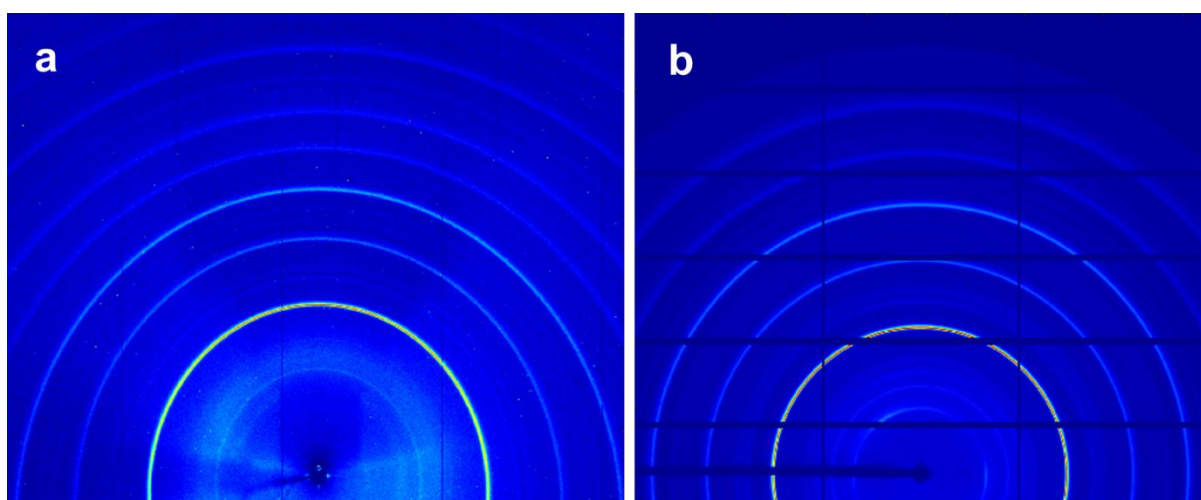


Figure S5. 2D X-ray diffraction pattern from a) a 2D Dexela detector of $\text{LaNi}_{0.70}\text{Pt}_{0.30}\text{O}_3$ before the 2 weeks extended heat treatment ($\lambda = 0.50467 \text{ \AA}$) and b) a 2D Pilatus detector of $\text{LaNi}_{0.70}\text{Pt}_{0.30}\text{O}_3$ after the 2 weeks extended heat treatment ($\lambda = 0.71490 \text{ \AA}$). The varying intensity in the inner rings is scattering from the sample setup. The pictures are generated using Albula and matlab R2017a.

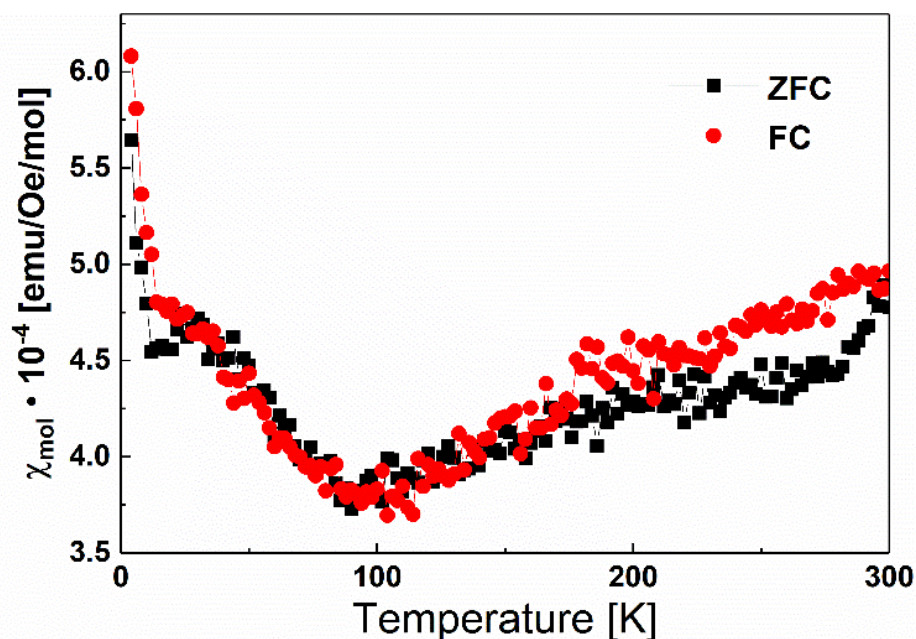


Figure S6. Zero field cooled (ZFC) and field cooled (FC) DC magnetization measurement of LaNiO_3 using a 2000 Oe external DC-field.

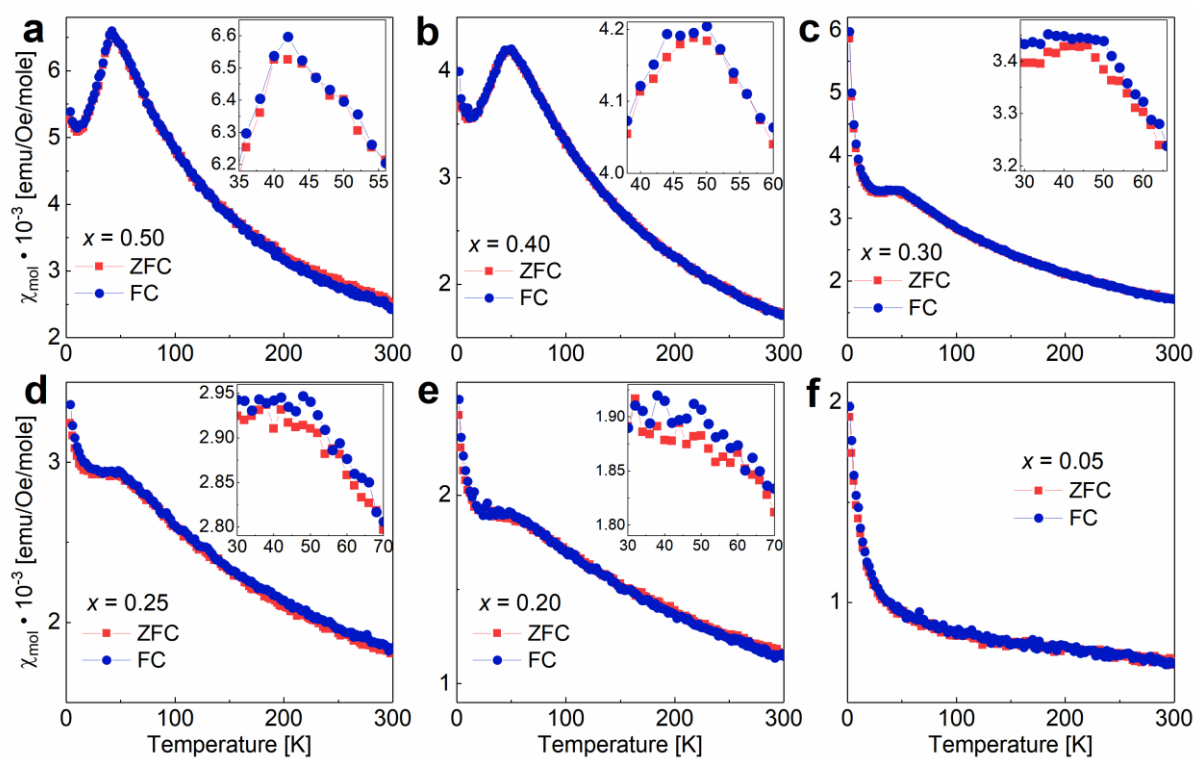


Figure S7. Zero field cooled (ZFC) and field cooled (FC) DC magnetization measurements of $\text{LaNi}_{1-x}\text{Pt}_x\text{O}_3$ ($0.05 \leq x \leq 0.50$) using a 2000 Oe external DC-field. The sample compositions are indicated in the figure.

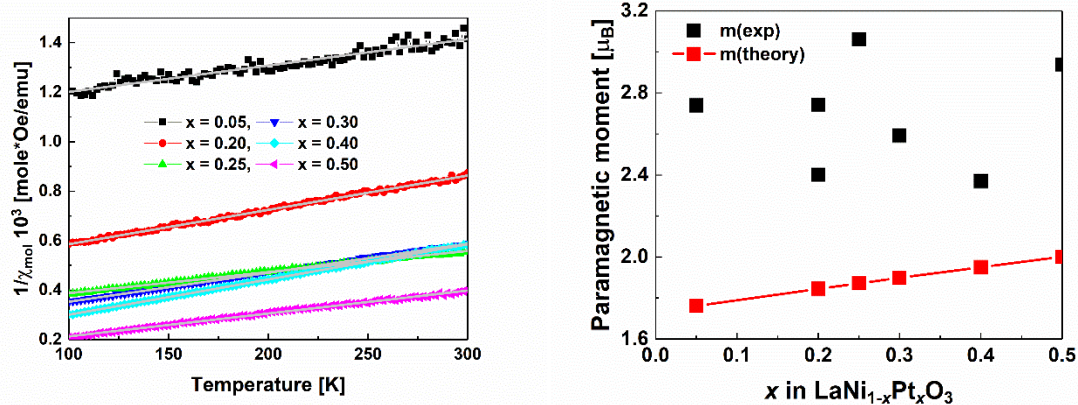


Figure S8. Linear fit of $1/\chi$ using the Curie-Weiss relation (left) and the obtained magnetic moment compared with theoretical magnetic moment (right).

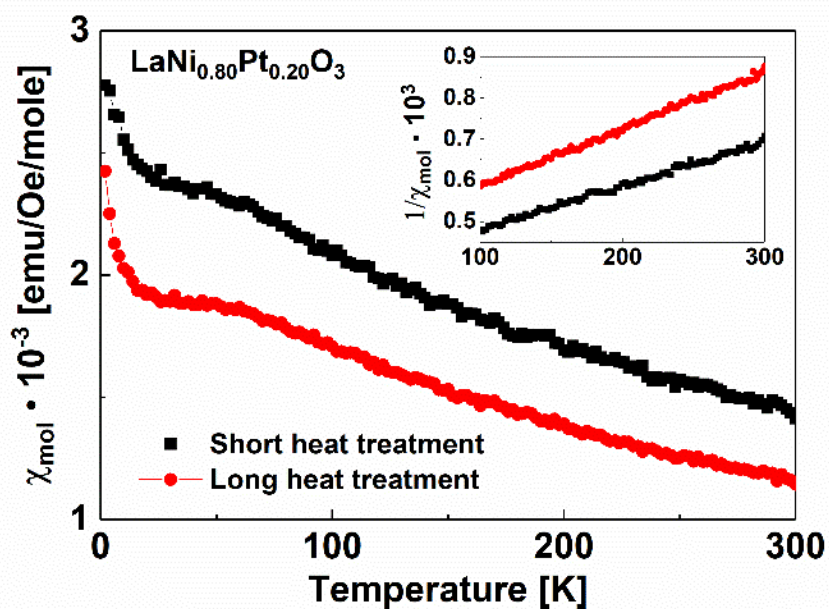


Figure S9. Comparison between ZFC magnetic measurement of $\text{LaNi}_{0.80}\text{Pt}_{0.20}\text{O}_3$ after a short (2×12 hours) and long (additional two weeks) heat treatment. χ_{mol} is shown in the figure and $1/\chi_{mol}$ is shown in the inset.

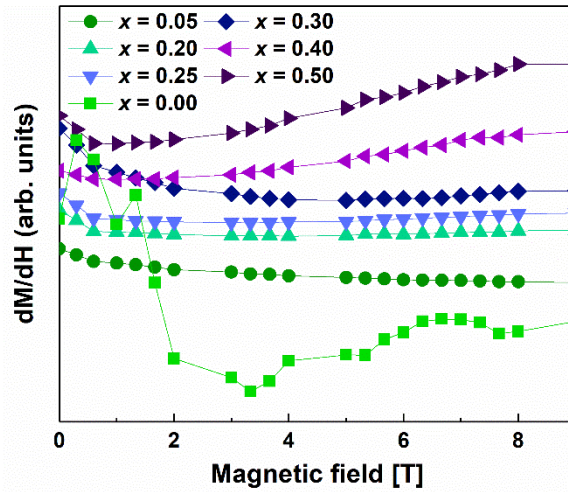


Figure S10. The derivative of the field dependent magnetization 0 to 9 T at 4 K (Figure 6) for all samples in $\text{LaNi}_{1-x}\text{Pt}_x\text{O}_3$.

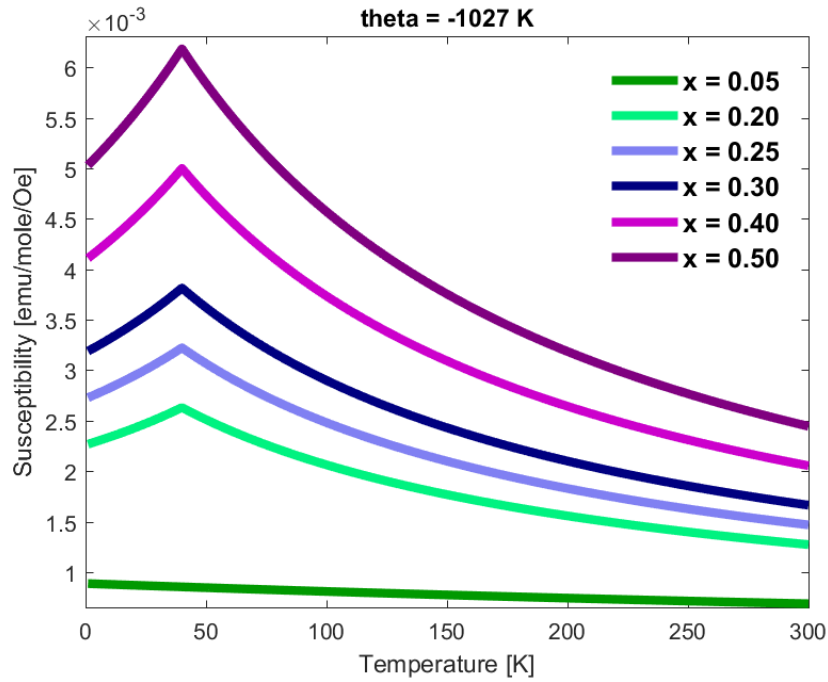


Figure S11. Example showing the susceptibility of a combination of an antiferromagnetic ($x = 0.50$) and a paramagnetic phase ($x = 0.05$) coexisting in $\text{LaNi}_{1-x}\text{Pt}_x\text{O}_3$. The data is calculated using the Curie-Weiss relation for both the paramagnetic phase and for the AFM phase (in paramagnetic conditions) above $T_N = 40$ K. Below T_N in this example (40-0 K), the AFM phase is assumed to have the same susceptibility as from 40-80 K. The magnetic moment and θ shown in Table 1 are used for modelling the susceptibility for both the paramagnetic ($m = 2.7 \mu\text{B}$, $\theta = -1027$ K) and AFM ($m = 2.9 \mu\text{B}$, $\theta = -130$ K) phase.

Paper V

Interplay of valence states and magnetic interactions in the perovskite system $\text{LaNi}_{1-x}\text{Rh}_x\text{O}_3$

A. S. Fjellvåg, Ø. S. Fjellvåg, S. Kumar, A. Ruud and A. O. Sjøstad

Journal of Solid State Chemistry, **2021**, 298, 122124



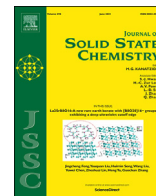
V

V



Contents lists available at ScienceDirect

Journal of Solid State Chemistry

journal homepage: www.elsevier.com/locate/jssc

Interplay of valence states and magnetic interactions in the perovskite system $\text{LaNi}_{1-x}\text{Rh}_x\text{O}_3$



A. Slagtern Fjellvåg^{a,*}, Ø. Slagtern Fjellvåg^b, S. Kumar^a, A. Ruud^{a,1}, A. Olafsen Sjøstad^{a,*}

^a Centre for Materials Science and Nanotechnology, Department of Chemistry, University of Oslo, P.O. Box 1033, N-0315, Oslo, Norway

^b Department for Neutron Materials Characterization, Institute for Energy Technology, PO Box 40, NO-2027, Kjeller, Norway

ABSTRACT

We report on the structural, magnetic and electronic properties of Rh substituted LaNiO_3 , $\text{LaNi}_{1-x}\text{Rh}_x\text{O}_3$ ($0 \leq x \leq 1$). Increased Rh contents are associated with increased structural distortion, and we observe a phase transformation and an immiscibility gap between $0.15 \leq x \leq 0.25$, separating the *R-3c* and *Pnma* perovskite structure regimes. Structural evaluation by synchrotron X-ray diffraction, X-ray absorption spectroscopy and DC magnetic measurements suggest variations in oxidation state for the *B*-site cations, with Ni(II)/Rh(IV), in addition to Rh(III), dominating for high Rh-contents. Although ordering of Ni(II)/Rh(IV) is possible, no *B*-site ordering between Ni and Rh is observed for any composition. A metal-to-insulator transition occurs upon Rh-substitution, correlating with the structural transition. DC- and AC magnetic measurements reveal that several of the compositions are magnetically frustrated with both antiferro- and ferromagnetic behaviour at low temperatures. The antiferromagnetic interactions are dominating, while the ferromagnetic interactions increase with increasing Rh-content, to a maximum at $x = 0.80$ and $x = 0.90$ in $\text{LaNi}_{1-x}\text{Rh}_x\text{O}_3$. The mixed valence states are assumed to contribute with a ferromagnetic super-exchange interaction between Ni(II) and Rh(IV).

1. Introduction

Materials displaying correlated electron behaviour has received an increasing amount of attention over the last decades due to the multitude of exotic phenomena in such systems. An important example is the simple perovskite LaNiO_3 and related derivatives [1–8], which are continuously under investigation after the discovery of the first superconducting nickelate $\text{Sr}_{0.2}\text{Nd}_{0.8}\text{NiO}_2$ [9]. Upon *B*-site substitution, *B*-site ordering may also occur, creating an entire new family of materials [10]. Internal variations in ordering phenomena is also possible, such as in $\text{Sr}_2\text{FeMoO}_6$, where the grain structure and degree of short range and long range Fe–Mo ordering is closely related to variations in magnetoresistance and the ferromagnetic strength [11,12].

In investigations of LaNiO_3 , total scattering analysis has been used to probe the short range ordering, which reveal that LaNiO_3 may be at the borderline of insulating behaviour due to Jahn-Teller distortions of the e_g^1 electron configuration of Ni(III), which would force localization [1]. For long, LaNiO_3 was expected to be a weak ferromagnet due to the itinerancy e_g^1 electron [8]. However, recent investigations of LaNiO_3 single crystals display an antiferromagnetic-like transition around 150–160 K [13,14], causing uncertainty of the true magnetic ground state of LaNiO_3 . Modifications of the electronic properties of LaNiO_3 may further be promoted through *A*- or *B*-site substitution, giving rise to metal-insulator

transitions (MIT) [3,6,15–19] or magnetic transitions [20–24]. In general, the MIT is caused by a reduction (sharpening) of the Ni–O–Ni bond angle by *A*-site (or *B*-site) substitution, or reduction of the electron population of the Ni e_g -orbitals from *B*-site substitution. On the other hand, the magnetic properties emerging from *B*-site substitution may seem unpredictable, such as in the system $\text{LaNi}_{1-x}\text{Co}_x\text{O}_3$, where changes in oxidation- and spin states lead to modifications in the magnetic properties [21,25]. In this way, non-stoichiometric compositions may give new and unexpected electronic properties.

The ferromagnetic interaction between Ni(II) and Rh(IV), first predicted by Goodenough [26], then investigated by Battle and Vente [24], and Schinzer [23], has attracted our attention. They focused on the stoichiometric compound, $\text{LaNi}_{0.50}\text{Rh}_{0.50}\text{O}_3$, searching for ferromagnetic super-exchange interactions between Ni(II) and Rh(IV). However, the compound was found to contain only Ni(III) and Rh(III), showing spin glass behaviour at low temperatures, and insulating properties over a wide temperature range [27]. In the current study, we investigate the entire system $\text{LaNi}_{1-x}\text{Rh}_x\text{O}_3$, aiming to obtain deeper insight into the oxidation states of Ni and Rh through this system, and correlate this to magnetic interactions. Because Rh and Co have the same *d*-electron configuration, and the +IV oxidation state is more easily stabilized for Rh, a comparison with Co-substituted LaNiO_3 is very interesting. Here, we demonstrate the effect of a wet chemical synthesis route to produce phase pure samples in

* Corresponding authors.

E-mail addresses: a.s.fjellvag@smn.uio.no (A.S. Fjellvåg), a.o.sjastad@kjemi.uio.no (A.O. Sjøstad).

¹ Current address: Nordic Institute of Dental Materials, Sognsveien 70 A, Oslo, 0855, Norway.

<https://doi.org/10.1016/j.jssc.2021.122124>

Received 18 December 2020; Received in revised form 9 March 2021; Accepted 9 March 2021

Available online 17 March 2021

0022-4596/© 2021 Elsevier Inc. All rights reserved.

the perovskite system $\text{LaNi}_{1-x}\text{Rh}_x\text{O}_3$. We pay special attention to the crystal structure and oxidation states of Ni/Rh through synchrotron radiation X-ray diffraction (SR-XRD) and X-ray absorption spectroscopy (SR-XAS), as variations in structure and oxidation state is expected to influence both magnetic and conduction properties. Additionally, the known metallic properties of Sr_2RhO_4 [28,29] and the high pressure phase SrRhO_3 [30] leads us to ask how Rh-substitution and possible redox reactions with Ni may affect the metallic properties in this system compared to other $\text{LaNi}_{1-x}\text{M}_x\text{O}_3$ systems, where $M = 3d$ -element.

2. Experimental

Nitrate salts of the relevant elements, $\text{La}(\text{NO}_3)_3 \times 6\text{H}_2\text{O}$ (99.9 %; Alfa), $\text{Ni}(\text{NO}_3)_2 \times 6\text{H}_2\text{O}$ (99 %; KEBO Lab) and $\text{Rh}(\text{NO}_3)_3 \times \text{H}_2\text{O}$ (99.9 %; Sigma-Aldrich) were dissolved in water and their molal concentrations (mol/g) were determined by thermogravimetric analysis. $\text{Mg}(\text{CH}_3\text{COO})_2 \times 4\text{H}_2\text{O}$ (99.5 %; Fluka) were used as received. All $\text{LaRh}_{1-x}\text{Ni}_x\text{O}_3$ samples and $\text{La}_2\text{MgRhO}_6$ (reference sample for SR-XAS) were synthesized following a citric acid complexation method. Stoichiometric amounts of nitrate solutions were weighed out for each element (La, Ni, Rh) and $\text{Mg}(\text{CH}_3\text{COO})_2 \times 4\text{H}_2\text{O}$, and 50 g of citric acid monohydrate ($\text{C}_6\text{O}_7\text{H}_8 \cdot \text{H}_2\text{O}$, 99 %, Sigma-Aldrich) was added per gram of oxide product. The solution was boiled until complete removal of water and nitrous gasses, followed by overnight heat treatment at 180 °C in a heating cabinet. The obtained crust was crushed and calcined at 400 °C for 12 h in static air, before pelletizing and sequential high temperature heat treatment at 850 °C and 1000 °C, both for 12 h in 1 atm of dynamic O_2 (from AGA, 5.0 purity). For LaNiO_3 the high temperature heat treatment was performed twice at 850 °C in 1 atm O_2 (from AGA, 5.0 quality) for 48 h. Samples were annealed in pure O_2 in order to produce samples with stoichiometric oxygen content.

Structural characterization by synchrotron X-ray diffraction (SR-XRD) and synchrotron X-ray absorption spectroscopy (XAS) was performed at beamline BM01B at the Swiss-Norwegian Beam Lines (SNBL), European Synchrotron Radiation Facility (ESRF), Grenoble France [31]. SR-XRD experiments were performed using a 2D DEXELA detector with wavelength $\lambda = 0.50506 \text{ \AA}$. Rietveld refinements were performed using the software TOPAS V5 [32] on data sets with ~ 3630 data points, Q -range from 1.3 to 11.48 \AA^{-1} , and 254 ($R\text{-}3c$) and 832 ($Pnma$) hkl indices. The refinements were performed with basis in structures reported by Kojima et al. [33] and Battle and Vente [24]. The Thompson-Cox-Hasting pseudo Voigt function was used to describe the peak shape for all samples, and the zero error, scale factor, unit cell parameters, atomic positions and Debye-Waller factors were refined. Refinements with negative Debye-Waller factors were excluded, and crystallite size was not included in the models. SR-XAS data for the Rh K-edge were measured in transmission mode using a Si(111) channel-cut monochromator with a second detuned crystal to reduce higher harmonics. The ATHENA software was used in SR-XAS data analysis for spectrum normalization to an edge jump of unity [34], with all scans calibrated to the theoretical Rh K-edge at 23220 eV based on Rh metal foil. Oxidation state reference materials for Rh(III) and Rh(IV) are LaRhO_3 and $\text{La}_2\text{MgRhO}_6$, respectively. $\text{La}_2\text{MgRhO}_6$, which was solely used as a reference for Rh(IV), was found by means of XRD to contain minute quantities of La_2O_3 (<1 mol%).

Magnetic and electronic transport measurements were performed using a Quantum Design physical properties measurement system (QD-PPMS). Temperature dependent DC magnetization measurements were performed from 4 to 300 K using a 2 kOe persistent external DC-field, and field dependent DC magnetization measurements were performed at 4 K with a DC field varying between ± 90 kOe. Temperature dependent AC magnetization data were collected from 4 to 45 K with and without a 2 kOe persistent external DC field, and with a 10 Oe AC field with frequencies of 177, 1117 and 9917 Hz, respectively. For resistivity measurements, regular pellets annealed at 1000 °C in O_2 (850 °C in O_2 for LaNiO_3) was used, with silver paste electrodes coated on the sample and gold wires between the sample and the transport puck. The applied

electrical current for the measurements of the individual samples was selected to achieve a linear IV-curve with zero crossing before starting the measurement.

3. Results and discussion

3.1. Structural aspects

Initial attempts using a solid state synthesis route on selected compositions in the system $\text{LaNi}_{1-x}\text{Rh}_x\text{O}_3$ yielded samples with significant Rh_2O_3 -impurities. To obtain homogeneous and phase pure samples, we therefore turned to a wet chemical synthesis route. According to SR-XRD, all $\text{LaNi}_{1-x}\text{Rh}_x\text{O}_3$ ($0 \leq x \leq 1$) samples prepared by a wet-chemical synthesis route are phase pure, except LaRhO_3 ($x = 1$), which contains < 1 mol% of Rh_2O_3 .

The two end members in the system, LaNiO_3 and LaRhO_3 , are reported to adopt distorted perovskite type structures with different symmetries; $R\text{-}3c$ and $Pnma$, respectively [8,35]. Through analysis of the SR-XRD patterns, we find that the $\text{LaNi}_{1-x}\text{Rh}_x\text{O}_3$ series obtain these two space groups for the entire compositional range. When substituting Rh for Ni in LaNiO_3 , the large size of Rh causes an increased tilt of the octahedra, reducing the symmetry to orthorhombic. The characteristic low angle (011)-peak for the orthorhombic phase ($Pnma$) is absent in the diffraction patterns (Fig. S1), indicating the absence of B -site ordering for all compositions [23,24]. Furthermore, an immiscibility gap is observed in the compositional interval $0.10 < x < 0.30$, see Fig. 1a. For the compositions $0.15 \leq x \leq 0.25$, the two phases co-exist (space group $R\text{-}3c$ and $Pnma$), with an observed volume increase through the phase transformation (shaded area, Fig. 1a). We observe an increase of the pseudocubic unit cell volume with increasing Rh content (Fig. 1a) on both sides of the immiscibility gap, consistent with a larger average ionic radii when Rh is substituted for Ni. Rh-substitution also causes an increase in $M\text{-O}$ bond distances and a reduction of the $M\text{-O-M}$ bond angles, which deviate increasingly from 180° (Table S1). This correlates with increased structural distortions, in line with the decrease in tolerance factor (Table S1).

In the structural analysis, a volume increase is found for the orthorhombic ($Pnma$) samples ($x = 0.15\text{--}0.25$) inside the structural two-phase region (Fig. 1a). However, we believe this to be an artefact (Fig. 1a). The Rietveld refinement (Fig. S1) may be easily influenced by the fact that the pseudocubic cell parameters are very similar for most compositions ($b \approx \sqrt{2}a \approx \sqrt{2}c$). Through the entire system, the a and b cell parameters increase, while the change in the c -axis is small. Additionally, around $x = 0.40$ the a - and c -axis are equally large, before the c -axis contracts, see Fig. 1b. This may originate from the large anisotropy of the orthorhombic b^+a^- tilt-deformation of the perovskite structure [36], and is similar to observations reported by Li et al. [37] for $\text{LaCo}_{1-x}\text{Rh}_x\text{O}_3$. The MO_6 -octahedra are slightly asymmetric in terms of bond lengths (Table S1), but compared to the heavily Jahn-Teller distorted compound LaMnO_3 , the bond length asymmetry is small. At most, we observe a $M\text{-O}$ bond length difference of 0.12 Å for the $x = 0.50$ composition, while in LaMnO_3 the largest Mn-O bond length difference is 0.28 Å [38].

Notably, the pseudocubic unit cell volume (Fig. 1a) of the orthorhombic samples ($Pnma$) shows a deviation from Vegard's law [39], with a distinct change in the slope at $x \approx 0.60$. Such a deviation may come from mixed oxidation states through the perovskite system, causing different ionic sizes to dominate the different compositions. Using reported ionic radii (radius: Ni(III)/Rh(III) = 0.56/0.67 Å; Ni(II)/Rh(IV) = 0.67/0.60 Å [40]), the theoretical unit cell volume is evaluated in the two scenarios; Ni(III)/Rh(III) and Ni(II)/Rh(IV) (Fig. S3a). In the case of the Ni(III)-Rh(III) solid solution, a linear increase in unit cell volume is expected with increasing substitution level of Rh, following Vegard's law. In the case of Ni(II)-Rh(IV), we expect a larger unit cell volume throughout the solid solution ($\text{LaNi}_{1-x}\text{Rh}_x\text{O}_3$), but with a distinct shift in the slope of the pseudocubic unit cell volume for $x = 0.50$ (Fig. S3a). The

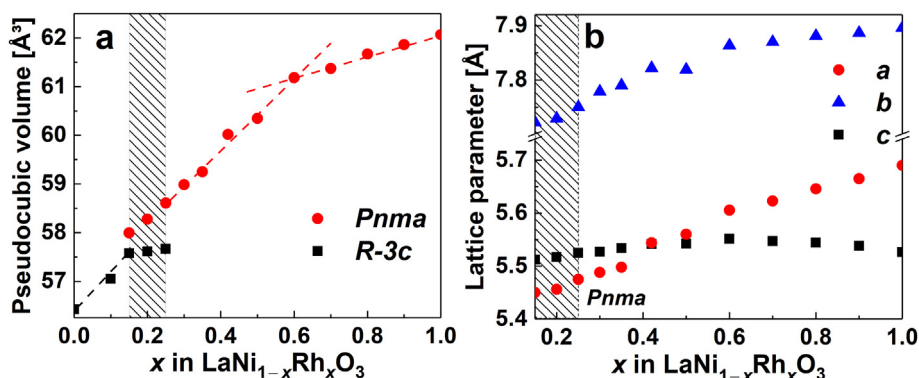


Fig. 1. (a) Pseudocubic unit cell volume of $\text{LaNi}_{1-x}\text{Rh}_x\text{O}_3$ as a function of x ($0 \leq x \leq 1$). The dashed lines indicate areas with a linear increase in the pseudocubic unit cell volume. (b) Unit cell parameters for orthorhombic ($Pnma$) $\text{LaNi}_{1-x}\text{Rh}_x\text{O}_3$ versus x ($0.15 \leq x \leq 1$). The hatched area indicates the two-phase region. The lattice parameters for the rhombohedral ($R-3c$) samples can be found in Fig. S2.

experimental unit cell volume lies between the two models, indicating a mixed situation between the two models. Thus, analysis of the crystal structure suggests mixed oxidation states with both Ni(III)/Rh(III) and Ni(II)/Rh(IV) present.

Relative to Vegard's law, the experimental volume shows a maximum deviation at $x \approx 0.60$ (Fig. 1 a), which is close to the theoretical maximum deviation at $x = 0.50$ (Fig. S3a). We can estimate the relative amount of the Ni(II)/Rh(IV) pair by comparing the theoretical models and experimental volume (Fig. S3b). For samples with high Rh-content ($x \geq 0.6$), $\sim 60\%$ of the Ni exist as Ni(II), and a corresponding amount of Rh is oxidized to Rh(IV). Mixed oxidation states with mainly Ni(II)-Rh(IV) is therefore in compliance with the experimental data. The fact that we do not have any indication of a complete charge division from Ni(III)/Rh(III) into Ni(II)/Rh(IV) may explain why no B-site ordering is observed (Fig. S1), in compliance with reports by Vasala and Karppinen [10].

The likely presence of Ni(II)/Rh(IV) species in the solid solution is further corroborated by SR-XAS, Fig. 2. We have compared the Rh K-edge for $\text{LaNi}_{1-x}\text{Rh}_x\text{O}_3$ ($0.58 \leq x \leq 1.00$) with reference samples (Rh(III): LaRhO_3 , Rh(IV): $\text{La}_2\text{MgRhO}_6$). With increasing Ni content, we clearly observe a shift in the K-edge of Rh from the Rh(III) reference edge towards the Rh(IV) reference edge, see black arrow in Fig. 2. We also

observe that the two main absorption peaks at 23226 and 23237 eV for the $\text{LaNi}_{1-x}\text{Rh}_x\text{O}_3$ samples shifts in line with the Rh(III)- and Rh(IV) references. These observations support the presence of the Ni(II)/Rh(IV) configuration, and agree with our unit cell volume considerations above. In addition, our findings corroborates well with reports by Shibasaki et al. [41] and Smith et al. [27] on the Ni(II)/Rh(IV) couple in $\text{LaNi}_{1-x}\text{Rh}_x\text{O}_3$ and our DC-magnetization measurements presented below.

The solid solution $\text{LaNi}_{1-x}\text{Rh}_x\text{O}_3$ hence shows a significant degree of charge division into Ni(II) and Rh(IV), however, without any sign of Ni and Rh to adopt different sites in the crystal structure. Similarities can be drawn to the order-disorder phenomena in $\text{Sr}_2\text{FeMoO}_6$ [11], where short-range ordering between Fe and Mo is always present, regardless of the long-range order achieved by heat treatments. The charge division into Ni(II) and Rh(IV) could therefore be an indication of short-range ordering between Ni and Rh in the $\text{LaNi}_{1-x}\text{Rh}_x\text{O}_3$ system.

3.2. Electronic transport properties

LaNiO_3 and $\text{LaNi}_{0.90}\text{Rh}_{0.10}\text{O}_3$ both display metallic conductivity, while compositions with $x \geq 0.30$ display semiconducting/insulating behaviour, see Fig. 3. Of the two metallic compounds, the resistivity of $\text{LaNi}_{0.90}\text{Rh}_{0.10}\text{O}_3$ is one order of magnitude higher than that of LaNiO_3 . The Fermi-liquid behaviour of LaNiO_3 (Fig. S3, Table S2) [8] is absent in $\text{LaNi}_{0.90}\text{Rh}_{0.10}\text{O}_3$, as the latter becomes significantly less metallic

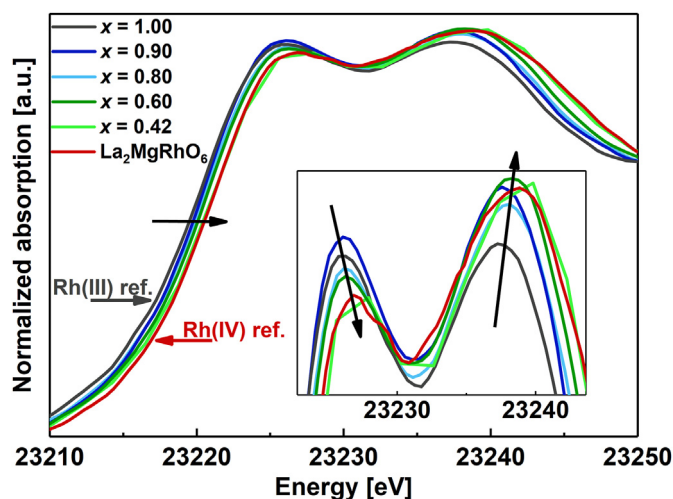


Fig. 2. SR-XAS data of the Rh K-edge for selected samples in the $\text{LaNi}_{1-x}\text{Rh}_x\text{O}_3$ series ($0.42 \leq x \leq 1.00$). LaRhO_3 (dark grey) acts as a Rh(III) reference and $\text{La}_2\text{MgRhO}_6$ (dark red) acts as Rh(IV) reference. The black arrows indicate the changes in the absorption spectra from the Rh(III) reference and towards the Rh(IV) reference with increasing amounts of Ni in $\text{LaNi}_{1-x}\text{Rh}_x\text{O}_3$. (For interpretation of the references to colour in this figure legend, the reader is referred to the Web version of this article.)

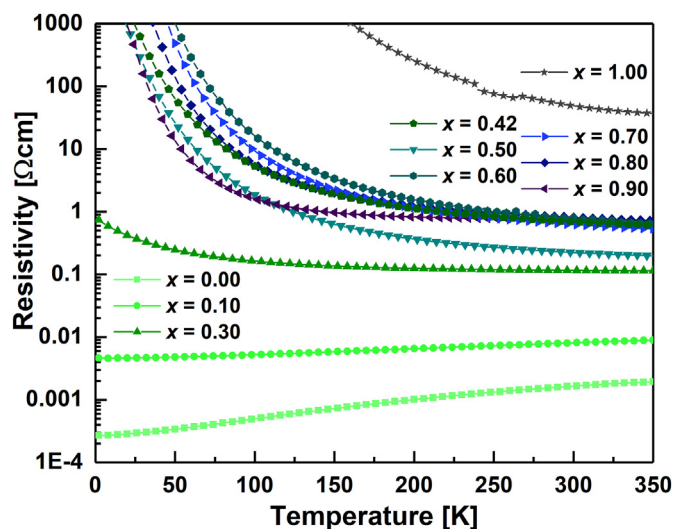


Fig. 3. Measured resistivity of $\text{LaNi}_{1-x}\text{Rh}_x\text{O}_3$ ($0 \leq x \leq 1.00$) versus temperature. Sample compositions are given in the figure.

compared to LaNiO_3 due to the increased disorder introduced by the 10 % B -site Rh-substitution (Fig. S4). This is evident from the T^3 -temperature dependency of the resistivity [42] in the temperature range 28–12 K, followed by an increase in resistivity below 10 K (Fig. S5). We interpret the increase in resistivity as weak electron localization due to the B -site disorder in the compound, a common feature for materials close to a metal-insulator transition due to substitution [6,43]. However, this does not necessarily mean that the material becomes insulating below 10 K. More detailed low temperature ($T < 1$ K) resistivity experiments are recommended to evaluate this fully. At elevated temperature ($T > 50$ K), however, the two compounds behave similarly, and electron-phonon interactions dominate the resistivity for both compounds; see the results from the temperature dependent analysis presented in Figs. S4-S5 and Table S2.

For $\text{LaNi}_{1-x}\text{Rh}_x\text{O}_3$ samples with $x \geq 0.30$, the semiconducting/insulating behaviour is observed in the entire analysed temperature region, with resistivity values slightly higher, but similar, to previous reports [27,41]. A compositional driven MIT therefore occurs somewhere in the interval $0.10 < x < 0.30$, correlating with the structural phase transformation where $\text{LaNi}_{1-x}\text{Rh}_x\text{O}_3$ transform from $R-3c$ to $Pnma$ (described above). The MIT is therefore likely caused by the increased structural deformations induced by substituting Ni with the significantly larger Rh-atom. This causes the $M-O-M$ bond angle to be reduced beyond the necessary angle to maintain a metallic interaction ($\theta > \sim 156^\circ$ [3]) between the Ni e_g and O $2p_\sigma$ orbitals. A similar effect due to B -site substitution is reported in several other $\text{LaNi}_{1-x}\text{M}_x\text{O}_3$ systems ($M = \text{Co}, \text{Fe}, \text{Mn}$) [18,44,45], and furthermore as a temperature dependent transition in RENiO_3 ($RE = \text{La-Dy}$) [3,15,17], where increased distortions (low t -factor) result in a higher transition temperature for the MIT. The effect of structural deformations is evident from the MIT in $\text{LaNi}_{1-x}\text{Co}_x\text{O}_3$. Here, the structure is not further distorted by B -site substitution and remain rhombohedral ($R-3c$) for all x , allowing high Co-substitutions before the MIT occurs ($x_{MIT} \approx 0.65$ [6]). This stands in contrast to Rh-substitution, where much lower substitutions cause the MIT ($0.10 < x_{MIT} < 0.30$). One can furthermore speculate on the fact that Rh(IV) is known to cause metallic properties in some oxides (SrRhO_3 [30], Sr_2RhO_4 [29]), and if this should impact in the $\text{LaNi}_{1-x}\text{Rh}_x\text{O}_3$ system, where significant amounts of Rh(IV) is present (Fig. 2). With detailed analysis, we observe that the sample with $x = 0.30$ is at the border of being metallic at elevated temperatures (Fig. S6), making it almost possible to fit resistivity data using a power law, such as for metals [6]. However, we believe that $x = 0.30$ remains insulating, and we conclude that the structural impact of the large Rh-atom exceeds the gain from Rh(IV) on the metallicity in this substitutional series.

For all insulating compositions ($x \geq 0.30$) we analyse the temperature dependence of the resistivity at elevated temperature ($T > 80$ K) using the Arrhenius model for $x \leq 0.80$ and the Polaron model [46,47] for $x \geq 0.90$, based on what provides the best fit (Figs. S7-S8). We find that both the magnitude of the resistivity and the activation energy increases with increasing Rh-content (x), as expected from the non-conducting nature of Rh(III) (Fig. S9, Table S3). However, for $x = 0.90$ and $x = 1.00$ the activation energy is significantly lowered due to the formation of polarons (Fig. S9), which aid in the conduction of the electrons. We find that $x = 0.90$ contains large polarons with a low effective mass and that $x = 1.00$ contains small polarons with a high effective mass (see calculations in Supplemental).

It is still important to remember that even though the activation energy for electron hopping is reduced for these two compositions, it is mainly the temperature dependence of the resistivity which is changed, as the overall value of the resistivity depend on several factors. The cause of polaron formation in samples with $x \geq 0.90$, but not in samples with $x \leq 0.80$, is not known. But the low activation energy for $x = 0.90$ compared to $x = 1.00$ is most probably caused by the larger amount of charge carriers in $x = 0.90$, due to the valence state interplay between Ni and Rh, which is not present in $x = 1.00$.

Moving on to lower temperatures ($T < \sim 80$ K), where electron-

electron interactions dominate, we find that different theories of variable range hopping (VRH) conduction [46,48–50] fits well with the $\text{LaNi}_{1-x}\text{Rh}_x\text{O}_3$ system for all insulating samples ($0.30 \leq x \leq 1.00$) (Fig. S10, Table S3). In VRH conduction, the localized charge carriers hop from one to another localized state near the Fermi level. Here, the subtle interplay between the lowest energy differences and shortest hopping distance defines where the localized charge carrier will hop. Therefore, it may hop different distances, depending on which atom that contains the lowest energy state nearby. In the $\text{LaNi}_{1-x}\text{Rh}_x\text{O}_3$ system, we find that

3-dimensional Mott VRH $\left(\log \rho \propto T^{-\frac{1}{4}}\right)$ [48] fits best for $x = 0.30$, that

2-dimensional (2D) Mott VRH $\left(\log \rho \propto T^{-\frac{1}{3}}\right)$ [48] fits best for $x = 0.40$

and $x = 0.50$, and that the 2D Efros-Shklovskii VRH $\left(\log \rho \propto T^{-\frac{1}{2}}\right)$ [50]

fits best for $x = 0.60$ – 1.00 . This implies that there is a compositional driven change in conduction mechanism through the system, and that it changes towards preferring 2D hopping for $x \geq 0.40$. However, the structure is described as a perovskite with a 3D network of corner-connected octahedra, where the only structural feature which could explain such 2D hopping is the highly anisotropic $M-O$ bond distances and the low t -factor (Table S1). The electron may therefore, on a local scale, see the most desirable hopping locations nearby in a 2D plane. Additionally, this feature may also be correlated to the change in valence states through the system, and the change in magnetic interactions upon Rh-substitution (see section below). We recommend further investigations of the observed conduction phenomena at both high and low temperature, with focus on correlations with valence states and magnetic interactions.

3.3. Magnetic measurements

3.3.1. High temperature region (paramagnetic region)

We find LaNiO_3 and LaRhO_3 to be Pauli paramagnetic and diamagnetic, respectively (Fig. S10), in agreement with previous work on powder samples [8,41]. For the intermediate compositions in $\text{LaNi}_{1-x}\text{Rh}_x\text{O}_3$, paramagnetic behaviour is observed above ~ 30 K (Fig. S11), also for the weakly metallic sample with $x = 0.10$. By using the Curie-Weiss relation, we find a linear $1/\chi$ temperature dependency above ~ 150 K for compositions with $0.10 \leq x \leq 0.90$. However, the metallic conductivity for $x = 0.10$ makes the results inconclusive for this sample. For the compositions crystallizing with orthorhombic symmetry ($x \geq 0.30$) the experimental magnetic moments are compared to theoretical magnetic moments calculated using a Russel-Saunders coupling scheme (Fig. S12 and Table S4) [51]. The experimental paramagnetic moments are higher than those expected when fixing the oxidation states to Ni(III) and Rh(III). The difference between observed and calculated magnetic moments can be explained by the presence of significant contributions of Ni(II) and Rh(IV), in compliance with structural considerations and SR-XAS. Further, it cannot be ruled out if spin orbit coupling of Rh(IV) gives a small additional contribution to the magnetic moment (Fig. S12).

The Curie-Weiss analysis further provides θ_{CW} -values, and thereby indicate the type of dominating magnetic interactions for each composition. At high Ni-content, θ_{CW} is large and negative, while for increasing Rh-content, θ_{CW} becomes much less negative, but still remaining negative (Table S4). This indicates strong antiferromagnetic short-range interactions for the Ni-rich compositions, which decrease significantly in strength with increasing Rh-content.

3.3.2. Low temperature magnetic measurement

For several compositions in the $\text{LaNi}_{1-x}\text{Rh}_x\text{O}_3$ series, a small difference is observed between the field- and zero-field cooled DC-

magnetization curves below 10–20 K (Fig. S11). This has previously been suggested to be caused by a spin-glass transition at $T_g \approx 10$ K for $\text{LaNi}_{0.50}\text{Rh}_{0.50}\text{O}_3$ [23,24]. To characterize the low temperature state, field dependent magnetic measurements were performed at 4 K, see Fig. 4. An interesting trend appears when considering the field dependent magnetization for the different compositions. For $x \leq 0.50$, a linear magnetization with no hysteresis is observed, like the behaviour of para- or antiferromagnetic materials. However, for $0.60 \leq x \leq 0.80$, the magnetization signal increases significantly and obtains a S-like shape versus applied magnetic field. The samples show a small hysteresis when reversing the magnetic field, and the $M(H)$ magnetization show tendencies towards saturation, although not complete. For $x = 0.90$ the magnetization is reduced, but with a strong tendency towards saturation. Finally, for $x = 1.00$ the sample turns completely diamagnetic.

Among all the samples in the compositional series $\text{LaNi}_{1-x}\text{Rh}_x\text{O}_3$, the saturation magnetization is highest for $x = 0.80$. The magnetization at 90 kOe for $x = 0.80$ is $\sim 0.15 \mu_B/\text{f.u.}$, which is one quarter of the maximum magnetization assuming pure ferromagnetic ordering in $\text{LaNi(II)}_{0.20}\text{Rh(III)}_{0.60}\text{Rh(IV)}_{0.20}\text{O}_3$, when assuming complete charge division from Ni(III)/Rh(III) into Ni(II)/Rh(IV). Considering the $x = 0.90$ sample, the magnetization of $\sim 0.09 \mu_B/\text{f.u.}$ is approximately one third of the maximum magnetization, assuming pure ferromagnetic ordering in $\text{LaNi(II)}_{0.10}\text{Rh(III)}_{0.80}\text{Rh(IV)}_{0.10}\text{O}_3$. Furthermore, by dividing the $M(H)$ -magnetization on the amount of available Ni(II)–Rh(IV) pairs from the stoichiometry of the structure, i.e. 0.2 for $x = 0.90$ and 0.4 for $x = 0.80$, the relative saturation magnetization becomes highest for $x = 0.90$ (inset in Fig. 4). This indicates the existence of ferromagnetic properties for $0.60 \leq x \leq 0.90$, which increases with increasing Rh-content, and is strongest for $x = 0.90$.

To further investigate the low temperature phenomena, AC-magnetization measurements were performed for $x = 0.42, 0.50, 0.70$ and 0.80 , see Fig. 5. For $x = 0.50$, a weak transition occurs at 30 K, which can be easily suppressed by a 2 kOe DC-field, the same field as used in DC-magnetic measurements (Fig. S14). Furthermore, for all four samples, a transition occurs at $T_m \approx 10$ K, which show intensities both for the real and imaginary component of the susceptibility, indicating a transition from a paramagnetic to a ferro-/ferrimagnetic state [52]. Notably, the

transition temperatures do not change with frequency, and only a small increase in intensity for lower frequencies is observed. Compared to other reported spin-glass systems, the observed frequency dependence is low [53], ruling out the likeliness of a spin-glass transition. We therefore believe that the magnetic transition at $T_m \approx 10$ K is not a spin glass transition, but a transition from paramagnetic to a mixed ferro-/antiferromagnetic state, which depend on short range interactions and local structural ordering inside the compound.

Considering the intensity of the AC- and DC-magnetization measurements (Fig. 5, Fig. S11), the saturation magnetization in the field dependent measurement (Fig. 4, Fig. S13) and the θ_{CW} values (Table S4), we see that they all increase with increasing Rh-content. This indicates a trend of increased ferromagnetic interactions with increasing Rh-content. Considering the rules from Goodenough [26], which expects a moderate ferromagnetic super-exchange interaction between Ni(II) and Rh(IV), the increased ferromagnetism for increasing Rh-contents may be explained by the corresponding shift in valence states from Ni(III)/Rh(III) to Ni(II)/Rh(IV), as discussed above. We therefore believe that the magnetic transition at $T_m \approx 10$ K is into a mixed ferro-/antiferromagnetic state, with competing magnetic interactions depending on valence states. In this scenario, Ni(III)/Rh(III) will favour antiferromagnetism, while Ni(II)/Rh(IV) may favour ferromagnetic interactions. However, due to the random distribution of Ni and Rh in the structure, it is highly difficult to imagine how a ferro- or antiferromagnetic ordering would look like in the structure. The local structure may therefore dictate the magnetic ordering.

It is also possible that the compounds adopt a ferrimagnetic state, due to the mixture in oxidation states and several possible magnetic interactions. This may also cause increased magnetization with increased Rh-content, and it is beyond the scope of this investigation to understand the true magnetic interactions in the compounds. If the Ni(II) and Rh(IV) sub-lattice was ordered, the magnetic interactions could have been much stronger than in the present case, and the origin behind the observed trend in magnetization could be resolved. With the current results, we believe an ordered Ni(II)/Rh(IV) compound could be the path to a new ferromagnetic compound, and provide insight into the magnetic interactions of Ni(II) and Rh(IV).

4. Conclusion

We have demonstrated that a wet chemical synthesis route can be used to successfully synthesize all compositions in the perovskite system $\text{LaNi}_{1-x}\text{Rh}_x\text{O}_3$ ($0 \leq x \leq 1$). Our main findings of the structure-property relations of the $\text{LaNi}_{1-x}\text{Rh}_x\text{O}_3$ system are summarized in Fig. 6. Through the system, a structural phase transformation from $R-3c$ to $Pnma$ occurs due to the large size of the substituent Rh-atom, with an immiscibility gap for $0.15 < x < 0.25$. Rh-substitution is also associated with mixed valence states for Ni and Rh, where Ni(II)/Rh(IV) dominates for high Rh-contents ($x \geq 0.60$). The structural distortions of the phase transformation also result in a compositionally driven metal-to-insulator transition for $0.10 < x_{MIT} < 0.30$, caused by the decrease in the $M-O-M$ bond angle. The reduced amount of Ni atoms contributing to metallic conductivity also contributes to the MIT, however, the effect is low compared to $\text{LaNi}_{1-x}\text{Co}_x\text{O}_3$. On the metallic side of the MIT ($x \leq 0.10$), Rh-substitution introduces disorder, resulting in reduced metallicity and high resistivity compared to other metals. While for the compositions showing insulating behaviour ($x \geq 0.30$), conduction occurs by activated hopping. At temperature above approximately 80 K, Arrhenius-type and polaron-type thermally activated hopping occur, while variable range hopping occurs at temperatures below approximately 70 K. The system further shows a magnetic transition at low temperature ($T_m \approx 10$ K) into a mixed ferro- and antiferromagnetic state. With increasing Rh-content, a change from dominating antiferro- to ferromagnetic interactions occurs, with a maximum at $x = 0.80$ and $x = 0.90$. This occurs due to mixed valence states for the different compounds, where Ni(III)/Rh(III) result in

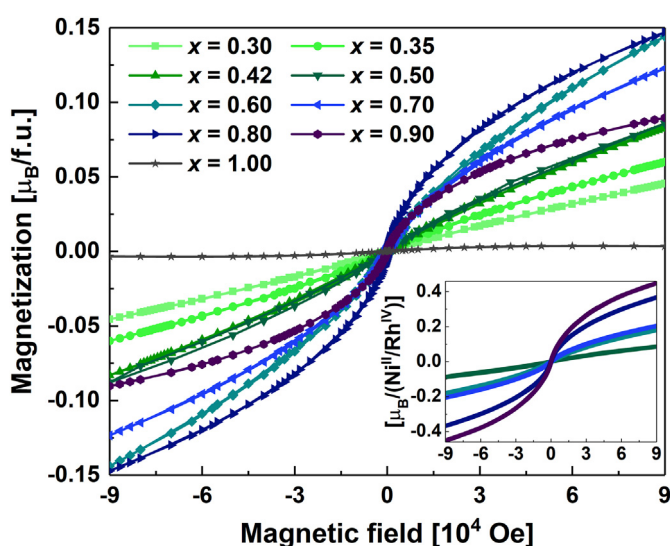


Fig. 4. Field dependent magnetization measurements of selected members ($x = 0.30, 0.35, 0.42, 0.50, 0.60, 0.70, 0.80, 0.90, 1.00$) in the $\text{LaNi}_{1-x}\text{Rh}_x\text{O}_3$ series at $T = 4$ K between ± 90 kOe. The sample compositions are indicated in the figure by its x value. The intensity unit is in Bohr magnetons per formula unit ($\mu_B/\text{f.u.}$). The inset shows the field dependent magnetization measurement where the intensity is divided by the amount of available Ni(II)/Rh(IV) pairs, i.e. 0.2 for $x = 0.90$ and 0.4 for $x = 0.80$.

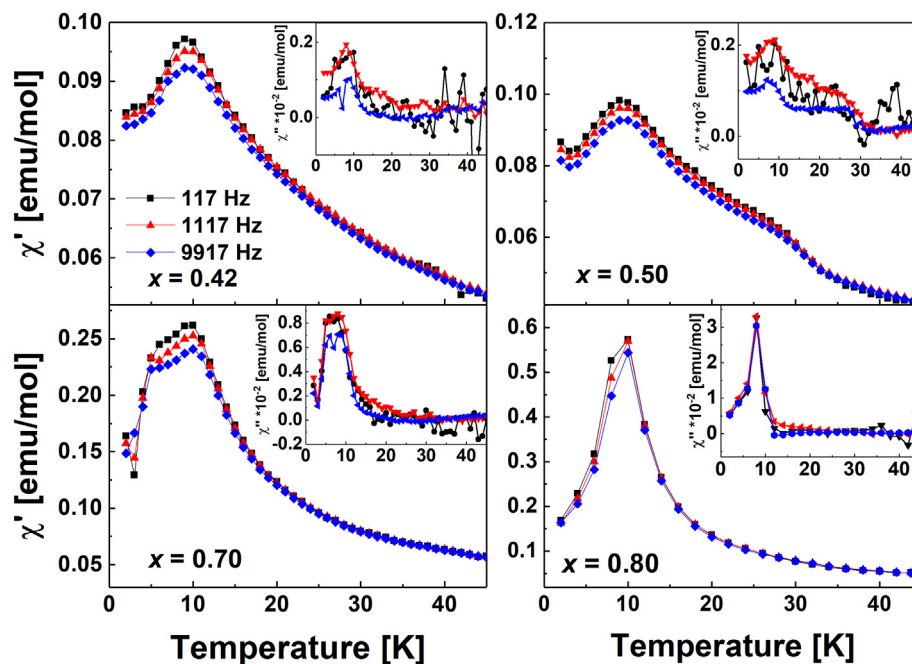


Fig. 5. AC-susceptibility from 2 to 45 K using a 10 Oe and 117, 1117 and 9917 Hz AC-field for four different compositions in the $\text{LaNi}_{1-x}\text{Rh}_x\text{O}_3$ series, with the x -value written in the figure. The real component of the susceptibility (χ') is shown in the main graph, and the imaginary component (χ'') is shown in the inset.

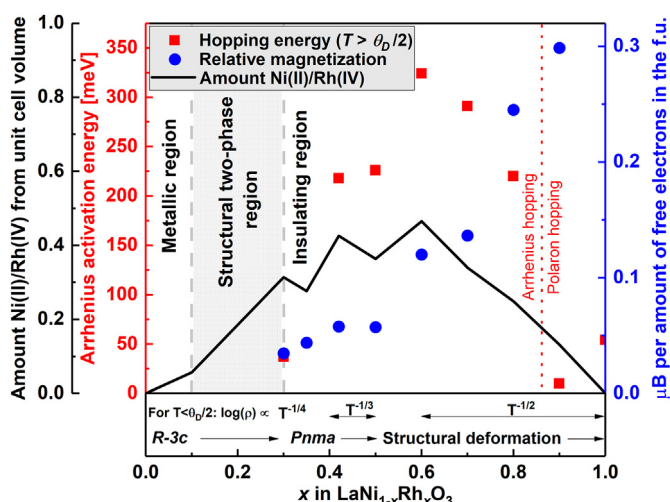


Fig. 6. Summary of structural and electronic properties in the $\text{LaNi}_{1-x}\text{Rh}_x\text{O}_3$ system as function of Rh-content (x). It displays the amount of Ni(II) and Rh(IV) scaled to 1 from the change in slope in the unit cell volume (solid black line with left black axis), the development of the activation energy of the resistivity (red dots and left red axis) and the saturation magnetization [μ_B] relative to the amount of free electrons available on Ni(II), Ni(III) and Rh(IV) (blue points and right blue axis). The metallic region is indicated on the left, and the structural two-phase region with a grey area. The change from Arrhenius-type to polaron-type hopping is indicated with the red dotted line. The temperature dependency of the resistivity is shown near the bottom of the figure, and the space group and increased structural deformations are indicated at the bottom of the figure. (For interpretation of the references to colour in this figure legend, the reader is referred to the Web version of this article.)

antiferromagnetism, while Ni(II)/Rh(IV) lead to mixed ferro- and anti-ferromagnetism. The ferromagnetism is believed to originate from the Ni(II)–O–Rh(IV) super-exchange interactions, or related phenomena due to mixed oxidation states, and we believe that new ferromagnetic compounds with Ni(II)/Rh(IV) may exist.

CRediT authorship contribution statement

A. Slagtern Fjellvåg: Conceptualization, Methodology, Validation, Formal analysis, Investigation, Writing – original draft, Writing – review & editing, Visualization. Ø. Slagtern Fjellvåg: Validation, Formal analysis, Writing – original draft, Writing – review & editing, Visualization. S. Kumar: Formal analysis, Investigation, Writing – original draft. A. Ruud: Formal analysis, Investigation, Writing – original draft. A. Olafsen Sjøstad: Conceptualization, Methodology, Writing – original draft, Writing – review & editing, Supervision, Project administration, Funding acquisition.

Declaration of competing interest

The authors declare that they have no known competing financial interests or personal relationships that could have appeared to influence the work reported in this paper.

Acknowledgements

The authors would like to acknowledge the help and competence of the Swiss-Norwegian Beam Lines at ESRF, Grenoble, for help with SR-XRD and SR-XAS data collection. In addition, we greatly appreciate fruitful discussions on structure-property relations in the NAFUMA group at the University of Oslo. The Research Council of Norway financed the work through the projects RIDSEM (project no. 272253) and iCSI (project no. 237922).

Appendix A. Supplementary data

Supplementary data to this article can be found online at <https://doi.org/10.1016/j.jssc.2021.122124>.

References

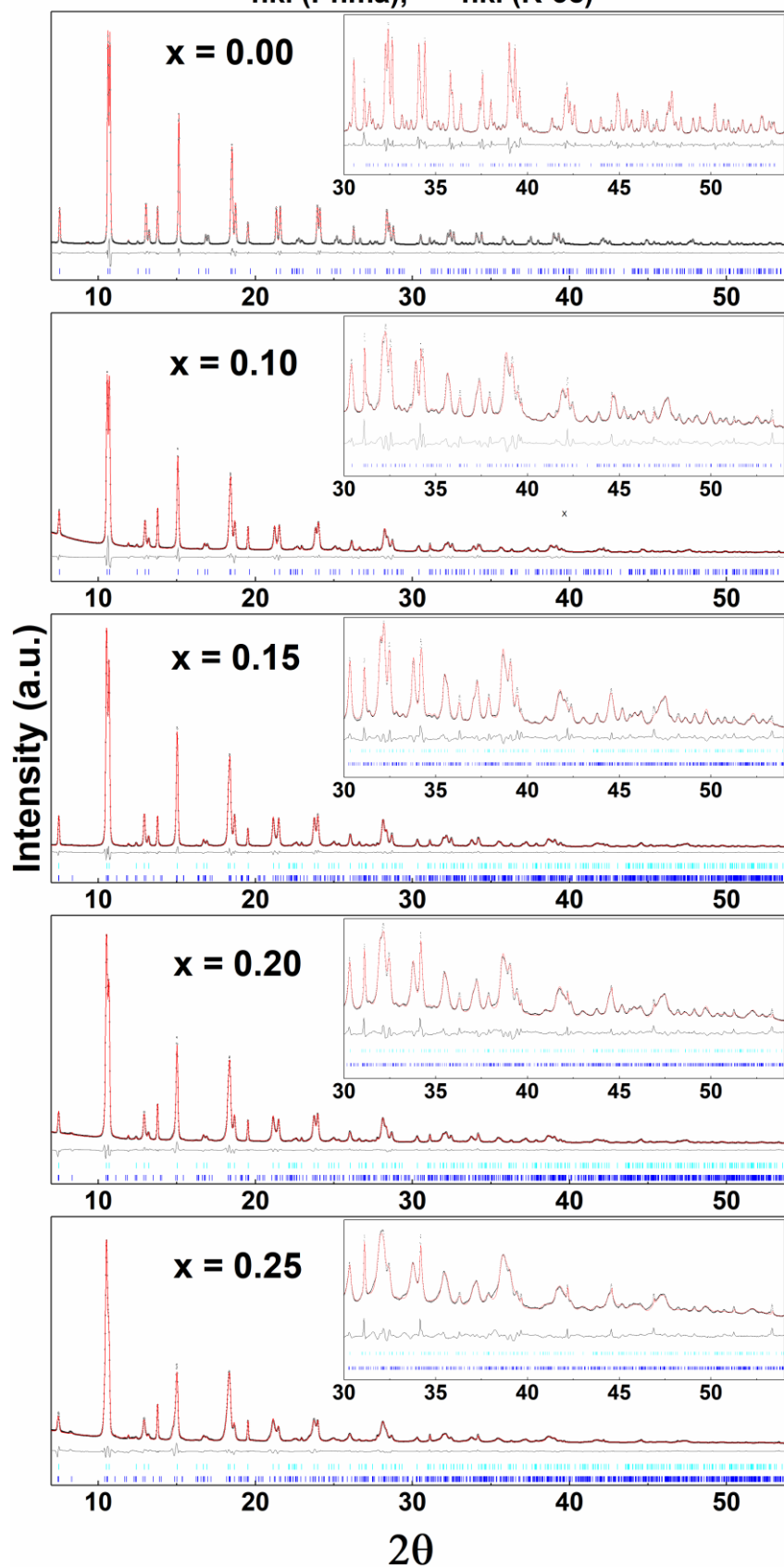
- [1] B. Li, D. Louca, S. Yano, L.G. Marshall, J. Zhou, J.B. Goodenough, Insulating pockets in metallic LaNiO_3 , *Advanced Electronic Materials* 2 (2) (2016) 1500261.
- [2] J.S. Zhou, J.B. Goodenough, B. Dabrowski, Exchange interaction in the insulating phase of RNiO_3 , *Phys. Rev. Lett.* 95 (12) (2005) 127204.

- [3] J.S. Zhou, J.B. Goodenough, Chemical bonding and electronic structure of $RNiO_3$, R = rare earth, *Phys. Rev. B* 69 (15) (2004) 153105.
- [4] S. Kumar, Ø. Fjellvåg, A.O. Sjøstad, H. Fjellvåg, Physical properties of Ruddlesden-Popper ($n = 3$) nickelate: $La_4Ni_3O_{10}$, *J. Magn. Mater.* 496 (2020) 165915.
- [5] M. Periyasamy, L. Patrab, Ø.S. Fjellvåg, P. Ravindranb, H.S. Magnus, K. Susmit, A.O. Sjøstad, H. Fjellvåg, Electron Doping of $La_4Ni_3O_{10}$ by Aluminium Substitution, *submitted, 2020.
- [6] K. Rajeev, A. Raychaudhuri, Quantum corrections to the conductivity in a perovskite oxide - a low-temperature study of $LaNi_{1-x}Co_xO_3$ ($0 \leq x \leq 0.75$), *Phys. Rev. B* 46 (3) (1992) 1309–1320.
- [7] K.P. Rajeev, G.V. Shivashankar, A.K. Raychaudhuri, Low-temperature electronic properties of a normal conducting perovskite oxide ($LaNiO_3$), *Solid State Commun.* 79 (7) (1991) 591–595.
- [8] J.S. Zhou, L.G. Marshall, J.B. Goodenough, Mass enhancement versus Stoner enhancement in strongly correlated metallic perovskites: $LaNiO_3$ and $LaCuO_3$, *Phys. Rev. B* 89 (24) (2014) 245138.
- [9] D. Li, K. Lee, B.Y. Wang, M. Osada, S. Crossley, H.R. Lee, Y. Cui, Y. Hikita, H.Y. Hwang, Superconductivity in an infinite-layer nickelate, *Nature* 572 (7771) (2019) 624–627.
- [10] S. Vasala, M. Karppinen, $A_2B'B'O_6$ perovskites: a review, *Prog. Solid State Chem.* 43 (1–2) (2015) 1–36.
- [11] C. Meneghini, S. Ray, F. Liscio, F. Bardelli, S. Mobilio, D.D. Sarma, Nature of "Disorder" in the ordered double perovskite Sr_2FeMoO_6 , *Phys. Rev. Lett.* 103 (4) (2009), 046403.
- [12] D.D. Sarma, S. Ray, K. Tanaka, M. Kobayashi, A. Fujimori, P. Sanyal, H.R. Krishnamurthy, C. Dasgupta, Intergranular Magnetoresistance in Sr_2FeMoO_6 from a magnetic tunnel barrier Mechanism across grain boundaries, *Phys. Rev. Lett.* 98 (15) (2007) 157205.
- [13] H. Guo, Z.W. Li, L. Zhao, Z. Hu, C.F. Chang, C.Y. Kuo, W. Schmidt, A. Piovano, T.W. Pi, O. Sobolev, D.I. Khomskii, L.H. Tjeng, A.C. Komarek, Antiferromagnetic correlations in the metallic strongly correlated transition metal oxide $LaNiO_3$, *Nat. Commun.* 9 (1) (2018) 43.
- [14] K. Dey, W. Hergett, P. Telang, M.M. Abdel-Hafiez, R. Klingeler, Magnetic properties of high-pressure optical floating-zone grown $LaNiO_3$ single crystals, *J. Cryst. Growth* 524 (2019) 125157.
- [15] J.L. Garcia-Munoz, J. Rodriguez-Carvajal, P. Lacorre, J.B. Torrance, Neutron-diffraction study of $RNiO_3$ ($R = La, Pr, Nd, Sm$): electronically induced structural changes across the metal-insulator transition, *Phys. Rev. B Condens. Matter* 46 (8) (1992) 4414–4425.
- [16] P. Lacorre, J.B. Torrance, J. Pannetier, A.I. Nazzari, P.W. Wang, T.C. Huang, Synthesis, crystal structure, and properties of metallic praseodymium nickel oxide ($PrNiO_3$): comparison with metallic neodymium nickel oxide ($NdNiO_3$) and semiconducting samarium nickel oxide ($SmNiO_3$), *J. Solid State Chem.* 91 (2) (1991) 225–237.
- [17] J.A. Alonso, M.J. Martínez-Lope, M.T. Casais, J.L. García-Muñoz, M.T. Fernández-Díaz, M.A.G. Aranda, High-temperature structural evolution of $RNiO_3$ ($R = Ho, Y, Er, Lu$) perovskites: Charge disproportionation and electronic localization, *Phys. Rev. B* 64 (9) (2001), 094102.
- [18] J. Androulakis, Z. Viskadourakis, N. Katsarakis, J. Giapintzakis, Magnetoresistance And Percolation in the $LaNi_{1-x}Co_xO_3$ Solid Solution, 2003.
- [19] J.A. Alonso, J.L. García-Muñoz, M.T. Fernández-Díaz, M.A.G. Aranda, M.J. Martínez-Lope, M.T. Casais, Charge Disproportionation in $RNiO_3$ perovskites: simultaneous metal-insulator and structural Transition in $YNiO_3$, *Phys. Rev. Lett.* 82 (19) (1999) 3871–3874.
- [20] N.Y. Vasanthacharya, P. Ganguly, J.B. Goodenough, C.N.R. Rao, Valence states and magnetic properties of $LaNi_{1-x}Mn_xO_3$ (for $0 \leq x \leq 0.2$ and $x = 0.5$), *J. Phys. C Solid State Phys.* 17 (15) (1984) 2745–2760.
- [21] K. Asai, H. Sekizawa, K. Mizushima, S. Iida, Magnetic Properties of $LaNi_{1-x}Co_xO_3$ ($0 \leq x \leq 0.5$), *J. Phys. Soc. Jpn.* 43 (3) (1977) 1093–1094.
- [22] K. Asai, H. Sekizawa, K. Mizushima, S. Iida, Magnetic Properties of $LaNi_{1-x}Fe_xO_3$ ($0 \leq x \leq 0.2$), *J. Phys. Soc. Jpn.* 45 (4) (1978) 1417–1418.
- [23] C. Schinzer, Spin-glass behavior of disordered perovskite $LaNi_{1/2}Rh_{1/2}O_3$, *J. Alloys Compd.* 288 (1–2) (1999) 65–75.
- [24] P.D. Battle, J.F. Vente, Structural and magnetic Characterization of La_2NiRhO_6 , *J. Solid State Chem.* 146 (1) (1999) 163–167.
- [25] C.N.R. Rao, O.M. Parkash, P. Ganguly, Electronic and magnetic properties of $LaNi_{1-x}Co_xO_3$, $LaCo_{1-x}Fe_xO_3$ and $LaNi_{1-x}Fe_xO_3$, *J. Solid State Chem.* 15 (2) (1975) 186–192.
- [26] Goodenough, J.B., Magnetism And the Chemical Bond. Interscience Monographs on chemistry, Inorganic Chemistry Section. Vol. vol. 1. 1963, New York: Interscience.
- [27] A.E. Smith, A.W. Sleight, M.A. Subramanian, Electrical and magnetic properties of new rhodium perovskites: La_2MRhO_6 , $M = Cr, Fe, Cu$, *Mater. Res. Bull.* 45 (4) (2010) 460–463.
- [28] K. Yamaura, Q. Huang, D.P. Young, Y. Noguchi, E. Takayama-Muromachi, Crystal structure and electronic and magnetic properties of the bilayered rhodium oxide $Sr_3Rh_2O_7$, *Phys. Rev. B* 66 (13) (2002) 134431.
- [29] R.S. Perry, F. Baumberger, L. Balicas, N. Kikugawa, N.J.C. Ingle, A. Rost, J.F. Mercure, Y. Maeno, Z.X. Shen, A.P. Mackenzie, Sr_2RhO_4 : a new, clean correlated electron metal, *New J. Phys.* 8 (9) (2006) 175, 175.
- [30] K. Yamaura, E. Takayama-Muromachi, Enhanced paramagnetism of the 4d itinerant electrons in the rhodium oxide perovskite $SrRhO_3$, *Phys. Rev. B Condens. Matter* 64 (22) (2001) 2244241–2244245.
- [31] W. van Beek, O.V. Safonova, G. Wiker, H. Emerich, SNBL, a dedicated beamline for combined in situ X-ray diffraction, X-ray absorption and Raman scattering experiments, *Phase Transitions* 84 (8) (2011) 726–732.
- [32] A.A. Coelho, TOPAS and TOPAS-Academic: an optimization program integrating computer algebra and crystallographic objects written in C++, *J. Appl. Crystallogr.* 51 (1) (2018) 210–218.
- [33] T. Kojima, K. Nomura, Y. Miyazaki, K. Tanimoto, Synthesis of various $LaMO_3$ Perovskites in molten carbonates, *J. Am. Ceram. Soc.* 89 (12) (2006) 3610–3616.
- [34] B. Ravel, M. Newville, A. Athena, HEPHAESTUS: data analysis for X-ray absorption spectroscopy using IFEFFIT, *J. Synchrotron Radiat.* 12 (Pt 4) (2005) 537–541.
- [35] P.T. Barton, R. Seshadri, M.J. Rosseinsky, Electrical and magnetic properties of the complete solid solution series between $SrRuO_3$ and $LaRhO_3$: Filling t_{2g} versus tilting, *Phys. Rev. B Condens. Matter* 83 (6) (2011), 064417/1-064417/8.
- [36] A.M. Glazer, The classification of tilted octahedra in perovskites, *Acta Crystallogr. B* 28 (11) (1972) 3384–3392.
- [37] J. Li, A.E. Smith, K.-S. Kwong, C. Powell, A.W. Sleight, M.A. Subramanian, Lattice crossover and mixed valency in the $LaCo_{1-x}Rh_xO_3$ solid solution, *J. Solid State Chem.* 183 (6) (2010) 1388–1393.
- [38] J. Rodríguez-Carvajal, M. Hennion, F. Moussa, A.H. Moudden, L. Pinsard, A. Revcolevschi, Neutron-diffraction study of the Jahn-Teller transition in stoichiometric $LaMnO_3$, *Phys. Rev. B* 57 (6) (1998) R3189–R3192.
- [39] L. Vegard, Die Konstitution der Mischkristalle und die Raumfüllung der Atome, *Z. Phys.* 5 (1) (1921) 17–26.
- [40] R.D. Shannon, Revised effective ionic radii and systematic studies of interatomic distances in halides and chalcogenides, *Acta Crystallogr. A* 32 (5) (1976) 751–767.
- [41] S. Shibusaki, Y. Takahashi, I. Terasaki, Thermoelectric properties of $LaRh_{1-x}Ni_xO_3$, *J. Phys. Condens. Matter* 21 (11) (2009) 115501/1–115501/4.
- [42] Y. Kagan, V.N. Flerov, Theory of the resistivity and magnetoresistance of metals at low temperatures, *J. Exp. Theor. Phys.* 66 (4) (1974) 1374–1386.
- [43] A. Chainani, D.D. Sarma, I. Das, E.V. Sampathkumaran, Low-temperature electrical conductivity of $LaNi_{1-x}Fe_xO_3$, *J. Phys. Condens. Matter* 8 (43) (1996) L631–L636.
- [44] I. Chaitanya Lekshmi, A. Gayen, M.S. Hegde, Electrical transport properties of $LaNi_{1-x}M_xO_3$ ($M = Co, Mn$) thin films fabricated by pulsed laser deposition, *J. Phys. Condens. Matter* 17 (41) (2005) 6445–6458.
- [45] E. Niwa, C. Uematsu, E. Miyashita, T. Ohzeki, T. Hashimoto, Conductivity and sintering property of $LaNi_{1-x}Fe_xO_3$ ceramics prepared by Pechini method, *Solid State Ionics* 201 (1) (2011) 87–93.
- [46] I.G. Austin, N.F. Mott, Polarons in crystalline and non-crystalline materials, *Adv. Phys.* 50 (7) (2001) 757–812.
- [47] D. Varshney, N. Dodiya, Metallic and semi-conducting resistivity behaviour of $La_{0.7}Ca_{0.3-x}K_xMnO_3$ ($x = 0.05, 0.1$) manganites, *J. Theor. Appl. Phys.* 9 (1) (2015) 45–58.
- [48] N.F. Mott, in: E.A. Davis (Ed.), *Electronic Processes in Non-crystalline Materials*, second ed. The International Series of Monographs on Physics, Clarendon Press, Oxford, 1979.
- [49] N.F. Mott, Conduction in glasses containing transition metal ions, *J. Non-Cryst. Solids* 1 (1) (1968) 1–17.
- [50] A.L. Efros, B.I. Shklovskii, Coulomb gap and low temperature conductivity of disordered systems, *J. Phys. C Solid State Phys.* 8 (4) (1975) L49–L51.
- [51] R.J.D. Tilley, *Understanding Solids: the Science of Materials*, second ed., Wiley, Chichester, 2013.
- [52] M. Balanda, *AC Susceptibility Studies of Phase Transitions and Magnetic Relaxation: Conventional, Molecular and Low-Dimensional Magnets*, 2013, pp. 964–976.
- [53] V.K. Anand, D.T. Adroja, A.D. Hillier, A.D. Anand, Ferromagnetic cluster spin-glass behavior in $PrRhSn_3$, *Phys. Rev. B Condens. Matter* 85 (1) (2012).

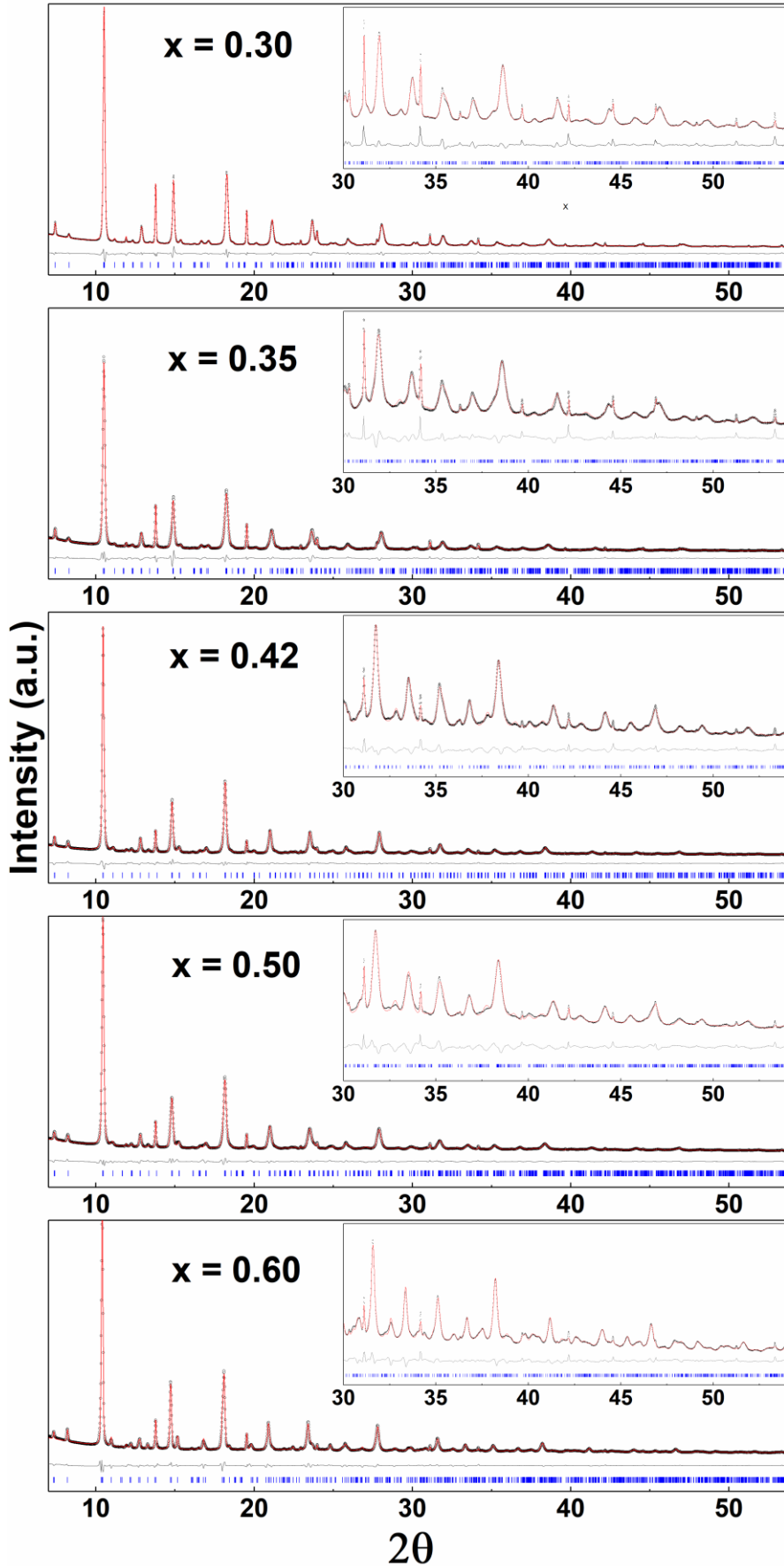
Supplemental data and information

■ Observed, — Calculated, — Difference

■ hkl (Pnma), ■ hkl (R-3c)



• Observed, — Calculated, — Difference, | hkl (Pnma)



■ Observed, — Calculated, — Difference, · hkl (Pnma)

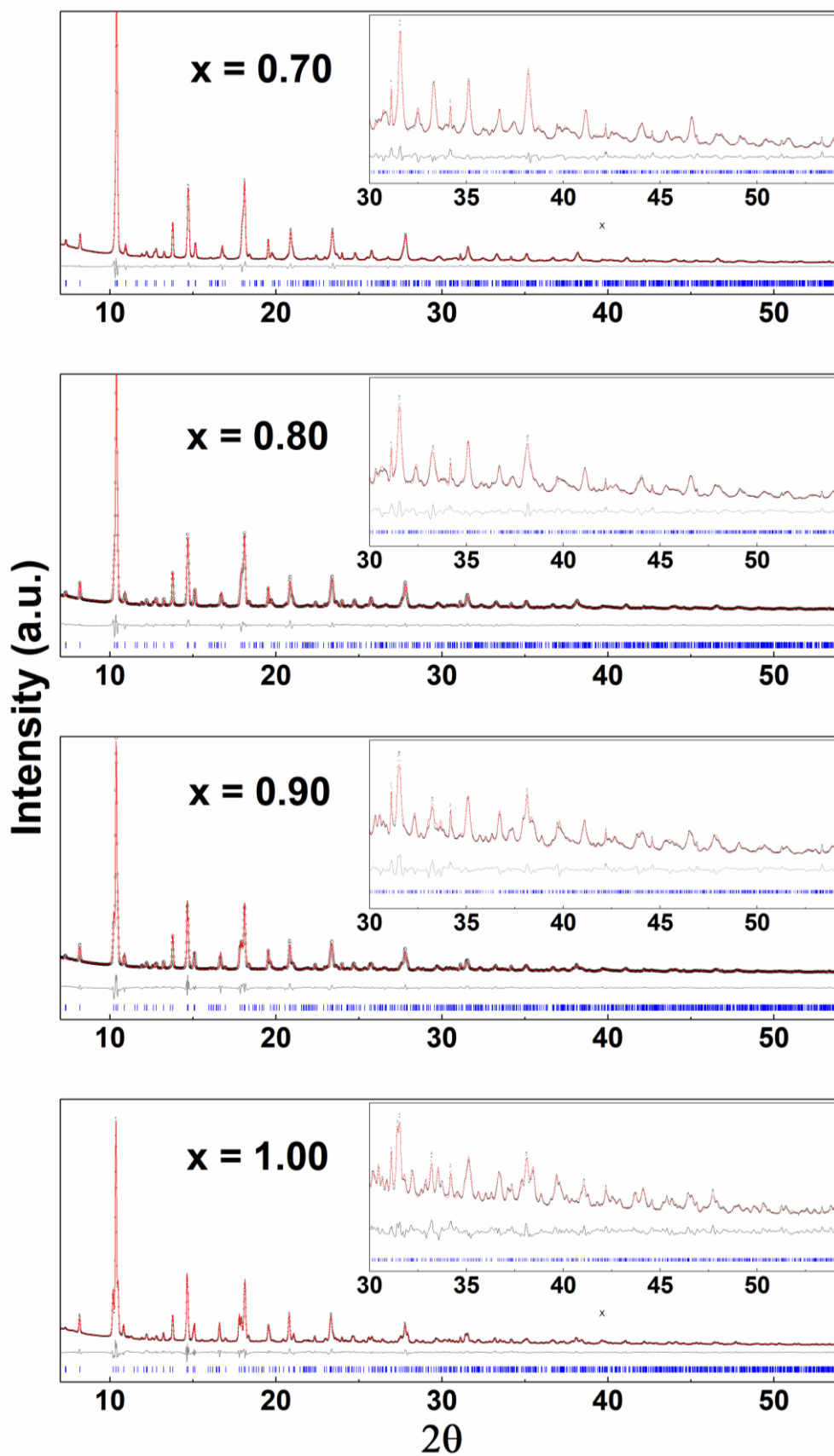


Figure S1. Rietveld refinements for all samples in the system $\text{LaNi}_{1-x}\text{Rh}_x\text{O}_3$.

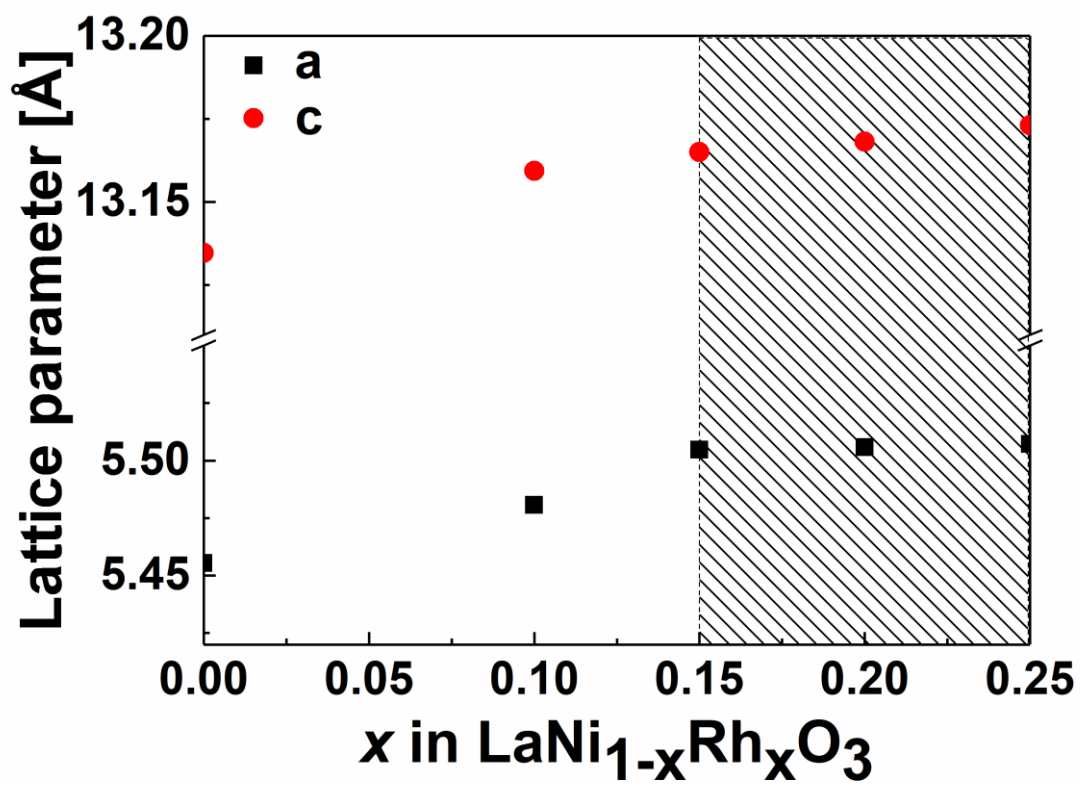


Figure S2. Lattice parameters for the rhombohedral (*R-3c*) samples in the perovskite system $\text{LaNi}_{1-x}\text{Rh}_x\text{O}_3$.

Table S1. List of M-O-distances [Å] and M-O-M bond angles in $\text{LaNi}_{1-x}\text{Rh}_x\text{O}_3$ ($0 \leq x \leq 1$) extracted from Rietveld refinements using TOPAS, where M is the B-site element. The La-O distance is the average of the 8 shortest La-O bonds. The Goldschmidt t-factor is calculated from the average of the 8 shortest La-O bonds and the 6 M-O bonds. The estimated standard deviation (brackets) are collected from Topas during Rietveld refinements.

x	M-O	M-O	M-O	M-O-M	M-O-M	La-O (avg.)	t-factor
0	1.9334(3)			165.38(16)		2.623(3)	0.96
0.1	1.9461(5)			163.4(3)		2.622(4)	0.95
0.3	1.934(16)	1.975(4)	2.034(16)	157.2(10)	160.8(15)	2.602(16)	0.93
0.35	1.96(2)	2.000(7)	2.01(2)	157.4(15)	152.7(18)	2.586(22)	0.92
0.42	1.982(17)	2.007(5)	2.032(16)	155.1(10)	154.0(13)	2.579(15)	0.91
0.5	1.955(18)	1.990(5)	2.085(17)	152.6(10)	158.3(16)	2.584(15)	0.91
0.6	1.977(15)	2.046(5)	2.064(14)	154.9(8)	147.7(11)	2.573(14)	0.90
0.7	2.004(12)	2.041(12)	2.049(4)	155.0(7)	147.6(8)	2.573(12)	0.90
0.8	2.029(12)	2.030(13)	2.058(4)	154.2(7)	146.3(8)	2.572(12)	0.89
0.9	2.028(10)	2.043(3)	2.060(10)	151.3(5)	149.6(7)	2.573(10)	0.89
1	1.999(11)	2.073(3)	2.086(10)	152.2(6)	144.4(6)	2.558(10)	0.88

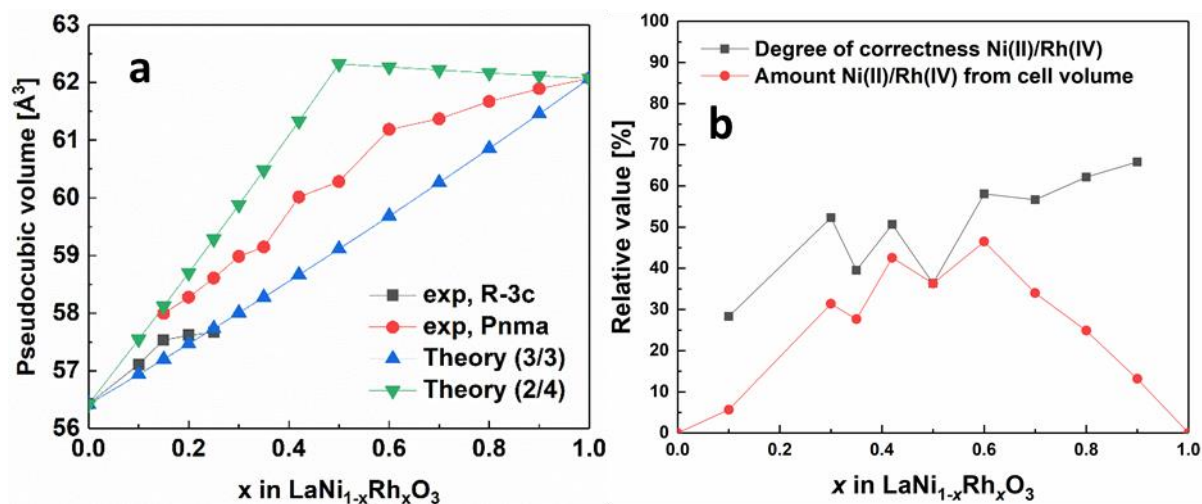


Figure S3. a) Comparison of experimental pseudocubic volume and calculated pseudocubic volume for the two different scenarios with valence states of Ni(III)/Rh(III) and Ni(II)/Rh(IV). The calculations are done from the experimental volume of LaNiO_3 and LaRhO_3 and tabulated ionic radii from Shannon [1] of the different species. b) Relative degree of how correct the model of Ni(II)/Rh(IV) is (black), where 1 means that the model is in perfect fit with experimental unit cell volume data. The relative amount of Ni(II) and Rh(IV) this translates to is shown in red (1 means all B-site atoms are either Ni(II) or Rh(IV)).

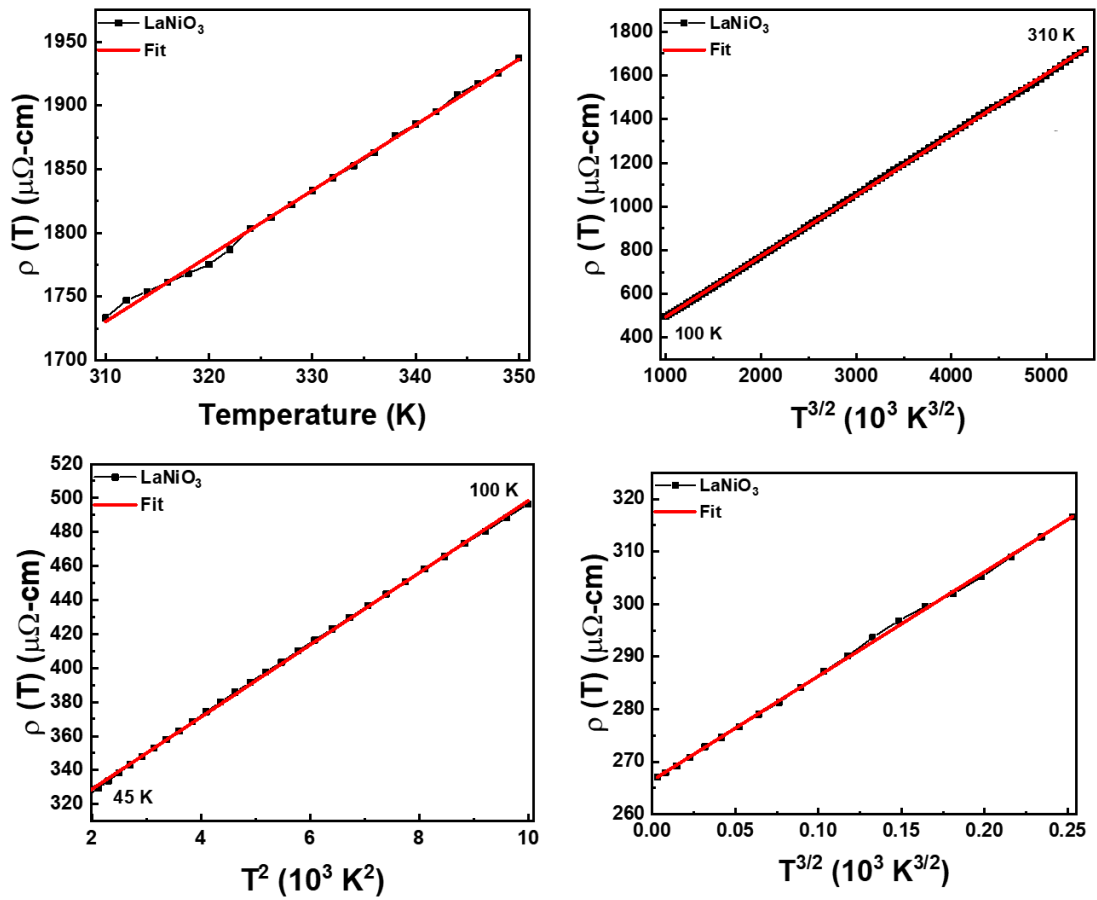


Figure S4. Linear fits for the metallic sample LaNiO_3 , plotted vs different temperature dependencies as shown in the figure.

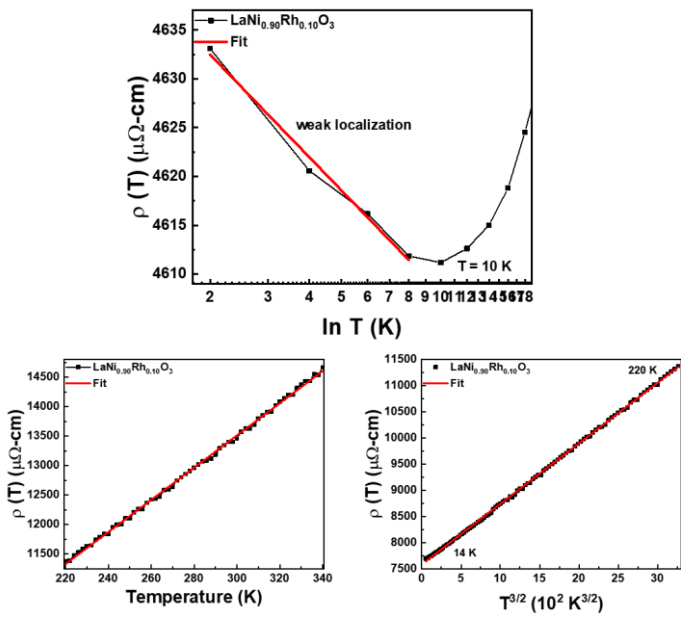


Figure S5. Linear fits for different temperature dependencies for $\text{LaNi}_{0.90}\text{Rh}_{0.10}\text{O}_3$.

Table S2. Results from analysis of temperature [K] dependence of $x = 0.00$ and $x = 0.10$ in $\text{LaNi}_{1-x}\text{Rh}_x\text{O}_3$.

$\text{LaNi}_{1-x}\text{Rh}_x\text{O}_3$	T	$T^{3/2}$	T^2	T^3	Weak localization
$x = 0.00$	$T > 200$	60 – 200, 4 – 28	32 – 60		
$x = 0.10$	$T > 200$	30 – 200		12 – 28	$T < 10$

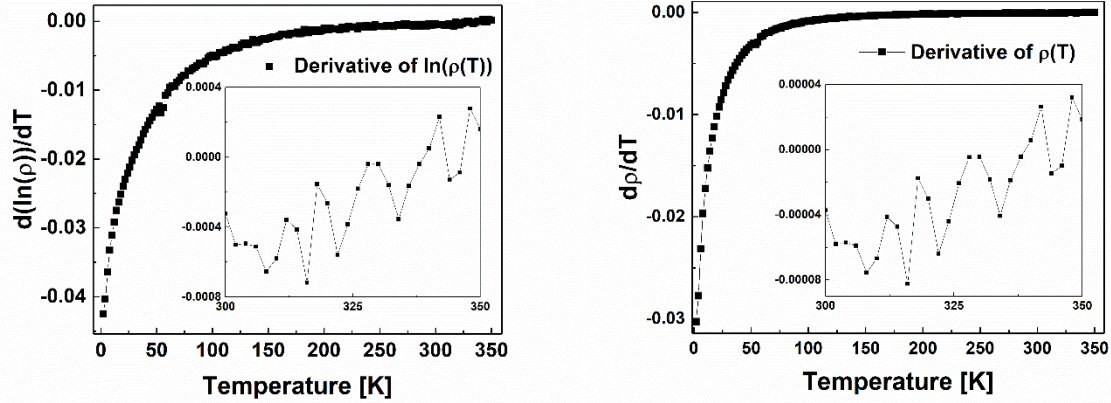


Figure S6. Analysis of temperature dependence of resistivity for $\text{LaNi}_{0.70}\text{Rh}_{0.30}\text{O}_3$. A negative value indicates insulating behaviour, which simply translates to a reduction in resistivity upon lowering of the temperature.

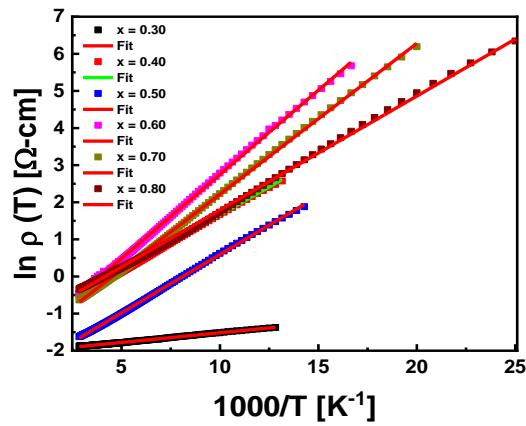


Figure S7. $1/T$ Arrhenius fit to find activation energies of the insulating compounds with $0.30 \leq x \leq 0.80$.

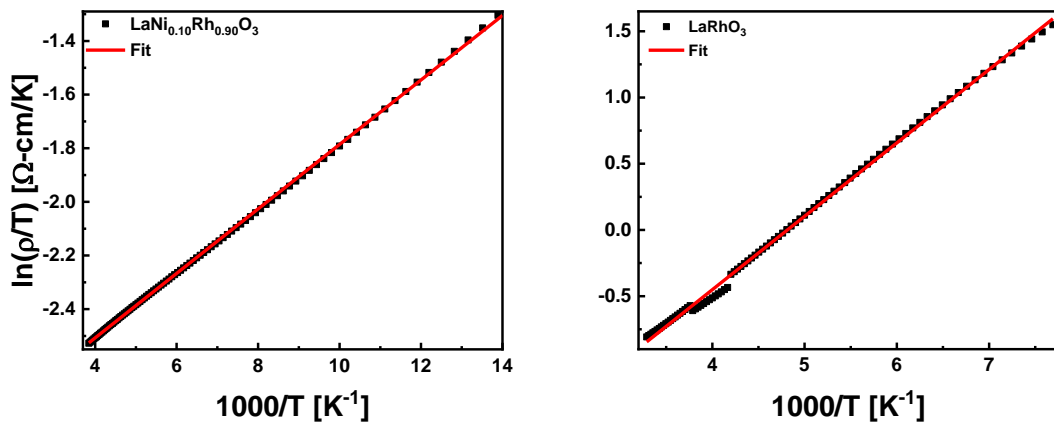


Figure S8. Fit of $\text{LaNi}_{0.10}\text{Rh}_{0.90}\text{O}_3$ (main graph) and LaRhO_3 using the fitting equation for the polaron model ($\rho = \rho_0 T \exp\left(\frac{W_H}{kT}\right)$).

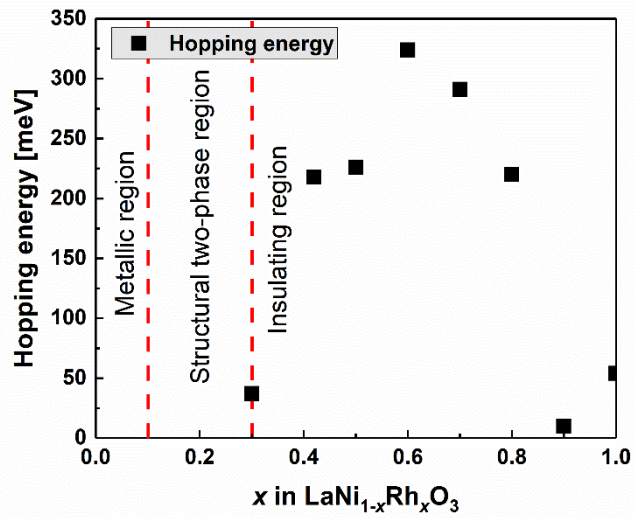


Figure S9. Activation energy for hopping for all insulating samples ($x \geq 0.30$) in the $\text{LaNi}_{1-x}\text{Rh}_x\text{O}_3$ system.

Table S3. Table summarizing results found from resistivity analysis. The left part is the high temperature region, the right part is the low temperature region. Arrhenius equation used is $\rho = \rho_0 \exp\left(\frac{W_H}{kT}\right)$, equation used for polaron model is $\rho = \rho_0 T \exp\left(\frac{W_H}{kT}\right)$, and the equation used for the variable range hopping (VRH) is $\rho = \rho_0 \exp\left(\frac{T_0}{T}\right)^{\frac{1}{\alpha}}$, $\alpha = 4$ (Mott 3D), 3 (Mott 2D), 2 (ES 2D)

x	T-interval [K]	Model	W_H [eV]	R^2	m_p/m^*	T-interval [K]	$\log \rho \propto$
0.30	70-320	Arrhenius	0.03735	99.97		30-80	$T^{-\frac{1}{4}}$
0.42	70-320	Arrhenius	0.21778	99.97		30-80	$T^{-\frac{1}{3}}$
0.50	70-320	Arrhenius	0.22558	99.98		30-80	$T^{-\frac{1}{3}}$
0.60	60-320	Arrhenius	0.32448	99.98		30-70	$T^{-\frac{1}{2}}$
0.70	50-320	Arrhenius	0.29123	99.98		30-70	$T^{-\frac{1}{2}}$
0.80	40-320	Arrhenius	0.21996	99.97		30-70	$T^{-\frac{1}{2}}$
0.90	70-300	Polaron	0.01054	99.97	2.6	30-70	$T^{-\frac{1}{2}}$
1.00	130-310	Polaron	0.05351	99.96	119	110-150	$T^{-\frac{1}{2}}$

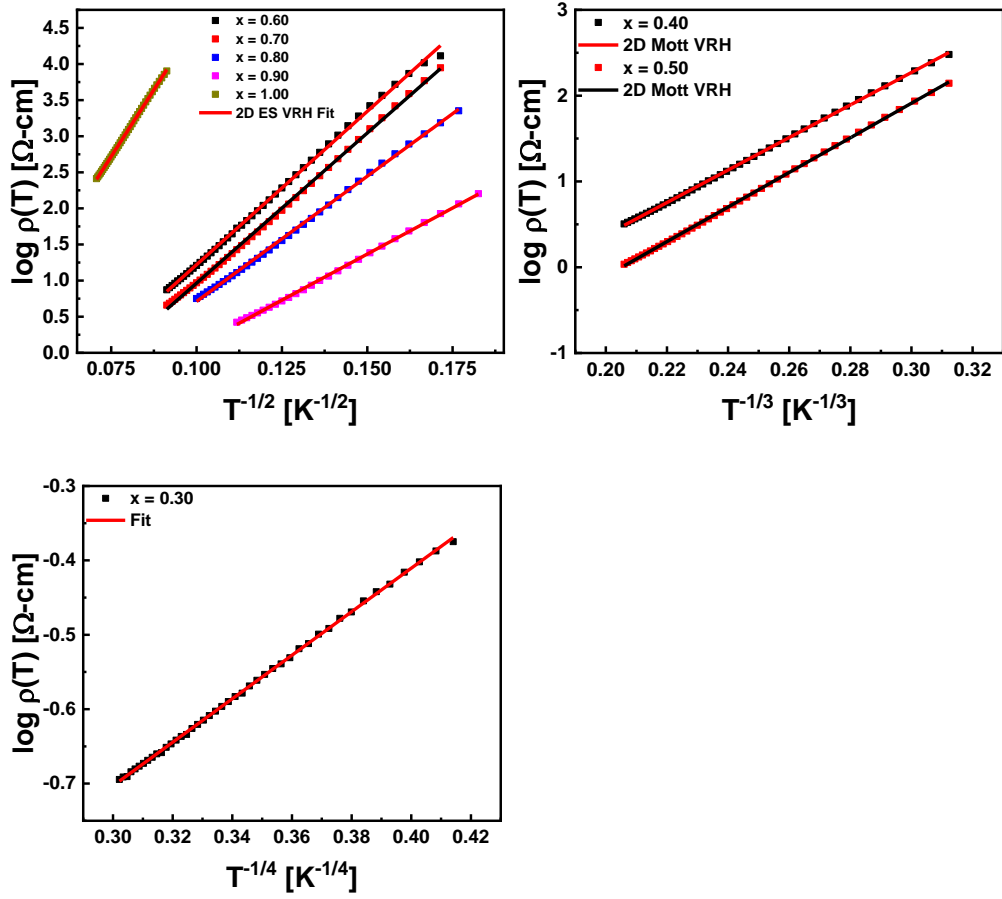


Figure S10. Top left: $T^{-1/2}$ -fit showing fit to 2D ES variable range hopping, top right: $T^{-1/3}$ -fit to show fit to 2D Mott variable range hopping, bottom left: $T^{-1/4}$ -fit to show fit to 2D Mott variable range hopping.

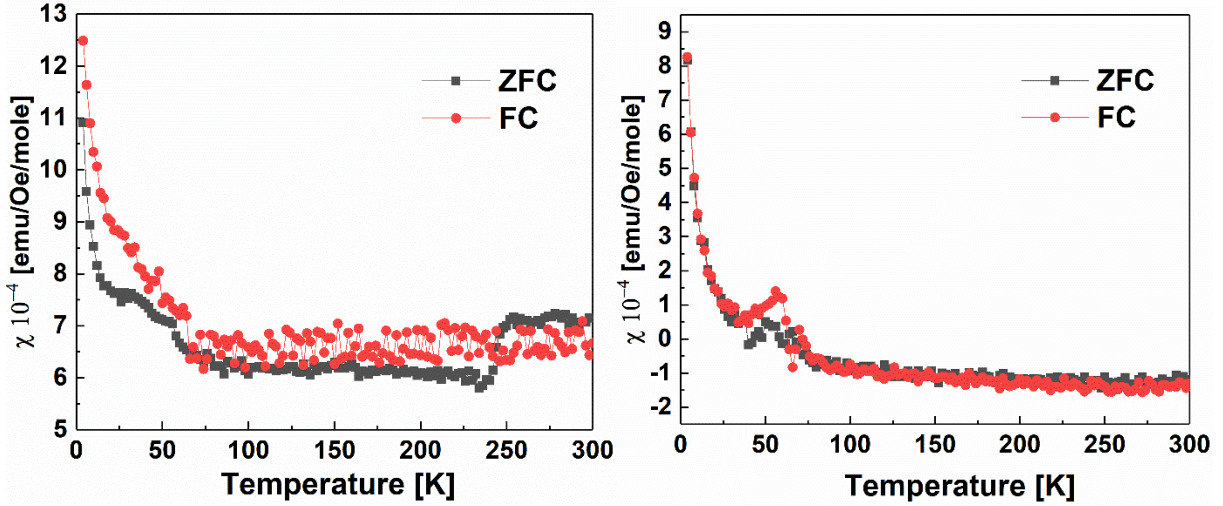


Figure S11. DC magnetic measurements of LaNiO₃ (left) and LaRhO₃ (right) as function of temperature, measured using a 0.2 T DC persistent field.

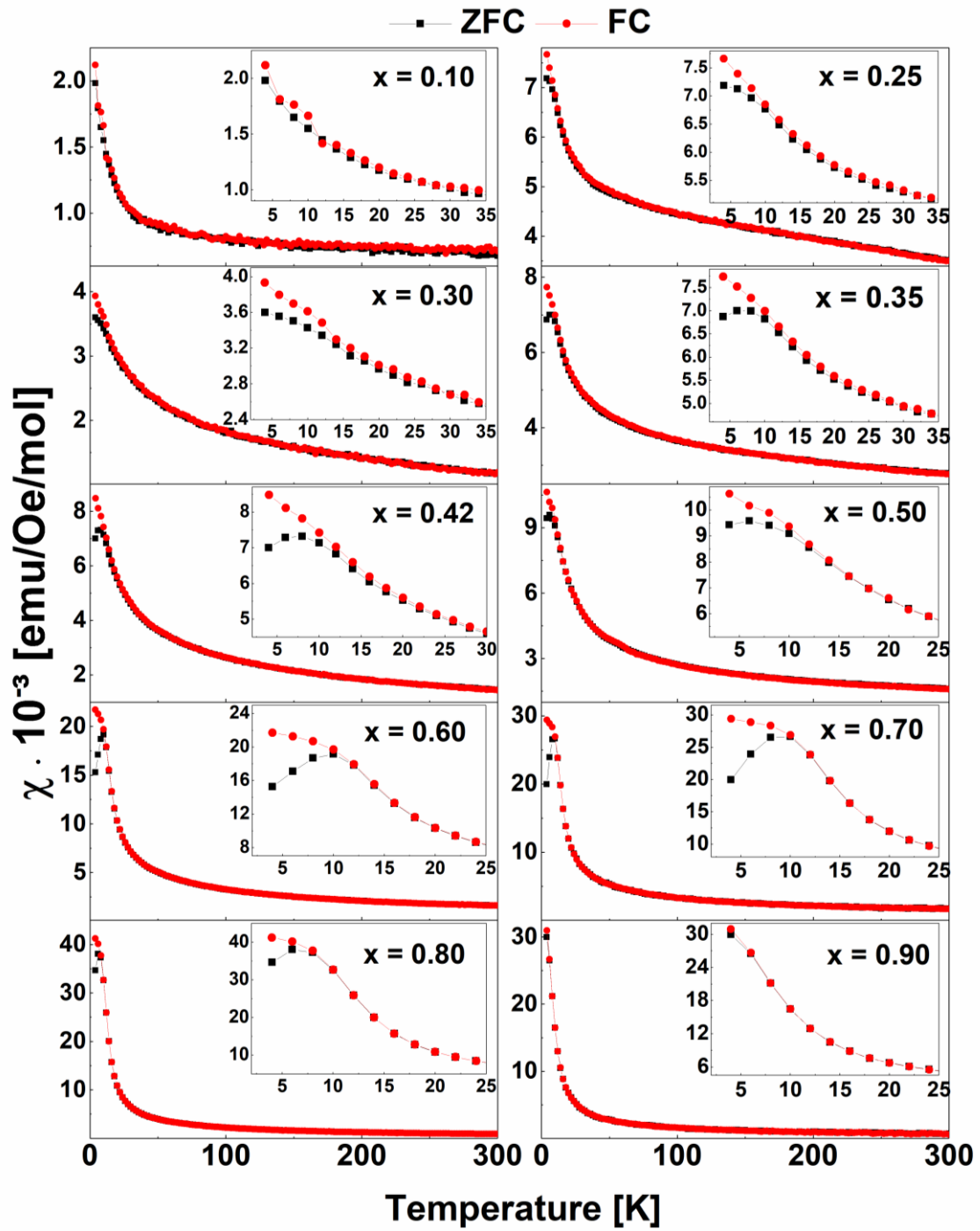


Figure S12. DC magnetic susceptibility of $\text{LaNi}_{1-x}\text{Rh}_x\text{O}_3$ as a function of temperature measured using a 0.2 T persistent field. The composition of the sample measured is indicated with a x -value in the upper right corner of each measurement.

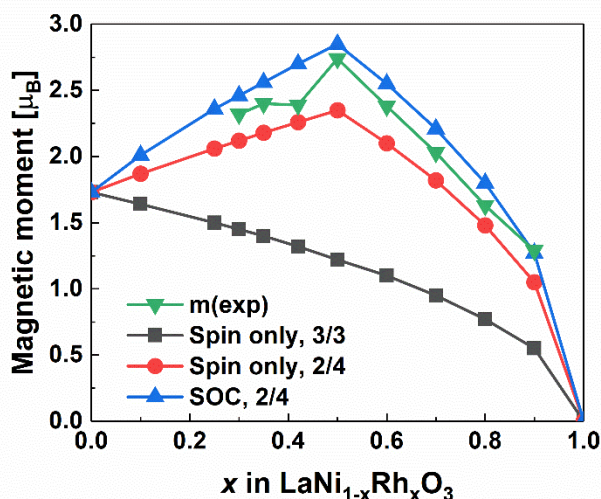


Figure S13. Comparison between experimental magnetic moment using the Curie-Weiss relation and the theoretical magnetic moment calculated assuming free spins.

The three models that were considered are explained below, with the data summarized in Table S4.

1. Spin only values of low spin Ni(III) and Rh(III).
2. For $x = 0.50$ only Ni(II) and Rh(IV) exist. For $x < 0.50$ the amount of Ni(II) and Rh(IV) equals x , while the amount of Ni(III) equals $2x$. For $x > 0.50$ the amount of Ni(II) and Rh(IV) equals $(x - 0.50)$, while the amount of Rh(III) equals $2(x - 0.50)$. All ions are in the low spin state, and spin only values are used.
3. Same as model 2, except that Rh(IV) has a contribution from spin orbit coupling, considering an electronic configuration of t_{2g}^5 .

Table S4. Experimental and theoretical magnetic moment of LaNi_{1-x}Rh_xO₃ (all units are in μ_B), and the θ -value, calculated using the Curie-Weiss relation.

	1	2	3	Experimental	Experimental
	Spin only	Spin only	SOC*	150-300 K	150-300 K
x	μ (theo.)	μ (theo.)	μ (theo.)	μ (exp.)	θ
0.00	1.73	1.73	1.73	P.P.	P.P.
0.10	1.64	1.87	2.01	3.15	-1500.2
0.30	1.45	2.12	2.46	2.32	-277.2
0.35	1.40	2.18	2.56	2.40	-286.7
0.42	1.32	2.26	2.70	2.39	-192.4
0.50	1.22	2.35	2.85	2.74	-279.7
0.60	1.10	2.10	2.55	2.38	-142.5
0.70	0.95	1.82	2.21	2.03	-99.0
0.80	0.77	1.48	1.80	1.63	-70.4
0.90	0.55	1.05	1.27	1.29	-14.7
1.00	0	0	0	Diamagnetic	Diamagnetic

*includes spin orbit coupling (SOC). P.P. means Pauli Paramagnetic.

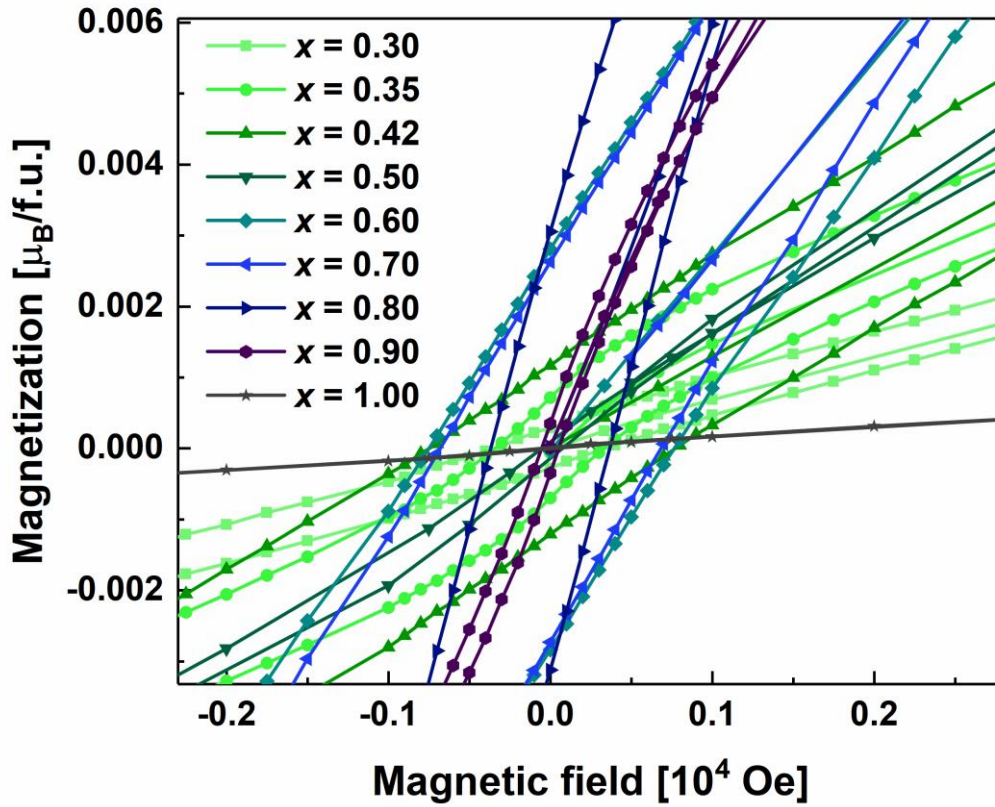


Figure S14. Field dependent magnetization measurements of selected members ($x = 0.30, 0.35, 0.42, 0.50, 0.60, 0.70, 0.80, 0.90, 1.00$) in the $\text{LaNi}_{1-x}\text{Rh}_x\text{O}_3$ series at $T = 4$ K between -2.3 and 2.8 kOe, zoomed in on low field values. The sample compositions are indicated in the figure by its x value. The intensity unit is in Bohr magnetons per formula unit ($\mu_B/\text{f.u.}$).

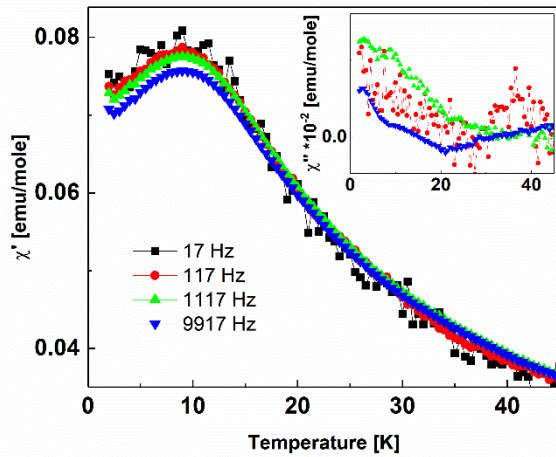


Figure S15. AC-magnetization measurement of $\text{LaNi}_{0.50}\text{Rh}_{0.50}\text{O}_3$ using a 2000 Oe external DC-field, a 10 Oe AC field and the AC-field frequencies indicated in the figure.

Analysis of resistivity in the polaron model.

Analysis of resistivity in the polaron model [2].

The difference between the Arrhenius model and the polaron model is the relative hopping frequency of the electrons and the phonons. In the Arrhenius model, the hopping frequency of electrons is higher than that of the phonons, so the phonons simply scatter the electrons and cause resistance. For the polaron, the phonons move with a sufficiently high frequency to aid the movement of the electron, lowering the activation energy for electron hopping.

In our analysis, we first fit the temperature dependent resistivity using the relation

$$\rho = \rho_0 T \exp\left(\frac{W_H}{k_B T}\right), \text{ where } \rho_0 = \frac{ne^2 R^2 \omega_0}{k_B}$$

Where n is the density of polaron, ω_0 is the optical phonon frequency, k_B is the Boltzmann constant, e is the electron charge and R is the hopping distance of the phonon. We then calculate the optical phonon frequency (ω_0) using the activation energy for hopping and the estimated Debye temperature (θ_D), using the equation below.

$$\omega_0 = \frac{\theta_D k_B}{h}$$

Where h is Planck's constant. In our calculation, we use a Debye temperature of 260 K, estimated from the change in slope in the resistivity measurements, and we use the same value for $x = 0.90$ and $x = 1.00$ due to their structural similarity.

In Holstein's polaron model [3], we can calculate the polaron band width J and the electron transfer integral ϕ from the equations below.

$$J = 0.67 h \omega_0 (T/\theta_D)^{1/4}, \quad \phi = (2k_B T W_H / \pi)^{1/4} (h \omega_0 / \pi)^{1/2}$$

Furthermore, we evaluate the relative size of J and ϕ . We find that $J > \phi$, and that confirms that we are correctly in the non-adiabatic polaron model by Holstein [3].

Furthermore, one can estimate the size of the polaron from the polaron band width. The polaron is said to be large for $J > W_H/3$ and small for $J < W_H/3$. From this relation, we find that $x = 0.90$ has a large polaron, while $x = 1.00$ has a small polaron.

Furthermore, we can calculate the electron-phonon coupling constant of the electron-phonon interaction from the equation given below.

$$\gamma_P = 2W_H / h\omega_0$$

For $\gamma_P > 4$, the electron-phonon interaction is said to be strong. We find $\gamma_P = 0.9$ and $\gamma_P = 4.8$ for $x = 0.90$ and $x = 1.00$, respectively, indicating a weak coupling for $x = 0.90$ and strong coupling for $x = 1.00$.

Using the same electron-phonon coupling constant, we can also extract the ratio of effective mass of the polaron m_P to rigid-lattice effective mass m^*

$$m_p = \left(\frac{\hbar^2}{\pi^2 J R^2} \right) e^{\gamma_P} = m^* e^{\gamma_P}.$$

We find m_p/m^* values of 2.6 and 119 for $x = 0.90$ and $x = 1.00$, respectively.

In summary, this means that we have different polarons for the two samples. For $x = 0.90$ we have a large polaron with weak coupling, and thus a small polaron mass. This coincides well with the low activation energy. For $x = 1.00$, we have a small polaron with strong coupling, and thus a large mass. This coincides well with the activation energy that is higher than that of $x = 0.90$. The higher activation energy for $x = 1.00$ is because the polaron is small, heavy and has strong structural deformations during movement.

Finally, we can compare the calculations with the density of state for hopping (DOS) calculated from the model of ES variable range hopping [4]. We find that the DOS is higher for $x = 0.90$ with a factor of ~ 8 . This supports our analysis, and relates in well to the structural features of the materials. For $x = 0.90$, we have 10 % of the B-site atoms as Ni, which is absent in $x = 1.00$. This can cause the higher availability for hopping sites, and thus cause a low activation energy for hopping.

References

1. Shannon, R.D., *Revised effective ionic radii and systematic studies of interatomic distances in halides and chalcogenides*. Acta Crystallographica Section A, 1976. **32**(5): p. 751-767.
2. Austin, I.G. and N.F. Mott, *Polarons in crystalline and non-crystalline materials*. Advances in Physics, 2001. **50**(7): p. 757-812.
3. Mott, N.F., *Electronic processes in non-crystalline materials*. 2nd ed. ed. The International series of monographs on physics, ed. E.A. Davis. 1979, Oxford: Clarendon Press.
4. Efros, A.L. and B.I. Shklovskii, *Coulomb gap and low temperature conductivity of disordered systems*. Journal of Physics C: Solid State Physics, 1975. **8**(4): p. L49-L51.